

# Vertically resolved monitoring of atmospheric aerosols over Portugal with a multi-wavelength Raman lidar

A thesis submitted to the University of Évora  
elaborated at the Évora Geophysics Center  
in Earth and Space Sciences  
by

Jana Preißler

to obtain the degree *Doutoramento Europeu* (European Doctorate).

February 12, 2013

Supervisor: Doutor Frank Wagner  
Co-Supervisor: Prof<sup>a</sup> Dr<sup>a</sup> Ana Maria Guedes de Almeida Silva



## **Abstract: "Vertically resolved monitoring of atmospheric aerosols over Portugal with a multi-wavelength Raman lidar"**

For the first time, lidar measurements were performed in Portugal on a regular basis. Highly resolved measurements of the vertical distribution of aerosols were done with a multi-wavelength Raman lidar at the Évora Geophysics Center (Centro de Geofísica de Évora) (CGE) (38.57° N, 7.91° W, 290 m above sea level (asl)) in Évora since September 2009. A two-year climatology of different types of aerosols is presented within this work. Free tropospheric aerosol layers were characterised regarding their optical properties. Besides regular measurements performed on fixed dates, intensive studies of special events were realised. Aerosol from volcanic eruptions in the free troposphere and stratosphere, forest fire smoke as well as mineral dust from the Sahara were transported towards the southern Iberian peninsula and were investigated thoroughly. For such studies, the data of the ground based lidar were combined with other active and passive remote sensing and ground based in-situ instruments to allow a comprehensive aerosol characterisation.

## **Resumo: "Monitorização dos perfis verticais de aerossóis atmosféricos em Portugal com um Lidar Raman multi-espectral"**

Foram realizadas pela primeira vez em Portugal medições regulares com Lidar. As medições com alta resolução da distribuição vertical dos aerossóis foram efetuadas com um Lidar Raman multi-espectral instalado no Centro de Geofísica de Évora (38.57° N, 7.91° W, 290 m acima do nível do mar) em Évora, desde Setembro de 2009. Neste trabalho é apresentada uma climatologia de dois anos de tipos diferentes de aerossóis. Foram caracterizadas camadas de aerossóis na troposfera livre do ponto de vista das suas propriedades ópticas. Além das medições regulares efetuadas em datas pré estabelecidas, foram também realizados estudos intensivos durante eventos específicos: aerossóis de erupções vulcânicas na troposfera e estratosfera, de incêndios florestais e poeiras minerais do Sahara foram estudados detalhadamente. Nestes casos, os dados de Lidar foram combinados com dados de outros instrumentos de detecção remota activa e passiva e também in-situ instalados na superfície, para obter uma caracterização mais completa dos aerossóis.

## **Zusammenfassung: "Vertikal aufgelöste Beobachtung atmosphärischer Aerosole über Portugal mit einem Mehrwellenlängen-Raman-Lidar"**

Erstmalig wurden regelmäßige Lidarmessungen in Portugal durchgeführt. Mit einem Mehrwellenlängen-Raman-Lidar wird seit September 2009 am Centro de Geofísica de Évora (38.57° N, 7.91° W, 290 m über dem Meeresspiegel) in Évora die vertikale Aerosolverteilung gemessen. Anhand von Daten eines Zeitraumes von zwei Jahren wurde eine Charakterisierung verschiedener Aerosoltypen erstellt. Dafür wurden die optischen Eigenschaften von Aerosolschichten in der freien Troposphäre bestimmt. Neben regelmäßigen Messungen zu festen Zeiten wurden intensive Langzeitmessungen durchgeführt, z. B. von Vulkanaerosol in der Troposphäre und Stratosphäre, Waldbrandaerosol und Wüstenstaub aus der Sahara. Für eine umfassende Untersuchung der Aerosoleigenschaften wurden für diese Studien die Lidardaten mit Daten aus anderen aktiven und passiven Fernerkundungsmessungen sowie bodengebundenen in-situ Messungen kombiniert.

## Acknowledgements

First of all I would like to thank my supervisors, namely Frank Wagner for his supervision, motivation and abundance of patience, but also for a smooth start in the foreign country and working environment; and Ana Maria Silva, for her scientific advice, comments and suggestions, and also for her help in obtaining the scholarship, which enabled me to realise this work. Furthermore, I am thankful to the jury members for reviewing this work.

This work was funded through the scholarship (SFRH/BD/47521/2008) by the Portuguese Foundation for Science and Technology (FCT). Data from external sources were included in some parts of this work, namely model sounding profiles from the Global Data Assimilation System (GDAS), trajectories from the Hybrid Single-Particle Lagrangian Integrated Trajectory (HYSPLIT) model, aerosol forecasts and archives from the models Dust Regional Atmospheric Model (DREAM) and Navy Aerosol Analysis and Prediction System (NAAPS), as well as data from the Terra, Aqua, Landsat and CALIPSO satellite missions by the National Aeronautics and Space Administration (NASA). I want to acknowledge all institutions and individuals involved in creating and providing all these data.

I highly appreciate the education, help and shared experience from the lidar group of the Leibniz-Institute for Tropospheric Research e. V. in Leipzig, Germany. Especially I want to thank Ronny Engelmann for his support with PAOLI from the very beginning, and for valuable advice whenever needed - which was often the case. I would also like to thank Birgit Heese for very interesting hours in the lab setting up PAOLI, as well as Patric Seifert and Ina Mattis for providing lidar data analysis software and data conversion scripts.

I am thankful to the lidar team of the Andalusian Center for Environmental Research in Granada, Spain for their great hospitality and excellent working atmosphere. Namely, I want to express my gratitude to Juan Antonio Bravo-Aranda and Juan Luis Guerrero-Rascado for the fruitful collaboration in Granada and Évora as well as for their friendship.

The participation in the lidar intercomparison campaign in Madrid in October and November 2010 was an invaluable experience. I am thankful for the opportunity of the cooperation with the lidar teams from Potenza, Italy as well as from Madrid, Barcelona and Granada, Spain. I also want to thank for the collaboration and exchange of experience with the colleagues from the European Aerosol Research Lidar Network (EARLINET) and the Spanish and Portuguese Aerosol Lidar Network (SPALINET).

Finally, I am profoundly grateful for the remote, but none the less valuable, support by my family and friends in Germany and around the world. Particularly, I want to thank Karin, Julia and Peter for reading the thesis, finding even smallest mistakes and giving valuable comments. Furthermore, I also want to thank all the new friends I found here, who made my time in Portugal a unique and unforgettable experience.

# Contents

<b>Abstracts</b>	<b>i</b>
<b>Acknowledgements</b>	<b>ii</b>
<b>1. Introduction</b>	<b>1</b>
1.1. Measurement site . . . . .	2
1.2. State of the art . . . . .	3
1.3. Objectives . . . . .	4
1.4. Structure of this thesis . . . . .	5
<b>2. Instrument and methodology</b>	<b>6</b>
2.1. Multi-wavelength Raman lidar PAOLI . . . . .	6
2.1.1. General features . . . . .	6
2.1.2. Optics . . . . .	7
2.2. Lidar data analysis . . . . .	9
2.2.1. Lidar equation . . . . .	9
2.2.2. Radio sounding profiles . . . . .	11
2.2.3. Elastic backscattering . . . . .	11
2.2.4. Raman extinction and backscattering . . . . .	13
2.2.5. Aerosol layer heights . . . . .	14
2.2.6. Aerosol optical properties . . . . .	15
2.2.7. Depolarisation . . . . .	15
2.3. Overview over corrections and uncertainties . . . . .	18
<b>3. Lidar performance</b>	<b>23</b>
3.1. Technical challenges . . . . .	24
3.1.1. Temperature instability . . . . .	24
3.1.2. Photomultiplier tubes . . . . .	25
3.1.3. Laser . . . . .	26
3.2. Quality assurance . . . . .	27
3.2.1. Telecover test . . . . .	27
3.2.2. Rayleigh fit . . . . .	28
3.2.3. Zero bin . . . . .	31
3.2.4. Dead time correction . . . . .	31
3.2.5. Software intercomparison . . . . .	33
3.3. Improvement of the optical alignment . . . . .	34
3.3.1. Beam position . . . . .	34
3.3.2. Beam divergence . . . . .	35
3.3.3. Pinhole position . . . . .	36
3.3.4. Overlap correction function . . . . .	38

3.3.5. Lidar intercomparison SPALI10 . . . . .	42
3.4. Summary: System improvements . . . . .	44
<b>4. Aerosol characterisation results</b>	<b>46</b>
4.1. Measurement example . . . . .	46
4.2. Additional information . . . . .	60
4.2.1. CIMEL sun photometer . . . . .	60
4.2.2. Satellite borne lidar CALIOP . . . . .	60
4.2.3. Satellite borne spectroradiometer MODIS . . . . .	61
4.2.4. Ground based in-situ measurements . . . . .	61
4.2.5. Source identification . . . . .	61
4.3. Case studies . . . . .	63
4.3.1. Stratospheric aerosol, September 2009 . . . . .	64
4.3.2. Volcanic aerosol from Eyjafjallajökull, April 2010 . . . . .	69
4.3.3. Exceptionally strong Saharan dust event, April 2011 . . . . .	75
4.3.4. Volcanic aerosol from Nabro, June 2011 to February 2012 . . . . .	78
4.3.5. Free tropospheric aerosol layers observed in Évora and Granada . . . . .	81
4.4. Climatology . . . . .	88
4.4.1. Seasonal characterisation . . . . .	90
4.4.2. Characterisation of aerosol types . . . . .	93
4.4.3. Summary: Aerosol climatology . . . . .	98
<b>5. Summary and conclusions</b>	<b>100</b>
<b>6. Future work</b>	<b>103</b>
<b>A. Appendix</b>	<b>105</b>
A.1. Background correction . . . . .	105
<b>Bibliography</b>	<b>111</b>
<b>List of Acronyms</b>	<b>126</b>
<b>List of Symbols</b>	<b>129</b>

# 1. Introduction

Significant effort has been made during the past decades to gain a better knowledge of atmospheric aerosols. However, the influence of atmospheric aerosols on the Earth's radiation budget is still uncertain (*Solomon et al.*, 2007). Aerosols have a direct effect and an indirect effect on atmospheric processes and hence on climate. A review on the direct aerosol effect is given by *Yu et al.* (2006). *Lohmann and Feichter* (2005) published a review on the indirect effect. A thorough characterisation of atmospheric aerosol particles is a key factor for reliable radiation models as well as global chemical transport models, and consequently for accurate climate modelling. The impact of aerosols on radiative processes depends on their physical, especially optical, properties and their spatial and temporal distribution (*Sokolik et al.*, 2001). The vertical profile of atmospheric aerosols is particularly important for the study of aerosol transport within the free troposphere, and of the radiative forcing in case of absorbing particles.

Active remote sensing with lidar<sup>1</sup> systems provides vertical profiles of atmospheric constituents. Light generated by a laser<sup>2</sup> is emitted into the atmosphere. A part of the photons is backscattered on molecules, hydrometeors and aerosol particles. The backscattered photons are then detected by a telescope. In atmospheric research, the lidar technique is not only employed for aerosol studies. For example, lidars are also used for the profiling of temperature (*Keckhut et al.*, 1990; *Whiteman*, 2003a; *Li et al.*, 2011), water vapour mixing ratio (*Ansmann et al.*, 1992a; *Whiteman*, 2003b; *Froidevaux et al.*, 2013) or concentrations of other gases (*Papayannis et al.*, 1990; *Whiteman et al.*, 2007; *Ishii et al.*, 2012). The specific application is determined by the emitted and detected wavelengths of the system. In case of aerosol lidars, the obtained optical aerosol properties can give valuable information on the radiative effects of aerosols.

Vertical aerosol profiles can be obtained using ground based lidars (*Whiteman et al.*, 1992; *Ansmann et al.*, 2000), airborne lidars (*Flamant et al.*, 2000; *Wagner et al.*, 2009) or space-borne lidars (*Winker et al.*, 2010). Besides, measurements with balloons (*Maletto et al.*, 2003) or with airborne in-situ instrument (*Brenninkmeijer et al.*, 1999; *Haywood et al.*, 2003; *Esteve et al.*, 2012) can be applied. The different methods all have advantages and disadvantages in terms of expenses as well as temporal and spatial coverage. For frequent or even continuous observations of the vertical distribution of atmospheric constituents at one place, ground based lidars are the most advantageous.

A global coverage of vertical profiling of aerosols is desirable for the investigation of the horizontal aerosol distribution, transportation procedures and aerosol ageing processes. A high horizontal resolution can be achieved by satellite lidar measurements, but at the expense of the temporal resolution. Ground based lidar systems are capable of aerosol profiling at both, a high vertical and temporal resolution. However, they are usually restricted to measurements at one site.

---

<sup>1</sup>Lidar: commonly used acronym for light detection and ranging, first introduced by *Middleton and Spilhaus* (1953).

<sup>2</sup>Laser: commonly used acronym for light amplification by stimulated emission of radiation.

## 1.1. Measurement site

This work was realised at the Évora Geophysics Center (Centro de Geofísica de Évora) (CGE) (38.57° N, 7.91° W, 290 m above sea level (asl)) in Évora, which is situated in the southern part of Portugal, about 140 km east of the Atlantic coast. Évora is the capital of Alentejo, a rural region with a very low population density. There are no polluting industries close to the city. The main local anthropogenic aerosol sources are traffic, and domestic fuel burning in winter. The nearest industrial and urban area is Lisbon and its surroundings. This region is situated about 100 km west of Évora. Therefore, the aerosol load near the ground is generally low at this measurement site.

Portugal is very suitable for measuring aerosol particle properties. The local background aerosol concentration is low in the rural areas and hence any transport of aerosols from different origins can easily be detected. In spite of such favourable conditions aerosol investigations, especially studies of the vertical distribution of aerosols, are rare in Portugal. For that reason it was chosen as a main observation site in the Second Aerosol Characterization Experiment (ACE2) (Ansmann *et al.*, 2001, 2002; Silva *et al.*, 2002). This campaign was conducted in Sagres, a town at the south-westernmost point of continental Portugal, in summer 1997.

For the given reasons, Évora as a rural site is especially appropriate for the study of aerosols from different source regions. Saharan dust is frequently transported towards the southern Iberian peninsula and can be observed in Évora. Furthermore, dry and hot conditions in summer favour forest fires in the north of Portugal and Spain. At times, the smoke is transported towards Évora. The general westward circulation pattern often leads to advection of marine air masses or anthropogenic pollution from the industrial coastal regions and the urban area of Lisbon near the ground. In higher altitudes, long range transported aerosol from North America or even from Asia can be observed frequently. Occasionally, aerosol of anthropogenic origin from western or central Europe is advected to Évora as well.

Another important advantage of Évora as an aerosol measurement site is the frequent occurrence of clear sky conditions. From late spring until autumn the weather in southern Portugal is generally dry and clouds are rare. This enables frequent observations of the troposphere and lower stratosphere with lidar and other remote sensing instruments, such as sun photometers.

Only few observations of the vertical distribution of atmospheric aerosols and their optical properties existed in Portugal before the year 2009. However, a new lidar system was acquired by CGE and started operating in September 2009. A multi-wavelength Raman lidar with the capabilities of measuring backscatter coefficients at three wavelengths, extinction coefficients at two wavelengths and depolarisation at one wavelength (3+2+1) is operated at CGE. For the first time, the vertical profiling of optical aerosol and cloud properties by lidar is done in Portugal on a regular basis. The lidar station in Évora plays an important role for aerosol studies on a continental scale. For example, CGE can act as alert station for other European aerosol observatories, for free tropospheric aerosol plumes approaching Europe from west and south west. The collaboration with other lidar stations in Europe is part of this work. As CGE is member of the Aerosol Robotic Network (AERONET), comparisons of lidar and sun photometer measurements are possible. Besides, ground based in-situ observations of aerosols are performed at CGE.

## 1.2. State of the art

Different types of lidar systems are applied for the investigation of atmospheric constituents. Many lidars operated at present were developed and built by individual research groups according to their means and purposes. This led to a large variety in capabilities, but also in restrictions of the systems. Only few commercial instruments are available. Due to the complexity of lidars, a fully automatic and unattended operation is not possible in most cases. Multi-wavelength Raman lidars with 3+2+1 capabilities are sophisticated and expensive instruments. However, they increasingly become standard tools for the ground based profiling of the atmosphere at research institutions around the world. The CGE lidar is such a system.

Lidars are increasingly organised within networks, on subcontinental scale e.g. in the Spanish and Portuguese Aerosol Lidar Network (SPALINET) (*Sicard et al.*, 2011) or the Commonwealth of Independent States Lidar Network (CIS-LiNet) (*Chaikovskiy et al.*, 2006), on continental scale like in the European Aerosol Research Lidar Network (EARLINET) (*Bösenberg et al.*, 2003) or the Asian Dust Network (AD-Net) (*Murayama et al.*, 2001), or on global scale in the Micro-Pulse Lidar Network (MPLNET) (*Welton et al.*, 2001) or the Global Atmosphere Watch Aerosol Lidar Observation Network (GALION) (*Bösenberg et al.*, 2008). CGE is a member of SPALINET and EARLINET. It is the westernmost EARLINET station on continental Europe and therefore important for the investigation of aerosol transportation within the network. EARLINET is integrated in GALION, and since 2011 in the FP7<sup>3</sup> project Aerosols, Clouds, and Trace gases Research Infrastructure Network (ACTRIS). CGE is associated member of ACTRIS.

Long term studies for the characterisation of aerosols from different sources exist from various other lidar stations in Europe (*Mattis et al.*, 2008; *Giannakaki et al.*, 2010). For such studies, usually specific aerosol types are classified, for example mineral dust, biomass burning smoke, volcanic aerosol and anthropogenic aerosol depending on their source region. However, long term studies often suffer from a high variability in the optical aerosol properties (*Balis et al.*, 2004; *Amiridis et al.*, 2009). This is mainly due to the high variability of the aerosol itself, depending, among other things, on the composition, on ageing processes and on the transport path (*Mona et al.*, 2006).

Comprehensive studies of mineral dust including lidars, were performed relatively close to the aerosol source in Africa (*Freudenthaler et al.*, 2009; *Tesche et al.*, 2009), in Europe (*De Tomasi et al.*, 2003; *Papayannis et al.*, 2005; *Wagner et al.*, 2009) and in Asia (*Liu et al.*, 2002; *Papayannis et al.*, 2007). *Guerrero-Rascado et al.* (2009) presented a study of a strong Saharan dust outbreak monitored with several remote sensing instruments on the southern Iberian peninsula. They underlined the importance of combining various instruments for a thorough characterisation of aerosols. However, Saharan dust was monitored also in central and northern Europe (*Ansmann et al.*, 2003; *Rodríguez et al.*, 2012).

Stratospheric aerosol is often caused by volcanic activities. It consists mainly of sulphuric acid droplets (*Deshler*, 2008). It was shown recently (*Bourassa et al.*, 2012), that also small volcanic eruptions can contribute to the stratospheric aerosol load. In such cases, strong convection may cause intrusion of volcanic aerosol into the stratosphere. Stratospheric aerosol is only very slowly transported back down into the troposphere. Therefore, it has a long term radiative influence (*Wendler*, 1984), which results in the cooling of the

---

<sup>37th</sup> Framework Programme of the European Commission

## 1. Introduction

surface temperature and an increase of the temperature in the lower stratosphere. Furthermore, stratospheric aerosols have an impact on ozone and other gases (*Prata et al.*, 2007; *Carn et al.*, 2007). However, volcanic eruptions can also cause high aerosol loads in the free troposphere, often with severe economic consequences. This became evident after the eruption of Eyjafjallajökull, Iceland in April and May 2010, which forced the closing of the air space over large parts of Europe. Those strong impacts of volcanic aerosols emphasise the importance of detailed studies of this type of aerosols. Lidar observations of volcanic aerosols from different eruptions were presented before by *Villani et al.* (2006); *Wang et al.* (2006); *Ansmann et al.* (2010) and *Sicard et al.* (2012).

Biomass burning aerosol can be caused by wildfires or by anthropogenic activities. Wildfires are often ignited by lightning. In remote regions, the fires cannot be controlled (*Stocks et al.*, 2002), which enhances the magnitude of the fires as well as the emission of particles and gases. In the northern hemisphere, wildfires in Canada, Alaska and Russia contribute to the aerosol load on a large scale (*Wotawa et al.*, 2001). Review articles about particle properties of biomass burning aerosol were published by *Reid et al.* (2005a) and *Reid et al.* (2005b). Smoke plumes from agricultural burning observed by lidar were investigated by, e.g. *Amiridis et al.* (2009) and *Badarinath et al.* (2009). Studies on fresh and aged forest fire smoke were performed, among others, by *Balis et al.* (2003); *Müller et al.* (2005) and *Alados-Arboledas et al.* (2011).

Various sources of anthropogenic aerosols exist, including fossil fuel burning, traffic and industry. Anthropogenic aerosol can be observed constantly in the boundary layer in densely populated regions. However, the aerosols can also be transported over long distances, especially when they were lifted into the free troposphere. The transport and properties of anthropogenic aerosol was studied intensively during the Indian Ocean Experiment (INDOEX) (*Ramanathan et al.*, 2001). But also in other aerosol characterisation experiments conducted around the world (*Bates et al.*, 1998; *Russell et al.*, 1999). Besides, anthropogenic pollution plumes from Europe were investigated during ACE2 on the southwesternmost point of continental Portugal by lidar as well as by star and sun photometers (*Ansmann et al.*, 2001, 2002; *Silva et al.*, 2002).

Besides the lidar measurements, ground based in-situ measurements (*Silva et al.*, 2003; *Pereira et al.*, 2008, 2009, 2011) as well as model studies (*Santos et al.*, 2008) are performed at CGE, in order to investigate optical aerosol properties. A characterisation of aerosol extinction and solar radiation in Évora in summer was done by means of sun photometer, radiometer and nephelometer data by *Elias et al.* (2006). Also, short term lidar studies were performed in Évora before (*Guerrero-Rascado et al.*, 2007, 2010).

### 1.3. Objectives

For the first time, a long term study of aerosol profiles by means of a ground based lidar system was conducted in Portugal. The aim is the characterisation of aerosols in terms of optical properties as well as vertical and temporal distributions. A unique data set of vertical profiles of optical aerosol properties was created.

Besides a climatology of two years of aerosol profiling by lidar, certain aerosol events were studied in detail. Such studies give insight on the presence of aerosols in the free troposphere as well as in the stratosphere close to the western shore of continental Europe. Valuable information on the aerosol transport towards or from Europe could be obtained.

The intensive studies also enabled a thorough characterisation of specific aerosol types. To achieve this, not only lidar data was used. The vertical profiles were also combined with columnar remote sensing data as well as ground based in-situ measurements and aerosol models.

## **1.4. Structure of this thesis**

This thesis is structured in six chapters. The lidar system is introduced in section (2.1). An overview on all lidar data analysis procedures used in this work is given in section (2.2). The performance of the lidar at CGE is described in chapter (3). Initial difficulties, quality assurance procedures and system improvements are presented in sections (3.1) to (3.3), respectively. The aerosol studies are given in chapter (4). In section (4.1) the analysis procedure is described by means of example measurements. For some of the studies, lidar measurements were combined with data from other instruments. Those complementary information are briefly introduced in section (4.2). Case studies are presented in section (4.3). The characterisation of aerosol types observed at CGE during two years is given in section (4.4). In chapter (5) the results are summarised. An outlook is given in chapter (6).

## 2. Instrument and methodology

The lidar principle is applied in atmospheric sciences since the 1930s (*Wandinger, 2005*). Lidars consist of a light emitting unit, which nowadays is a pulsed laser, and a receiving unit, which consists of a telescope and photon detectors.

The lidar system Polly<sup>XT</sup> (Portable Raman Lidar System With Extended Capabilities) (*Althausen et al., 2009*) was developed at the Leibniz-Institute for Tropospheric Research e. V. (Leibniz-Institut für Troposphärenforschung e. V.) (TROPOS) in Leipzig, Germany. It was designed for automatic operation under remote control. The Portable Aerosol and Cloud Lidar (PAOLI) of the Évora Geophysics Center (Centro de Geofísica de Évora) (CGE), a multi-wavelength Raman lidar of the type Polly<sup>XT</sup>, was built by the company LISTaR (Leipzig Institute for Science, Technology and Research GmbH, Germany) with the support of TROPOS. A detailed description of the instrument follows in section (2.1).

Although lidars enable the observation of a great variety of atmospheric constituents and their properties, this work focuses on the investigation of aerosols. The determination of aerosol properties from lidar data is described in section (2.2).

### 2.1. Multi-wavelength Raman lidar PAOLI

PAOLI is operated at CGE on a regular basis since September 2009. The lidar system is part of the European Aerosol Research Lidar Network (EARLINET) and the Spanish and Portuguese Aerosol Lidar Network (SPALINET). It is placed at the north side of a building. Therefore, the lidar is only exposed to direct sunlight a few hours per day. A level platform was constructed for the instrument, which enables easy access for the transportation of the lidar.

#### 2.1.1. General features

PAOLI is shown in figure (2.1) from the front (left) and from the top (right). It is housed in a waterproof cabinet. The roof has two round quartz windows, one for the emitted beams and one above the receiving telescope. Those windows are protected by a cover, which is only removed during the operation of the system. In figure (2.1), the system is shown with open roof cover. The opening and closing mechanisms are coupled to a measurement programme but also to a rain sensor, which is mounted on the upper left edge of the cabinet. In case of rain, the measurement is interrupted automatically and the roof cover closes. A device for monitoring the ambient temperature and pressure is mounted outside of the cabinet next to the rain sensor. Inside the cabinet, there are two sensors measuring the temperature. For temperature stability, the cabinet contains an air conditioner and two heaters. The external part of the air conditioner can be seen in figure (2.1) on the lower left side of PAOLI. The sensitive optics are protected by a housing of blackened aluminium. For changes or tests of the optical components the covers can be removed. Monitoring of the instrument and the laser performance and controlling during operation



**Figure 2.1.:** PAOLI with open roof cover from the front (left) and from the top (right).

is possible via an internet connection. Laser, roof cover, detectors and data acquisition are coordinated by the measurement programme, but they can also be controlled manually. Measurements can be started manually from the system computer and via remote control or automatically on a fixed schedule.

### 2.1.2. Optics

The optical components of the system are mounted on a breadboard, which is tilted from the back of the cabinet by  $5^\circ$ , thus the lidar system measures at a zenith angle ( $\Theta$ ) of  $5^\circ$ . The tilt of the outgoing beam avoids specular reflection on horizontally oriented ice crystals in clouds. Those reflections would enhance the signal detected by the lidar and thereby distort the determination of the ice or mixed phase cloud optical properties.

The optical set-up of PAOLI is shown schematically in figure (2.2). The system is working with a neodymium-doped yttrium aluminium garnet (Nd:YAG) laser<sup>1</sup> with a pulse frequency of 20 Hz and a pulse length of 5 to 8 ns. The laser emits at 1064 nm. In a second harmonic generator (SHG) and a third harmonic generator (THG) the frequency of parts of the emitted light is doubled and tripled, which results in the wavelengths 532 and 355 nm, respectively. The emitted energy after the THG is 140, 110 and 60 mJ at 1064, 532 and 355 nm, respectively. After passing two redirecting prisms the beams enter an achromatic beam expansion telescope. The beams are expanded by a factor of 7.5 from a diameter of 6 mm to a diameter of 45 mm. Additionally, the divergence is reduced. The position of the lens at the exit of the beam expansion telescope can be shifted on the plane perpendicular to the beams, for the fine adjustment of the direction of the outgoing beams. An optimal position of the beams is important for a low range of complete overlap of the beams and the receiver field of view (FOV), which will be discussed in section (3.3). Furthermore, the optimal beam position and divergence ensure, that the beams remain within the FOV also in the far field. A CCD (charge-coupled device) camera ("Cam" in figure (2.2)) is used to monitor the alignment of the emitted beams and the receiver optics. It receives photons at 532 nm. Therefore, the alignment control is valid for the outgoing beam at this wavelength. The alignment of the outgoing beams at 355 and 1064 nm cannot be monitored. Therefore, the assumption is made that light of all three wavelengths is sent out as parallel beams on one vertical axis.

<sup>1</sup>type Inlite<sup>TM</sup>III-20 of the manufacturer Continuum<sup>®</sup> (<http://www.continuumlasers.com>)

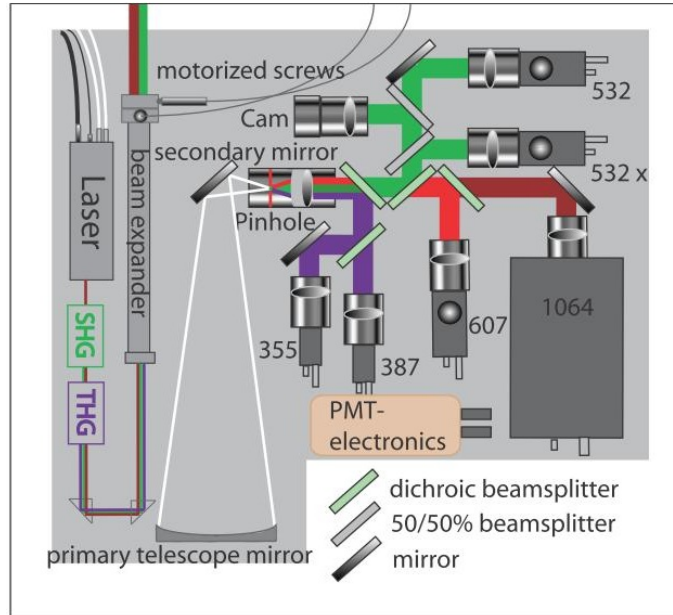


**Figure 2.2.:** Scheme of the optical set-up of PAOLI (from the system manual (Heese, 2009)).

The receiver consists of a Newtonian telescope with a diameter of 300 mm. The primary mirror is parabolic with a focal length of 900 mm and a silver coating. The secondary mirror is flat and elliptical and has an aluminium coating. It is mounted 700 mm in front of the primary mirror. The photons are directed through a pinhole with an opening of 0.9 mm. This corresponds to a FOV of 1 mrad. Behind the pinhole, a lens is inducing a quasi parallel beam with a diameter of 25 mm. Dichroic beam splitters and mirrors direct the photons of different wavelengths to the respective detectors. Photomultiplier tubes (PMTs) are used in photon counting mode to detect the elastically backscattered photons at the wavelengths 355, 532 and 1064 nm as well as the inelastically backscattered photons at 387 and 607 nm, corresponding to the Raman-shift on nitrogen molecules of radiation of the wavelengths 355 and 532 nm, respectively. Additionally, the cross polarised component at 532 nm is detected by means of a polarisation filter in front of a sixth PMT. This filter is adjusted to minimise the signal during a measurement without depolarising aerosol. Consequently, parallel polarised light, i.e. light with the same polarisation orientation as the laser beam, is blocked. With this sixth channel the determination of the linear depolarisation ratio is possible. In front of each PMT an interference filter suppresses light of other wavelengths and lenses focus the ray of photons on the cathodes of the PMTs. Neutral density filters (NDFs) can be placed in front of each PMT to avoid saturation. PMTs are highly sensitive to low signals. However, in case of high photon count rates the detectors show non-linear behaviour. Incident photons cannot be detected separately if the time difference between their occurrence is too short. The minimum time difference for the detection of single photons is called dead-time.

The maximum altitude of detection and the vertical resolution of the raw signal is determined by the capabilities of the data acquisition cards. In case of PAOLI the counting frequency of 400 MHz and the maximum number of bins (2048) result in a vertical resolution of 30 m and a maximum altitude of about 61 km.

## 2.2. Lidar data analysis

The lidar profiles are typically stored as the sum of 600 shots, which corresponds to a time resolution of 30 s. This integration time can be adjusted. However, storage in shorter time intervals leads to larger data files. Whereas longer averaging might result in loss of information on the atmospheric variability. The profiles of particle extinction coefficients at 355 and 532 nm, particle backscatter coefficients at 355, 532 and 1064 nm as well as the particle linear depolarisation ratio at 532 nm can be obtained from PAOLI measurements.

The applied fundamental lidar data analysis procedures are given in the following. The lidar equation is introduced in section (2.2.1). For solving this equation, the molecular extinction and backscatter is needed. Their retrieval is presented in section (2.2.2). The retrieval of the profiles mentioned above is described in sections (2.2.3), (2.2.4) and (2.2.7). Different intensive and extensive aerosol optical properties can be derived from the profiles of the particle extinction and backscatter coefficients. They are introduced in section (2.2.6). Aerosol layer heights can be obtained from the lidar profiles as well, applying the procedure explained in section (2.2.5). Parts of this chapter were described by *Preißler* (2008) and can also be found in literature (*Kovalev and Eichinger, 2004; Weitkamp, 2005*). Some general remarks about uncertainties in lidar measurements and an estimation of errors in PAOLI measurements are made in section (2.3).

### 2.2.1. Lidar equation

A lidar detects the photons scattered on atmospheric constituents, i.e. particles, hydrometeors and molecules time-resolved at an angle of  $180^\circ$ . The relation  $\Delta r = (c\Delta t)/2$  is used to convert the time  $\Delta t$ , from the emission of the laser pulse to the detection of the photon, to the distance  $\Delta r$ , of the scattering particle from the lidar system, applying the speed of light  $c$ . In case of PAOLI range  $r$  is not equal to the height  $z$ , as the system is not vertically aligned. The conversion is done with  $z = r \cos(\Theta)$ , for the zenith angle  $\Theta = 5^\circ$ .

The foundation of any lidar data analysis is the lidar equation, here written in a basic form valid for single scattering

$$P(z, \lambda) = K(\lambda) G(z, \lambda) \beta(z, \lambda) T(z, \lambda). \quad (2.1)$$

This form of the equation as well as the general considerations throughout this section were described in detail by *Wandinger* (2005) and *Kovalev and Eichinger* (2004). In equation (2.1)  $P(z, \lambda)$  is the received power at a wavelength  $\lambda$  from the distance  $z$ .  $K(\lambda)$  is a system factor, which describes the performance of the lidar.  $G(z, \lambda)$  is the geometric term,  $\beta(z, \lambda)$  the backscatter coefficient and  $T(z, \lambda)$  the transmission term. The terms on the right hand side of the equation will be discussed in the following.

$K(\lambda)$  is independent of the distance from the system and only depends on the wavelength.

$$K(\lambda) = P_0(\lambda) \frac{c\Delta t_p}{2} A\eta \quad (2.2)$$

includes the mean power of the emitted pulse  $P_0(\lambda)$ , the temporal length of the pulse  $t_p$ , the area of the primary receiver optics  $A$ , and the system efficiency  $\eta$ . The geometric term is

$$G(z, \lambda) = \frac{O(z, \lambda)}{z^2}. \quad (2.3)$$

## 2. Instrument and methodology

The signal intensity decreases quadratically with  $z$ , because the area covered by the telescope is part of the surface of a sphere with radius  $z$ .  $O(z, \lambda)$  describes the overlap of the laser beam and receiver field of view depending on the distance from the lidar system. Due to wavelength dependent optical components, this function can be different for each wavelength. Close to the lidar  $O(z, \lambda) = 0$  and in the distance of full overlap ( $z_{ovl}$ ) applies  $O(z_{ovl}, \lambda) = 1$ .  $O(z, \lambda)$  can be determined experimentally for Raman lidars (*Wandinger and Ansmann, 2002*). Further considerations of the overlap function of PAOLI can be found in section (3.3.4).

The backscatter coefficient  $\beta(z, \lambda)$  is the scattering coefficient for the scattering angle of  $180^\circ$ . Therefore, it can be described as

$$\beta(z, \lambda) = \sum_j N_j(z) \frac{d\sigma_j^{sca}}{d\Omega}(\pi, \lambda), \quad (2.4)$$

with  $N_j(z)$  being the concentration of scatterer of type  $j$  within the volume probed by the laser and  $d\sigma_j^{sca}(\pi, \lambda)/d\Omega$  being the differential scattering cross section of the particles at the scattering angle  $\pi$  and the wavelength  $\lambda$ .

The transmission term in equation (2.1) follows from the Beer-Lambert law, which states the existence of an exponential relation between the transmittance  $T(z, \lambda)$ , and the product of the path length of the light through a medium and the extinction cross section. Specifically for lidar the term can be written as

$$T(z, \lambda) = \exp \left[ -2 \int_0^z \alpha(z', \lambda) dz' \right]. \quad (2.5)$$

In this equation, the factor 2 accounts for the two-way path of the light and  $\alpha(z', \lambda)$  is the extinction coefficient.

Combining equations (2.2), (2.3) and (2.5) with the lidar equation (2.1) leads to

$$P(z, \lambda) = P_0(\lambda) \frac{c\Delta t_p}{2} A\eta \frac{O(z, \lambda)}{z^2} \beta(z, \lambda) \exp \left[ -2 \int_0^z \alpha(z', \lambda) dz' \right]. \quad (2.6)$$

The solution of this equation is an under-determined problem with the two unknown parameters extinction coefficient  $\alpha(z, \lambda)$  and backscatter coefficient  $\beta(z, \lambda)$ .

Absorption of photons by gases can be neglected at the emitted wavelengths 355, 532 and 1064 nm. Hence, for the application considered here, extinction is the sum of scattering (sca) on and absorption (abs) by particles (par) and scattering on molecules (mol). Therefore,

$$\alpha(z, \lambda) = \alpha_{par}^{abs}(z, \lambda) + \alpha_{par}^{sca}(z, \lambda) + \alpha_{mol}^{sca}(z, \lambda). \quad (2.7)$$

In analogy to the extinction, the total backscattering is the sum of the backscattering on particles and on molecules,

$$\beta(z, \lambda) = \beta_{par}(z, \lambda) + \beta_{mol}(z, \lambda). \quad (2.8)$$

The extinction and backscattering on molecules is calculated from meteorological data. Profiles of temperature, pressure and humidity can be obtained from radio soundings. Further remarks on this subject follow in section (2.2.2). The extinction-to-backscatter

ratio, or lidar ratio, is defined as  $S(z, \lambda) = \alpha(z, \lambda) / \beta(z, \lambda)$ . Following equations (2.7) and (2.8), a particle lidar ratio can be defined as

$$S_{par}(z, \lambda) = \frac{\alpha_{par}(z, \lambda)}{\beta_{par}(z, \lambda)}. \quad (2.9)$$

The molecular lidar ratio follows from the Rayleigh scattering theory. It is known and constant,

$$S_{mol} = \frac{\alpha_{mol}(z, \lambda)}{\beta_{mol}(z, \lambda)} = \frac{8\pi}{3} sr. \quad (2.10)$$

Two different approaches for the solution of the under-determined problem, which the lidar equation imposes, are presented in sections (2.2.3) and (2.2.4).

### 2.2.2. Radio sounding profiles

Profiles of the temperature and pressure, for example from radio sounding measurements, are needed for the calculation of the extinction and backscattering on molecules, also referred to as Rayleigh extinction and Rayleigh backscattering. The retrieval of the molecular extinction was described and modelled by *Elterman* (1968). *Teillet* (1990) provided modifications to this model. The molecular extinction is obtained as

$$\alpha_{mol}(z, \lambda) = \frac{8\pi}{3} \frac{C}{\lambda^4} \left( \frac{p(z)}{p_s} \right) \left( \frac{T_s}{T(z)} \right), \quad (2.11)$$

with the temperature  $T$  and the pressure  $p$  at height  $z$  and the standard surface temperature  $T_s$  (288.15 K) as well as the standard surface pressure  $p_s$  (1013.25 hPa). Factor  $C$  contains the columnar and molecular number density, the refractive index of air and the depolarisation ratio of molecules in particle free conditions. From the molecular extinction, the molecular backscattering is calculated by applying the constant molecular lidar ratio  $S_{mol}$  (equation (2.10)).

Often, no radio sounding profiles exist correlative to lidar measurements to provide the profiles of pressure and temperature. The spatial and temporal distance to the closest radio sounding launch can be several hundred kilometres and up to 12 h, respectively. The radio sounding station closest to Évora is at the airport in Lisbon, Portugal. The distance is about 120 km and only one radio sounding is launched per day, at 12 UTC. Alternatively, profiles of the standard atmosphere ISO 2533 (1975) are commonly used (*Amiridis et al.*, 2005; *Mamouri et al.*, 2009), but deviations from the real atmospheric conditions can be large (*Ansmann et al.*, 1992b). A good option are model sounding profiles (*Mona et al.*, 2009), for example from data of the Global Data Assimilation System (GDAS) using the Medium Range Forecast (MRF) model provided by the Air Resources Laboratory of the National Oceanic and Atmospheric Administration (NOAA ARL). Those profiles are available globally with a horizontal resolution of  $1^\circ$ , archived from December 2004 for every three hours at the NOAA ARL webpage (<http://ready.arl.noaa.gov/readyamet.php>). By spatial interpolation, a radio sounding for any point on the Earth can be calculated.

### 2.2.3. Elastic backscattering

The solution of the lidar equation for elastic scattering profiles bases on findings in radar technology by *Hitschfeld and Bordan* (1954). An analytic solution including the contributions of both molecules and particles was proposed by *Fernald et al.* (1972). A simpler

## 2. Instrument and methodology

approach for the solution of the Bernoulli equation (2.16), and consequently a more applicable way of solving the lidar equation, was introduced by *Klett* (1981). This led to the restatement of the more general solution by *Fernald* (1984). *Klett* (1985) proposed a non-linear relationship between backscattering and extinction and applied a lidar ratio in dependence of the extinction magnitude. The approach described in the following is often referred to as Klett or Fernald-Klett method. A detailed derivation of this solution was provided by *Ansmann and Müller* (2005).

From the combination of the lidar equation (2.6) with equations (2.7) and (2.8) and the introduction of the range and overlap corrected lidar signal

$$P_{corr}(z, \lambda) \equiv (z^2/O(z, \lambda)) P(z, \lambda), \quad (2.12)$$

follows

$$P_{corr}(z, \lambda) = K(\lambda) [\beta_{par}(z, \lambda) + \beta_{mol}(z, \lambda)] \exp \left[ -2 \int_0^z [\alpha_{par}(z', \lambda) + \alpha_{mol}(z', \lambda)] dz' \right]. \quad (2.13)$$

*Sasano et al.* (1985) introduced the normalised total extinction coefficient

$$Y(z, \lambda) \equiv \alpha_{par}(z, \lambda) + \frac{S_{par}(z, \lambda)}{S_{mol}} \alpha_{mol}(z, \lambda). \quad (2.14)$$

The combination of equations (2.13) and (2.14) and the substitution of  $\alpha_{par}(z, \lambda)$  and  $\alpha_{mol}(z, \lambda)$  by the respective lidar ratios from equations (2.9) and (2.10) yields

$$\begin{aligned} P_{corr}(z, \lambda) S_{par}(z, \lambda) \exp \left[ -2 \int_0^z [S_{par}(z', \lambda) - S_{mol}] \beta_{mol}(z', \lambda) dz' \right] \\ = K(\lambda) Y(z, \lambda) \exp \left[ -2 \int_0^z Y(z', \lambda) dz' \right]. \end{aligned} \quad (2.15)$$

The Bernoulli equation follows after taking the logarithm of both sides of this equation and differentiating with respect to  $z$ :

$$\begin{aligned} \frac{d}{dz} \ln \left( P_{corr}(z, \lambda) S_{par}(z, \lambda) \exp \left[ -2 \int_0^z [S_{par}(z', \lambda) - S_{mol}] \beta_{mol}(z', \lambda) dz' \right] \right) \\ = \frac{1}{Y(z, \lambda)} \frac{dY(z, \lambda)}{dz} - 2Y(z, \lambda). \end{aligned} \quad (2.16)$$

This equation can be solved for the boundary conditions

$$Y(z_0, \lambda) = S_{par}(z_0, \lambda) [\beta_{par}(z_0, \lambda) + \beta_{mol}(z_0, \lambda)], \quad (2.17)$$

which yields a solution for the total backscatter coefficient (*Sasano et al.*, 1985):

$$\beta_{par}(z, \lambda) + \beta_{mol}(z, \lambda) = \frac{P_{corr}(z, \lambda) \exp \left[ -2 \int_{z_0}^z [S_{par}(z', \lambda) - S_{mol}] \beta_{mol}(z', \lambda) dz' \right]}{\frac{P_{corr}(z_0, \lambda)}{\beta_{par}(z_0, \lambda) + \beta_{mol}(z_0, \lambda)} - 2 \int_{z_0}^z S_{par}(z', \lambda) P_{corr}(z', \lambda) T(z', z_0, \lambda) dz'}, \quad (2.18)$$

with

$$T(z', z_0, \lambda) = \exp \left[ -2 \int_{z_0}^{z'} [S_{par}(z'', \lambda) - S_{mol}] \beta_{mol}(z'', \lambda) dz'' \right]. \quad (2.19)$$

Equation (2.18) can be integrated from reference height  $z_0$  with  $z > z_0$  or  $z < z_0$ . Numerical stability is only given by backward integration ( $z < z_0$ ) as proposed by *Klett* (1981). The particle backscatter coefficient at the reference height should be negligible compared to the molecular backscatter coefficient ( $\beta_{par}(z_0, \lambda) \ll \beta_{mol}(z_0, \lambda)$ ). For studies concerning tropospheric aerosol, the reference height is typically set to nearly particle free height ranges in the upper troposphere in order to minimise the uncertainties resulting from the assumption of a particle backscatter coefficient.

One drawback of the *Klett* method is the retrieval of both, extinction and backscatter coefficient from one measured quantity. This requires the assumption of a particle lidar ratio, which can be a source of large uncertainties. In section (2.3) a discussion of this error source is given.

#### 2.2.4. Raman extinction and backscattering

With the application of the so-called Raman method, no assumption of the lidar ratio is necessary for the calculation of the particle backscatter and extinction coefficients. The following approach for the retrieval of the extinction coefficient was first presented by *Ansman et al.* (1990). It is based on the independent measurements at the laser wavelength  $\lambda_0$  as well as at the wavelength of the inelastically scattered light  $\lambda_{Ra}$ . The detected signal at  $\lambda_{Ra}$  is independent from particle backscatter and only affected by particle extinction.

The lidar equation (equation (2.1)) can be adjusted accordingly to

$$P(z, \lambda_{Ra}) = K(\lambda_0) \frac{O(z, \lambda_{Ra})}{z^2} \beta_{Ra}(z, \lambda_0) \exp \left[ - \int_0^z [\alpha(z', \lambda_0) + \alpha(z', \lambda_{Ra})] dz' \right]. \quad (2.20)$$

In this form of the lidar equation  $\alpha(z', \lambda_0)$  is the extinction coefficient on the way from the lidar to the scattering volume and  $\alpha(z', \lambda_{Ra})$  the extinction coefficient on the way back to the lidar. The Raman backscatter coefficient  $\beta_{Ra}(z, \lambda_0)$ , can be obtained from the relation

$$\beta_{Ra}(z, \lambda_0) = N_{Ra}(z) \frac{d\sigma_{Ra}^{sca}}{d\Omega}(\pi, \lambda_0), \quad (2.21)$$

where  $N_{Ra}(z)$  is the molecular number density of the specific gas (nitrogen in the case of PAOLI) and  $d\sigma_{Ra}^{sca}(\pi, \lambda_0)/d\Omega$  is the molecular differential scattering cross section at wavelength  $\lambda_0$  for the scattering angle  $\pi$ . Replacing  $\beta_{Ra}(z, \lambda_0)$  in equation (2.20) by equation (2.21), taking the logarithm and differentiating with respect to  $z$  yields

$$\alpha(z, \lambda_0) + \alpha(z, \lambda_{Ra}) = \frac{d}{dz} \ln \left( \frac{N_{Ra}(z)}{P_{corr}(z, \lambda_{Ra})} \right). \quad (2.22)$$

As mentioned before,  $\alpha(z, \lambda)$  consists of the particle extinction and the molecular extinction. Therefore, equation (2.22) can be written as

$$\alpha_{par}(z, \lambda_0) + \alpha_{par}(z, \lambda_{Ra}) = \frac{d}{dz} \ln \left( \frac{N_{Ra}(z)}{P_{corr}(z, \lambda_{Ra})} \right) - \alpha_{mol}(z, \lambda_0) - \alpha_{mol}(z, \lambda_{Ra}). \quad (2.23)$$

The Ångström exponent  $\hat{a}(z, \lambda_0, \lambda_{Ra})$  describes the wavelength dependence of the extinction coefficient

$$\frac{\alpha_{par}(z, \lambda_0)}{\alpha_{par}(z, \lambda_{Ra})} = \left( \frac{\lambda_{Ra}}{\lambda_0} \right)^{\hat{a}(z, \lambda_0, \lambda_{Ra})}. \quad (2.24)$$

## 2. Instrument and methodology

The assumption of a value of the Ångström exponent, enables the determination of the particle extinction coefficient

$$\alpha_{par}(z, \lambda_0) = \frac{\frac{d}{dz} \ln \left( \frac{N_{Ra}(z)}{P_{corr}(z, \lambda_{Ra})} \right) - \alpha_{mol}(z, \lambda_0) - \alpha_{mol}(z, \lambda_{Ra})}{1 + \left( \frac{\lambda_0}{\lambda_{Ra}} \right)^{\hat{a}(z, \lambda_0, \lambda_{Ra})}}. \quad (2.25)$$

The following approach for the retrieval of the Raman backscatter coefficient was first proposed by *Cooney et al.* (1969) and *Melfi* (1972). A detailed description was given by *Ansmann et al.* (1992b) and an overview by *Ansmann and Müller* (2005).

The total and the molecular signal in two distances from the lidar,  $z$  and  $z_0$ , are necessary to calculate the backscatter coefficient with the Raman method. The ratio of the elastic signals and the Raman signals is formed, which yields

$$\begin{aligned} & \beta_{par}(z, \lambda_0) + \beta_{mol}(z, \lambda_0) \\ &= [\beta_{par}(z_0, \lambda_0) + \beta_{mol}(z_0, \lambda_0)] \frac{P(z_0, \lambda_{Ra}) P(z, \lambda_0)}{P(z_0, \lambda_0) P(z, \lambda_{Ra})} \\ & \times \frac{N_{Ra}(z)}{N_{Ra}(z_0)} \frac{\exp \left[ - \int_{z_0}^z [\alpha_{par}(z', \lambda_{Ra}) + \alpha_{mol}(z', \lambda_{Ra})] dz' \right]}{\exp \left[ - \int_{z_0}^z [\alpha_{par}(z', \lambda_0) + \alpha_{mol}(z', \lambda_0)] dz' \right]}. \end{aligned} \quad (2.26)$$

Equation (2.26) holds under the assumption that both channels are well aligned. In this case, the overlap function for  $\lambda_0$  and for  $\lambda_{Ra}$  are the same and cancel out. Hence, the profile of the backscatter coefficients obtained with the Raman method is independent of overlap effects. As for the Klett method (section (2.2.3)), a nearly particle free height range in the upper troposphere is generally chosen as the reference height  $z_0$ .

### 2.2.5. Aerosol layer heights

Different approaches exist for the determination of aerosol layer boundaries from lidar profiles. Depending on the system capabilities, the aerosol load is often used as an indicator for the planetary boundary layer (PBL) top height, although the PBL is defined by convective and turbulent processes and not by the presence of aerosols (*Stull*, 1988). However, the aerosol concentration is generally higher in the PBL than in the free troposphere.

The gradient method (*Flamant et al.*, 1997; *Bösenberg et al.*, 2003), also used in the EARLINET community, is based on the detection of local minima and maxima in the gradient of the range corrected signal. Within this work, the gradient  $d \ln P_{corr}^2(z, \lambda) / dz$  was used. Maxima correspond to an increase of  $P_{corr}(z, \lambda)$  with height and therefore the aerosol layer bottom. Minima correspond to a decrease and therefore the aerosol layer top. The absolute minimum is often treated as equivalent to the top of the PBL. However, the probability is high that aerosol layers directly above the PBL cannot be distinguished from the PBL itself. Another difficulty of the gradient method is the identification of relevant minima and maxima. Especially in measurements with low aerosol load in the boundary layer or weak free tropospheric aerosol layers it can be hard to distinguish those extrema from noise. For automatic retrievals, system dependent thresholds are defined. Although the gradient method can be applied to single profiles of  $P_{corr}(z, \lambda)$ , temporal averaging reduces the noise and facilitates the definition of the extrema. For this work the gradient was calculated from data, which was not vertically smoothed. The gradient method was applied manually, introducing subjectivity to some extend.

### 2.2.6. Aerosol optical properties

From the obtained profiles of the particle extinction and backscatter coefficients, different aerosol optical properties can be derived. Many publications exist, presenting climatologies (Müller *et al.*, 2007), single case studies (Preißler *et al.*, 2011a) or simulations (Ackermann, 1998) of typical values of aerosol optical properties.

The definition of the particle lidar ratio  $S_{par}(z, \lambda)$  was given before (equation (2.9)). This intensive quantity depends on chemical properties of the aerosol, the relative humidity, as well as the size and shape of the particles. As those properties may change throughout the atmosphere, the particle lidar ratio depends on  $z$ .  $S_{par}(z, \lambda)$  also depends on the wavelength, with typically larger values at smaller wavelengths. The magnitude of this dependence generally varies with the aerosol type. Typical values of  $S_{par}$  for atmospheric aerosols vary between 20 and 100 sr.

The Ångström exponent  $\mathring{a}_\alpha$  (Ångström, 1964), introduced in equation (2.24), describes the wavelength dependence of the extinction coefficient. Analogically, the wavelength dependence can be calculated from the particle backscatter coefficient,  $\mathring{a}_\beta$ . It requires the measurement at two or more different wavelengths. The Ångström exponent depends on the aerosol size distribution. Large values of  $\mathring{a}$  signify a higher number of smaller particles, relative to the number of larger particles and vice versa. Values between 0 and 2.5 are typically found for atmospheric aerosols.

The aerosol optical depth (AOD)  $\tau$  is defined as

$$\tau(\lambda) = \int_{z_1}^{z_2} \alpha(z', \lambda) dz'. \quad (2.27)$$

The AOD for the whole column is derived from  $z_1 = 0$  to  $z_2 = \text{TOA}$  (top of the atmosphere). From lidar measurements, the determination of  $\tau$  of individual aerosol layers is possible, defining  $z_1$  as the layer bottom and  $z_2$  as the layer top. In Évora, as a rural region with very few local aerosol sources, the columnar optical depth is generally small. According to Elias *et al.* (2006),  $\tau(441 \text{ nm})$  obtained from sun photometer measurements in Évora was less than 0.3 in more than half of the summer measurements during the years 2002 and 2003. In rare cases of high aerosol load, values of the columnar  $\tau(441 \text{ nm})$  may exceed 1 at this site.

### 2.2.7. Depolarisation

The emitted laser beam is linearly polarised. In the atmosphere, the orientation of the polarisation is changed by scattering on molecules and non-spherical particles, for example mineral dust and volcanic ash. According to Mie-theory, scattering processes on spherical particles conserve the orientation of the polarisation. At 532 nm, PAOLI detects the backscattered signal of all orientations (total, index: 532) as well as the cross polarised fraction separately (cross, index: 532x).  $P^\perp(z, \lambda)$  represents the randomly polarised photons caused by above mentioned processes. The total signal is the sum of the cross ( $\perp$ ) and parallel ( $\parallel$ ) polarised components,

$$P(z, \lambda) = P^\perp(z, \lambda) + P^\parallel(z, \lambda). \quad (2.28)$$

## 2. Instrument and methodology

From the two detected signals, the depolarisation ratio can be obtained. The linear volume depolarisation ratio  $\delta_v(z, \lambda)$  is defined as

$$\delta_v(z, \lambda) = \frac{P^\perp(z, \lambda)}{P^\parallel(z, \lambda)}. \quad (2.29)$$

It results from the backscattering on molecules, hydrometeors and aerosol particles within the volume illuminated by the light pulse produced by the laser. For a system with polarisation independent efficiency and perfect alignment, i.e.  $K^\perp(\lambda) = K^\parallel(\lambda)$  and  $O^\perp(z, \lambda) = O^\parallel(z, \lambda)$ ,  $\delta_v(z, \lambda)$  is often written as

$$\delta_v(z, \lambda) = \frac{\beta^\perp(z, \lambda)}{\beta^\parallel(z, \lambda)} \exp\left(\tau^\parallel(\lambda) - \tau^\perp(\lambda)\right), \quad (2.30)$$

(*Schotland et al.*, 1971; *Sassen*, 2005). Generally, the transmission term in equation (2.30) can be neglected because atmospheric extinction does not affect the polarisation (*Höhn*, 1969). In practice, the ratio of the backscatter coefficients  $\beta^\perp(z, \lambda)$  and  $\beta^\parallel(z, \lambda)$  are often used (*Schotland et al.*, 1971). However, the physical meaning of this solution is questionable. The detected light consists of a parallel polarised and an unpolarised component. The measured cross polarised signal  $P^\perp(z, \lambda)$  is determined by the occurrence of unpolarised light, but the latter also contributes to the parallel polarised signal  $P^\parallel(z, \lambda)$ . Thus, the definition of  $\delta_v$  as the ratio of those two quantities is physically arbitrary. *Gimmestad* (2008) proposed the determination of a depolarisation parameter  $d(z, \lambda)$  from the detected signals

$$d(z, \lambda) = \frac{2P^\perp(z, \lambda)}{P^\parallel(z, \lambda) + P^\perp(z, \lambda)}. \quad (2.31)$$

It describes the capability of the scattering medium to depolarise the light. This factor can also be obtained from the commonly used  $\delta_v(z, \lambda)$  as

$$d(z, \lambda) = \frac{2\delta_v(z, \lambda)}{1 + \delta_v(z, \lambda)}. \quad (2.32)$$

It follows, that  $d(z, \lambda)$  deviates strongly from  $\delta_v(z, \lambda)$  in case of small depolarisation.

For the determination of the depolarisation, lidar systems have to be calibrated. *Alvarez et al.* (2006) and *Freudenthaler et al.* (2009), among others, presented overviews over existing calibration methods. The calibration procedure of PAOLI includes the assumption of a calibration constant  $k(\lambda)$ , similar to the calibration for the retrieval of the particle backscatter coefficients

$$\delta_v(z, \lambda) = k(\lambda) \frac{P^\perp(z, \lambda)}{P^\parallel(z, \lambda)}. \quad (2.33)$$

In a particle free height  $z_0$ , only  $\delta_{mol}(z_0, \lambda)$  has to be taken into account. Which yields

$$k(\lambda) = \delta_{mol}(z_0, \lambda) \frac{P^\parallel(z_0, \lambda)}{P^\perp(z_0, \lambda)}. \quad (2.34)$$

The calibration constant  $k(\lambda)$  represents the unknown efficiencies of the two channels used for the calculation of the depolarisation. The linear depolarisation ratio of molecules  $\delta_{mol}(z, \lambda)$  depends on the bandwidth of the interference filters in the receiver and the atmospheric temperature (*Behrendt and Nakamura*, 2002).

In principal, the transmission efficiency  $\eta_i(z)$  is different for each receiving channel  $i$  of the lidar. The efficiency also depends on the polarisation of the detected light. In case of PAOLI this effect cannot be neglected. The receiver unit of this system contains one beam splitter, which causes a polarisation dependence of the efficiency of the detection channel at 532 nm (total) (Preißler *et al.*, 2011a). A procedure to correct for this behaviour was introduced by Mattis *et al.* (2009) and is briefly presented here. From equation (2.28) follows the relation

$$P_i(z, \lambda) = \eta_i^\perp(z) P^\perp(z, \lambda) + \eta_i^\parallel(z) P^\parallel(z, \lambda). \quad (2.35)$$

Index  $i$  represents the receiving channel.  $P_i(z, \lambda)$  is the signal measured by the detector and  $P^\perp(z, \lambda)$  and  $P^\parallel(z, \lambda)$  is the power reaching the telescope at the detected wavelength. The transmission efficiencies  $\eta_i^\perp$  and  $\eta_i^\parallel$  are assumed to be height independent. The transmission ratio  $D_i$  is defined as

$$D_i = \frac{\eta_i^\perp}{\eta_i^\parallel}. \quad (2.36)$$

$D_i$  can be determined experimentally for all receivers (Mattis *et al.*, 2009). For the signal detected in the polarisation dependent channel follows from equations (2.29), (2.35) and (2.36)

$$P_i(z, \lambda) = \eta_i^\parallel(z) P_0(z, \lambda) \left( \frac{1 + D_i \delta_v(z, \lambda)}{1 + \delta_v(z, \lambda)} \right), \quad (2.37)$$

(Grein, 2006).

Considering those effects,  $\delta_v(z, \lambda)$  can be obtained by forming the ratio of the signals of the two channels,  $P_{532x}(z, \lambda)$  and  $P_{532}(z, \lambda)$  in case of PAOLI, with different transmission ratios  $D_{532x}$  and  $D_{532}$ , which yields

$$\delta_v(z, \lambda) = \frac{k(\lambda) - \left( \frac{P_\perp(z, \lambda)}{P_{total}(z, \lambda)} \right)}{D_{total} \left( \frac{P_\perp(z, \lambda)}{P_{total}(z, \lambda)} \right) - D_\perp k(\lambda)}. \quad (2.38)$$

The calibration factor  $k(\lambda)$  represents the unknown ratio  $\eta_\perp^\parallel / \eta_{total}^\parallel$ , or  $\eta_{532x}^\parallel / \eta_{532}^\parallel$  in case of PAOLI.

Following Biele *et al.* (2000) and Freudenthaler *et al.* (2009), the linear particle depolarisation ratio  $\delta_{par}(z, \lambda)$  is determined as

$$\delta_{par}(z, \lambda) = \frac{\beta_{par}^\perp(z, \lambda)}{\beta_{par}^\parallel(z, \lambda)} = \frac{(1 + \delta_{mol}(z, \lambda)) \delta_v(z, \lambda) R(z, \lambda) - (1 + \delta_v(z, \lambda)) \delta_{mol}(z, \lambda)}{(1 + \delta_{mol}(z, \lambda)) R(z, \lambda) - (1 + \delta_v(z, \lambda))}, \quad (2.39)$$

with the backscatter ratio  $R(z, \lambda)$ , which is defined as

$$R(z, \lambda) = \frac{\beta_{mol}(z, \lambda) + \beta_{par}(z, \lambda)}{\beta_{mol}(z, \lambda)}, \quad (2.40)$$

and the linear particle depolarisation ratio of molecules  $\delta_{mol}$ , which is

$$\delta_{mol}(z, \lambda) = \frac{\beta_{mol}^\perp(z, \lambda)}{\beta_{mol}^\parallel(z, \lambda)}. \quad (2.41)$$

In order to obtain  $R(z, \lambda)$  the particle backscatter coefficient is necessary. It can be retrieved by previously described methods (see sections (2.2.3) and (2.2.4)).

### 2.3. Overview over corrections and uncertainties

Uncertainties in lidar measurements arise from a large number of causes. In the system itself, each component in the optical path contributes to errors in the detected signal. Furthermore, various assumptions with consequences of different magnitudes are made for the data analysis. The range dependent signal-to-noise ratio (SNR) is another factor and the reason for increasing uncertainties with distance. Detailed studies about uncertainties in lidar measurements have been presented before (*Russel et al.*, 1979; *Klett*, 1981; *Bissonnette*, 1986; *Ansmann et al.*, 1992b). The relative statistical errors in the troposphere are typically below 10 % for the particle extinction coefficients and less than 5 % for the particle backscatter coefficients. They are mainly caused by noise in the detected signal. This type of error is estimated by applying Poisson statistics (*Ansmann et al.*, 1992b). This approach is valid for small count rates. For higher rates, the Poisson distribution merges into the Gauss distribution.

Further errors are introduced to the profiles of particle extinction and backscatter coefficients by averaging processes, both in time and space, by correction procedures and by the assumption of input parameters, namely a reference value in a certain reference height, profiles of temperature and pressure, lidar ratio for the Klett method and Ångström exponent for the Raman method. Errors arising from those assumptions often depend on the particle load, with smaller relative errors in regions of high load and vice versa. The effect of the correction procedures and assumptions on the lidar profiles is described in section (4.1) by means of example measurements.

#### Background correction

The detectors of a lidar system do not only capture photons emitted by the lidar beam, but any radiation at the same wavelengths incident on the telescope. However, skylight and light sources on the ground are temporarily constant<sup>2</sup> and therefore their contribution to the lidar signal appears constant in altitude. The bias of the signal profile caused by this effect has to be corrected for. For the background correction, the detected signal at the far end of the lidar profile is averaged over several kilometres. In case of PAOLI the maximum altitude of detection is around 61 km. There, the SNR is so low, that the signal caused by the lidar beam can be neglected. The thus obtained height constant background signal  $P_{BG}(\lambda)$  is subtracted from the whole profile of the lidar signal to retrieve  $P(z, \lambda)$  used in the lidar equation (2.1). Hereby, overestimation of  $P_{BG}(\lambda)$  can lead to negative values of  $P(z, \lambda)$ , which are physically unrealistic. Whereas underestimation of  $P_{BG}(\lambda)$  results in artificially higher values of  $P(z, \lambda)$  (*Kovalev and Eichinger*, 2004).

#### Dead time correction

The photon counting behaviour of a PMT gets non-linear if there are too many photons arriving at the detector at the same time. Then, they cannot be distinguished individually by the PMT. The time after detection of a photon in which the PMT is practically blind is called dead time  $t_d$ . By using neutral density filters (NDFs), this effect can be suppressed. For PAOLI measurements the NDFs are generally chosen in a way that the count rates

---

<sup>2</sup>The assumption is, that the background radiation is constant during the time period of 600 laser shots (30 s).

in the signal maximum are around 10 Mcps<sup>3</sup>. But even so, the dead time can affect a measurement in case of clouds or high aerosol load. The correction of this non-linear effect is done after the relation first given by *Hayes and Schoeller (1977)*

$$n = n' e^{-n' t_d}, \quad (2.42)$$

where  $n$  is the true count rate and  $n'$  is the registered count rate. An error estimation of the dead time correction was done for PAOLI measurements and is described in detail in section (3.2). The influence of the dead time on the raw data was found to be small. Therefore, the dead time correction was not applied for most of the lidar measurements presented in this work.

#### Overlap correction

The overlap correction is another source of uncertainty by using the Klett method, but also by calculating the particle extinction profiles. The correction function is retrieved experimentally and contains uncertainties with a strong influence close to the instrument. The accuracy of the overlap correction function mainly depends on the accuracy of the calculated particle backscatter profiles. Information on the overlap behaviour of PAOLI are presented in section (3.3.4).

#### Averaging and smoothing

In general, profiles of atmospheric quantities are more accurate, if averaged over a certain time interval (*Kovalev and Eichinger, 2004*). On the other hand, averaging over an inappropriate time period, for example too long or during unstable atmospheric conditions, would introduce large errors. The influence of noise is also reduced by vertical sliding averages. Applying height dependent smoothing lengths allows the calculation of profiles up to high altitudes. The uncertainties arising from the vertical smoothing depend on the variability of the lidar signal with height and on the smoothing length.

#### Molecular profiles

For the determination of the molecular extinction, the temperature and pressure profiles are needed. An uncertainty in the radio sounding profile of 1-2% at the reference height  $z_0$  can lead to errors of 20 to 40% in the particle backscatter coefficient (*Kent and Hansen, 1998; Kovalev and Eichinger, 2004*). Such errors can easily occur, if the radio sounding is not launched correlative to the lidar measurement. According to *Ansmann et al. (1992b)*, the temperature gradient is the most crucial atmospheric quantity. Especially for temperature inversions, the true temperature profile deviates strongly from often assumed standard atmospheric conditions. This can yield a relative error in the particle extinction coefficients of 10% in case of high particle load and more in case of low particle load. For the particle backscatter coefficients this systematic error is less than 10%. *Mona et al. (2009)* compared non-routine radio sounding profiles from southern Italy with the GDAS model soundings of NOAA ARL and found very good agreement. The influence of the assumption of a standard atmosphere against the use of model soundings has also been investigated by *Mona et al. (2009)*. The authors found deviations in the attenuated

---

<sup>3</sup>Mcps: megacounts per second =  $10^6$  counts s<sup>-1</sup>

## 2. Instrument and methodology

backscatter<sup>4</sup> profiles well below 5% up to 10 km. Within this work, temperature and pressure profiles from the GDAS model soundings were used for the calculation of the molecular profiles.

### Reference height and reference value

Term  $K(\lambda)$  of the lidar equation (see section (2.2.1), equation (2.2)) is generally unknown. This fact requires the calibration of the backscatter coefficient profiles by assuming a value of the backscatter coefficient (reference value) in a certain height range (reference height) (see sections (2.2.3) and (2.2.4)). At the reference height  $z_0$  the error of this assumption is equal to the error of the reference value. With decreasing optical depth, which means closer to the lidar, the error decreases and with increasing optical depth, i.e. beyond  $z_0$ , the error increases (*Kovalev and Moosmüller, 1994*). For shorter wavelengths, the slope of this effect is steeper than for longer wavelengths because of the higher contribution of molecular scattering. That means, at shorter wavelengths the error is smaller for  $z < z_0$ . For all wavelengths follows, that  $z_0$  should be chosen as high as possible (*Kovalev and Eichinger, 2004*), always considering particle free conditions. The limiting factors in the far range are the SNR and the accuracy of the background signal, because the impact of an error in  $P_{BG}(\lambda)$  is larger in higher ranges.

### Lidar ratio

The most critical assumption in the retrieval of the backscatter coefficients with the Klett method (section (2.2.3)) is that of the particle lidar ratio  $S_{par}(z, \lambda)$  (*Ansmann and Müller, 2005*).  $S_{par}(z, \lambda)$  can vary strongly with altitude. Therefore, assuming a height constant value of  $S_{par}(\lambda)$  can lead to large errors in the profile of the particle backscatter coefficient.  $S_{par}(z, \lambda)$  also depends on the wavelength. The influence of the error differs with  $\lambda$  as well, with a higher effect at shorter wavelengths. This spectral dependence is linked to the strong contribution of the molecular signal to the total signal at short wavelengths (*Takamura and Sasano, 1987*). In general, the errors in the profiles obtained with the Klett method are larger in case of an overestimation of  $S_{par}(\lambda)$  (*Kovalev, 1995*).

### Ångström exponent

Besides reference height and value, the Raman method requires the assumption of the wavelength dependence of the signals at the elastic and the Raman wavelength. This parameter is represented by the Ångström exponent  $\hat{a}$ . According to *Ansmann and Müller (2005)*, an absolute error of 0.5 in  $\hat{a}$  causes a relative deviation in the resulting profile of the particle extinction in the order of 5%. This is a small contribution to the total uncertainty considering that the range of typical values of  $\hat{a}$  of atmospheric aerosol is about 0 to 2.5.

### Multiple scattering

Multiple scattering effects can be neglected for aerosol studies by ground based lidar measurements (*Wandinger et al., 2010*). However, this effect is of significance for lidar

---

<sup>4</sup>Attenuated backscatter is the backscatter multiplied with the transmittance:

$$\beta_{att}(z, \lambda) = \beta(z, \lambda) T(z, \lambda).$$

measurements of clouds. The magnitude of errors caused by the multiple scattering depends on the FOV. For example, *Ansmann et al.* (1992b) gives relative errors in the profile of the particle extinction coefficient of 5 to 10%.

### Depolarisation calibration

The accuracy of the linear volume depolarisation ratio  $\delta_v(z, \lambda)$  is influenced by the purity of the polarisation of the laser beam, the performance of the SHG, THG and each optical component in the emitting and receiving part of the system, as well as the alignment of the polariser in front of the detector (*Sassen, 2005*). Those effects are specified by means of the system calibration (see section (2.2.7)). The influence of particles within the calibration height is the most critical factor for this procedure. The assumption of an erroneous calibration value  $k$  can introduce large deviations to  $\delta_v(z, \lambda)$ . To estimate the uncertainty of  $\delta_{par}(z, \lambda)$ , the error of  $\delta_{mol}$  and of the particle and molecular backscatter coefficients have to be considered additionally. As mentioned before,  $\delta_{mol}$  mainly depends on the bandwidth of the interference filters in the receiver. According to *Behrendt and Nakamura (2002)*, the temperature dependence is small for all receivers of PAOLI (bandwidths between 0.3 and 1.2 nm FWHM<sup>5</sup>). Neglecting this dependence results in errors of  $\delta_{mol}$  of much less than 10%.

### Polarisation dependent receiver transmission

Another source of a systematic error arises from polarisation dependent receiver transmission. It is significant in the case of the detection of depolarising scatterers, especially for systems detecting the total signal with a single channel (*Mattis et al., 2009*). The ratio of the transmission efficiencies of the total channel at 532 nm of PAOLI,  $D_{532}^{total}$  is  $3.9 \pm 0.2$ . Without the correction, the relative systematic error of the particle backscatter coefficient would be up to 70% for  $\delta_v = 0.3$ , with smaller errors for smaller depolarisation values. The transmission ratio of the channel detecting the cross polarised fraction at 532 nm  $D_{532}^{\perp}$  is naturally very high ( $394.7 \pm 0.8$ ). For the other channels,  $D_i$  is between 0.9 and 1.1 and the arising relative systematic error in the particle backscatter coefficient is less than 5%. Following *Mattis et al. (2009)*, the signal  $P'_i(z, \lambda)$  corrected for depolarisation dependent receiver transmission is calculated as

$$P'_i(z, \lambda) = \frac{P_i(z, \lambda)}{f_T(z, \lambda, D_i)}, \quad (2.43)$$

with the transmission function

$$f_T(z, \lambda, D_i) = \frac{D_i \delta_v(z, \lambda) + 1}{\delta_v(z, \lambda) + 1}. \quad (2.44)$$

The uncertainty of this correction depends on the error of  $f_T(z, \lambda, D_i)$ , which is estimated by linear error propagation, considering the errors in  $D_i$  and  $\delta_v(z, \lambda)$ . For PAOLI, the error introduced with the correction of the signal at 532 nm (total) is smaller than 10% for  $\beta_{par}$  and  $\delta_{par}$ .

<sup>5</sup>FWHM: commonly used acronym for full width at half maximum.

### Summary

Common error propagation (linear or non-linear) considering all the sources of uncertainties listed above can lead to unrealistically high uncertainties of  $\beta_{par}$ ,  $\alpha_{par}$  and  $\delta_{par}$ . A good alternative could be the application of the Monte Carlo method for a more realistic error estimation. Currently, investigations concerning this approach are done in the framework of EARLINET. However, no results were published yet.

Overall, the relative errors of  $\beta_{par}$  obtained with the Raman method,  $\beta_{par}$  obtained with the Klett method,  $\alpha_{par}$  and  $\delta_{par}$  are generally less than 15%, 20%, 25% and 25%, respectively (Franke *et al.*, 2001; Alados-Arboledas *et al.*, 2011; Preißler *et al.*, 2011a). A detailed study on the influence of different assumptions and corrections on a PAOLI measurement is presented in section (4.1).

### 3. Lidar performance

The operation of a new instrument can hold certain difficulties, especially of a complex system such as a lidar. The optical elements are the most important parts of a lidar system. Figure (3.1) shows a timeline of changes in the optics of the Portable Aerosol and Cloud Lidar (PAOLI) and also the availability of the six detection channels. The photomultiplier tubes (PMTs) at 355, 387, 532 (total) and 607 nm were working well since their setting up in Leipzig. The PMT at 532 nm (cross polarised) was implemented in the system in November 2009. It was performing well until the middle of February 2010, when it started producing electronic noise. Also the PMT at 1064 nm was degrading. Details on those issues are given in section (3.1).

A good optical alignment is crucial for high quality lidar data. Various procedures exist for testing and optimising the alignment. Those used within this work are explained in section (3.2).

One of the main difficulties was to reach a height of full overlap, which allows the observation of the boundary layer. The experimentally determined overlap height was about 4 to 5 km during the first measurements. In order to improve the alignment, the beam position was changed several times since September 2009, the divergence of the outgoing beam was reduced, and the position of the pinhole was changed. Those technical improvements and the optimisation of the beam position by means of a two dimensional scan are discussed in section (3.3). Finally, a summary of the changes in the lidar system is given in section (3.4).

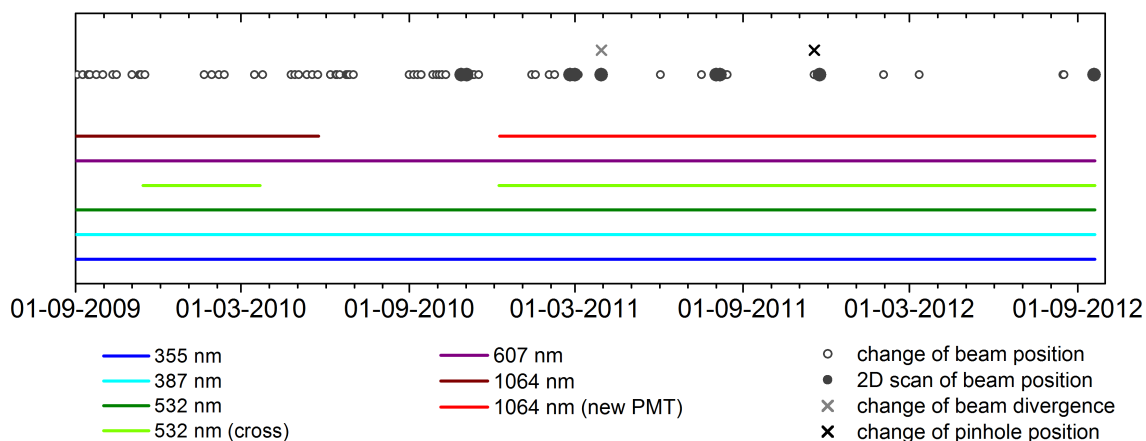


**Figure 3.1.:** Availability of the detection channels of PAOLI and changes in the optics since the start of regular measurements on 1 September 2009.

### 3.1. Technical challenges

A very critical parameter in the operation of PAOLI proved to be the temperature inside the cabinet. This subject is treated in section (3.1.1). But also ageing processes of certain components contribute to data loss or instrument failure. Problems with PMTs and with the laser were encountered and are discussed in sections (3.1.2) and (3.1.3).

#### 3.1.1. Temperature instability

Originally, PAOLI was equipped with an air conditioner and a heater. The air conditioner is necessary when operating the lidar, as the laser head, the laser cooling unit, the computer and the PMTs are producing heat. The lidar is placed on the north side of the building of the Évora Geophysics Center (Centro de Geofísica de Évora) (CGE), protected from direct sunlight during morning and evening. However, during midday it is not shaded by the building and the sun can heat up the system. On hot days, or when the sun is shining directly on the lidar, the air conditioner is needed to protect the system from overheating. The heater is implemented to prevent the laser cooling circuit from freezing but also to ensure a stable temperature. With the additional heat source the air conditioner has to cool continuously to keep the temperature under a certain threshold. When reaching the temperature threshold, the air conditioner switches off automatically. However, a continuous cooling is desirable in order to prevent temperature oscillations. In cold nights, the heater was not powerful enough to keep the air conditioner from switching on and off. Thus, a temperature oscillation occurred. The cabinet temperature is monitored by two sensors, one on each of the lateral walls.

The position of the outgoing beam of PAOLI is very sensitive to temperature changes. As mentioned before, a camera is capturing an image of the receiving telescope at 532 nm and thereby enables the monitoring of the position of the outgoing beam. In figure (3.2) two of such images are shown, one at a cabinet temperature of 14 °C (left) and one at 17 °C. At 14 °C the beam image had a symmetric, roughly triangular shape. While the temperature increased, the beam image shifted to the upper side of the field of view (FOV) of the receiving telescope and was cut off at the edge.

This temperature dependence is reflected in the detected signal. Figure (3.3)(left) shows the range corrected signal at 532 nm (total) in a time-height plot of a night time measurement on 2 March 2010. For comparison, a night time measurement without temperature oscillations is shown on the right hand side of figure (3.3). The range corrected signal of

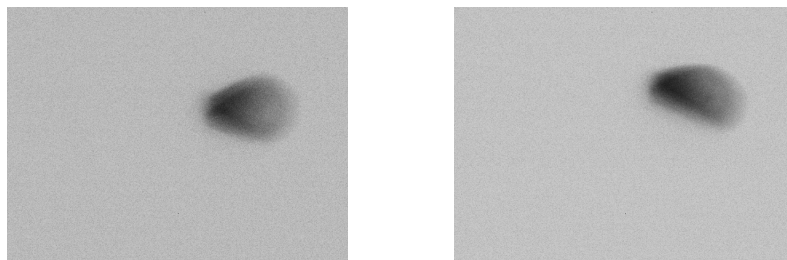


**Figure 3.2.:** Image of the outgoing beam seen through the receiving telescope. Photos taken by the implemented camera on 18 November 2011 with a cabinet temperature at 14 °C (left) and 17 °C (right).

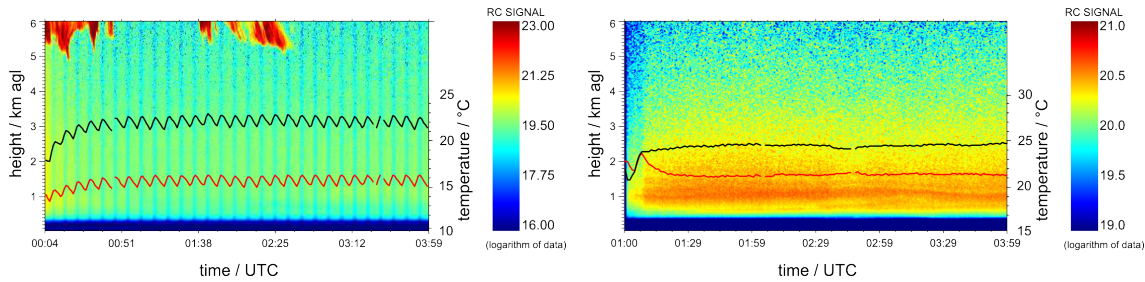


**Figure 3.3.:** Range corrected signal at 532 nm (total) (colour plot) and the temperature measured on two points in the lidar cabinet (lines) between 0:04 and 3:59 UTC on 2 March 2010 (left) and between 1:00 and 3:59 UTC on 25 February 2011 (right).

the other channels were similar to those at 532 nm (total). The temperature inside the lidar cabinet is continuously monitored at two points. Those values are plotted as lines. The structures with high signal above 5 km above ground level (agl) on 2 March 2010 were clouds. In the beginning of the measurements, the lidar was warming up. On 2 March 2010 this warm-up period lasted about 30 min. During this time the signal was decreasing with increasing temperature. After that, the temperature inside the cabinet was oscillating around a certain value by  $\pm 0.5$  to  $\pm 1.0$  K. Correlating with the oscillation of the temperature was the oscillation of the range corrected signal. This signal oscillation was likely caused by the efficiencies of the second harmonic generator (SHG) and the third harmonic generator (THG) or by a slight shift in the beam position. The overlap of laser beam and FOV of the receiver was too small to get any signal below 0.3 km agl. But also this altitude, the transition from light to dark blue in figure (3.3), oscillated. This indicates, that the overlap is not stable during measurements with oscillating temperature. To overcome those problems another heater was built into the system on 12 February 2011. Since then, the temperature oscillation occurred less frequently.

### 3.1.2. Photomultiplier tubes

In February 2010 the channel at 532 nm (cross polarised) sporadically produced unexpectedly high background values. Those became more frequent in time. Two example night time measurements from 10 and 11 March 2010 are shown in figure (3.4). The time-height plot of the range corrected signal at 532 nm (total) is given as reference. The malfunction in the 532 nm (cross polarised) channel was clearly related to the temperature oscillation. This became evident especially in the measurement from 11 March 2010.

The pre-amplifier and all cables of the PMT were replaced for testing purposes. The problem remained. Therefore, they could be excluded as reason for the noise. This led to the conclusion, that the PMT was causing the distorted signal. It was removed from the lidar on 23 March 2010 and sent to the manufacturer for further testing and repair. The repaired PMT was reintegrated into the lidar on 9 December 2010 and is working without problems since then.

From the beginning of the operation of PAOLI, the PMT at 1064 nm returned very low signals. No neutral density filters (NDFs) were used, but the counts were about ten times lower than in the other channels with NDFs. As the signal at 1064 nm is least susceptible to noise, the data could still be used. With time, the PMT degraded further and the signal became too weak to ensure an acceptable signal-to-noise ratio (SNR). Therefore, the PMT

### 3. Lidar performance

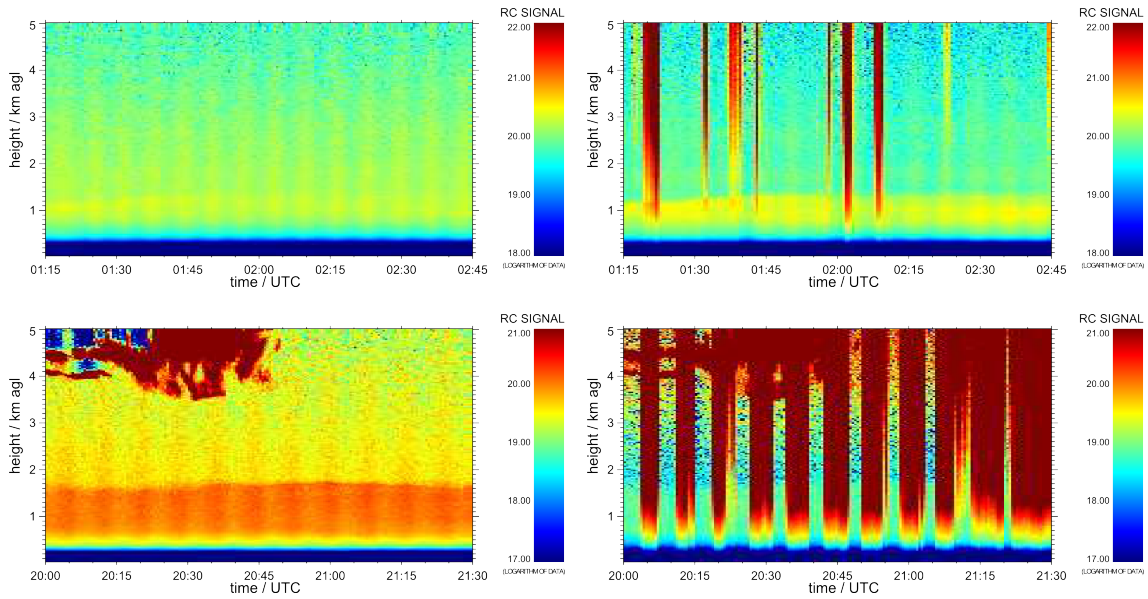


**Figure 3.4.:** Range corrected signal at 532 nm total (left) and cross polarised (right) on 10 March 2010 (upper plots) and 11 March 2010 (lower plots).

was sent to the manufacturer together with the PMT of the 532 nm (cross polarised) channel. It was also repaired and reinstalled into the system on 9 December 2010, and is working well since then.

#### 3.1.3. Laser

The laser flash lamps of PAOLI have a lifetime of  $120 \times 10^6$  shots. They need to be replaced in regular intervals. On 28 September 2010 the flash lamps of the laser were changed. For that, the laser head was opened. On the front<sup>1</sup> face of the Nd:YAG rod some marks were found. They are shown on the left picture in figure (3.5). On the right photograph, the

<sup>1</sup>The front is the light emitting side of the laser.

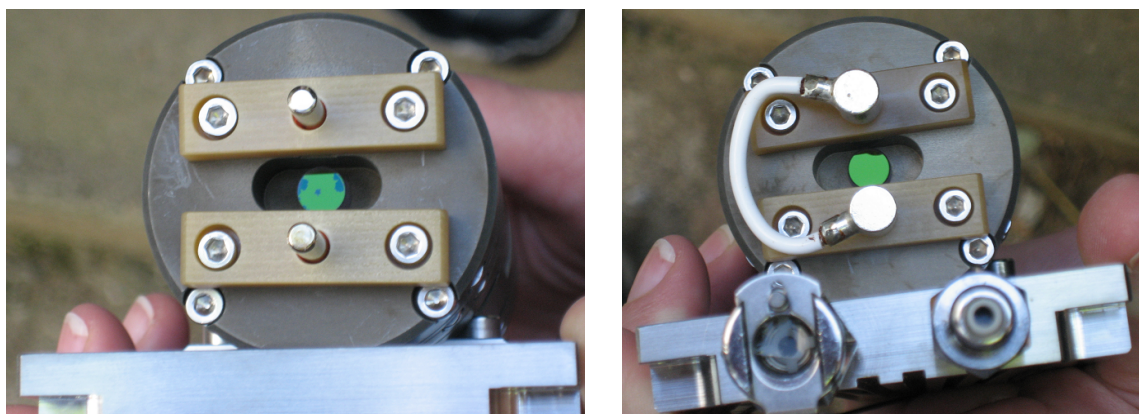


**Figure 3.5.:** Interior of the laser head from the front side (left) and from the rear side (right). The green round surface in the middle is the respective end of the Nd:YAG rod.

intact rear face of the Nd:YAG rod is shown. Those marks are probably an indicator for missing coating. They could have been caused by reflections of the emitted light on components in the path of the laser beam. However, a tilted quartz plate is placed in front of the laser head in order to prevent such reflections back into the laser head. The marks could also result from the ageing process of the rod. However, during another change of flash lamps on 3 July 2012, the marks were still visible, but unchanged. They are probably causing an imperfectly shaped laser beam cross section. However, this should not affect the retrieval of optical aerosol properties in a negative way.

## 3.2. Quality assurance

PAOLI is part of the European Aerosol Research Lidar Network (EARLINET) and the Spanish and Portuguese Aerosol Lidar Network (SPALINET). Various quality assurance tests were developed in the framework of EARLINET. Those tests give valuable information on the performance of different components of a lidar system. The procedures and results of the telecover test and the Rayleigh fit are given in the following (sections (3.2.1) and (3.2.2)). Additionally, the determination of the zero bin and the characterisation of the PMTs are explained in sections (3.2.3) and (3.2.4), respectively.

Every EARLINET station is obliged to perform the telecover test and Rayleigh fit on an annual basis. Furthermore, a software intercomparison should be done in the beginning of the regular operation within the network. The testing of the software used for the analysis of PAOLI data is described in section (3.2.5).

### 3.2.1. Telecover test

The telecover test is a quality assurance tool developed in the framework of EARLINET (*Freudenthaler, 2008*). The annual execution of this test is mandatory for EARLINET members to assure high quality lidar measurements within the network. It is also a powerful tool to determine the performance of the lidar in the near range after changes in the optical set-up. By covering parts of the receiving telescope, the alignment of the outgoing beam and the receiver channels can be tested. In case of PAOLI, three quarters of the primary mirror are covered at a time. Figure (3.6) shows a scheme of the receiving telescope and the four quarters, which are named after the cardinal points with north pointing to the outgoing beam. The telecover test usually starts with the measurement of the north sector (N1). It is continued clockwise, measuring the sectors east (E), south (S) and west (W), and ends with another measurement of the north sector (N2). This repetition is done to estimate the change of the atmosphere during the test. From the

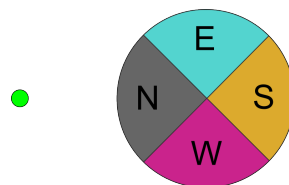


**Figure 3.6.:** Scheme of the outgoing beam (small green circle) and the receiving telescope (big circle) for the quadrant telecover test of a biaxial system (looking down on the mirror). The letters correspond to the sector names north, east, south and west.

### 3. Lidar performance

range corrected signals  $P_{RC}$ , the mean signal can be calculated

$$P_{RC}^{mean}(z, \lambda) = \frac{1}{4} (P_{RC}^N(z, \lambda) + P_{RC}^E(z, \lambda) + P_{RC}^S(z, \lambda) + P_{RC}^W(z, \lambda)). \quad (3.1)$$

The relative deviation of each profile from the mean is obtained as follows

$$\Delta^x(z, \lambda) = \frac{P_{RC}^x(z, \lambda) - P_{RC}^{mean}(z, \lambda)}{P_{RC}^{mean}(z, \lambda)}, \quad (3.2)$$

with  $x$  representing any of the four sectors. The ratio

$$\Delta_{atm}(z, \lambda) = \frac{P_{RC}^{N1}(z, \lambda) - P_{RC}^{N2}(z, \lambda)}{P_{RC}^{mean}(z, \lambda)}, \quad (3.3)$$

is a measure for the atmospheric stability during the telecover test.

The north sector is closest to the outgoing beam. Therefore, the signal in sector N (1 and 2) should be detected first, i.e. at the lowest altitude, and it should also have the largest signal maximum. The signal in sector S should be detected last and it should have the smallest signal maximum. The signal in sectors E and W should increase at the same altitude and have a similar magnitude in the signal maximum.

Figure (3.7) shows the results of a telecover test conducted on 20 January 2012 at night. The data were averaged over 3 min. The two channels at 532 nm were least affected by noise, the SNR was low. The signal in sector N was detected at lowest altitudes in all channels. Furthermore, in sectors E and W the altitude of first detection and the signal in the maximum were similar. The signal in sector S was detected last. However, in the channel at 607 nm the signal maximum of the sector S was larger than the ones of sectors E and W. This is due to the noise in the normalisation range, which was chosen between 4 and 6 km agl for all channels. The relative deviations in the near range above 600 m agl were smaller than  $\pm 15\%$ ,  $\pm 20\%$ ,  $\pm 8\%$ ,  $\pm 10\%$ ,  $\pm 30\%$  and  $\pm 20\%$  at 355 nm, 387 nm, 532 nm (total), 532 nm (cross polarised), 607 nm and 1064 nm, respectively.

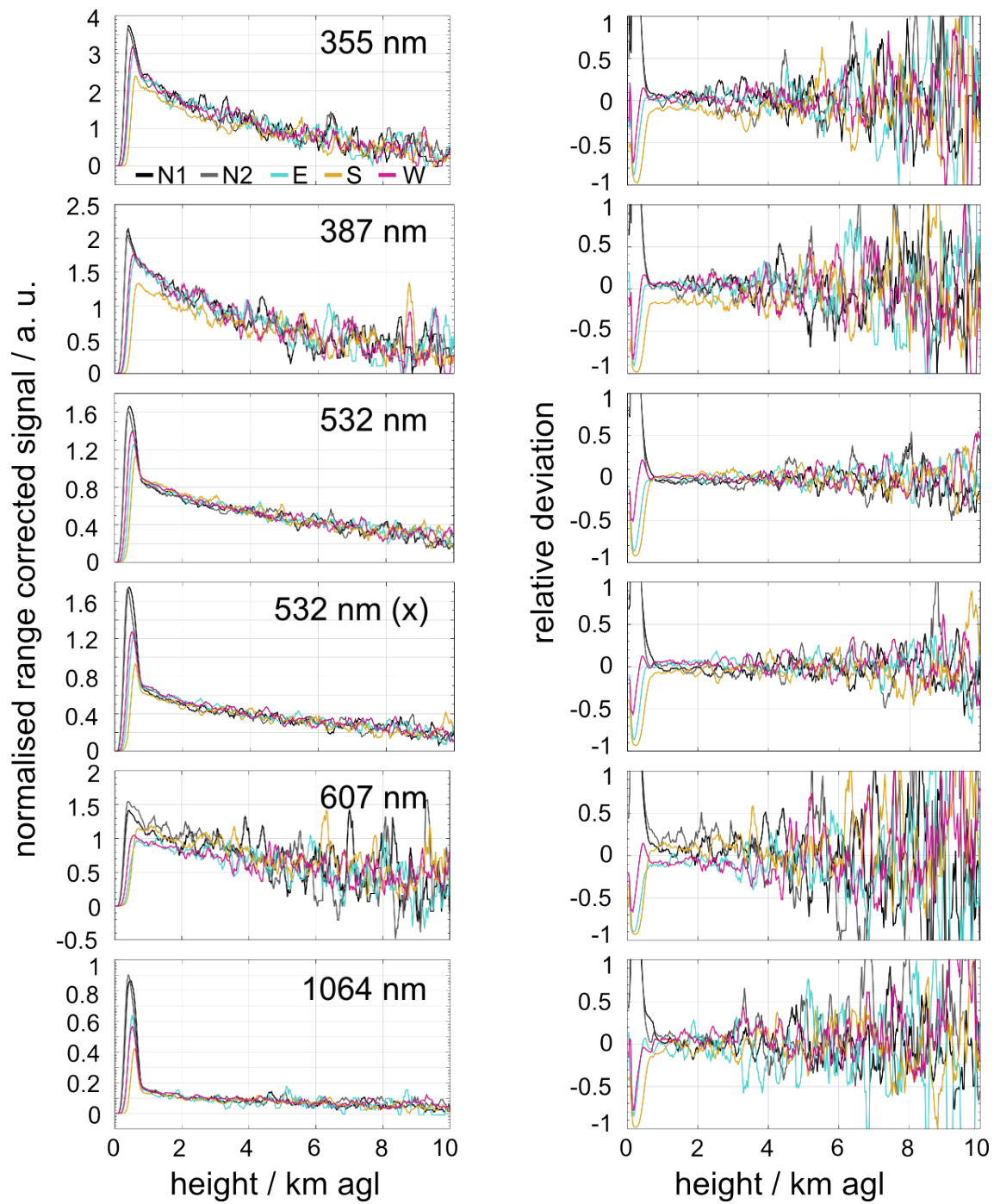
The ratio  $\Delta_{atm}$  is shown in figure (3.8). In all channels it was smaller than 30% from 0.5 to 3.0 km agl. The relative root mean square deviations for all channels are plotted in figure (3.9). They were smaller than 18% between 0.5 and 3.0 km agl.

#### 3.2.2. Rayleigh fit

The Rayleigh fit is an indicator for the behaviour of the instrument in the far range. Problems can occur, if the beam crosses the receiver FOV and exits on the other side, or if the overlap of beam and FOV is incomplete in all heights, for instance due to large beam divergence or wrong orientation of the outgoing beam. The Rayleigh fit is a comparison of the profiles of the range corrected lidar signal and the attenuated molecular backscatter coefficient. The attenuated backscatter coefficient  $\beta_{att}$  is the product of the backscatter coefficient and the transmittance

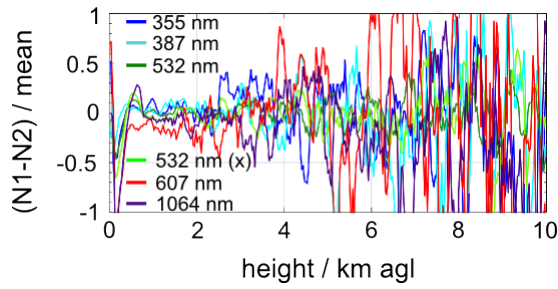
$$\beta_{att}(z, \lambda) = \beta(z, \lambda) \exp \left[ -2 \int_0^z \alpha(z', \lambda) dz' \right]. \quad (3.4)$$

Figure (3.10) shows the Rayleigh fits for all detection channels during the night time measurement on 25 February 2011. The PMT at 1064 nm was detecting rather low signal. Therefore, the SNR was low, especially in the far range. The other channels performed very well. The signals were following the curves of the attenuated molecular backscattering up to about 20 km agl. Above this altitude the profiles represented the background signals.



**Figure 3.7.:** Normalised range corrected signal (in arbitrary unit (a.u.)) detected in the four sectors (left) and the relative deviation of this signal from the mean value (right). The telecover test was performed on 20 January 2012. Data were averaged over 3 min and normalised between 4 and 6 km agl.

### 3. Lidar performance



**Figure 3.8.:** Atmospheric change, calculated as the ratio of the difference between the two measurements at sector N (1 and 2) and the mean value from the measurements of the sectors N (1), E, S and W. Same telecover test as in figure (3.7).

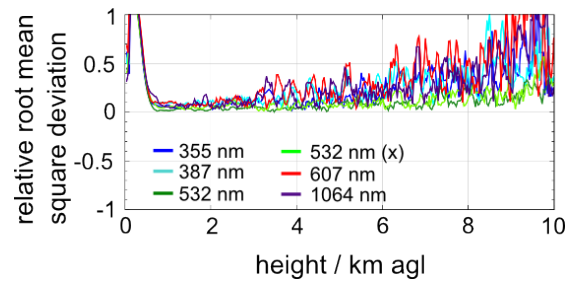


**Figure 3.9.:** Relative root mean square deviation of the signals detected in each channel. Same telecover test as in figure (3.7).

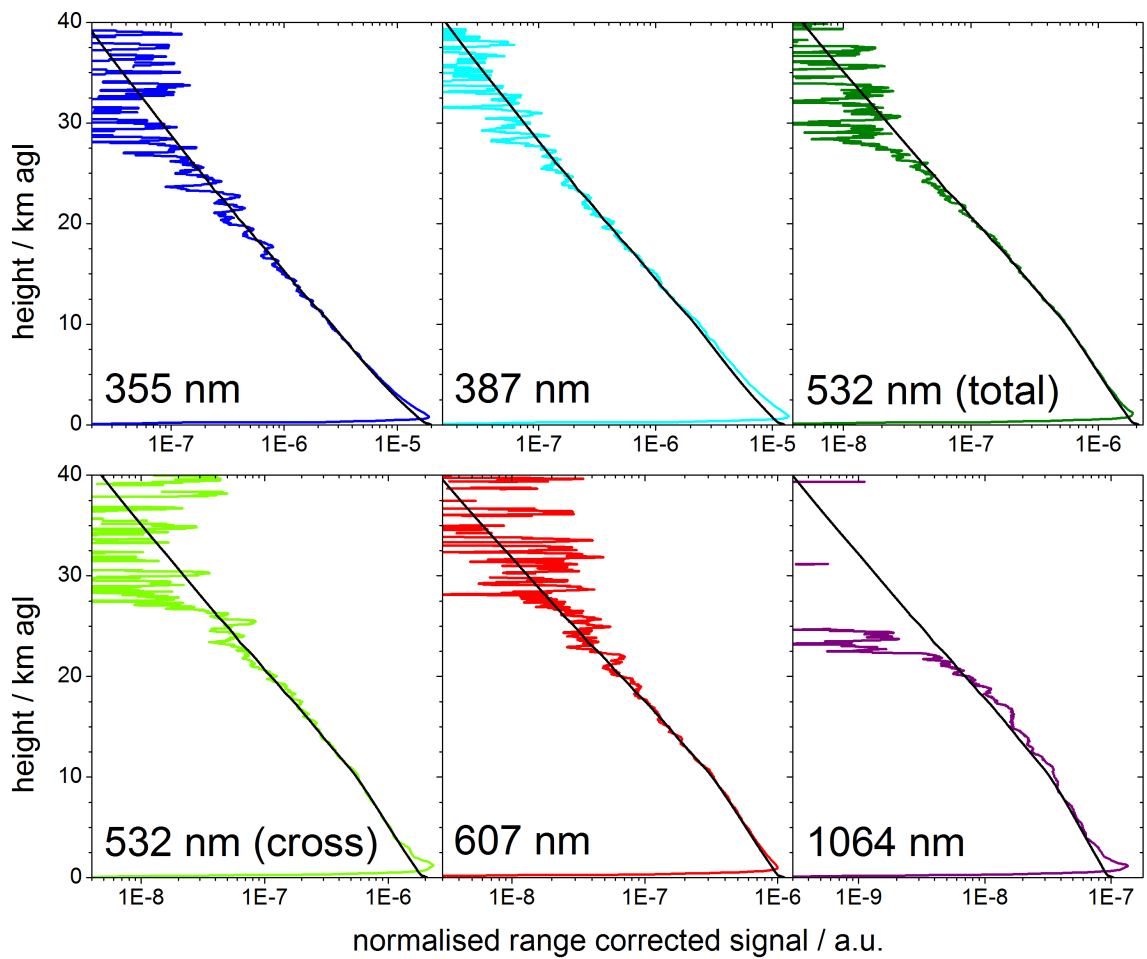


**Figure 3.10.:** Normalised range corrected signal from PAOLI measurements (coloured lines) and attenuated molecular backscatter obtained from model soundings (black lines) during night time on 25 February 2011 for all channels. The fit range was 7.5 to 9.0 km agl. Data were averaged over two hours and vertically smoothed over 500 m.

### 3.2.3. Zero bin

The data acquisition of PAOLI is triggered by the emission of the laser pulse by means of a photo diode placed between the laser and the SHG next to the optical axis. The triggering process takes more time than the pulse on the way from the laser to the exit of the lidar. The delay is mainly caused by the start-up behaviour of the data acquisition cards. Knowing this delay is especially important for an exact range correction in the near range. For the analysis of the data presented in this work a zero bin shift of 52.5 m (corresponding to a trigger delay of 175 ns) was used, according to the specification of the data acquisition cards.

### 3.2.4. Dead time correction

High photon count rates can lead to the saturation of the detector. As mentioned before, the behaviour of the PMT gets non-linear in such a case. The raw signal obtained from the saturated PMT at 532 nm (cross) is shown in figure (3.11). Apparently the photon count rate in the 532 nm (cross) channel was too high between about 550 and 700 m agl during some minutes of the measurement on 27 June 2012. In this height range, the PMT was not counting linearly. The signal maximum was at about 660 m agl at that time, exceeding about 34 Mcps. During routine measurements such high count rates are usually prevented by the application of NDFs.

To avoid such distortions in the lidar data, the photon counting behaviour of the PMTs needs to be specified. Therefore, the influence of the dead time of the PMTs was tested. From equation (2.42)(see section (2.3)) the dead time  $t_d$  of the PMTs can be calculated, if the true count rate  $n$  is known:

$$t_d = \frac{1}{n} \ln \left( \frac{n}{n'} \right). \quad (3.5)$$

It can be determined experimentally by applying a defined neutral filter (*Heroux, 1968*).

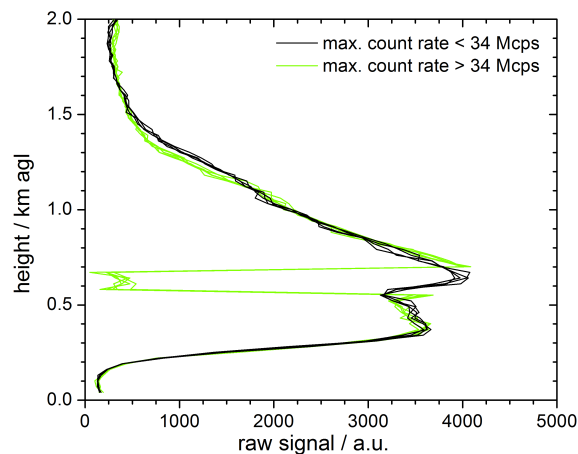


**Figure 3.11.:** Raw lidar signal with count rates at the signal maximum below (black) and above (green) 34 Mcps, illustrating the non-linear behaviour of the PMT at 532 nm (cross). Non-averaged 30 s profiles of the measurement on 27 June 2012 around 6:30 UTC (black) and 6:40 UTC (green).

### 3. Lidar performance

This could be realised for example by using NDFs (*Darland et al.*, 1979; *Whiteman et al.*, 1992; *Donovan et al.*, 1993) or by partially covering the telescope. The thus reduced count rate has to be corrected for this attenuation, so that it can be compared to the count rate at full intensity. The count rate at full intensity,  $n'$  in equations (2.42) and (3.5), is affected by the dead time of the detectors. The reduced signal is assumed not to be affected by the dead time and therefore represents the true count rate  $n$ .

The use of NDFs introduces uncertainties, as the optical depths of the NDFs are specified only for the visible spectral range. The optical depths can deviate strongly in the ultra-violet or infra-red ranges. Therefore, a telecover test (see section (3.2.1)) was used for the characterisation of the detectors of PAOLI. Before this test, a measurement without cover was done, giving  $n'$ . Then, the count rates were reduced by shading three quarters of the telescope, respectively. The count rates of the four sectors N (1), E, S and W were summed up in order to get  $n$ . The count rates at full intensity and the dead times in the signal maximum obtained from the telecover test on 18 November 2011 are given in table (3.1). Also listed are typical count rates observed by PAOLI ( $n^*$ ) and the relative errors caused by the dead time effect at those values. During the used measurement, the signal maximum was at 0.4 km agl.

For routine measurements, the NDFs are adjusted in a way that the maximum count rates are around 10 Mcps. At night time, the PMT at 607 nm generally counts less than the other channels. No NDFs were used in front of this PMT before and during the telecover test on 18 November 2011. Thus, the rather low count rate at 607 nm was the maximum possible during this measurement. The count rates of the other channels were comparable to the count rates during routine measurements or even exceeding those (355 and 532 nm). The mean values of  $t_d$  were below 5 ns for the PMTs at 355 nm, 387 nm, 532 nm (total) and 532 nm (cross polarised). The longest  $t_d$  was found for the PMT detecting at 607 nm at low count rates. The influence of the dead time effect on the raw lidar signal was between 2.6 and 5.4% for count rates at full intensity between 4 and 10 Mcps, depending on the channel. Due to the incomplete overlap in low altitudes, the lidar signal close to the signal maximum is only used for the Raman retrieval of the particle

**Table 3.1.:** Count rates and dead times at signal maximum of all channels on 18 November 2011, as well as typical count rates and relative errors resulting from the dead time effect.<sup>a</sup>

channel	$n' / 10^6 \text{ counts s}^{-1}$	$t_d / \text{ns}$	$n^* / 10^6 \text{ counts s}^{-1}$	rel. error / %
355 nm	$27.1 \pm 0.6$	$3.6 \pm 1.0$	10	3.5
387 nm	$10.8 \pm 0.3$	$4.7 \pm 1.9$	10	4.6
532 nm (total)	$16.6 \pm 0.5$	$3.5 \pm 1.2$	10	3.4
532 nm (cross)	$10.3 \pm 0.2$	$2.6 \pm 3.6$	10	2.6
607 nm	$3.9 \pm 0.2$	$14.0 \pm 6.2$	4	5.4
1064 nm	$8.9 \pm 0.2$	$-5.0 \pm 4.0$	7	-3.6

<sup>a</sup> Mean value and standard deviation of  $n'$  were obtained from time averaging over three minutes. Mean value and standard deviation of  $t_d$  were obtained from averaging over three values around the signal maximum.

backscatter coefficients and the calculation of the depolarisation ratio. The profiles of the particle extinction coefficients and of the particle backscatter coefficients by means of the Klett method were usually obtained from altitudes higher than 0.7 km agl. In this height range  $n'$  are lower than in the signal maximum and the relative errors are smaller.

The results for the PMT at 1064 nm are questionable due to strong atmospheric changes at this wavelength during the telecover test. The atmospheric change was verified by a second measurement of the N sector, as described in section (3.2.1). The ratio of the difference between those two measurements and the mean value from the measurements of the sectors N (1), E, S and W is plotted for all channels in figure (3.12). At 1064 nm the atmospheric change was large in the lower altitudes. In the height of the signal maximum, the ratio was around 40%. For the other channels a ratio of less than 20% was found up to 3 km agl. The signal was strongly decreasing during the telecover test. This change was most likely the reason for the unrealistic negative dead time found for the PMT at 1064 nm.

### 3.2.5. Software intercomparison

The software used at CGE for the EARLINET data analysis was developed at the Leibniz-Institute for Tropospheric Research e. V. (Leibniz-Institut für Troposphärenforschung e. V.) (TROPOS) in Leipzig, Germany and the algorithm was tested and approved in the framework of EARLINET. Results were published by *Pappalardo et al.* (2004). Another software intercomparison was performed in the framework of SPALINET. The Raman algorithm was tested in two stages similarly to the tests described by *Pappalardo et al.* (2004). During the first stage, no information on the critical input parameters reference height and value and the Ångström exponent were given. Those parameters were known during the second stage of the intercomparison. Profiles of the backscatter and extinction coefficients had to be calculated from simulated lidar signals at 355, 387, 532 and 607 nm.

The algorithm used for the analysis of PAOLI data was performing well. In the first stage, the relative deviation from the true solution was below 20% for all tested quantities, which were the profiles of the particle backscatter coefficients, the particle extinction coefficients and the particle lidar ratios, each at 355 and 532 nm. In the second stage, the relative deviations of the particle extinction coefficients and of the particle lidar ratios were smaller than 10%. Those of the particle backscatter coefficients were below 20%.

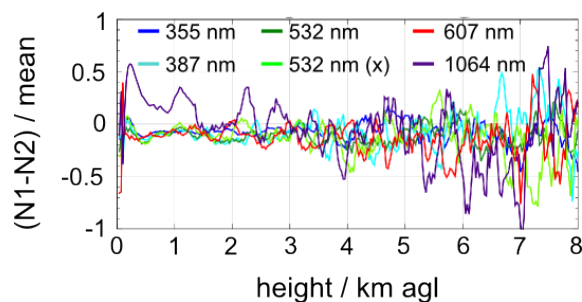


**Figure 3.12.:** Atmospheric change, calculated as the ratio of the difference between the measurements at sector N (1 and 2) and the mean value from the measurements of the sectors N (1), E, S and W. The telecover test was performed on 18 November 2011.

### 3.3. Improvement of the optical alignment

The main objective of the changes described in this section was the reduction of the overlap height. This parameter mainly depends on the orientation and the divergence of the outgoing laser beam. Those subjects are treated in sections (3.3.1) and (3.3.2). However, also the FOV of the receiver was adjusted (see section (3.3.3)). In section (3.3.4) different overlap correction functions are presented and discussed. Direct comparisons with other lidars are very useful to detect problems and to improve the system. The lidar intercomparison SPALI10 is introduced in section (3.3.5).

#### 3.3.1. Beam position

After the transport of PAOLI from Germany to Portugal, the outgoing beam was misaligned as shown on the left photograph in figure (3.13). This picture was taken on 2 September 2009. The cross section of the beam can be seen on the surface of the small quartz window in the roof of PAOLI. The image of the beam appears twice, once on each surface, inside and outside of the lidar. The cross section of the beam showed concentric circles. However, the beam was not in the centre of the window and also not in the centre of the beam expanding telescope, which cut off half of the beam. By changing the alignment of the two redirecting prisms the beam was centred in the beam expanding telescope. The centred beam is shown on the right photograph in figure (3.13), which was taken on 10 September 2009.

The beam position was adapted frequently, as already shown in figure (3.1). This was mainly necessary due to seasonal changes in the ambient temperature, which also affected the mean cabinet temperature. Furthermore, changes in the optical set-up required the adjustment of the outgoing beam. In figure (3.14) the development of the camera image of the outgoing beam in the first two weeks of operation is shown. From a well defined triangular shape on 4 and 9 September 2009, the image of the beam degraded to a diffuse spot as shown on the image taken on 15 September 2009. Between 9 and 15 September 2009 the beam was moved out of the FOV in order to obtain a better overlap behaviour. Before, the beam was too far in the FOV. The intensity was low due to changes in the camera settings. The exposure time was changed occasionally.

The image of the beam did not change strongly between the middle of September 2009 and March 2011. Pictures taken on 7 March, 2 April and 30 June 2011 are shown in figure (3.15). The divergence of the outgoing beam was reduced on 30 March 2011. Details about the measurement and change of the beam divergence are given in section (3.3.2).

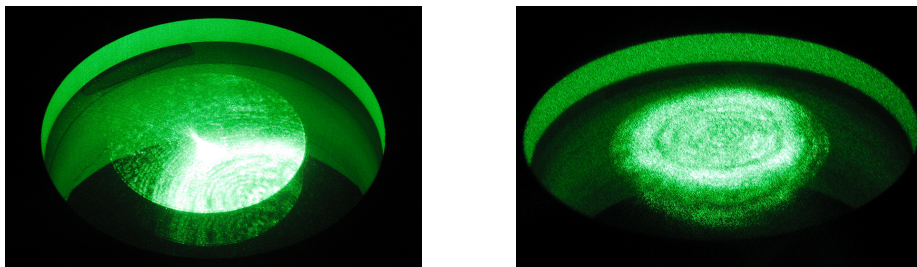


**Figure 3.13.:** Image of the beam cross section on the small roof window. Photos taken on 2 September 2009 before the adjustment (left) and on 10 September 2009 (right).

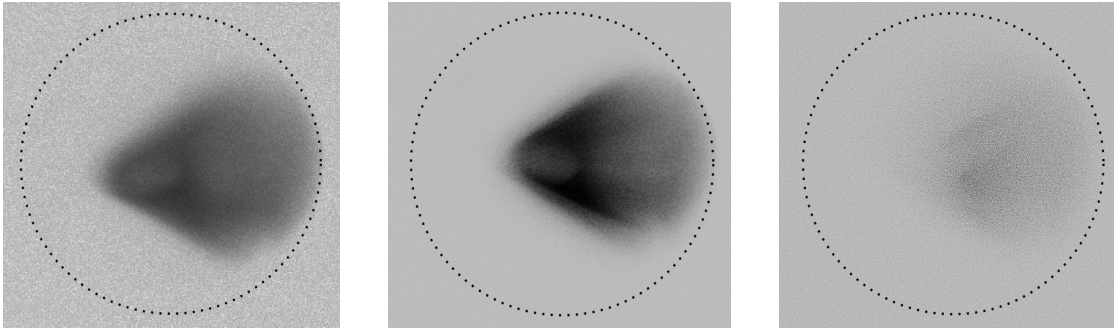


**Figure 3.14.:** Images of the outgoing beam seen through the receiving telescope (negative). The dotted circle indicates the telescope FOV. Photos taken by the implemented camera during night time measurements on 4, 9 and 15 September 2009 (from left to right).

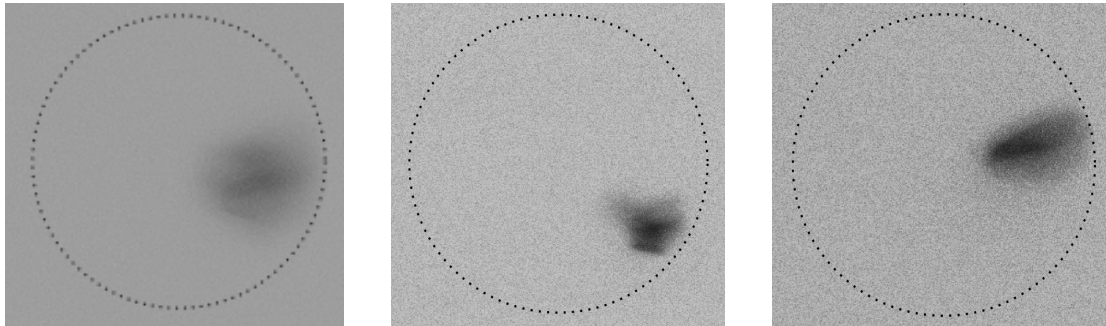


**Figure 3.15.:** Same as figure (3.14). Photos taken on 7 March, 2 April and 30 June 2011 (from left to right).

In the second picture of figure (3.15), which was taken shortly after this change, the beam image is smaller and more focussed, but also on the edge of the FOV. The triangular shape could not be observed on 2 April 2011. It is likely that parts of the beam were cut off. Therefore, the position of the beam was corrected. It can be adjusted on this small scales by shifting the lens at the end of the beam expanding telescope. The image taken on 30 June 2011 shows a narrow triangle closer to the other edge of the FOV.

In figure (3.16) images taken on 3 August, 18 November 2011 and 3 January 2012 are shown. In August 2011, the beam image had the triangular shape. After the adaptation of the pinhole position on 17 November 2011, which is described in section (3.3.3), the beam image was roughly triangular with rounded edges. The image looked similar on 3 January 2012. Despite various changes and tests, the clearly defined triangular shape of the beam image from the beginning of September 2009 (figure (3.14)) could not be regained. One possible reason could be the degradation of the laser, as already discussed in section (3.1.3).

### 3.3.2. Beam divergence

The divergence of the outgoing beam is a critical parameter in lidar application. It needs to be smaller than the FOV of the receiving telescope, which is 1 mrad in case of PAOLI. The divergence of the outgoing beam was specified with 0.5 mrad. It was measured and optimised during an experiment on 29 March 2011. For that, a fraction of the beam was

### 3. Lidar performance

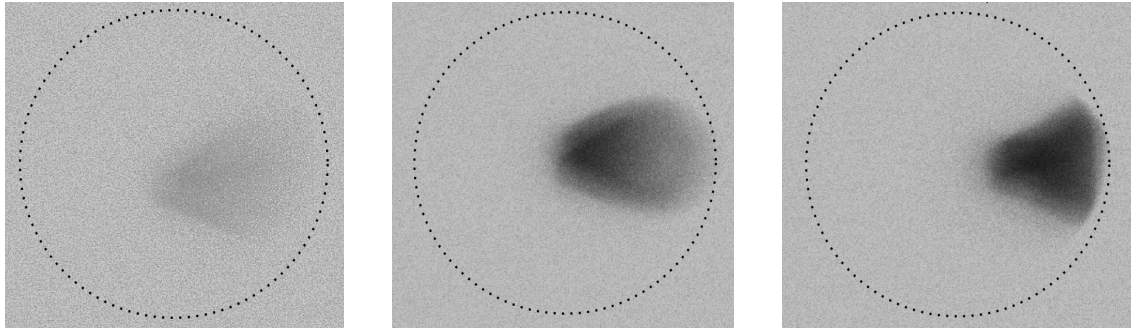


**Figure 3.16.:** Same as figure (3.14). Photos taken on 3 August, 18 November 2011 and 3 January 2012 (from left to right).

redirected to a horizontal axis by means of a quartz plate (plane accuracy of  $1/10 \lambda$  at 632.8 nm). The plate was placed in an angle of  $45^\circ$  over the beam exit window in the roof of PAOLI and partially reflected the outgoing beam. The experimental set-up is shown in figure (3.17). The experiment was conducted late at night and the area was blocked on a large scale, for security reasons.

The image of the beam cross section was projected on a vertically placed sheet of scale paper. Pictures of the projection were taken with a digital camera at the exit window and in different distances from the lidar, in 12.3, 19.7 and 32.7 m. After that, the beam divergence was changed by shifting the lower lens in the beam expanding telescope and another set of photos was taken. The diameter of the beam was determined by measuring the beam projections. The divergence could be calculated from the beam diameter and the distance from the system. The beam divergence was 1.0 mrad before shifting the lens. After the change, it was about 0.2 mrad.

#### 3.3.3. Pinhole position

The backscattered photons are collected with the parabolic primary mirror of the receiving telescope. They are redirected by a secondary mirror through a pinhole, which suppresses the background signal. The opening of the pinhole defines the receiver field of view. It

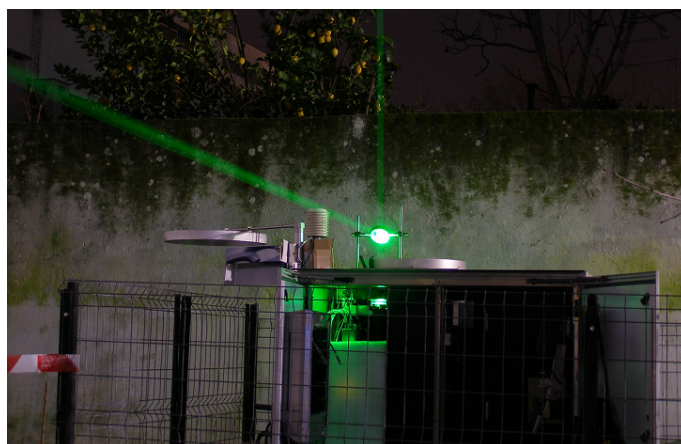


**Figure 3.17.:** Set-up of the beam divergence experiment conducted on 29 March 2011.

is crucial for meaningful lidar measurements, that the pinhole is placed close to the focal point of the primary mirror. Otherwise, the probability is high that the signal is cut off at the edges. The optical set-up, including both mirrors and the pinhole, was already shown in figure (2.2).

In order to improve the signal quality of PAOLI, and especially the overlap behaviour, the pinhole position was varied during a test measurement in the night from 17 to 18 November 2011. Telecover tests were done in order to identify the best position. The procedure of this test was explained in detail in section (3.2.1).

Before changing the pinhole position, a telecover test was done. Then, the pinhole was shifted by 4.5 mm towards the telescope. After a second telecover test, the pinhole was shifted away from the telescope beyond the original position. The signal became very weak with this change. Therefore, no telecover test was done and the pinhole was shifted to a position 2.6 mm from the original one, again towards the telescope. This position was tested with a telecover test as well. The profiles of the range corrected signal detected by the channel at 532 nm (total) during the telecover test is shown in figure (3.18). The test results presented here, were normalised in the height range from 6 to 7 km agl to facilitate the comparison. The signal from each sector was averaged over 3 min. With the original pinhole position the signal was first detected in sector S, then in sectors E and W and last in sector N. As mentioned before (see section (3.2.1)), this was contrary to what could be expected. It indicated, that the pinhole was placed behind the focal point of the parabolic mirror. After shifting the pinhole by 4.5 mm, the correct order of altitudes of all sectors was observed. However, the signal maximum in sectors E and W differed strongly, which was also the case during the first telecover test. Finally, with the pinhole at 2.6 mm from the original position, the order of the signals and the magnitudes of their maxima was satisfactory. The atmospheric change was low throughout the experiment, which shows the comparison of N1 and N2 in all graphics in figure (3.18). The results observed in channel 532 nm (total) were representative for all channels.

In figure (3.19) the relative deviation (equation (3.2)) for each sector at 532 nm (total) is shown. The telecover test with the old pinhole position resulted in relative deviations of up to 30% above 2 km agl. The shift of the pinhole by 4.5 mm led to very large relative deviations below 2 km agl. Above that altitude the relative deviations were less than 20%. With the last shift of the pinhole, the relative deviation could be reduced to less than 10% between 1 and 4 km agl, which meets the EARLINET requirements (internal documentation).

By adjusting the pinhole position, the signal in the near range could be improved sig-

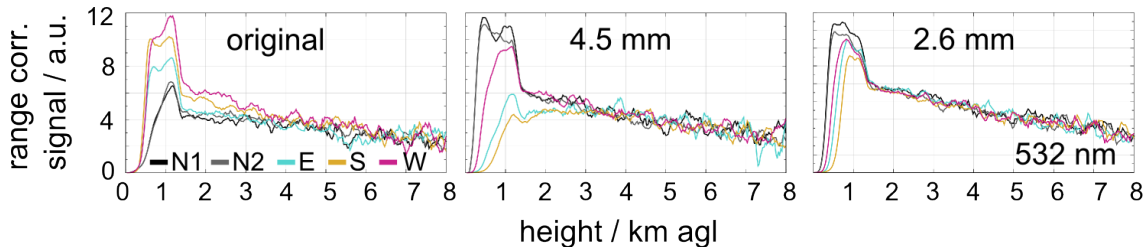


**Figure 3.18.:** Normalised range corrected signal at 532 nm (total) detected in the four sectors with the original pinhole position (left) as well as the pinhole position shifted by 4.5 (centre) and 2.6 mm (right) towards the telescope. The measurements were performed on 17 November 2011.

### 3. Lidar performance

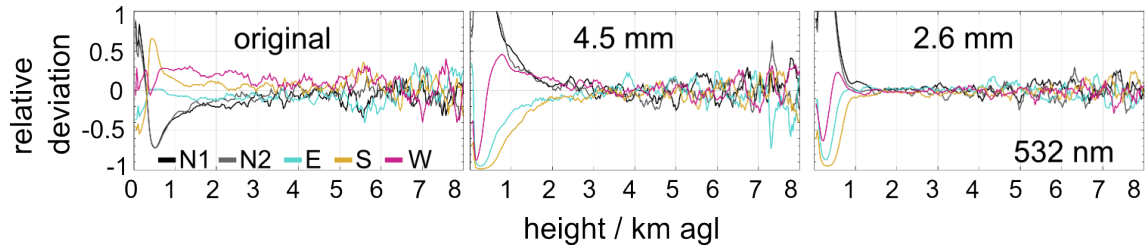


**Figure 3.19.:** Relative deviation of the signals from the mean value at 532 nm (total) with the original pinhole position (left) as well as the pinhole position shifted by 4.5 (centre) and 2.6 mm (right) towards the telescope. The measurements were performed on 17 November 2011.

nificantly. One reason for the misalignment of the pinhole could be uncertainties in the specifications of the parabolic mirror, including the focal length. The shift of the pinhole position was only 0.3% relative to the specified focal point distance of the mirror, which is 900 mm.

#### 3.3.4. Overlap correction function

Any lidar is blind in the range closest to the system. The signal can only be detected from an altitude where the outgoing beam enters the FOV of the receiving telescope. However, there the investigated volume is smaller than in the farther range, where the overlap of the outgoing beam and the FOV is complete. Therefore, the measured signal needs to be corrected up to this distance. Figure (3.20) illustrates the incomplete overlap and the overlap correction function  $O(z)$ . Close to the lidar system,  $O(z)$  is changing rapidly. There, it causes large uncertainties in profiles of the particle extinction coefficient and of the particle backscatter coefficient obtained with the Klett method. Above this height range close to the instrument, the incomplete overlap can be corrected for. As mentioned

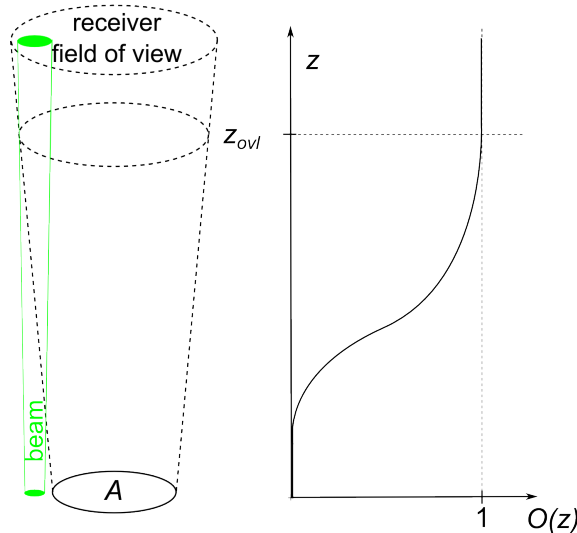


**Figure 3.20.:** Scheme of the overlap of outgoing beam and receiver field of view and corresponding overlap correction function.

before (section (2.2.1)),  $O(z)$  can be determined experimentally from night time data.

The overlap behaviour of PAOLI changed often during the last years. Various improvements of the system alignment, like the change of beam orientation, beam divergence and pinhole position, made previous  $O(z)$  invalid. New functions were calculated frequently. The overlap also changed with the temperature inside the system. In case of temperature oscillations the data were averaged over a sufficiently long time to obtain an average  $O(z)$ .

All  $O(z)$  determined during the year 2010 are shown in figure (3.21). The most frequently used function from 26 April 2010 is marked as bold line. It could be applied in more than 80% of the analysed measurements from 2010. The height of full overlap on 26 April 2010 was 2.75 and 2.93 km agl at 355 and 532 nm, respectively. Most of the other functions were only valid for single measurements.

Until October 2010, the alignment of the beam position was solely done by means of the camera image, as described in section (3.3.1). The accuracy of the beam alignment was verified regularly by calculating  $O(z)$ . However, flaws in the beam position on the east-west (E-W) axis cannot be identified in that way. For this, telecover tests were necessary. Since October 2010, another testing procedure for finding the optimal position of the outgoing beam is used. The beam orientation can be varied on a small scale by moving the upper lens of the beam expanding telescope, as mentioned before. This shift is realised with two motorised screws. The grid is defined by the positions of the screws, which specify the lens position and consequently the beam orientation. The test consists in shifting the beam position systematically over a two dimensional grid and measuring the signal at each grid point. Those signals are then compared at a certain height bin. It is important, that the atmosphere is very stable during this test, as the measurements require more than one hour of testing time.

The result of one of those scanning tests, on 24 November 2011, is shown at 355 nm

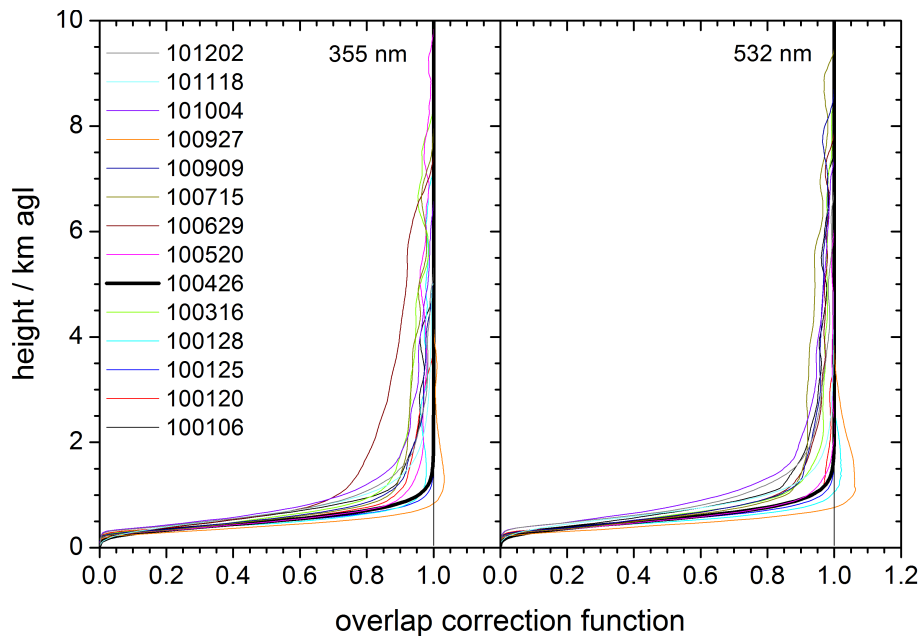


**Figure 3.21.:** Overlap correction functions valid for PAOLI during the year 2010 at 355 nm (left) and 532 nm (right). The dates of the respective measurements are in format YYMMDD.

### 3. Lidar performance

in figure (3.22). The change of the atmosphere was verified by measurements with the original beam position before and after the test. During the test period of about 1.5 h, the relative change of the range corrected signal, detected at the channels of 355, 387, 532 (total) and 607 nm, was less than 20% between 0.7 and 3.1 km agl and less than 30% at 532 nm (cross polarised). The largest change was observed at 1064 nm. It was below 50%.

The signals at all heights showed a maximum on the E-W axis at position 0.0. It could be detected most easily on the plot with the signal at height bin 15 (450 m agl). This is due to the relatively small overlap area of beam and receiver FOV at this altitude. Therefore, the signal close to the instrument is more sensitive to smallest changes in the beam orientation than the signal in higher altitudes. The signal maximum corresponds to the beam position with the largest overlap area between beam and FOV. At small altitudes this maximum indicates, that the beam is centred in the FOV on the E-W axis.

Shifting the beam towards the receiving telescope, i.e. to higher values of the position at the north-south (N-S) axis, the signal continuously increased at height bin 15. This is reasonable, because the lower the beam enters the FOV, the higher is the signal close to the system. However, at a certain beam tilt it would exit the FOV on the "southern" edge and the signal would decrease in higher altitudes. Therefore, it would not suffice to find the maximum signal along the N-S axis at one altitude close to the system. The signal in higher altitudes is a better indicator for the alignment of the beam on the N-S axis.

Figure (3.22) shows, that the signal at height bins 20, 30 and 40 became approximately stable from a certain position on the N-S axis. The positions of signal maxima and the beginning of the signal plateau from the scanning test on 24 November 2011 are given for all channels in table (3.2). They varied slightly by  $\pm 0.1$  on both axes.

The beam position along the E-W axis, which results in the signal maximum, is the optimum. However, along the N-S axis the determination of the absolute maximum can lead to the wrong position, due to the plateau shape. Calculations of  $O(z)$  from measurements after such scanning tests confirmed this. The beam would be placed too far "south", which is too far in the FOV, resulting in  $O(z)$  with values larger than 1. The

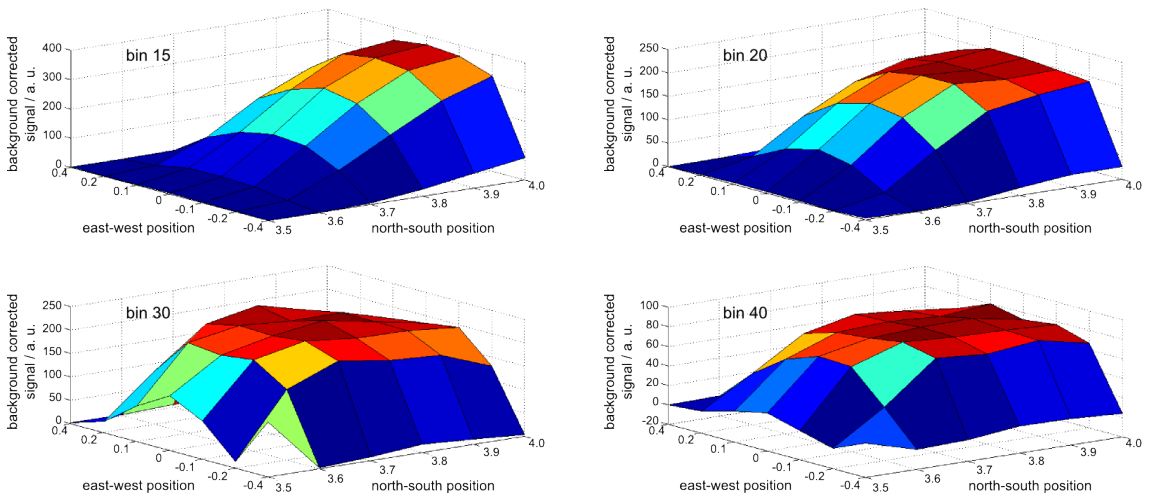


**Figure 3.22.:** Background corrected signal at 355 nm at height bins 15 (450 m agl), 20 (600 m agl), 30 (900 m agl) and 40 (1200 m agl) for different beam positions. The measurements were performed on 24 November 2011.

**Table 3.2.:** Position of signal maxima and beginning of signal plateau for all channels.<sup>a</sup>

channel	E-W	N-S (maximum)	N-S (plateau)
355 nm	0.0	3.8	3.7
387 nm	0.0	3.8	3.7
532 nm	0.1	3.8	3.7
532 nm (x)	0.0	3.8	3.8
607 nm	0.1	3.9	3.8
1064 nm	-0.1	3.7	3.8

<sup>a</sup> Position on the E-W axis was determined at bin 15 and on the N-S axis at bin 40. The test measurement was performed on 24 November 2011.

beginning of the signal plateau can be determined more precisely. Thus defined beam positions resulted in more reasonable  $O(z)$ . Concluding, the motor position on the E-W axis at the signal maximum and the one on the N-S axis at the beginning of the signal plateau are most appropriate. In the shown example measurement, the optimal beam position was at 0.00 (E-W) and 3.76 (N-S).

This method proved to be a useful tool for finding the optimal position of the outgoing beam. This could be confirmed with the calculation of  $O(z)$  for the beam position on the N-S axis, and with telecover tests for the beam alignment on both axes. The higher altitude, which is used to find the plateau, should be chosen as high as possible, but it should not be affected by noise. The test procedure could be improved by a higher resolution of the scanning grid. However, this would lead to longer scanning times and the atmospheric change would increase.

An improvement in the overlap behaviour of PAOLI was accomplished with the shift of the pinhole on 18 November 2011 (see also section (3.3.3)). Figure (3.23) shows  $O(z)$  determined from night time measurements on 26 April 2010 and 19 February 2012. The function from 26 April 2010 is representative for a reasonably aligned outgoing beam before the change of the pinhole position. The function from 19 February 2012 is representative for measurements after that change. As mentioned before,  $O(z)$  is calculated under the assumptions of a reference value at a reference height range and a lidar ratio. For each case, several profiles of  $O(z)$  were calculated with varying reference values and lidar ratios in order to estimate the quality of the correction function. The standard deviations of all profiles are shown in figure (3.23) as error bars. It indicates the uncertainty of the function itself, but gives no information about the applicability. The application of an inappropriate correction function can cause large errors. Therefore, the proper correction functions need to be selected carefully.

The height of full overlap is indicated as well in figure (3.23). It could be reduced by about 40%. At both wavelengths,  $O(z)$  was larger than 0.95 at altitudes around 1 km agl on 26 April 2010 and at around 0.6 km agl on 19 February 2012. Due to the change of the beam divergence, the slope of the correction function was steeper on 19 February 2012 and the beam entered the FOV later, i.e. at a higher altitude. With changes

### 3. Lidar performance

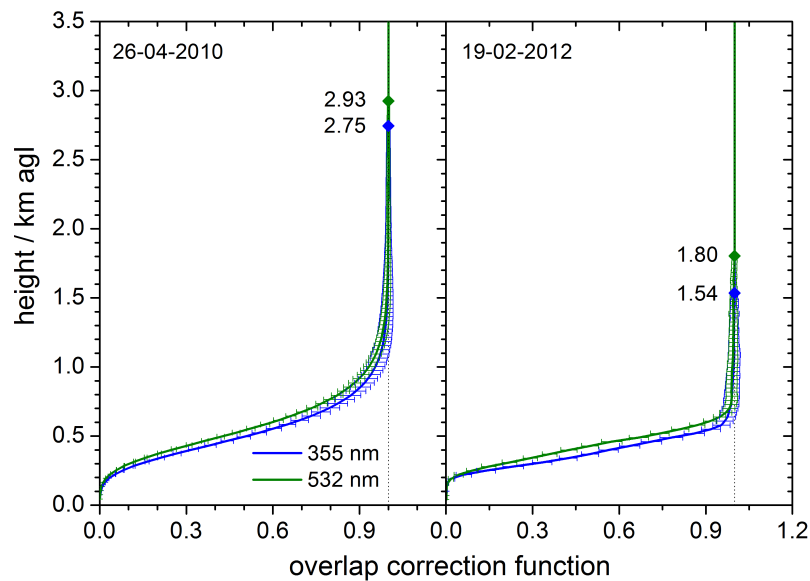


**Figure 3.23.:** Overlap correction functions on 26 April 2010 (left) and 19 February 2012 (right) at 355 nm (blue) and 532 nm (green) with standard deviation (error bars), and the height of full overlap (diamonds).

in the optical alignment and the application of appropriate tests, the overlap behaviour of the system could be improved significantly since the beginning of the measurements in September 2009.

#### 3.3.5. Lidar intercomparison SPALI10

In the framework of EARLINET, an intercomparison of a new lidar system with a reference lidar should be done in the beginning of the regular operation within the network. This intercomparison should be repeated after significant changes in the set-up.

For the Lidar Intercomparison Campaign in Spain 2010 (SPALI10) from 19 October 2010 to 4 November 2010, PAOLI was moved to Madrid. The performance of PAOLI and the EARLINET lidars from Madrid, Granada and Barcelona (all Spain) were directly compared to the EARLINET reference lidar from Potenza (Italy). Some comprehensive studies on the results of SPALI10, also including data from other ground based and air borne instruments, were published by *Molero et al.* (2011a,b).

During the campaign, the data analysis was done fully automatically by the Single Calculus Chain (SCC) software. Individual system specifications were stored in a central database. Due to the equal processing of all data, algorithm differences could be excluded as reasons for deviations in the results. The SCC software requires a specific input data format. A conversion of the PAOLI raw data had to be done before submission to the central data processing server. The SCC software will be applied for a centralised objective analysis of the data of all EARLINET stations in the near future. Therefore, the intercomparison campaign was a good opportunity for testing the performance of the SCC software and the data conversion by the participating stations.

Range corrected signals were compared during SPALI10. Figure (3.24) shows the comparison of PAOLI with the Multiwavelength System for Aerosol (MUSA), the reference

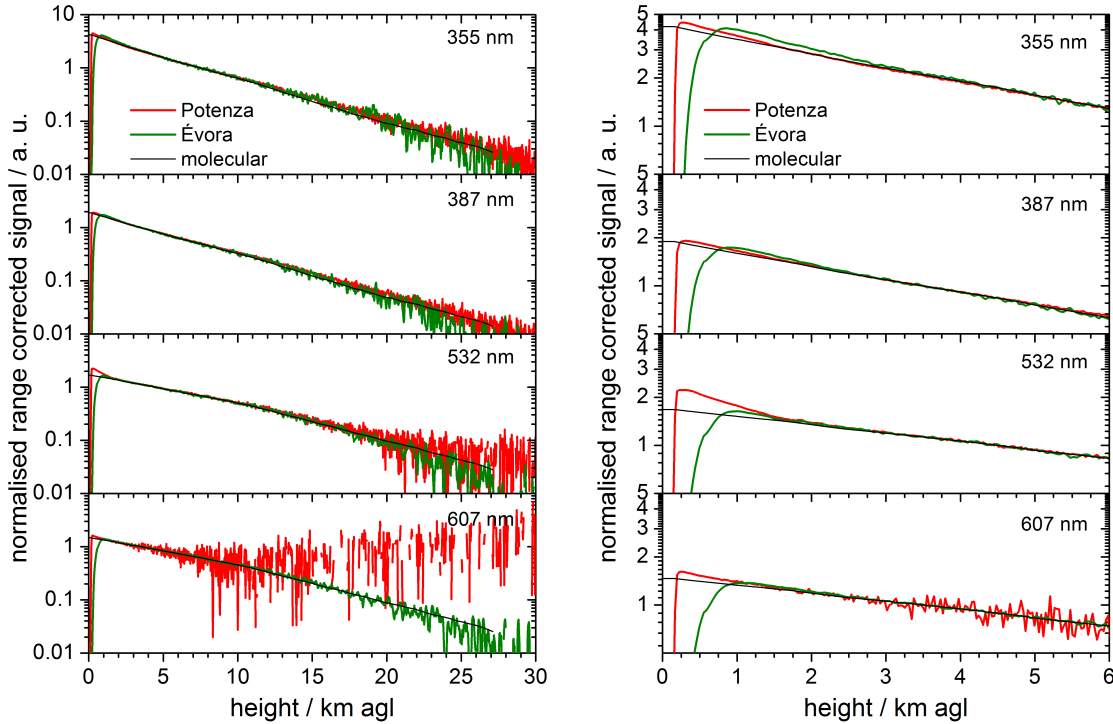


**Figure 3.24.:** Normalised range corrected signal in the far range (left) and the near range (right) from PAOLI (green) and MUSA (red) averaged from 22:15 to 23:59 UTC on 25 October 2010 as well as the molecular signal (black) obtained from the radio sounding at 0 UTC on 26 October 2010. The normalisation range was 7 to 8 km agl, 3 to 4 km agl, 4 to 5 km agl and 3 to 4 km agl at 355, 387, 532 and 607 nm, respectively.

instrument from Potenza, in the beginning of the campaign on 25 October 2010. The shown data were not overlap corrected. At that time, only four channels of PAOLI were operating (see section (3.1.2)) and could be compared. The signal detected by PAOLI was lower than that measured by MUSA in the far range, but followed the molecular signal up to about 22 km agl. At 607 nm the SNR of MUSA was very low and the signal was noisy above 8 km agl. In the near range, the signal from PAOLI was higher than that from MUSA up to 4 and 2.5 km agl, at 355 and 387 nm, respectively. At 532 and 607 nm the signals agreed well above 2 and 2.5 km agl, respectively. The overlap behaviour of MUSA was clearly different from the one of PAOLI. With MUSA data could be obtained from about 500 m agl, without overlap correction.

The example in figure (3.25) was a cloud measurement on 27 October 2010. The near range behaviour of the instruments were similar to those on 25 October 2010. Interesting were the differences within the clouds. The signal from PAOLI was systematically lower than the signal from MUSA, especially at 355 nm. This difference was very large at the first peak at around 5 km agl, which was almost not detected by PAOLI. The other instruments participating in SPALI10 also observed this well pronounced signal peak (not plotted). Depolarisation measurements by MUSA indicated the detection of ice clouds. PAOLI was the only lidar operating at an off-zenith angle. The tilt of the instrument prevented reflections of the beam on horizontally aligned ice crystals, which are usually concentrated on the bottom of clouds. This could explain the differences in the cloud

### 3. Lidar performance

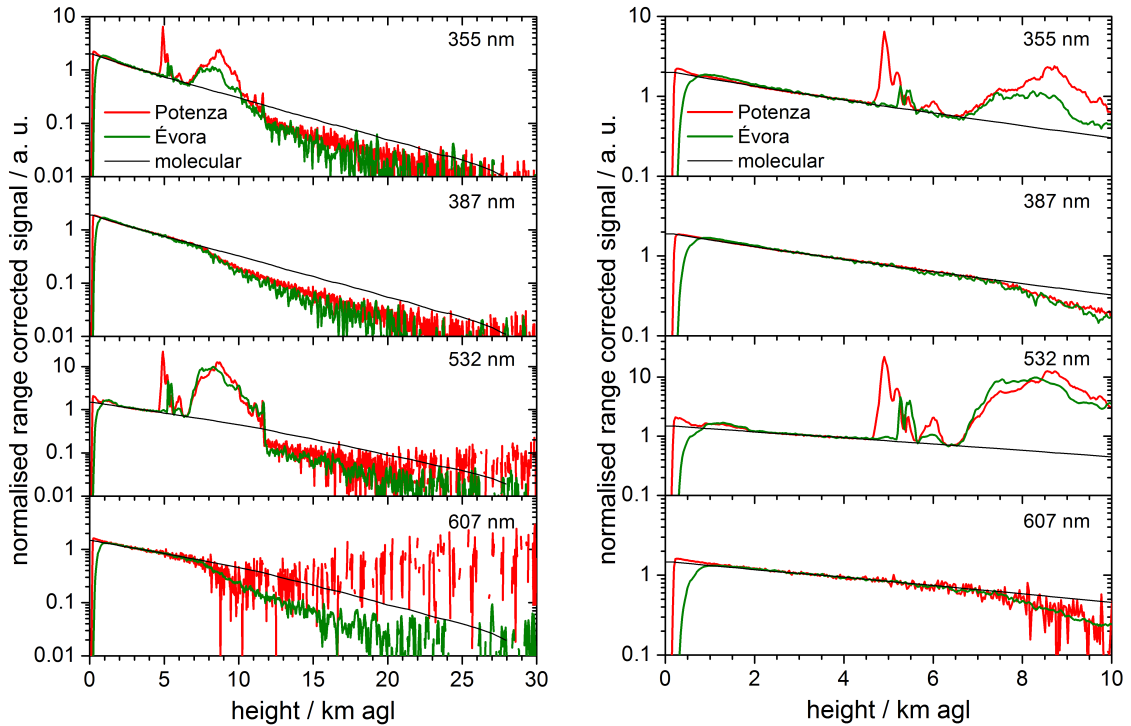


**Figure 3.25.:** As figure (3.24), for the measurement from 20:20 to 20:50 UTC on 27 October 2010 and the radio sounding at 0 UTC on 28 October 2010. The normalisation range was 3 to 4 km agl at all wavelengths.

detection. Above the cloud, in the far range, the lidar signal was lower than the molecular signal from radio sounding. This effect is due to the extinction within the cloud.

During the campaign, the beam alignment was changed repeatedly to improve the results of the comparison with the reference lidar MUSA. The height of full overlap could not be reduced then, but the larger signal in the near field at 355 and 387 nm could be reduced. In figure (3.26) an example measurement from the end of the campaign on 3 November 2010 is shown. The far range behaviour was stable during SPALI10. In the near range, the agreement between the signals from MUSA and PAOLI was very good above 1.5, 2, 3 and 2 km agl at 355, 387, 532 and 607 nm, respectively. The lidar signals were both smaller than the molecular signal from sounding data. For the comparison in figure (3.26) the radio sounding from 0 UTC on 3 November 2010 was used. The deviation in the near range were probably due to the long time lag.

Although the large range of incomplete overlap remained, the performance of PAOLI in the near range could be improved during the intercomparison campaign. However, the signal behaviour of PAOLI is wavelength dependent. The comparison showed the best agreement with MUSA at 355 nm. The height of complete overlap is lower at this wavelength, as shown in section (3.3.4).

### 3.4. Summary: System improvements

The optics of PAOLI are sensitive to temperature changes. Therefore it was an important objective to achieve temperature stability inside the cabinet. The implementation of a

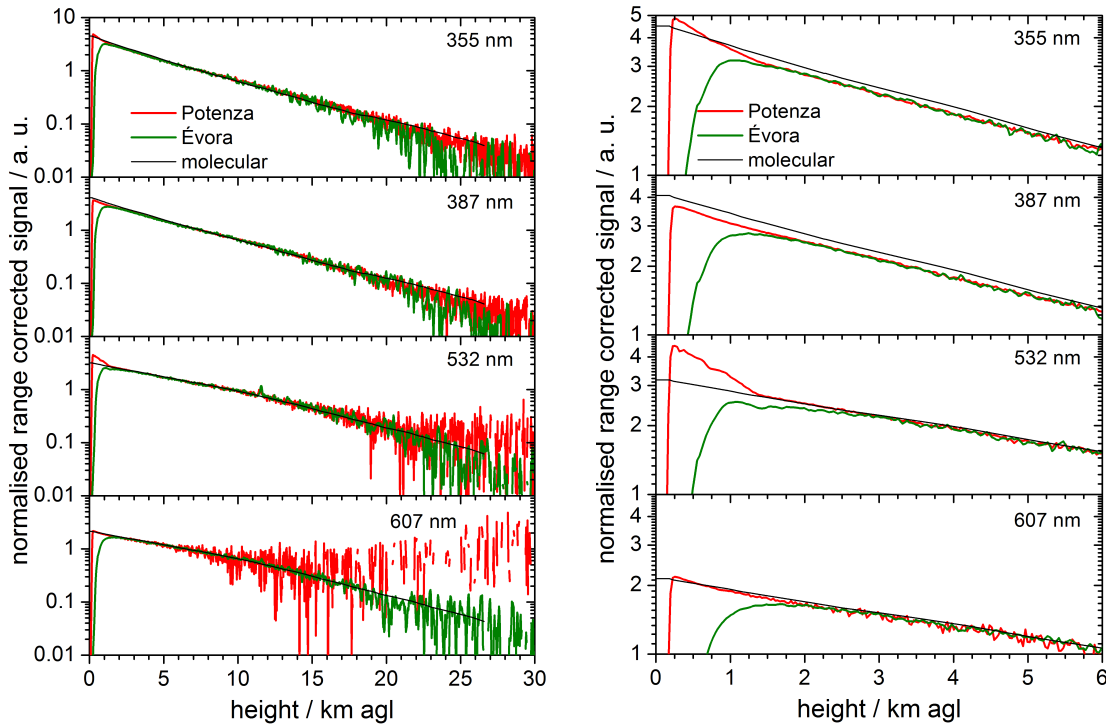


**Figure 3.26.:** As figure (3.24), for the measurement from 19:05 to 20:00 UTC on 3 November 2010. The normalisation range was 7 to 8 km agl, 8 to 9 km agl, 9 to 10 km agl and 6 to 7 km agl at 355, 387, 532 and 607 nm, respectively.

second heater reduced the number of measurements with temperature oscillations.

Changes in the optical alignment of PAOLI resulted in a higher lidar data quality. The beam position was optimised and is monitored carefully in order to ensure optimal data quality. A new tool for the optimisation of the beam position was introduced. The two-dimensional scanning test was implemented in order to increase the accuracy of the beam alignment.

The beam divergence and the FOV were both 1.0 mrad. However, the beam should be fully inside the FOV above the overlap height. To better meet this requirement, the beam divergence was reduced to 0.2 mrad.

A significant improvement in the overlap behaviour of PAOLI was accomplished by the adjustment of the pinhole position. The telecover test proved to be a very useful tool for the testing of the pinhole position. Thirteen telecover tests were done since the start of PAOLI measurements in September 2009. The results were always similar until the change of the position of the pinhole on 17 November 2011. Before that change, sectors S, E and W were detected first and sector N last, contrary to what could be expected. Since 18 November 2011 the telecover test results confirm a strongly improved optical alignment. Besides, the height of full overlap of outgoing beam and FOV could be reduced by about 40%.

A direct comparison of lidar systems helps in finding problems and is at the same time a good opportunity to improve the instrument. During the intercomparison campaign SPALI10 the behaviour of PAOLI in the near range could be improved and a good performance of PAOLI in the far range could be confirmed.

## 4. Aerosol characterisation results

Aerosol properties are highly variable in space and time and they are a large source of uncertainties in radiation and climate modelling. This is not only connected to a large quantity of aerosol sources and hence aerosol types. Large variations in aerosol optical properties also exist among an aerosol type. For example, lidar studies of anthropogenic aerosol originating in Europe resulted in lidar ratios at 355 nm of  $(32\pm 13)$  sr and  $(56\pm 23)$  sr, published by *Amiridis et al.* (2005) and *Giannakaki et al.* (2010), respectively. It is therefore important to better characterise aerosols, taking into account not only the aerosol type but also the source region and the transportation path.

Different types of aerosols have been observed over Évora and were analysed on a regular basis but also in detailed case studies. The results of those investigations are presented in this chapter. Section (4.1) introduces the data analysis procedure in detail by means of an example measurement. Detailed studies of aerosol of volcanic origin in the stratosphere and in the free troposphere (sections (4.3.1), (4.3.2) and (4.3.4)), of mineral dust (sections (4.3.3) and (4.3.5)), and of forest fire smoke (section (4.3.5)) were done. In section (4.4) the characterisation of different aerosol types by means of lidar measurements from more than two years is presented.

### 4.1. Measurement example

In this section, lidar data analysis is demonstrated in detail by means of an example. The measurement was done between 2 and 4 UTC on 19 February 2012. The time-height plot of the range corrected signal at 1064 nm is shown in figure (4.1). This example cannot be representative for all measurements, e.g. night time and daytime. Therefore, additional profiles of other measurements were used for the illustration of some procedures.

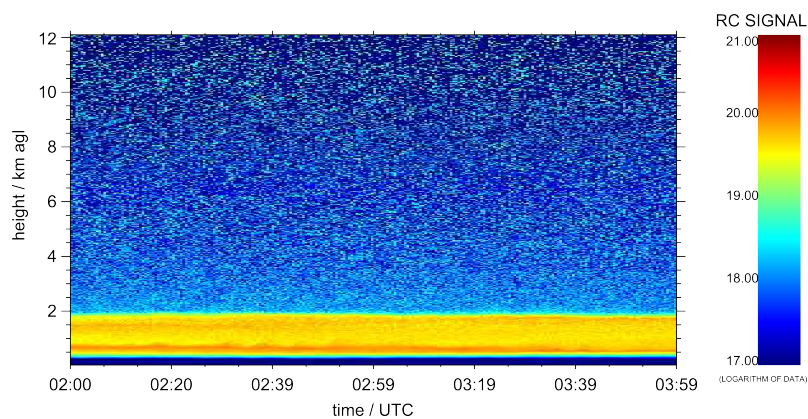


**Figure 4.1.:** Range corrected signal at 1064 nm of the measurement between 2 and 4 UTC on 19 February 2012 with a height resolution of 30 m and a temporal resolution of 30 s.

The theoretical approach of the used methods was already introduced in section (2.2) and the sources of uncertainties in section (2.3). In the following, the effects of corrections and input parameters on the profiles of the optical properties are discussed. To quantify uncertainties arising from different assumptions in the retrievals, the normalised difference  $\Delta_X(z, \lambda)$  between a profile  $X(z, \lambda)$  and the respective reference profile  $X_{ref}(z, \lambda)$  was calculated. It is determined through the relation

$$\Delta_X(z, \lambda) = \left| \frac{X(z, \lambda) - X_{ref}(z, \lambda)}{X_{ref}(z, \lambda)} \right| \times 100\%. \quad (4.1)$$

In this section,  $X_{ref}(z, \lambda)$  is usually chosen as the profile obtained with the optimal correction or assumption.

### Background correction

The raw lidar signal has to be corrected for the background signal, which is caused by skylight and light sources on the ground. The background signal is temporarily constant. The mean signal within a height range where the lidar return is negligible, is subtracted from the total signal. This height range has been varied for the example case in order to quantify the influence of the assumed altitude on the background corrected signal. The analysed height ranges were 1500 to 1600 bins (44.4 to 47.4 km agl), 1500 to 2000 bins (44.4 to 59.4 km agl), 1900 to 2000 bins (56.4 to 59.4 km agl) and 1947 to 2046 bins (58.5 to 61.4 km agl). The latter represents the far end of the profile and is the standard setting for PAOLI data analysis. The effect of different background correction heights on the range corrected signal  $P_{corr}$  was analysed. To calculate the normalised difference (equation (4.1)) of the range corrected signal  $\Delta_{P_{corr}}$ , the profiles corrected between 1947 and 2046 bins were used as the reference  $X_{ref}$ . For comparison, a daytime case was investigated in addition to the night time measurement. In figure (4.2) the profiles of the range corrected signal at 532 nm (total) in arbitrary unit (a.u.) is shown for the example night time measurement, corrected for the background signal in above mentioned height ranges. Furthermore, the respective profiles of the normalised differences are plotted. In figure (4.3) the same profiles are shown for a daytime measurement on the same day. The data were averaged over one hour, from 2 to 3 UTC and from 10 to 11 UTC of 19 February 2012, respectively. The scaling in the plot of the normalised difference as well as the plotted height range in figure (4.2) are different from the ones in figure (4.3). During the night time measurement, the normalised differences at 532 nm were below 1% up to about 15 km agl. At 355 and 1064 nm  $\Delta_{P_{corr}}$  were similar and at 532 nm (cross)  $\Delta_{P_{corr}}$  were slightly larger. The respective plots can be found in appendix (A.1). At daytime,  $\Delta_{P_{corr}}$  at 532 nm (total) were about 10% in 10 km agl and even larger in higher altitudes. At 355 nm they were similar. At 532 nm (cross)  $\Delta_{P_{corr}}$  were larger with approximately 20% in 6 km agl and at 1064 nm they were smaller, with about 5% in 15 km agl (see appendix (A.1)).

The effect of the background correction on the range corrected Raman signal is illustrated in figures (4.4) and (4.5) for night time and daytime data at 607 nm. The same measurements as for figures (4.2) and (4.3) were used, 2 to 3 UTC and 10 to 11 UTC of 19 February 2012. Vertical as well as horizontal axes are different in figure (4.4) and figure (4.5). The normalised differences of varying background correction ranges at 607 nm were smaller than 5% up to 12 km agl during night time. At daytime,  $\Delta_{P_{corr}}$  was very

4. Aerosol characterisation results

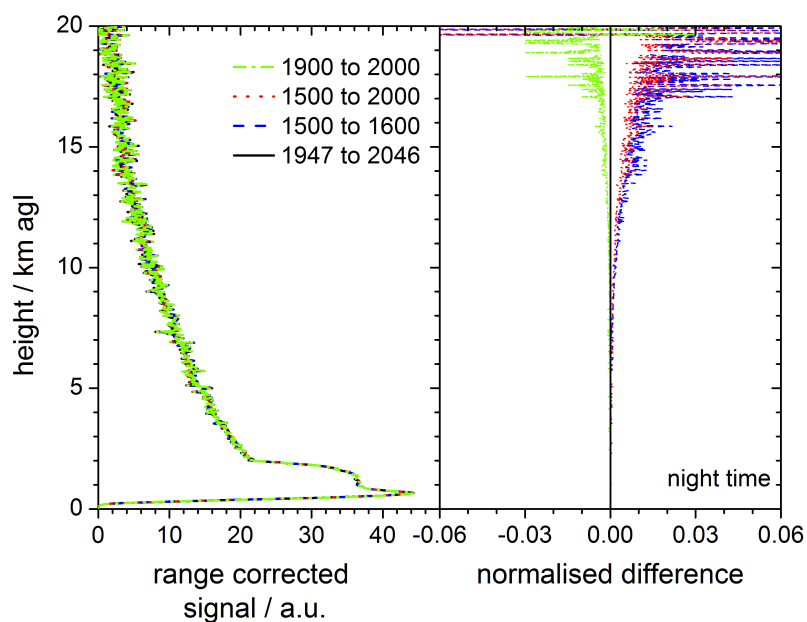


**Figure 4.2.:** Left: Range corrected signal at 532 nm (total) for different background correction heights (in bins) for night time data (2 to 3 UTC of 19 February 2012). Right: Normalised difference with reference to the profiles with the background correction between 1947 and 2046 bins. Line styles and colours correspond to those in the left plot.

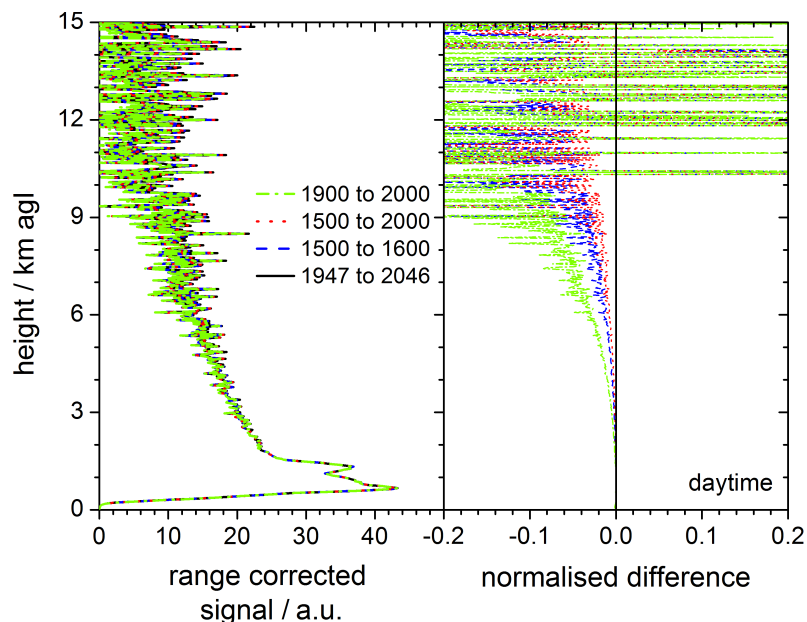


**Figure 4.3.:** Same as figure (4.2), but for daytime data (10 to 11 UTC of 19 February 2012).

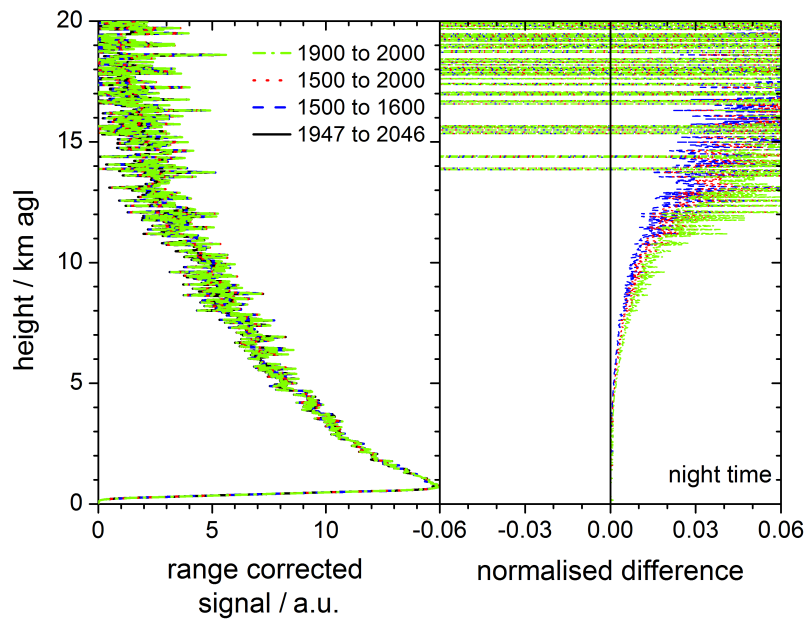


Figure 4.4.: Same as figure (4.2), but of the Raman signal at 607 nm.

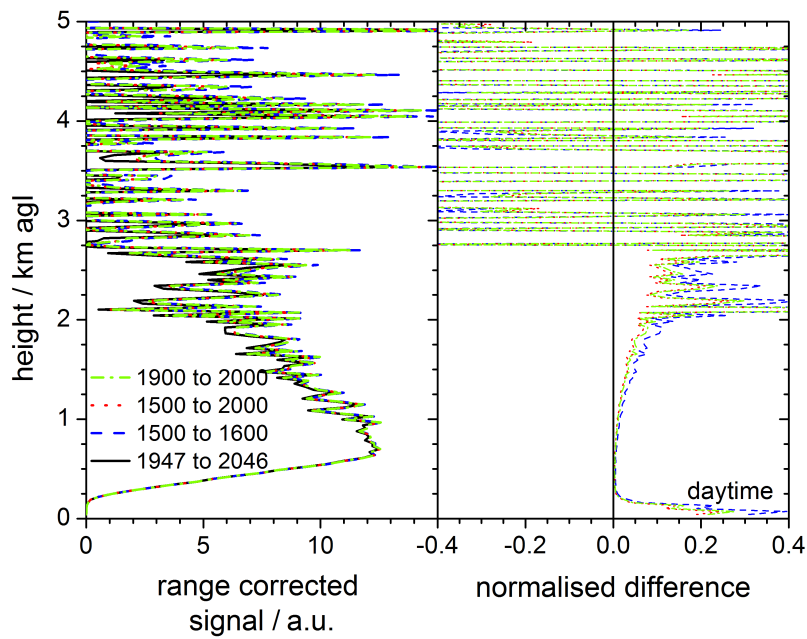


Figure 4.5.: Same as figure (4.2), but for daytime data (10 to 11 UTC of 19 February 2012) of the Raman signal at 607 nm.

#### 4. Aerosol characterisation results

large close to the ground as well as above 2 km agl where it exceeded 20%. During daytime as well as night time measurements,  $\Delta P_{corr}$  at 387 nm were smaller than at 607 nm (see appendix (A.1)).

The effect of the background correction range on the range corrected signal was smallest for the night time measurement at 355, 532 and 1064 nm. During daytime, the effect increased strongly with altitude. The Raman signal at daytime was most sensitive to changes in the background correction range. Considering all wavelengths, no clear pattern of over- or underestimation of the background signal was found. For this work, data were corrected for the background signal between 1947 and 2046 bins.

#### Averaging and smoothing

Appropriate temporal and vertical averaging improve the signal-to-noise ratio (SNR) and therefore also the accuracy of the data analysis. The effect of temporal averaging was investigated for the example case (19 February 2012, see figure (4.1)) and for one case of higher variability in the free troposphere, observed on 8 March 2012. A time-height plot of the range corrected signal at 1064 nm of this measurement is given in figure (4.6). In figures (4.7) and (4.8) the range corrected signals and normalised differences are shown. The profiles were averaged over 10 min, 30 min, 1 h and 2 h, centred at 3 UTC on 19 February 2012 and at 18:30 UTC on 8 March 2012. For the calculation of the normalised difference of the range corrected signal  $\Delta P_{corr}$ , the profile averaged over 1 h was used as reference profile ( $X_{ref}$  in equation (4.1)). In the shown examples, temporal averaging affects the profiles of the range corrected signals strongest within the boundary layer and close to aerosol layer boundaries. This is due to a large variability within the boundary layer caused by turbulence. The changes close to layer boundaries result from a descent or ascent of the layer. The peak at low altitude in the normalised difference of the profile at 1064 nm averaged over 10 min at 19 February 2012 is due to high variability in the aerosol load close to the ground. Except for this peak, the deviations were less than 15%. As shown for the measurement around 18:30 UTC of 8 March 2012, large deviations can occur if layers were only present during a small fraction of the averaging time period.  $\Delta P_{corr}$  of the 10 min profile at 1064 nm at 8 March 2012 was around 30% in the height region above 2.5 km agl. In both cases the deviations were largest for the profiles at 1064 nm.

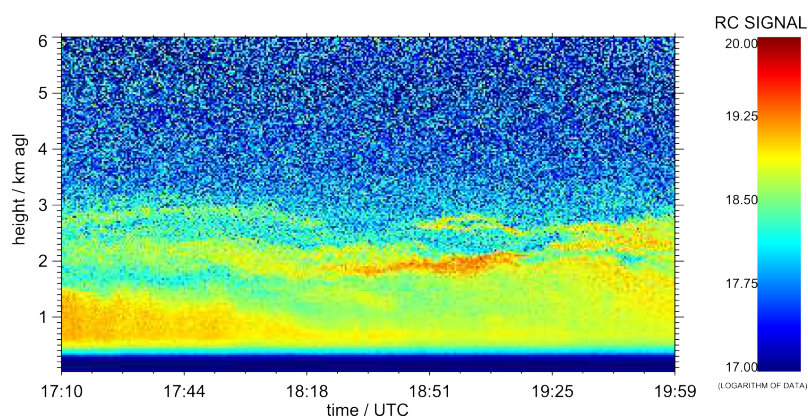


**Figure 4.6.:** Range corrected signal at 1064 nm of the measurement between 17:10 and 19:59 UTC on 8 March 2012 with a height resolution of 30 m and a temporal resolution of 30 s.

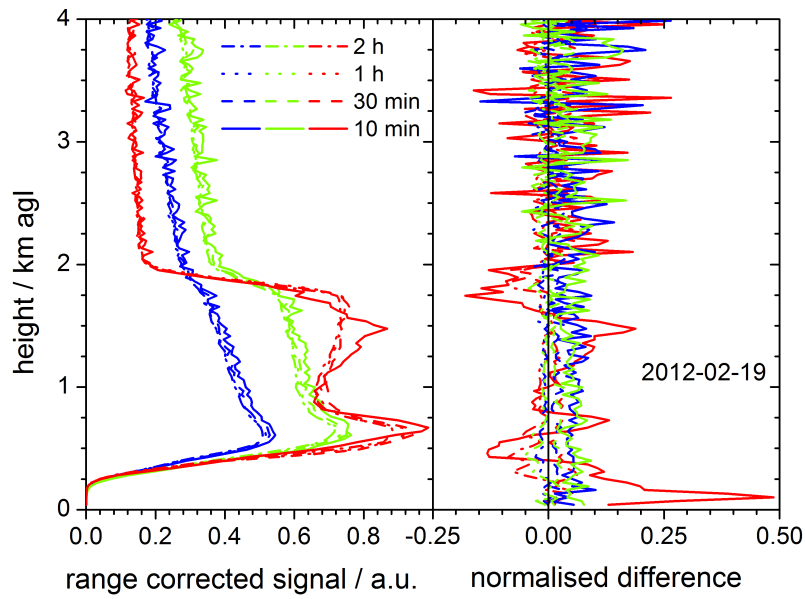


**Figure 4.7.:** Left: Range corrected signal at 355 (blue), 532 (green) and 1064 nm (red) averaged over 10 min, 30 min, 1 h and 2 h for a case with temporarily unstable boundary layer (3 UTC of 19 February 2012). Right: Normalised difference with reference to the profiles averaged over 1 h. Line styles and colours correspond to those in the left plot.

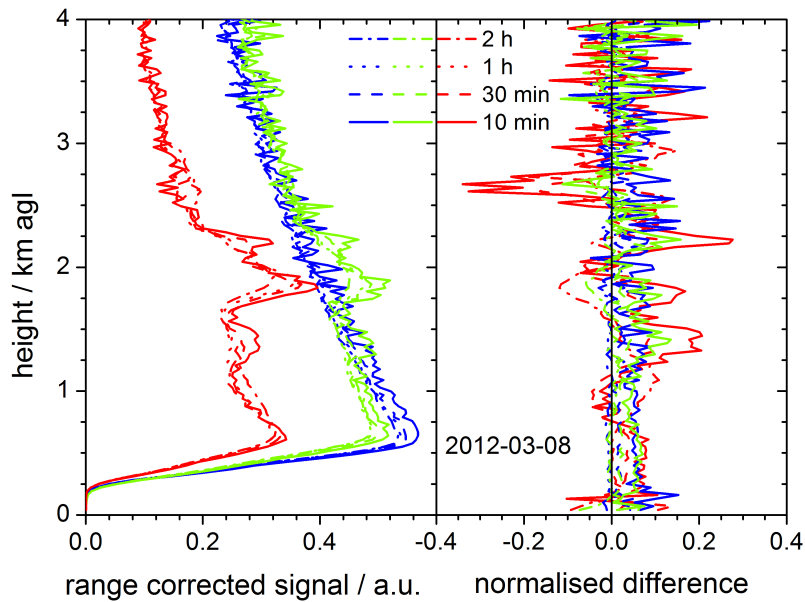


**Figure 4.8.:** Same as figure (4.7), but for a case with temporarily unstable free troposphere (18:30 UTC of 8 March 2012).

#### 4. Aerosol characterisation results

For this work the data were usually averaged over 30 min or 1 h. Longer averaging times were necessary for the analysis of stratospheric aerosol layers. Such layers are much more stable in time than tropospheric aerosol layers.

The influence of vertical smoothing on the lidar profiles is demonstrated in figures (4.9) and (4.10) for the example case and for the measurement from 8 March 2012, respectively. The range corrected signal at 1064 nm was vertically smoothed with sliding averages over 3, 7 and 17 bins (90, 210 and 510 m). Also shown is the non-smoothed profile, which was used as reference for the calculation of  $\Delta_{P_{corr}}$ . The shown data were averaged over one hour from 2 to 3 UTC of 19 February 2012 and from 18 to 19 UTC of 8 March 2012. Vertical smoothing causes the strongest deviations in height regions of strong gradients. Usually such gradients occur close to the lidar system due to the overlap characteristics. Large values of  $\Delta_{P_{corr}}$  were also found at the top of the aerosol layer around 2 km agl on 19 February 2012. During the measurement on 8 March 2012 the gradients were less steep. Consequently,  $\Delta_{P_{corr}}$  was much lower in this case. The smoothing lengths applied within this work were chosen individually for each case and optical profile.

#### Overlap correction

The incomplete overlap of laser beam and receiver field of view (FOV) leads to an underestimation of the signal close to the lidar system. This can be compensated by means of the overlap correction (see also section (3.3)). Different overlap correction functions were applied for illustration purposes. However, it is crucial to always use the overlap correction function appropriate for the respective alignment of the system.

Figure (4.11) shows the effect of different overlap correction functions on the profile of the range corrected signal at 532 nm (total). The data were averaged from 2 to 3 UTC of

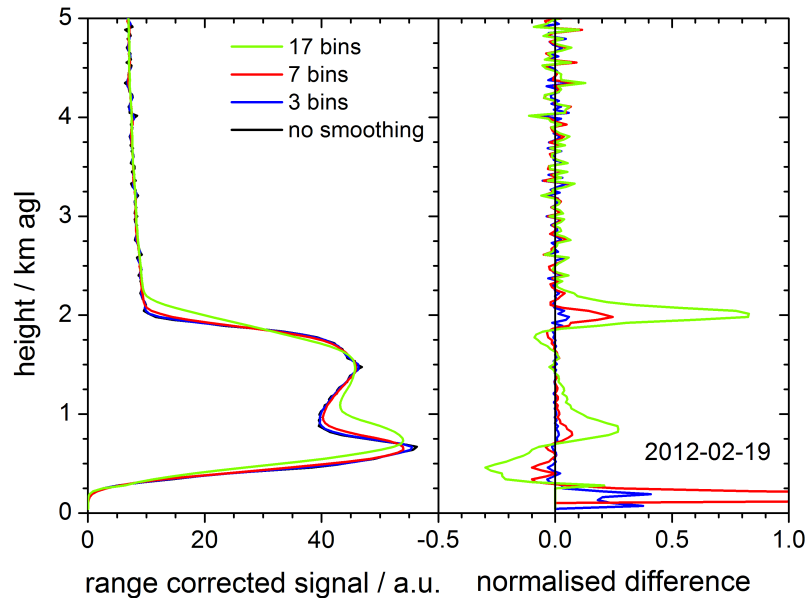


**Figure 4.9.:** Left: Range corrected signal at 1064 nm vertically smoothed over 0, 3, 7 and 17 bins for a case with strong vertical gradients (2 to 3 UTC of 19 February 2012). Right: Normalised difference with reference to the non-smoothed profile. The line colours correspond to those in the left plot.

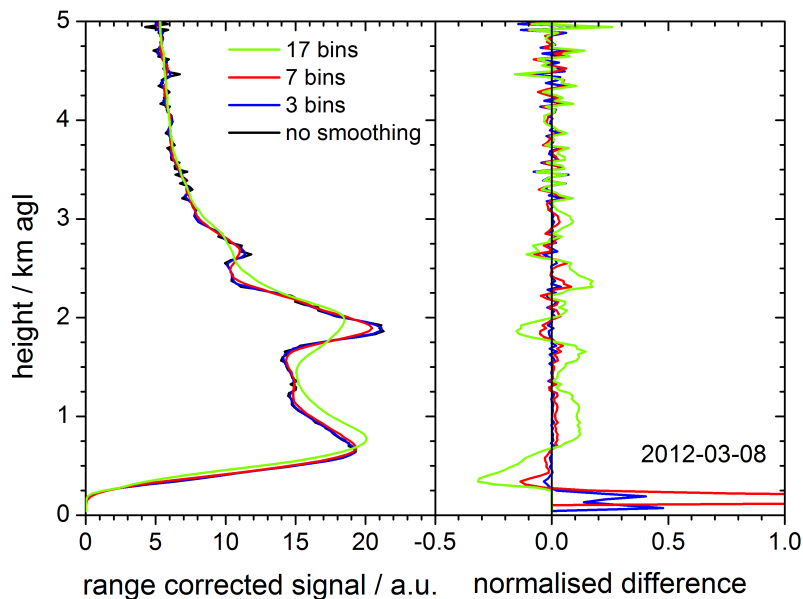


**Figure 4.10.:** Same as figure (4.9), but for a case with smaller vertical gradients (18 to 19 UTC of 8 March 2012).

19 February 2012. The applied overlap correction functions were all obtained from PAOLI measurements. The dates of the measurements used for the experimental determination of those functions are indicated (see also figure (3.21) for the overlap correction functions from the year 2010). A correction function could be obtained during the night of the example measurement. The height of complete overlap was 1.54 km agl at 532 nm (see section (3.3.4)). It was much higher on 15 July 2010 and 9 September 2010 (8.8 and 9.9 km agl, respectively). The other correction functions represent intermediate conditions.

Reference profile for the calculation of  $\Delta_{P_{corr}}$  was the range corrected signal, overlap corrected with the function from 19 February 2012. Of course, the influence of the correction function was largest in low altitudes. In higher altitudes, the impact was much smaller. The extreme cases, the correction functions from 15 July 2010 and 9 September 2010, caused deviations which were smaller than 10% down to 1.5 km agl. Below this height, also the other inappropriate correction functions led to very large  $\Delta_{P_{corr}}$ . The non-corrected profile is only 1% smaller than the reference profile above 0.75 km. In order not to mix the influence of different assumptions and corrections, the following profiles in this section are not corrected for the incomplete overlap of laser beam and receiver FOV. In the analysis of the data shown in the following sections, the overlap correction functions were applied according to the status of the instrument alignment.

### Reference height range and reference value

For the determination of the particle backscatter coefficient  $\beta_{par}$ , the assumption of a reference value in a certain reference height range is crucial. Reference value as well as reference height range were varied for the example measurement. The resulting profiles of the particle backscatter coefficients at 532 nm are shown in figures (4.12) and (4.13). The data were averaged over one hour from 2 to 3 UTC of 19 February 2012 and vertically smoothed over 7 bins (210 m). The particle backscatter profiles in figures (4.12)

#### 4. Aerosol characterisation results

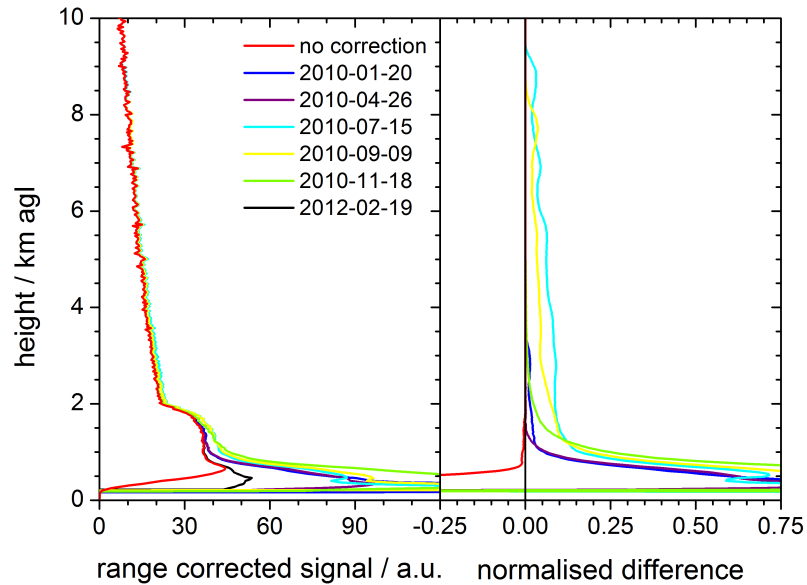


**Figure 4.11.:** Left: Range corrected signal at 532 nm (total) without overlap correction (red) and after application of the overlap correction function from the day of the measurement (black) as well as from different other days. Data were averaged from 2 to 3 UTC of 19 February 2012. Right: Relative deviation with reference to the profile with the overlap correction from 19 February 2012. The line colours correspond to those in the left plot.

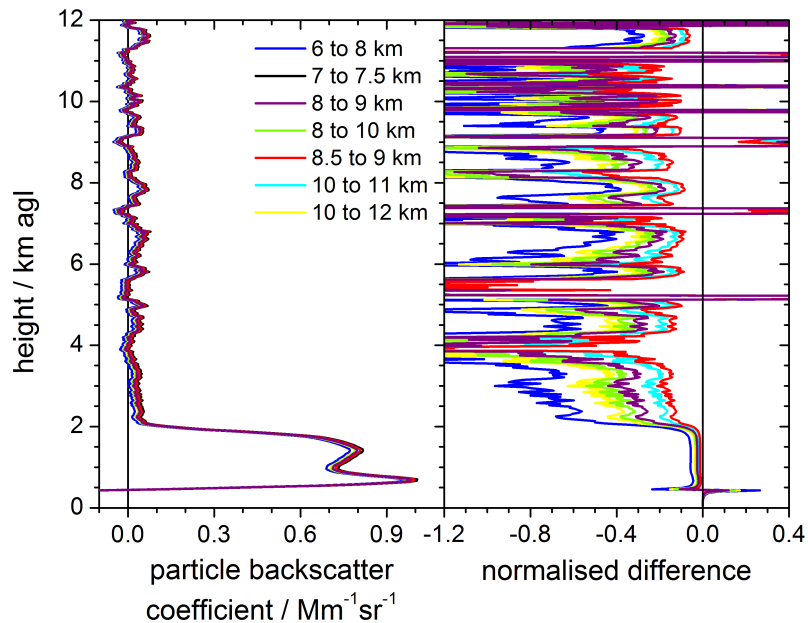


**Figure 4.12.:** Left: Particle backscatter coefficient at 532 nm (Klett) for different reference height ranges with constant reference value ( $0.01 \text{ Mm}^{-1} \text{ sr}^{-1}$ ). Right: Normalised difference with reference to the profile with reference height range at 7.0 to 7.5 km. The line colours correspond to those in the left plot. The data were averaged from 2 to 3 UTC of 19 February 2012.

and (4.13) were retrieved using the Klett method. The lidar ratio was assumed to be 40 sr. The free troposphere appeared to be aerosol free during the example measurement (see figure (4.1)). However, the minimum particle backscatter coefficient was found between 7.0 and 7.5 km agl. The reference value was assumed to be  $0.01 \text{ Mm}^{-1} \text{ sr}^{-1}$  at 532 nm. The application of this value in the height range between 7.0 and 7.5 km agl resulted in non-negative values of the particle backscatter coefficient throughout the profile.  $X_{ref}$  for the calculation of  $\Delta_\beta$  shown in figures (4.12) and (4.13), were the profile with the reference height range at 7.0 to 7.5 km agl and the profile with reference value  $0.01 \text{ Mm}^{-1} \text{ sr}^{-1}$ , respectively. Both, the variation of reference height range and reference value, resulted in very large values of  $\Delta_\beta$  in altitudes with low particle backscatter coefficients.  $\Delta_\beta$  was  $> 10\%$  in case of varying reference height ranges and  $> 20\%$  in case of varying reference values. However, the deviations were much smaller within the strong aerosol layer. Within this layer, the change of the reference height and of the reference value both led to  $\Delta_\beta < 10\%$ . Reference height ranges and values were chosen individually for every calculated profile. Those parameters depend too strongly on the atmospheric conditions to allow predefined settings.

### Assumption of the lidar ratio

The determination of the backscatter profiles with the Klett method requires the assumption of a particle lidar ratio  $S_{par}$ . A one hour average of the example measurement (from 2 to 3 UTC of 19 February 2012) was used to study the effect of the variation of this parameter on the profile of the particle backscatter coefficient  $\beta_{par}$ . In figure (4.14), the results at 532 nm with the reference height range from 7 to 7.5 km and the reference value of  $0.01 \text{ Mm}^{-1} \text{ sr}^{-1}$  are shown. The profiles were vertically smoothed over 7 bins (210 m).

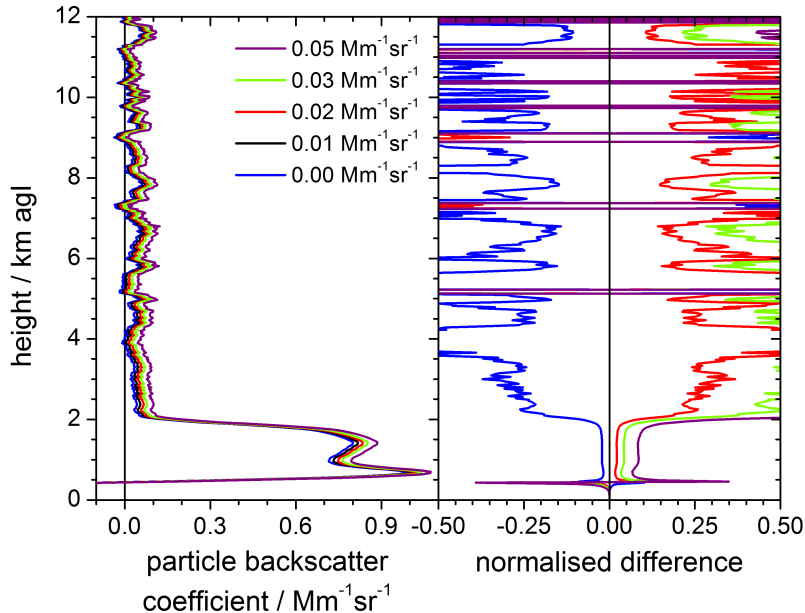


**Figure 4.13.:** Same as figure (4.12), but for different reference values within a constant reference height range (7 to 7.5 km), and normalised difference with reference to the profile with reference value  $0.01 \text{ Mm}^{-1} \text{ sr}^{-1}$ .

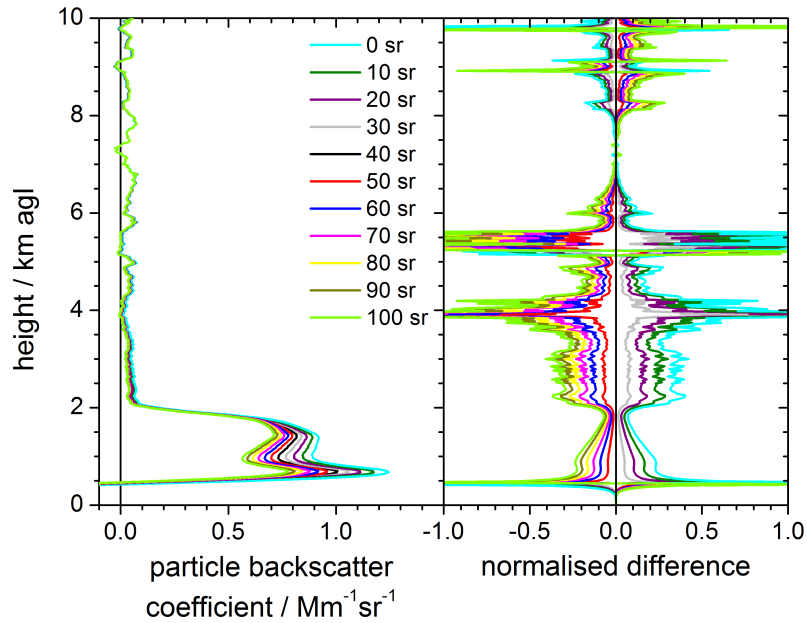


**Figure 4.14.:** Left: Particle backscatter coefficient at 532 nm (Klett) for different lidar ratios with constant reference height range (7 to 7.5 km) and reference value ( $0.01 \text{ Mm}^{-1} \text{ sr}^{-1}$ ). Right: Normalised difference with reference to the profile with a lidar ratio of 40 sr. The line colours correspond to those in the left plot. The data were averaged from 2 to 3 UTC of 19 February 2012.

As shown, increasing  $S_{par}$  results in decreasing of  $\beta_{par}$  and vice versa below the reference height range. Above the reference height range, this effect is reversed. The deviations of the profiles with different values of  $S_{par}$  depends strongly on the vertical distribution of the aerosols, the aerosol types and also on the relative humidity. For example in the discussed case,  $S_{par}$  was not constant throughout the layer between 1 and 2 km agl. The influence of the variation of  $S_{par}$  changed within this height range and was smaller at the layer top. In the weaker aerosol layer between 2 and 3.5 km agl,  $\Delta_\beta$  was larger and reached values up to 40%. As the reference height ranges and values, also the particle lidar ratios were chosen individually for every profile.

#### Assumption of the Ångström exponent

The Raman method is used to obtain the particle backscatter coefficient without the assumption of a particle lidar ratio. However, for the calculation of the particle extinction coefficient  $\alpha_{par}$  the Ångström exponent  $\hat{a}$  has to be assumed. Figure (4.15) shows the changes in the profiles of the particle extinction coefficient at 532 nm caused by varying  $\hat{a}$ . Data were averaged over one hour from 2 to 3 UTC of 19 February 2012 and vertically smoothed over 51 bins (1530 m). Generally, the profiles of the particle extinction coefficients are noisier and therefore a longer smoothing length needs to be applied than for the profiles of the particle backscatter coefficients. From equation (2.25) follows, that the variation of a height constant  $\hat{a}$  leads to a shift of the profile, which is also constant in altitude. Changing  $\hat{a}$  by 1 yields  $\Delta_\alpha$  of around 6% at 532 nm and around 4% at 355 nm (not plotted). For the data analysis discussed in the following sections, the Ångström exponents were set to an average value of 1.5.

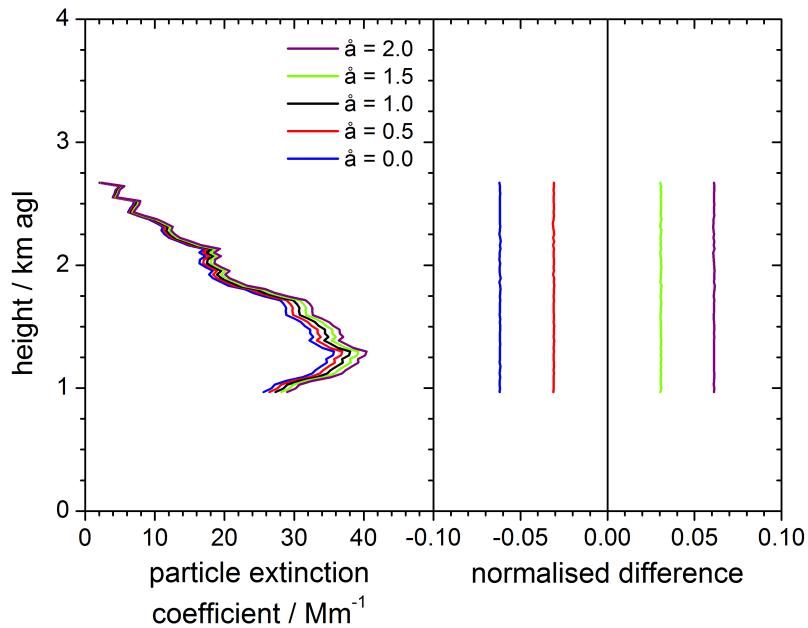


**Figure 4.15.:** Left: Particle extinction coefficient at 532 nm for different Ångström exponents. Right: Normalised difference with reference to the profile with an Ångström exponent of 1. The line colours correspond to those in the left plot. The data were averaged from 2 to 3 UTC of 19 February 2012.

### Rayleigh depolarisation factor

For the demonstration of the analysis of the depolarisation, a different example case was selected. In the measurement on 19 February 2012 no depolarising aerosol has been detected. Therefore, the measurement of a mineral dust layer between 21:30 and 22:30 UTC on 14 March 2012 was used to illustrate the specific procedures for the analysis of measurements of depolarising aerosol. The time-height plot of the range corrected signal at 1064 nm during this period is shown in figure (4.16). In figures (4.17) and (4.18) the vol-

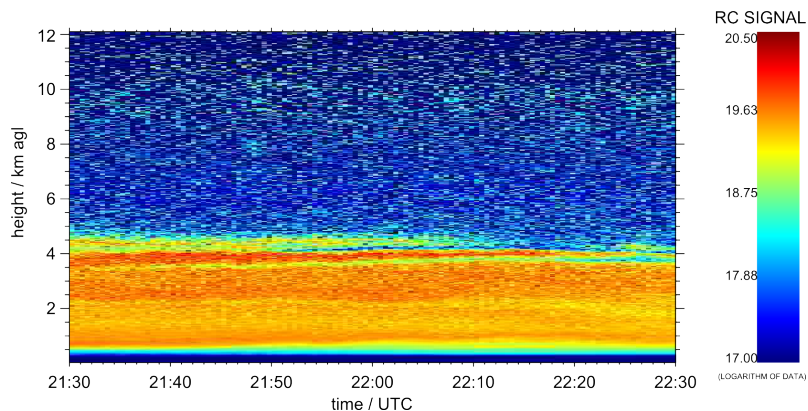


**Figure 4.16.:** Range corrected signal at 1064 nm of the measurement between 21:30 and 22:30 UTC on 14 March 2012 with a height resolution of 30 m and a temporal resolution of 30 s.

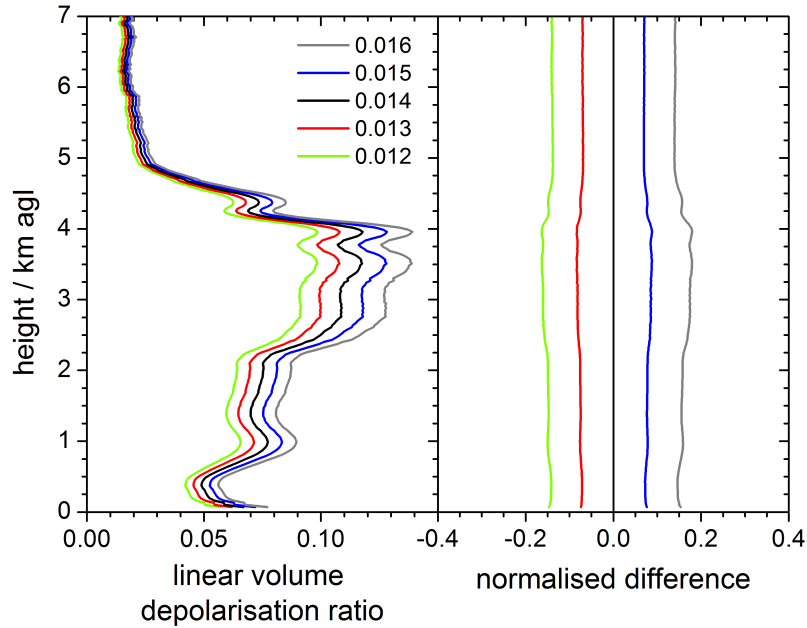


**Figure 4.17.:** Left: Linear volume depolarisation ratio at 532 nm for different calibration values. Right: Normalised difference with reference to the profile with calibration value of 0.014. The line colours correspond to those in the left plot. The data were averaged from 21:30 to 22:30 UTC of 14 March 2012.

ume depolarisation ratio  $\delta_v$  and the linear particle depolarisation ratio  $\delta_{par}$  at 532 nm are plotted, respectively. For illustration purposes, different Rayleigh depolarisation factors were applied to determine the profiles of  $\delta_v$  and  $\delta_{par}$ . In this case, the calibration height range was the nearly aerosol free height range from 11 to 12 km agl. The profile calibrated with a Rayleigh depolarisation factor of 0.014 was used as reference  $X_{ref}$ . Similar values of this factor can be found in literature (Hoyt, 1977; Biele et al., 2000). As shown in figure (4.17), the variation of the calibration value for calculating the linear volume depolarisation ratio  $\delta_v$  results in nearly height constant  $\Delta_{\delta_v}$ . A change in the calibration value by 0.2% led to deviations in  $\delta_v$  of less than 20%. In the shown example,  $\Delta_{\delta_{par}}$  was only height constant within the aerosol layer. The change in the calibration value by 0.2% led to deviations in  $\delta_{par}$  of about 20% within the aerosol layers. In the present work, the value 0.014 was applied for the calibration of  $\delta_v$  and  $\delta_{par}$ .

### Depolarisation correction

PAOLI data have to be corrected for depolarisation dependent transmission efficiencies in the receiving channel at 532 nm (total). In figure (4.19) the effect of the depolarisation correction on  $\beta_{par}$  at 532 nm, and its dependence on the depolarisation calibration value are shown.  $X_{ref}$  was the profile, which was corrected assuming a Rayleigh depolarisation factor of 0.014. The difference between corrected and uncorrected backscatter profiles is much larger than the differences among the three corrected profiles. In the case of 14 March 2012,  $\Delta_{\beta}$  reached 60% and 7%, respectively, within the dust layer.

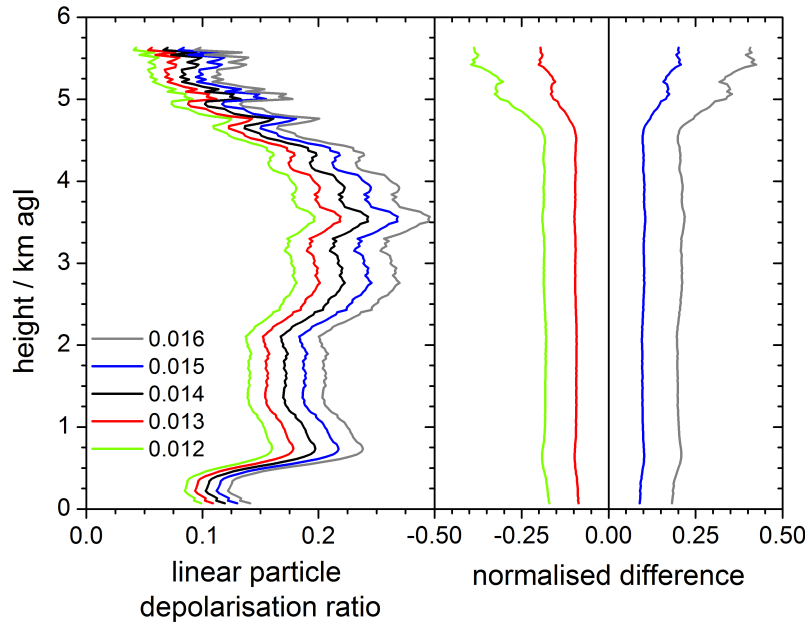


Figure 4.18.: Same as figure (4.12), but for the linear particle depolarisation ratio.

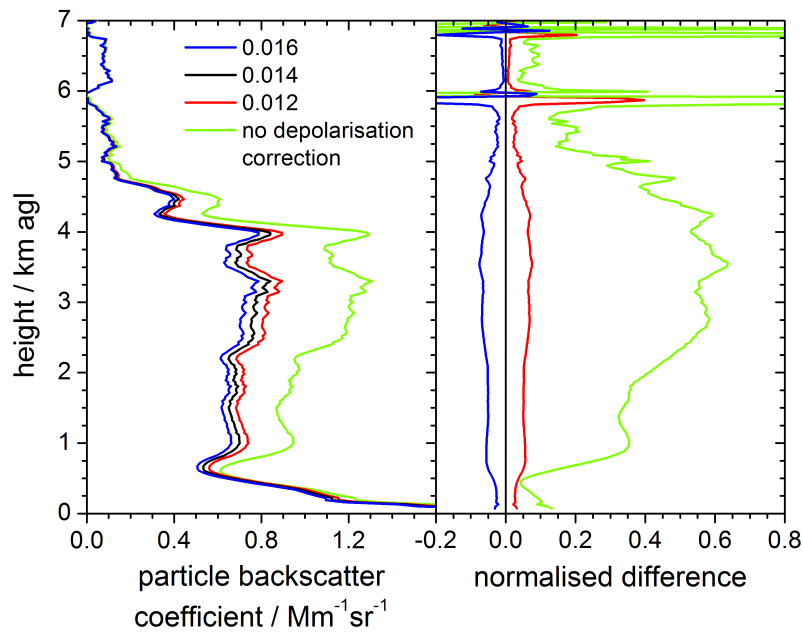


Figure 4.19.: Left: Particle backscatter coefficient at 532 nm, uncorrected, and corrected for depolarisation effects with different calibration values. Right: Normalised difference with reference to the profile corrected with the depolarisation calibration value of 0.014. The line colours correspond to those in the left plot. The data were averaged from 21:30 to 22:30 UTC of 14 March 2012.

## 4.2. Additional information

The combination of lidar data with other types of aerosol measurements can give valuable additional information on aerosol properties. CGE has two ground based stations for aerosol monitoring, which are included in the Aerosol Robotic Network (AERONET) (Holben *et al.*, 1998). One of the AERONET sun photometers is stationed in Évora. The operation of sun photometer and lidar at one site enables intensive studies of aerosol optical properties since both, columnar and vertically resolved data can be obtained. The sun photometer is briefly described in section (4.2.1).

Satellite measurements give additional information about the horizontal distribution of aerosol plumes, as for example the space borne lidar Cloud Aerosol Lidar with Orthogonal Polarization (CALIOP) (see section (4.2.2)) or the Moderate Resolution Imaging Spectroradiometer (MODIS) (see section (4.2.3)). Ground based in-situ measurements of optical and physical aerosol properties are performed at CGE as well. As the lidar is not detecting close to the ground, the in-situ measurements can be used for a more detailed study of boundary layer aerosols. They are complementing the information obtained from lidar and sun photometer. The operated instruments are introduced in section (4.2.4).

Another useful tool for the aerosol characterisation in combination with lidar measurements are backward trajectories or tracer models. Within this work, HYSPLIT (Hybrid Single-Particle Lagrangian Integrated Trajectory) (Draxler and Rolph, 2012) was used to roughly determine the sources of aerosol plumes detected by lidar. The procedure of source detection is described in section (4.2.5).

### 4.2.1. CIMEL sun photometer

Since July 2009, a sun photometer of type CIMEL CE-318-2 is operated in Évora in the framework of AERONET. It is measuring at eight wavelengths between 340 and 1640 nm. Before that, since 2003, a CIMEL with different capabilities was used. Sun photometers are passive remote sensing instruments, which provide columnar data of optical aerosol properties. Those can be used for comparisons with the height resolved values calculated from lidar data, as done by, among others, Balis *et al.* (2000); Porter *et al.* (2002) and Müller *et al.* (2003). Cloud screened AERONET level 1.5 data, which includes Ångström exponents and aerosol optical depths, were used for the studies presented in sections (4.3.1) and (4.3.3). The columnar aerosol optical depths  $\tau$  at the wavelengths of the sun photometer (380, 500, 1020 nm) were converted to the wavelengths detected by the lidar (355, 532, 1064 nm) by power fitting with the Ångström law ( $\tau(\lambda) = b\lambda^{-\alpha}$ ).

### 4.2.2. Satellite borne lidar CALIOP

The sun-synchronous satellite Cloud-Aerosol Lidar and Infrared Pathfinder Satellite Observations (CALIPSO), with the lidar CALIOP aboard, passes over Évora three times within every 16 days, twice in night time at around 2:40 and 2:45 UTC, respectively, and once in the afternoon at around 13:50 UTC. In agreement with the EARLINET specifications, overpasses are considered, if the ground-track distance to PAOLI is smaller than 100 km. The ground-track distances during the three different overpasses are between 8 and 80 km. Data of this space borne lidar were compared to PAOLI data for the study introduced in section (4.3.3).

CALIOP measures the elastic signals at 532 nm (parallel polarised), 532 nm (cross polarised) and 1064 nm. CALIOP level 1 data are profiles of the attenuated backscatter coefficients at 532 and 1064 nm. Level 2 data include profiles of the particle depolarisation ratio at 532 nm and the particle extinction coefficients. The extinction is calculated by multiplying the particle backscatter coefficient profiles with a constant lidar ratio. Level 2 data are provided by the National Aeronautics and Space Administration (NASA) via GES-DISC (Goddard Earth Sciences Data and Information Services Center) Interactive Online Visualization And Analysis Infrastructure (GIOVANNI) (*Acker and Leptoukh, 2007*). Version 3.01 (validated stage, *NASA Langley ASDC (2010)*) of those data products was used for this work.

### 4.2.3. Satellite borne spectroradiometer MODIS

MODIS is operated on two satellites, Terra and Aqua, which pass over Évora every day at around 12 and 14 UTC, respectively. The instrument is measuring at 36 wavelengths. The columnar aerosol optical depth (AOD) at 550 nm as well as images of the visible composite were used in some of the presented studies (see sections (4.3.3) and (4.3.5)). The AOD data are provided by NASA and were obtained via GIOVANNI as well. The AOD detected by MODIS (*Remer et al., 2005; Levy et al., 2010*) was mainly used to get an overview over the horizontal distribution of aerosol plumes.

### 4.2.4. Ground based in-situ measurements

At CGE, several ground based instruments for in-situ observation of aerosol properties are operated. A Tapered Element Oscillating Microbalance (TEOM), model 1400 (*Patashnick and Rupprecht, 1991*), measures the particle mass concentration  $M$ . A PM<sub>10</sub> sampling head limits the measurement to particles with an aerodynamic diameter of less than 10  $\mu\text{m}$ . The samples of the integrating nephelometer (model TSI-3563) (*Anderson et al., 1996*) also pass through a PM<sub>10</sub> sampling head. Aerosol spectral scattering coefficients and backscatter coefficients at 450, 550 and 700 nm are measured with the nephelometer. Furthermore, the aerosol size distribution  $dN/d\log D$  and number concentration  $N$  can be determined with an Aerodynamic Particle Sizer Spectrometer (APS) from the manufacturer TSI Incorporated, model 3321. More detailed descriptions of those instruments, of calibrations, corrections and specifications were given by *Pereira et al. (2008)* and *Preißler et al. (2011a)*. Data of those ground based in-situ instruments were used in the study on a Saharan dust event presented in section (4.3.3).

### 4.2.5. Source identification

For the determination of the origin of detected aerosol layers, HYSPLIT backward trajectories were calculated. In some cases, three trajectories were started over Évora within the height range the aerosol layer was detected in. Depending on the study, the trajectories were calculated backward for five to ten days.

For other cases, trajectories were calculated every 100 m between 0.5 and 12 km asl. Those were then combined with meteorological information, namely the PBL height from GDAS data. Air masses with trajectories, which had boundary layer contact, were assumed to be more likely to pick up aerosols. Therefore, by including this information, the identification of aerosol source regions was facilitated. One example of the procedure is

#### 4. Aerosol characterisation results

shown in figures (4.20) and (4.21). The whole ten day backward trajectories are plotted in figure (4.20). The colours of the trajectories change every 1000 m. Therefore, ten trajectories have the same colour. The same set of trajectories, but only the fractions within the PBL, are shown in figure (4.21). Between 500 and 900 m asl the air masses had boundary layer contact mainly in maritime and coastal areas west and north of the Iberian Peninsula and west of France and Ireland. The contributions closest to Évora should be considered most important at such low altitudes. The trajectories arriving at Évora between 2 and 3.9 km asl had boundary layer contact over the Sahara, as well as a small fraction of a trajectory between 8 and 8.9 km asl. Furthermore, a small part of a trajectory between 1 and 1.9 km asl entered the boundary layer over the Great Lakes in North America. However, not too much emphasis should be put on single trajectories which enter the boundary layer only for very short distances. Generally, the uncertainty of a trajectory is increasing with duration. *Rolph and Draxler (1990)* found horizontal deviation of up to 25% of the trajectory length for 96 h trajectories. In the documentation of the HYSPLIT model, uncertainties between 15 and 30% of the travel distance are given (*Draxler, 2012*). However, the deviations can be even higher (*Stohl, 1998*).

The lidar measurement corresponding to those trajectory calculations is shown in figure (4.22). The boundary layer height was about 1.2 km asl. Besides, a very distinct aerosol layer was observed in the free troposphere between 2.6 and 3.7 km asl. Trajectories in this altitude range had boundary layer contact over the Sahara. Therefore, in this case the aerosol type was classified as Saharan dust.

Besides the analysis of backward trajectories, aerosol model results were used to identify the aerosol origin. Saharan dust is forecasted by the Dust Regional Atmospheric Model (DREAM) (*Nickovic et al., 2001*). Volcanic ash alerts are provided by the Volcanic Ash Advisory Centres (VAACs). Furthermore, the transport of volcanic aerosol from the Iceland volcanoes Eyjafjallajökull and Grímsvötn was simulated by the Lagrangian particle dispersion model FLEXPART (*Stohl et al., 2005*) by means of different tracers. The results were available online. The Navy Aerosol Analysis and Prediction System (NAAPS) predicts surface concentration and total optical depth of sulphate, dust and smoke. Also

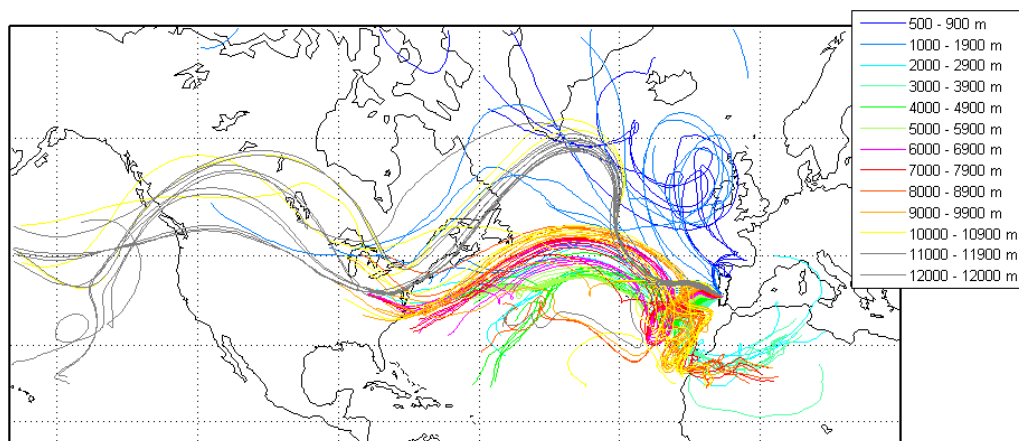


**Figure 4.20.:** Full lengths of ten day backward trajectories started over Évora every 100 m between 0.5 and 12 km asl. Altitudes are given in m asl. HYSPLIT results from 29 August 2011 at 21 UTC (meteorological data from GDAS).

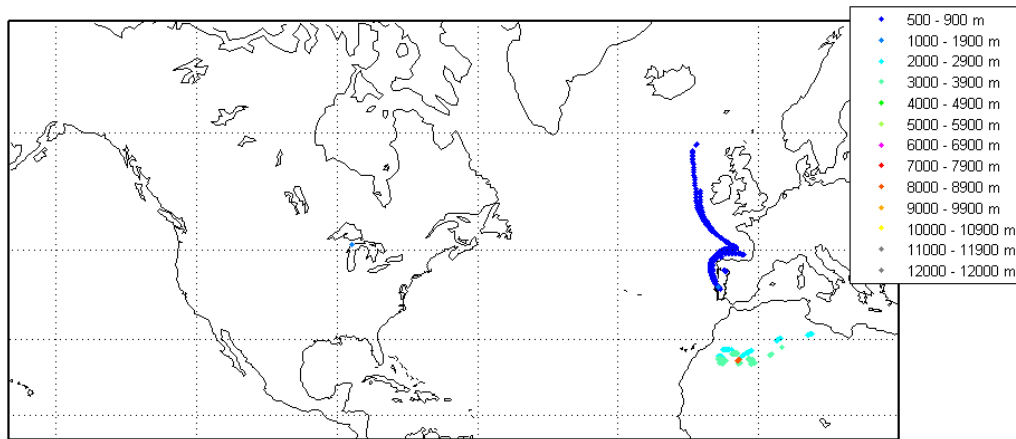


Figure 4.21.: Same trajectories as in figure (4.20), but only the fractions within the PBL.

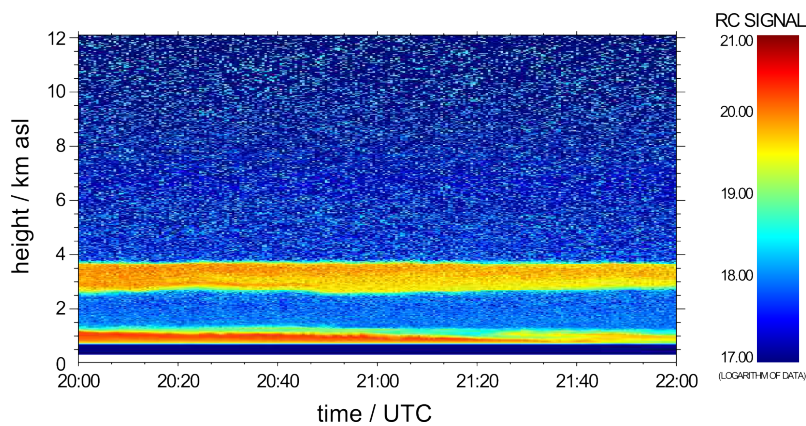


Figure 4.22.: Range corrected signal at 1064 nm from 20 to 22 UTC on 29 August 2011, without overlap correction. The white range on the bottom of the plot corresponds to the station height above sea level (290 m) and the dark blue range to the incomplete overlap of outgoing beam and receiver field of view.

satellite observations can provide useful information on aerosol sources and the transport path of aerosol plumes, for example the visible composite of MODIS or the MODIS Rapid Response System (*Giglio et al.*, 2003) for fire detection. Images provided by the satellite Landsat (*Landsat Project Science Office*, 2012) were also considered within this work.

### 4.3. Case studies

Occasionally, so-called special events occurred since the first measurements with PAOLI in September 2009. Some of them are discussed in this section. The measurements were selected to give an overview over different aerosol types. Lidar measurements of volcanic aerosol in the troposphere and stratosphere, mineral dust and forest fire smoke were investigated. During the first months, stratospheric aerosol could be observed. It was probably caused by different volcanic eruptions since 2008 (*Mattis et al.*, 2010). The aerosol layer in the lower stratosphere contributed significantly to the columnar aerosol optical depth. The analysis of this stratospheric layer is presented in section (4.3.1). In contrast, plumes

#### 4. Aerosol characterisation results

of tropospheric aerosol of volcanic origin were observed shortly after the eruption of Eyjafjallajökull, Iceland in April and May 2010. This provided the rare opportunity to study fresh volcanic aerosol in large parts of Europe. Results of the lidar measurements of the volcanic ash performed in Évora are discussed in section (4.3.2). Another volcanic eruption occurred in June 2011. Nabro in Eritrea, injected a large quantity of  $\text{SO}_2$  into the stratosphere. From this, droplets of sulphuric acid ( $\text{H}_2\text{SO}_4$ ) formed. A stratospheric layer was observed over Évora for more than 8 months. Those measurements are discussed in section (4.3.4). Those three studies illustrate the variability of aerosols in their vertical distribution as well as their optical properties, even if the aerosol type is the same, as in this case volcanic aerosol.

The Saharan desert is the largest source of mineral dust aerosol and therefore plays an important role in atmospheric processes on a global scale. An exceptionally strong Saharan dust event was monitored with PAOLI in April 2011. Details about those measurements are given in section (4.3.3). Furthermore, PAOLI measurements of a Saharan dust outbreak and a biomass burning smoke plume, both in June 2011, were compared to measurements of the EARLINET lidar in Granada in southern Spain. This study is presented in section (4.3.5).

If not stated otherwise, hourly averages of the lidar signal were used for the calculation of particle extinction and backscatter coefficient profiles in the presented case studies. The Klett method was applied for daytime profiles and the Raman method for night time profiles. For the profiles of the particle backscatter coefficients at 1064 nm, only the Klett method was used. As stated before, the overall relative errors of  $\beta_{par}$  obtained with the Raman method,  $\beta_{par}$  obtained with the Klett method,  $\alpha_{par}$  and  $\delta_{par}$  are generally less than 15%, 20%, 25% and 25%, respectively (see section (2.3)).

##### 4.3.1. Stratospheric aerosol, September 2009

Parts of this study were presented by *Preißler et al.* (2010a). During lidar measurements at the end of September 2009, a relatively high aerosol load could be observed in the lower stratosphere. This was most likely due to high volcanic activity in the northern hemisphere in 2008 and 2009. Before 2008, the volcanic activity was much lower and hence no stratospheric aerosol could be observed in Europe for more than ten years (*Mattis et al.*, 2010). The focus of this study is to emphasise the importance of the influence of stratospheric aerosol with regard to the columnar values as obtained e.g. by sun photometers.

An almost continuous measurement over more than 24 h from noon of 24 September 2009 to the afternoon of 25 September 2009 was investigated. To illustrate the development of the atmosphere during the day and to characterise the aerosol layers, hourly averaged profiles of the particle backscatter and extinction coefficients were calculated.

##### Aerosol layer heights

The boundary layer height was determined with the gradient method using the non-smoothed profiles of the range corrected signal at 355, 532 and 1064 nm. The boundaries of the stratospheric aerosol layer was found from the gradient of the backscatter profiles at 1064 nm. The height of the tropopause and of the top of the boundary layer were additionally obtained from GDAS model soundings using the profiles of temperature and relative humidity, respectively. The vertical distribution of the aerosol layers detected by

lidar and the top of the boundary layer and the tropopause height obtained from model soundings are shown in figure (4.23). The mean boundary layer height and the standard deviation were  $1.9\pm 0.3$  km agl averaged over the whole period excluding the time between 4:50 to 8:58 UTC on 25 September 2009, when a residual layer was detected. The mean boundary layer top was  $0.61\pm 0.07$  km agl during this time period. The comparison with boundary layer heights obtained from model sounding data showed a very good agreement, except for the shallow nocturnal boundary layer, which was not captured by the model. However, the residual layer top agrees well with the humidity maximum of the model sounding profiles.

A deep stratospheric layer was present over the whole period. There was a second, less distinct layer directly on top of this one. However, it could not be distinguished from noise at all times. The bottom of the lower stratospheric layer observed by lidar approximately coincided with the tropopause height determined from model sounding data. This stratospheric layer was more than 5 km deep between  $13.3\pm 0.5$  km agl and  $18.5\pm 0.6$  km agl. The mean top height of the second thinner layer was  $20.4\pm 0.4$  km agl.

### Aerosol origin

For the boundary layer aerosol, five day back trajectories were calculated for every six hours starting from 12 UTC at 24 September 2009 (not shown). They all had very similar patterns. According to those trajectories the air masses in the lower troposphere were coming from east crossing the western Mediterranean Sea and Spain within three days. It is likely that aerosols from the urban areas around Valencia or dust from the central Iberian Peninsula were picked up on the way to Évora. Also forest fires were detected in south-western Spain during that time. Conclusively, a mixture of anthropogenic urban, mineral and biomass burning aerosols from Spain were most likely observed in the boundary layer

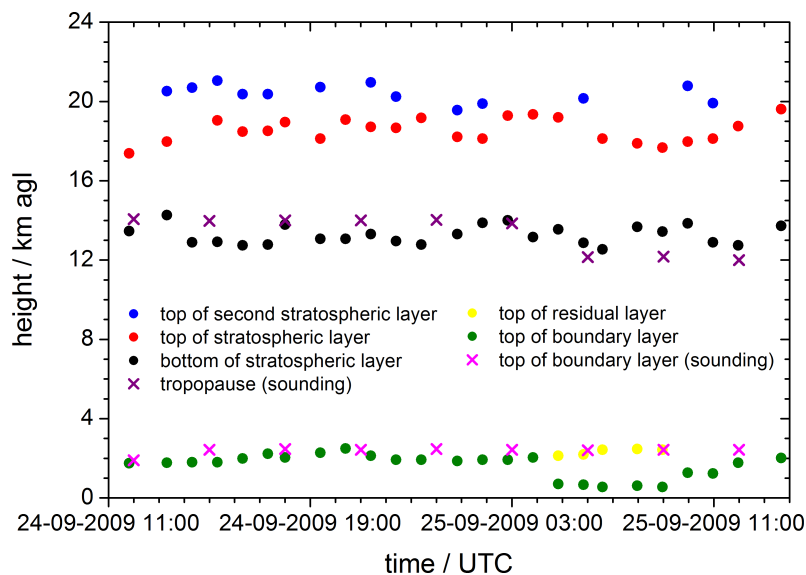


**Figure 4.23.:** Layer boundaries obtained from lidar measurements (dots) and model sounding data (crosses). Plotted are the boundary layer, a residual layer during night time, the tropopause and the stratospheric layers.

#### 4. Aerosol characterisation results

on 24 and 25 September 2009.

Back trajectories calculated for the stratospheric layer (not shown) do not indicate any entrainment from the troposphere up to ten days before the observation of the layer. It can be assumed that this layer was caused by several strong volcanic eruptions in the northern hemisphere in 2008 and 2009, e.g. of Okmok on the Aleutian Islands (July 2008)(*Neal et al.*, 2011), Mt. Redoubt in Alaska (March 2009)(*Schaefer*, 2012) and Sarychev Peak in Russia (June 2009)(*Venzke et al.*, 2009).

##### Optical aerosol properties

The lidar ratio for the Klett retrieval of the particle backscatter coefficient during daytime was assumed to be 32 sr at 355 nm and 47 sr at 532 nm. Those were the boundary layer mean values found from the Raman night time measurements (see also table (4.1)). The lidar ratio dependence of  $\beta_{par}$  was very weak in the stratospheric layer. At 1064 nm a lidar ratio of 45 sr was assumed.

From the profiles of  $\alpha_{par}$  and  $\beta_{par}$  the Ångström exponents  $\hat{a}$ , the aerosol optical depth  $\tau$  and the particle lidar ratios  $S_{par}$  were obtained applying equations (2.9), (2.24) and (2.27), respectively. However, the determination of the particle extinction profiles is problematic during daytime due to noise induced by background radiation. Hence, to avoid noisy extinction data during daytime, and to obtain  $\tau$  at 1064 nm the AOD was calculated as

$$\tau_{\beta}(\lambda) = \int_{z_1}^{z_2} \beta_{par}(z', \lambda) S_{par}(\lambda) dz'. \quad (4.2)$$

For this procedure, the same lidar ratios as for the Klett retrieval of the particle backscatter coefficients were used (32, 47 and 45 sr at 355, 532 and 1064 nm, respectively). Equation (4.2) could not be applied to obtain the aerosol optical depth of the stratospheric layers at 355 nm because of a low SNR in high altitudes.

The lidar data in the lowest 0.79 km agl were not used because of the critical height range of incomplete overlap. As the lowest part of the atmosphere contributes significantly to the aerosol concentration, it cannot be neglected. Therefore, height constant particle backscatter coefficients were assumed in the lowest height range. For this, the mean values between 0.79 km agl and the PBL top was used, which is illustrated in figure (4.24). However, the vertical distribution of aerosols close to the ground is highly variable and unknown, because it cannot be measured by PAOLI. Therefore, the assumption of height constant particle backscatter coefficients might cause over- or underestimation of the aerosol optical depth of the PBL, depending on the real vertical aerosol distribution at the low altitudes.

Figure (4.25) shows  $\tau_{\beta}(\lambda)$  of the boundary layer, including the residual layer during night, and of the stratospheric layer from lidar observations. The AOD of the stratospheric layer at 532 nm was 19% of the AOD of the boundary layer. At 1064 nm it was 18%. This signifies, that stratospheric aerosol layers can contribute significantly to the columnar aerosol optical depth.

In figure (4.26) the sum of  $\tau_{\beta}$  of the PBL and of the stratospheric layer from lidar measurements ( $\tau_{PAOLI}$ ) is compared to  $\tau$  of the whole column from sun photometer data ( $\tau_{CIMEL}$ ). Sun photometer data were available until 17 UTC on 24 September 2009 and from 8 UTC on 25 September 2009. Around 23 UTC on 24 September 2009  $\tau_{PAOLI}$  at 532 nm was decreasing and remained low until 2:50 UTC on 25 September 2009. This could be due to the assumption of a constant particle backscatter coefficient in the lower

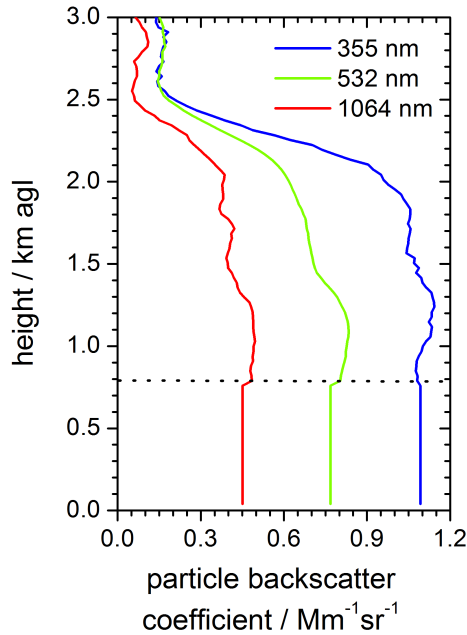


**Figure 4.24.:** Overlap corrected particle backscatter coefficient obtained with the Klett method above 0.79 km agl (dotted line) and a constant PBL mean value below; at 355 (blue), 532 (green) and 1064 nm (red). Data were averaged from 11:28 to 12:28 UTC on 25 September 2009.

part of the boundary layer, especially at night. During daytime the boundary layer is well mixed. But after sunset the aerosols tend to concentrate closer to the ground. For data from 4:50 UTC to 8:58 UTC on 25 September 2009 the residual layer was used to calculate the mean value of the particle backscatter coefficients close to the lidar, because the top of the shallow nocturnal boundary layer was below 0.79 km agl. This resulted in high values of  $\tau_{\beta}(\lambda)$ . However, as shown in figure (4.26),  $\tau_{PAOLI}$  was close to the values of  $\tau_{CIMEL}$  at 532 and 1064 nm. The mean normalised differences of the aerosol optical depths from lidar and sun photometer data  $\Delta_{\tau}$  with the columnar  $\tau_{CIMEL}$  as reference was -14% and -4%, at 532 and 1064 nm respectively.  $\Delta_{\tau}$  was not calculated at 355 nm,

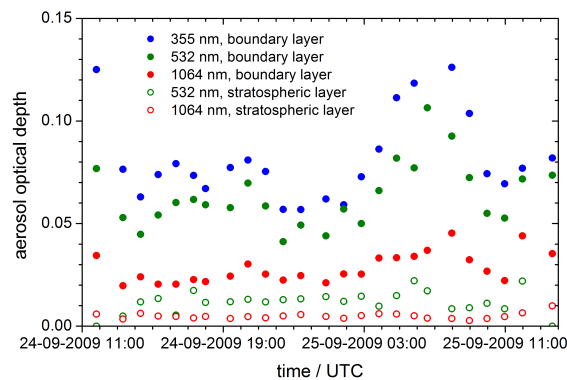


**Figure 4.25.:** Aerosol optical depth calculated with equation (4.2) from lidar particle backscatter coefficients for the boundary layer (including the residual layer at night time) at 355, 532 and 1064 nm (dots) and for the stratospheric layer at 532 and 1064 nm (circles).

#### 4. Aerosol characterisation results

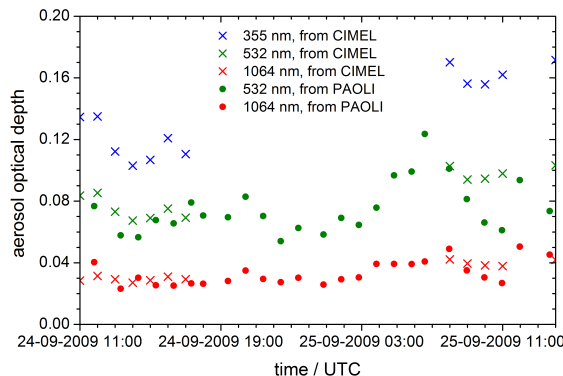


**Figure 4.26.:** Sum of aerosol optical depths from lidar particle backscatter coefficients of the boundary layer (including the residual layer at night time) and the stratospheric layer at 532 and 1064 nm (dots), and the aerosol optical depths of the whole column from CIMEL data (crosses).

because  $\tau_\beta$  of the stratospheric layer was not available at that wavelength due to a low SNR. Negative values of  $\Delta_\tau$  were expected, because lidar data are not available for the whole column. Besides, for the calculation of  $\tau_{PAOLI}$  only the AODs of the aerosol layers were considered.

Table (4.1) shows the mean values, the total and the relative standard deviations of the lidar ratios as well as Ångström exponents obtained from lidar and sun photometer measurements. The Ångström exponents obtained from lidar measurements were averaged

**Table 4.1.:** Optical properties from lidar and sun photometer measurements.<sup>a</sup>

	all profiles		night time only	
	mean value	standard deviation (in %)	mean value	standard deviation (in %)
$S_{par}$ (PBL, 355 nm)			32	5 (16)
$S_{par}$ (PBL, 532 nm)			47	9 (5)
$\hat{a}_\beta$ (PBL, 355, 532 nm)	1.2	0.5 (42)	1.5	0.3 (13)
$\hat{a}_\beta$ (PBL, 532, 1064 nm)	1.0	0.2 (20)	1.1	0.1 (9)
$\hat{a}_\alpha$ (PBL, 355, 532 nm)			0.7	0.3 (43)
$\hat{a}_\beta$ (St, 355, 532 nm)	1.6	0.7 (44)	1.6	0.7 (44)
$\hat{a}_\beta$ (St, 532, 1064 nm)	1.6	0.5 (31)	1.5	0.4 (27)
$\hat{a}_\alpha$ (St, 355, 532 nm)			1.0	0.9 (90)
$\hat{a}_\tau$ (column, 355, 532 nm)	1.2	0.1 (8)		
$\hat{a}_\tau$ (column, 532, 1064 nm)	1.4	0.1 (7)		

<sup>a</sup> Lidar ratios of boundary layer aerosol (PBL) as well as extinction- and backscatter related Ångström exponents of boundary layer aerosol and of stratospheric aerosol (St) from lidar measurements; and AOD related Ångström exponents for the whole column from sun photometer measurements.

over all hourly values and over ten night time values, respectively. The particle extinction coefficient, and consequently  $\hat{a}_\alpha$  and  $S_{par}$  were only calculated from night time lidar data. The AOD related Ångström exponents from the wavelength corrected sun photometer data were averaged over the available 13 daytime values. The standard deviations of  $\hat{a}_\tau$  at both wavelengths during this time period were very small. The standard deviations of  $\hat{a}_\alpha$  were highest due to noisy extinction profiles resulting from the high sensitivity of the Raman channels. Those of  $\hat{a}_\beta$  in the boundary layer calculated from night time data were clearly smaller than from the whole time period. Daylight induced noise was affecting the profiles of  $\beta_{par}$ . The mean Ångström exponents from lidar data were between 0.7 and 1.5 in the boundary layer and 1.0 to 1.6 in the stratospheric layer. Mean values of  $\hat{a}_\tau$  from sun photometer for the whole column were similar.

The medium lidar ratios indicate moderately absorbing aerosols in the boundary layer, and the mean  $\hat{a}_\beta$  hint at medium size particles. This agrees with the assumption of a mixture of different aerosol types, according to the back trajectories. During the Second Aerosol Characterization Experiment (ACE2) *Ansmann et al.* (2002) detected European pollution advected to Portugal. They found layer mean lidar ratios at 532 nm between 34 and 63 sr.

The Ångström exponents of the stratospheric layer indicate a slightly higher contribution of smaller particles than in the boundary layer. The backscatter-related Ångström exponents of stratospheric aerosol from the eruption of Mount Pinatubo, Philippines, in June 1991 were studied by *Kent and Hansen* (1998). They found  $\hat{a}_\beta$  ranging from about 0.5 to 2.5, with a tendency of medium  $\hat{a}_\beta$  between 1.0 and 1.5 within two years after the eruption. In general,  $\hat{a}_\beta$  (355, 532 nm) and  $\hat{a}_\beta$  (532, 1064 nm) were increasing with time. However, different volcanic eruptions may produce aerosols with different characteristics. Besides, the stratospheric aerosol observed by PAOLI in September 2009 was probably a mixture of aerosols from different volcanic eruptions.

### 4.3.2. Volcanic aerosol from Eyjafjallajökull, April 2010

Volcanic eruptions are known to be a natural cause for climate change (*Solomon et al.*, 2007). However, the influence of volcanic aerosol is hard to predict. Volcanic eruptions occur only infrequently and with irregular spatial and temporal distributions and different eruption intensities. Since measurements and observations depend on volcanic activity, they also can only be made occasionally. The eruptive activities of the Eyjafjallajökull volcano (63.6° N, 19.6° W) in Iceland started on 14 April and ended on 21 May 2010. During the first days, the aerosol plume was transported eastward due to a high pressure system south of Iceland over north-west Europe. Five day forward trajectories from 14 April 2010 are shown in figure (4.27). In the beginning of May the synoptic situation changed. Low pressure systems south-east of Iceland and over Great Britain favoured the southward advection of air masses from Eyjafjallajökull. The forward trajectories from 3 May 2010 are given in figure (4.28). Aerosol plumes from Iceland were detected by PAOLI from 5 May 2010. For the study presented here, measurements in the time period from 5 to 7 May 2010 as well as on 10, 13 and 14 May 2010 were analysed. No measurements were possible on 8, 9, 11 and 12 May 2010 due to low clouds and rain. Some of the results of the volcanic aerosol measurements were presented by *Preißler et al.* (2010b), *Sicard et al.* (2012) and *Pappalardo et al.* (2012).

For this study the Klett backscatter profiles were obtained by using a lidar ratio with a

4. Aerosol characterisation results

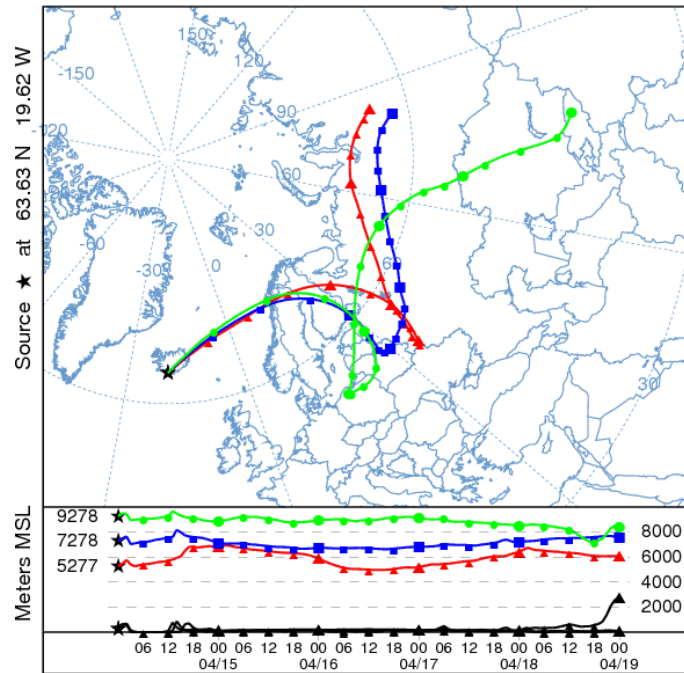


**Figure 4.27.:** Five day forward trajectories from HYSPLIT starting at Eyjafjallajökull at 0 UTC on 14 April 2010 at 5, 7 and 9 km agl.

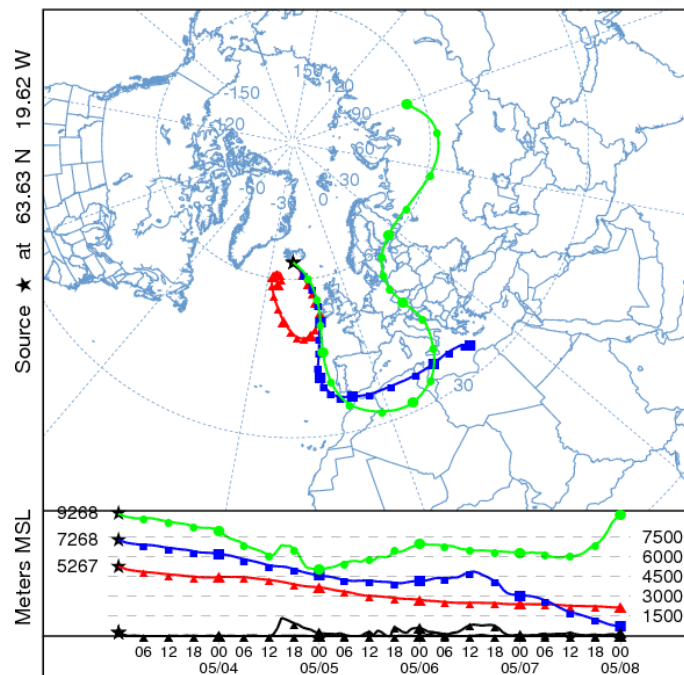


**Figure 4.28.:** Five day forward trajectories from HYSPLIT starting at Eyjafjallajökull at 0 UTC on 3 May 2010 at 5, 7 and 9 km agl.

constant value of 50 sr. Although volcanic ash particles are non-spherical, and therefore depolarising, no depolarisation correction could be applied. The photomultiplier tube (PMT) detecting at 532 nm (cross) was not working during the measurements. Therefore, no information on the depolarisation of the volcanic aerosol over Évora was available.

The first volcanic aerosol plumes were detected by lidar systems over central Europe from 16 to 24 April 2010 (Ansmann *et al.*, 2010). During this period, the EARLINET members in Munich, Germany (Gasteiger *et al.*, 2011; Groß *et al.*, 2012a) and in Potenza, Italy (Mona *et al.*, 2012) found large linear particle depolarisation ratios  $\delta_{par}$  (532 nm) of 0.35 to 0.38 and  $0.25 \pm 0.05$ , respectively. However, the characteristics of the aerosols changed during the time of volcanic activity. The optical properties of the volcanic aerosol differed clearly in lidar observations performed in May 2010 (Ansmann *et al.*, 2011). They resulted in smaller  $\delta_{par}$  within the volcanic aerosol plume. Mona *et al.* (2012) found values of  $\delta_{par}$  (532 nm) between  $0.10 \pm 0.09$  and  $0.16 \pm 0.07$  in Potenza and Sicard *et al.* (2012) found  $\delta_{par}$  (532 nm) of  $0.066 \pm 0.005$  and  $0.075 \pm 0.007$  in Granada, Spain.

The depolarisation correction of PAOLI data would lead to smaller particle backscatter coefficients at 532 nm ( $\beta_{par}$  (532 nm)). In case of  $\delta_{par}$  (532 nm) = 0.16, the correction would decrease  $\beta_{par}$  (532 nm) by about 28%. If  $\delta_{par}$  (532 nm) = 0.07,  $\beta_{par}$  (532 nm) would be about 16% smaller. This effect would propagate to the values of the lidar ratio at 532 nm as well as the backscatter related Ångström exponents containing this wavelength. As the depolarisation correction was not possible, no backscatter related values at 532 nm are shown for the volcanic aerosol layers.

In figure (4.29) a time-height plot of the hourly profiles of the particle backscatter coefficient at 1064 nm is shown. Also plotted is the height of the PBL top. Volcanic aerosol layers were observed up to about 8 km agl. During the whole period, several thin filaments with a minimum vertical extension of 60 m as well as thicker layers of 3.9 km were detected. The aerosol plumes were mostly descending. However, no intrusion of

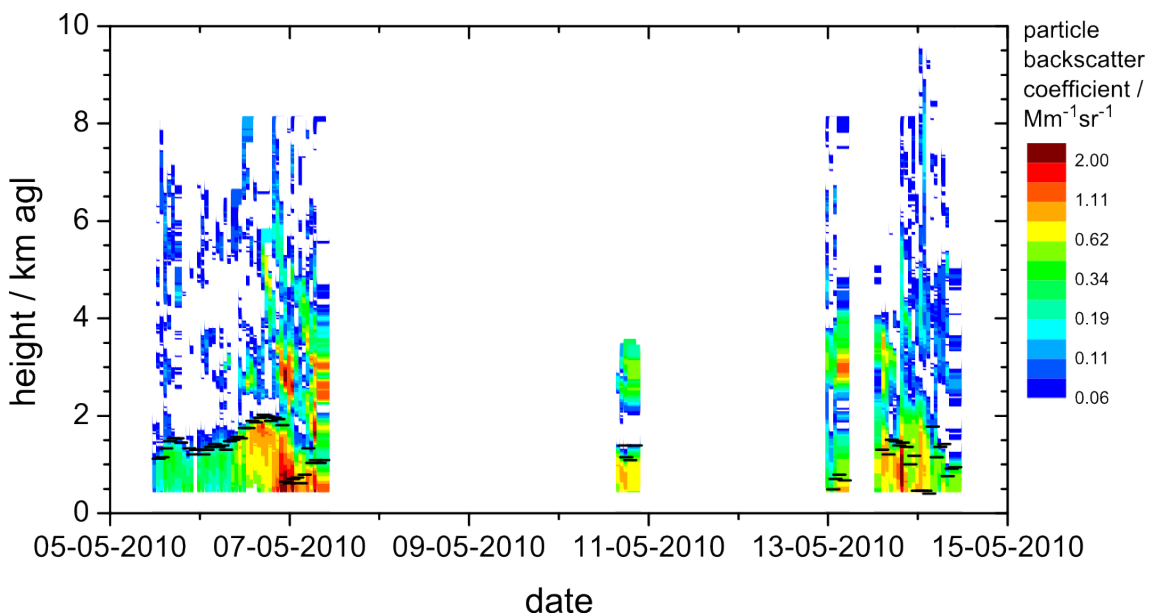


**Figure 4.29.:** Particle backscatter coefficient at 1064 nm on a logarithmic scale (colour map) and top of the PBL (black horizontal lines).

#### 4. Aerosol characterisation results

volcanic aerosol into the boundary layer could be observed in Évora. Maximum values of the particle backscatter coefficient within the volcanic aerosol layers were found in the night from 6 to 7 May 2010.

A set of lidar profiles from 5 UTC on 7 May 2010 is shown in figure (4.30). The aerosol layer heights are highlighted with bold lines. The particle backscatter coefficient at 532 nm was multiplied by 0.84 and 0.72 in order to simulate the depolarisation correction by 16 and 28%, corresponding to  $\delta_{par}(532 \text{ nm}) = 0.07$  and  $\delta_{par}(532 \text{ nm}) = 0.16$ , respectively. The resulting profiles are plotted within the aerosol layers. In total, four layers of presumably volcanic origin were observed between 4:30 and 5:30 UTC on 7 May 2010. The mean values and standard deviations of the optical properties of those layers are listed in table (4.2). The AOD was up to 0.027 and 0.018 at 355 and 532 nm, respectively. The lidar ratio at 355 nm was between 33 and 39 sr. The extinction related Ångström exponent varied strongly from layer to layer. Besides, the profile was noisy within the layers. The backscatter related Ångström exponent was between 0.9 and 1.5 with higher values in the lower layers.

Figure (4.31) shows  $\tau$  at 355 nm of all lidar measurements during night time between 21 UTC on 5 May 2010 until 5 UTC on 14 May 2010. The optical depth of each of the volcanic aerosol layers and the sum over all those layers are plotted. In the night between 5 and 6 May 2010  $\tau(355 \text{ nm})$  was very low. The detected free tropospheric volcanic aerosol layers were optically thin at that time. Much larger  $\tau(355 \text{ nm})$  could be observed during the following night, but also after 12 May 2010. During all night time lidar measurements, the sum of  $\tau(355 \text{ nm})$  of all layers with volcanic aerosol was highest at 0 UTC on 14 May 2010 ( $\tau(355 \text{ nm}) = 0.09$ ).

In figure (4.32) layer mean values of  $\hat{a}_\beta(355, 1064 \text{ nm})$  are shown for the whole period. The symbols are colour coded according to the mean height of the volcanic aerosol layers. During the first days of the episode, higher layers had generally lower  $\hat{a}_\beta(355, 1064 \text{ nm})$ . This indicates larger particles at higher altitudes. One exception was observed during the morning of 6 May 2010, when larger  $\hat{a}_\beta(355, 1064 \text{ nm})$  were detected in higher layers. This may indicate a descent of larger particles, which would result in smaller Ångström exponents in lower altitudes. The layer mean  $\hat{a}_\beta(355, 1064 \text{ nm})$  was similar for all layer altitudes after 10 May 2010. However, a temporal variation could be observed. The mean of  $\hat{a}_\beta(355, 1064 \text{ nm})$  of all volcanic aerosol layers during the whole period was  $0.8 \pm 0.5$ .

**Table 4.2.:** Optical properties of the volcanic aerosol layers at 5 UTC on 7 May 2010.<sup>a</sup>

$z / \text{ km agl}$	$\tau$ (355 nm)	$\tau$ (532 nm)	$S_{par} / \text{ sr}$ (355 nm)	$\hat{a}_\alpha$ (355, 532 nm)	$\hat{a}_\beta$ (355, 1064 nm)
2.05 – 2.62	0.021±0.001	0.018±0.003	39±3	0.4±0.3	1.5±0.2
3.57 – 3.96	0.018±0.003	0.009±0.003	36±7	1.9±0.5	1.4±0.4
4.11 – 4.56	0.027±0.001	0.014±0.002	34±6	1.6±0.3	1.3±0.1
4.80 – 4.92	0.005±0.001	0.003±0.001	33±5	1.6±0.2	0.9±0.1

<sup>a</sup> Layer bottom and top height, as well as mean values and standard deviations of the AODs, the lidar ratio and the Ångström exponents are given.

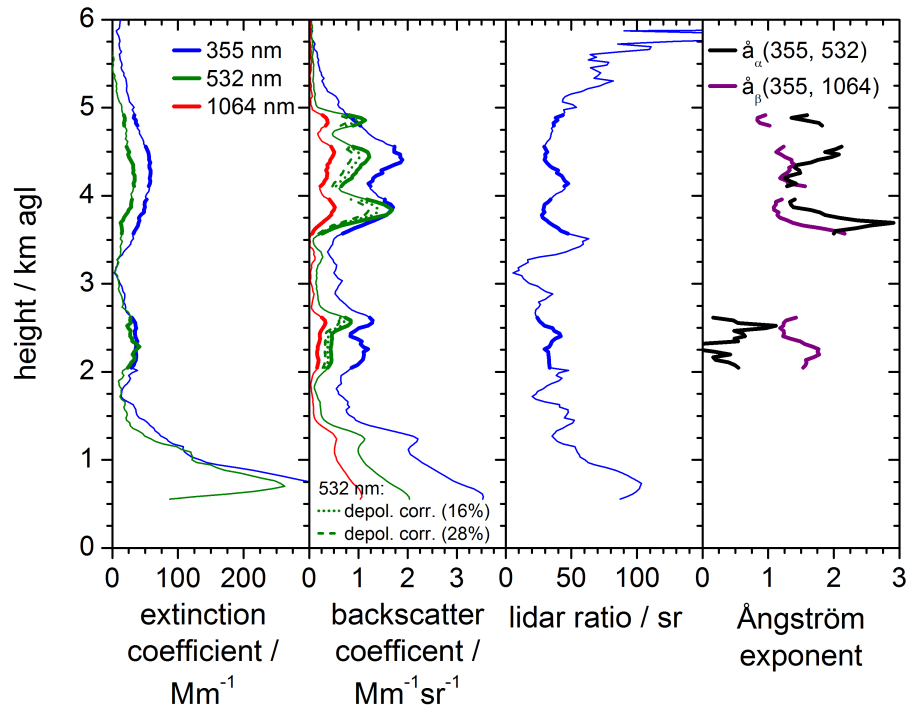


**Figure 4.30.:** Profiles of the particle extinction coefficient at 355 and 532 nm, the particle backscatter coefficient at 355, 532 and 1064 nm, the lidar ratio at 355 nm and the backscatter and extinction related Ångström exponents at the pair of wavelengths 355 and 1064 nm and 355 and 532 nm, respectively. The particle backscatter coefficient at 532 nm uncorrected (solid line), corrected for  $\delta_{par}(532 \text{ nm}) = 0.16$  (dashed) and for  $\delta_{par}(532 \text{ nm}) = 0.07$  (dotted). The data were averaged from 4:30 to 5:30 UTC on 7 May 2010.

#### 4. Aerosol characterisation results

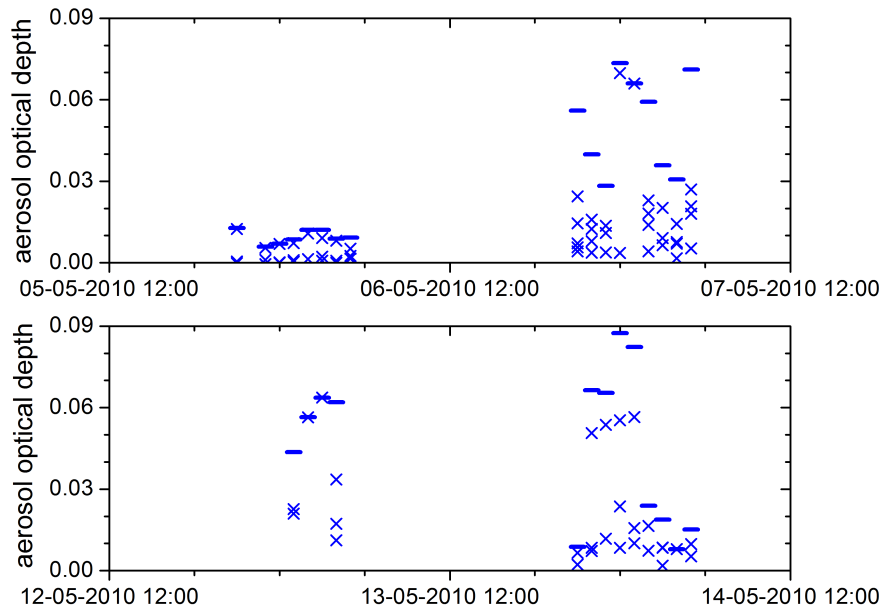


**Figure 4.31.:** Aerosol optical depth at 355 nm for single volcanic aerosol layers (crosses), and sum over the aerosol optical depth of those layers (lines). Plotted are night time data from 5 to 7 May 2010 (top) and 12 to 14 May 2010 (bottom).

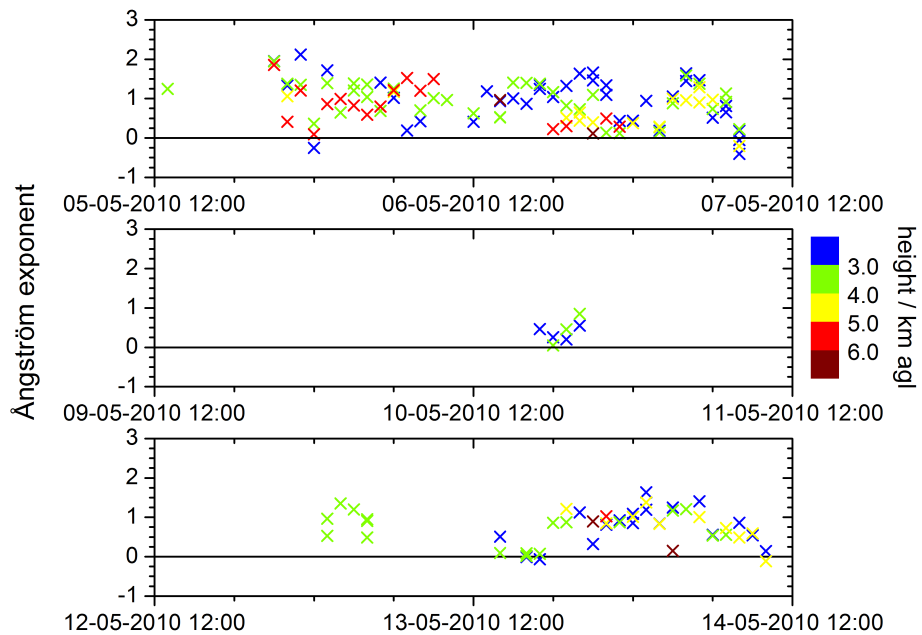


**Figure 4.32.:** Backscatter related Ångström exponent at the pair of wavelengths 355 and 1064 nm for single volcanic aerosol layers, colour coded with the mean height of the layer.

The mean extinction related Ångström exponent  $\hat{a}_\alpha$  (355, 532 nm) for all layers observed during night time was  $1.4 \pm 0.7$ . Those medium Ångström exponent values indicate no prominent existence of smaller or larger particles.

The lidar ratio at 355 nm for the night time measurements is shown in figure (4.33). Again, the symbols are colour coded as in figure (4.32). During the night from 5 to 6 May 2010 higher mean values of  $S_{par}$  (355 nm) were found for higher layers. In the night from 6 to 7 May 2010 and from 13 to 14 May 2010 this relation was reversed. The mean value of  $S_{par}$  (355 nm) of all volcanic aerosol layers observed during night time was  $(40 \pm 17)$  sr. The lidar ratios over Évora were significantly smaller than those found in central Europe in April. *Ansmann et al.* (2010) published mean lidar ratios of  $(55 \pm 5)$ sr and  $(60 \pm 5)$ sr, obtained from lidar measurements in Munich and Leipzig, Germany, respectively. This difference in the optical properties is another indicator for a change of aerosol characteristics, like their size and shape, during different periods of a volcanic eruption. The eruption with its different phases was described by *Gudmundsson et al.* (2012) and *Ilyinskaya et al.* (2011). Changes in the emission of ash and SO<sub>2</sub> during the eruption were also found by *Thomas and Prata* (2011), from the investigation of satellite data.

### 4.3.3. Exceptionally strong Saharan dust event, April 2011

A very strong plume of Saharan dust was observed over Évora from 4 to 9 April 2011. The lidar measurements were studied in combination with data from various other remote sensing instruments, like the sun photometer at CGE, MODIS and CALIOP, as well as from the ground based in-situ instruments APS, TEOM and nephelometer. Results were published and discussed extensively by *Preißler et al.* (2011a). An overview is given in the following.

#### Synoptical situation

Saharan dust outbreaks towards Portugal are usually linked to low pressure systems close to the north-western coast of Africa and over Morocco in combination with strong winds near the ground. On 4 April 2011 and the following days such a synoptic situation led to

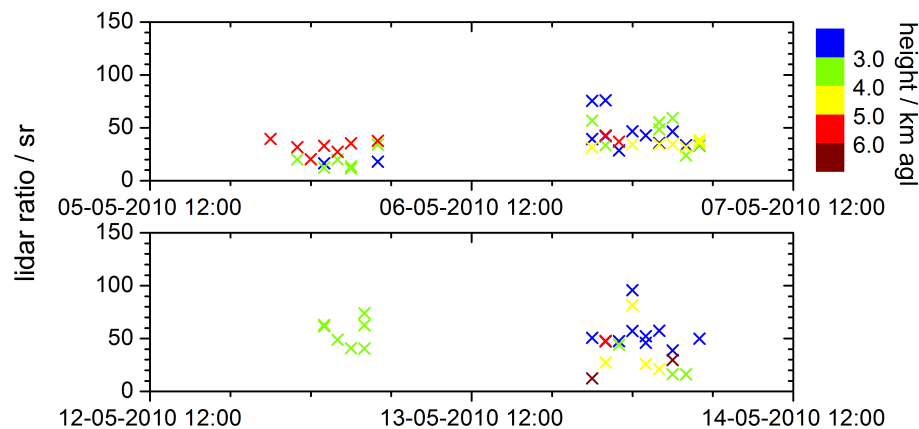


**Figure 4.33.:** Layer mean lidar ratio at 355 nm for single volcanic aerosol layers, colour coded with the mean height of the layer. Plotted are night time data from 5 to 7 May 2010 (top) and 12 to 14 May 2010 (bottom).

#### 4. Aerosol characterisation results

an intense emission of Saharan dust, originating in western Algeria and southern Morocco. The dust outbreak was predicted by DREAM. Until 6 April 2011, the low pressure system moved north-westward, advecting mineral dust partly over the Atlas Mountains towards south-western Spain and Portugal. The highest dust load was forecasted for Évora at 0 UTC on 6 April 2011.

##### Remote sensing measurements

The lidar data from five days of almost continuous measurements were averaged over one hour segments. The lowest 1 km agl of the PAOLI data was not used for this study, due to uncertainties in the region of incomplete overlap. Figure (4.34) shows the vertical distribution of mineral dust in the free troposphere as well as the height of the boundary layer. The layer mean particle extinction coefficient at 355 nm is indicated as well.

Data from PAOLI could not be compared directly to the  $\tau$  and  $\dot{a}$  from CIMEL and MODIS data. The lidar extinction profiles were noisy during daytime measurements, due to high background signal and low SNR. However, as shown in figure (4.35), the values of  $\tau$  around sunset and sunrise indicate a good agreement of PAOLI and CIMEL measurements. The highest total values of  $\tau$  in the free troposphere were observed with PAOLI between 1 and 2 UTC on 6 April 2011, with 1.8 and 1.9 at 355 and 532 nm, respectively. During that time, the layer mean values of  $\dot{a}_\beta$  (355, 532 nm),  $\dot{a}_\beta$  (532, 1064 nm) and  $\dot{a}_\alpha$  (355, 532 nm) were around 0. The layer mean  $S_{par}$  (355 nm),  $S_{par}$  (532 nm) and  $\delta_{par}$  (532 nm) were  $(57\pm 12)$ sr,  $(52\pm 12)$ sr and  $0.23\pm 0.05$ , respectively.

Considering all dust layers in the free troposphere during the whole dust period, the extinction related Ångström exponent was  $0.0\pm 0.2$ . The backscatter related Ångström exponents of all dust layers were slightly higher with  $0.4\pm 0.6$  and  $0.4\pm 0.2$ , at the pair of wavelengths 355 and 532 nm as well as 532 and 1064 nm, respectively. The extinction related Ångström exponent from PAOLI measurements were lower than the values from CIMEL data (not shown). This could be due to the different measurement methods of the two instruments. CIMEL provides columnar data, whereas PAOLI captures vertically resolved profiles. The lidar ratios averaged over the whole period were smaller than during the intense period between 1 and 2 UTC on 6 April 2011, with  $(45\pm 11)$ sr and  $(53\pm 7)$ sr

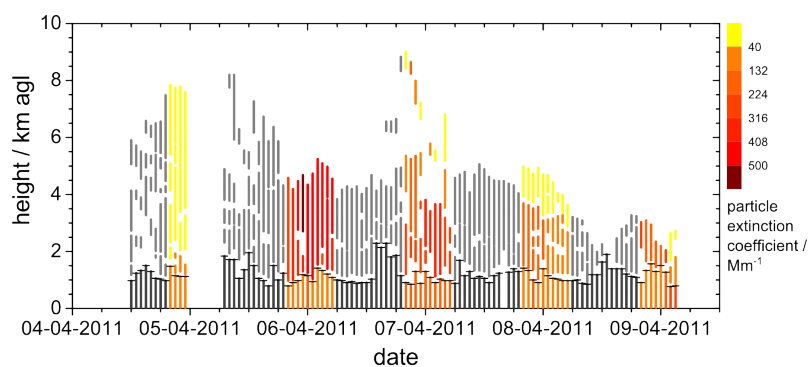


**Figure 4.34.:** Boundary layer (black) and vertical distribution of mineral dust layers in the free troposphere (grey) during daytime measurements. Night time data (between 21 and 5 UTC) are colour coded with the layer mean particle extinction coefficient at 355 nm (on a logarithmic scale).

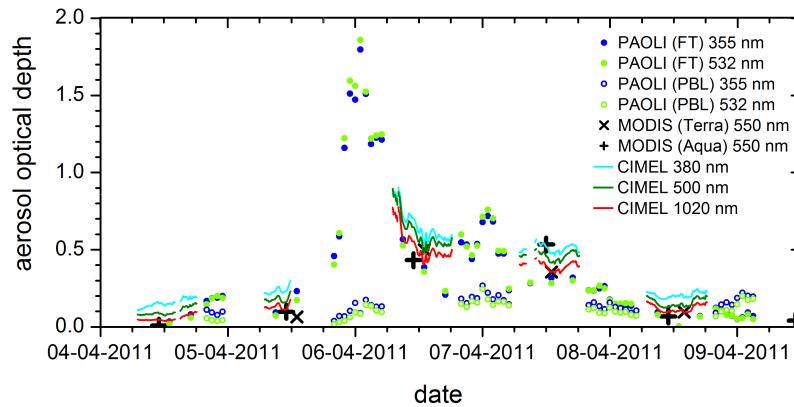


**Figure 4.35.:** Aerosol optical depth from columnar measurements of CIMEL (lines) and MODIS (crosses and plusses), as well as optical depth of the free tropospheric dust layer (FT) and the boundary layer (PBL) from PAOLI measurements (dots and circles, respectively). (*Preißler et al. (2011a), figure 4b*)

at 355 and 532 nm, respectively. The mean linear particle depolarisation ratio of all dust layers at all investigated times was  $0.28 \pm 0.04$ .

A comparison with CALIOP data was done as well. The minimum ground track distance of the overpass of CALIPSO on 7 April 2011 was about 160 km. To ensure the investigation of the same fraction of the dust plume, HYSPLIT forward trajectories starting from the crossing point of the plume with the ground track of CALIPSO were calculated. Consequently, CALIOP data from 13:42 UTC on 7 April 2011 were compared to PAOLI data measured between 20 and 21 UTC on 7 April 2011. Profiles of the optical particle properties are presented in figure (4.36). The particle backscatter coefficient profiles at 532 and 1064 nm obtained by both lidar systems, showed very good agreement. The dust layer mean  $\Delta\beta$ , with  $\beta_{par}$  from PAOLI as reference, was -6% and 1% at 532 and 1064 nm, respectively. However, the assumption of a constant lidar ratio of 40 sr by the CALIOP data analysis algorithm led to a large underestimation in the particle extinction coefficient. This would subsequently result in an underestimation of the aerosol optical depth as well. *Pappalardo et al. (2010)* investigated, over a period of more than two years,  $\Delta\beta$  from CALIOP with data from ground-based EARLINET lidars as reference and found a mean relative difference of 4.6% at 532 nm.

### Ground based in-situ observations

In figure (4.37) an overview over the dust observations near the surface is given. The main intrusion of dust into the PBL was detected by PAOLI at around 14 UTC on 6 April 2011 (compare figure (4.34)). This time is indicated in figure (4.37) with a vertical line. The Ångström exponent from scattering coefficients at 450 and 700 nm was smaller than 0.5 until the afternoon of 7 April 2011. Such low values indicate a strong contribution of large mineral dust particles to the aerosol load. In the afternoon of 7 April 2011, the values increased. From the early morning of 9 April 2011 the Ångström exponent was higher than 1. This indicated a change from a dominant fraction of large particles to a higher contribution of small particles.

The particle mass concentration  $M$  hints at mixing of dust into the PBL in the morning

#### 4. Aerosol characterisation results

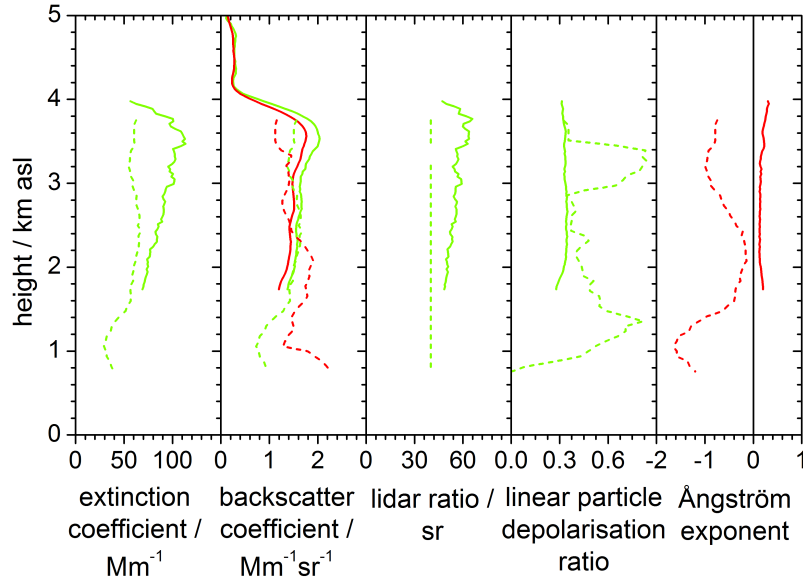


**Figure 4.36.:** Profiles of the particle extinction coefficient at 532 nm, the particle backscatter coefficient at 532 and 1064 nm, the lidar ratio at 532 nm, the linear particle depolarisation ratio at 532 nm and the backscatter related Ångström exponents at the pair of wavelengths 532 and 1064 nm; from PAOLI (solid) between 20 and 21 UTC and from CALIOP (dashed) at 13:42 UTC on 7 April 2011. (Preißler *et al.* (2011a), figure 5)

of 5 April 2011.  $M$  increased from background values below  $20 \mu\text{g m}^{-3}$  at midnight to values of about  $50 \mu\text{g m}^{-3}$  around noon. Within the same time period, the ratio of the coarse and fine mode number concentration  $N_{coarse}/N_{fine}$  increased. However, a stronger and steeper increase was detected during 6 April 2011. Maximum mass concentration values of  $162 \mu\text{g m}^{-3}$  were observed in the afternoon of 6 April 2011. The ratio  $N_{coarse}/N_{fine}$  reached the maximum value of 1.13 at the same time.

The mass scattering efficiency  $E_s$  at 550 nm was between 0.5 and  $1.2 \text{ m}^2 \text{ g}^{-1}$ . Similar mass scattering efficiencies for desert dust periods observed in Évora were published by Pereira *et al.* (2008). Comparable values of  $E_s$  for desert dust around 1 were found by Formenti *et al.* (2001) in South America and by Alfaro *et al.* (2003) in Asia.

The annual median value of the particle mass concentration in Évora is about  $20 \mu\text{g m}^{-3}$  (Pereira *et al.*, 2008) and the median value of the scattering coefficient  $\sigma_s(550 \text{ nm})$  about  $30 \text{ Mm}^{-1}$  (Pereira *et al.*, 2011). Hence, the aerosol concentration during the period of highest dust load was about four times higher, and the scattering coefficient more than two times higher than in typical conditions in Évora. During the dust outbreak studied here, the daily threshold of  $50 \mu\text{g m}^{-3}$ , imposed by the air quality legislation in Europe (2008/50/EC)(European Parliament, 2008), was exceeded on three consecutive days (6 to 8 April 2011) with mean values and standard deviations of  $(65 \pm 36)\mu\text{g m}^{-3}$ ,  $(75 \pm 13)\mu\text{g m}^{-3}$  and  $(55 \pm 17)\mu\text{g m}^{-3}$ , respectively.

#### 4.3.4. Volcanic aerosol from Nabro, June 2011 to February 2012

The eruption of Nabro ( $13.37^\circ \text{ N}$ ,  $41.70^\circ \text{ E}$ ), Eritrea, starting on 12 June 2011, injected large amounts of  $\text{SO}_2$  into the stratosphere. The eruption plume rose higher than

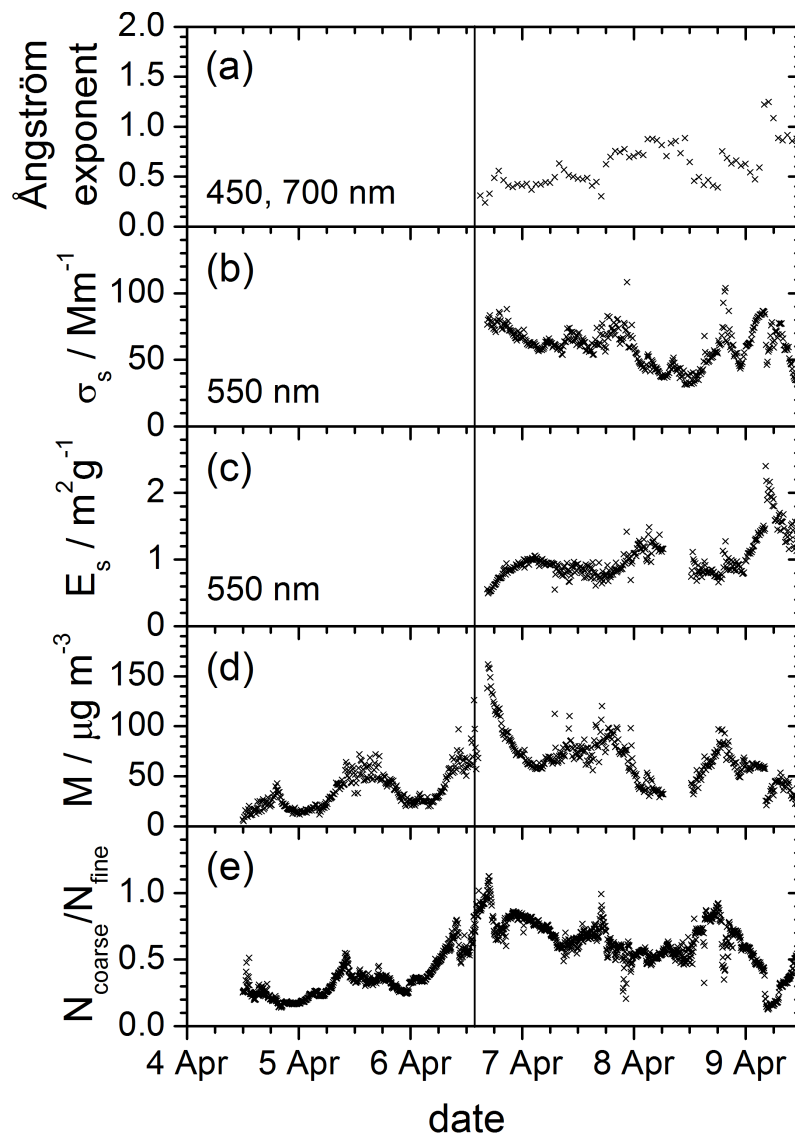


**Figure 4.37.:** Results of ground-based in-situ measurements: (a) 1-hour averages of the Ångström exponent from scattering coefficients at 450 and 700 nm; (b) 10-min averages of the scattering coefficient  $\sigma_s$  at 550 nm; (c) mass scattering efficiency  $E_s$  at 550 nm; (d) particle mass concentration  $M$ ; (e) ratio  $N_{\text{coarse}}/N_{\text{fine}}$ . The vertical line at 14 UTC on 6 April 2011 marks the main intrusion of dust into the PBL observed by PAOLI (Preißler *et al.* (2011a), figure 2)

#### 4. Aerosol characterisation results

13 km asl (*Smithsonian Institution*, 2012). The stratospheric layer resulting from this eruption spread towards western and northern Africa. It was first detected over Europe on 23 June 2011 (*Sawamura et al.*, 2012), and over the Iberian Peninsula and the Canary Islands on 26 June 2011 (*Guerrero-Rascado et al.*, 2012a). In Évora, stratospheric aerosol could be observed from 26 June 2011 as well. A stratospheric layer was detected until February 2012. However, it is possible, that meanwhile other volcanic eruptions on the northern hemisphere or strong forest fires contributed to the aerosol load in the stratosphere. The eruption of Shiveluch (56.39° N, 161.21° E), Central Kamchatka, Russia produced maximum plume heights from 9.0 to 10.6 km asl between 3 and 23 October 2011 (*Smithsonian Institution*, 2012). According to GDAS model sounding data, the tropopause height over Kamchatka was around 9 km asl at this time. Therefore, a contribution from this volcano is likely.

An overview over the lidar measurements in the framework of SPALINET during the first weeks after the eruption of Nabro was presented by *Guerrero-Rascado et al.* (2012a). A more detailed study of the lidar observations in Évora was done by *Wagner et al.* (2012). The applied methodology was published by *Wagner and Preißler* (2012).

The vertical distribution of the stratospheric layer from 26 June 2011 to 25 February 2012 is shown in figure (4.38). The tropopause height from GDAS model sounding data is plotted as well. The height resolution of the GDAS model is small in high altitudes, which results in large uncertainties in the determination of the tropopause height. In June 2011, the aerosol was concentrated between 15 and 19 km asl. The plume diverged strongly during the subsequent months. From the end of November 2011 the bottom of the plume was lower than the tropopause. Sinking of the volcanic aerosol or contributions from other aerosol sources could be the reason for this.

Optical properties of the plume were derived from a night time measurement conducted on 29 June 2011. The data were averaged over more than two hours. The signal was strong enough for the determination of the profiles of  $\beta_{par}$  at all wavelengths. However, the SNRs of the Raman signals were too low to obtain profiles of  $\alpha_{par}$ . The analysis could not be improved by longer vertical or temporal averaging. The profiles of the particle backscatter coefficients measured between 1:45 and 4:00 UTC on 29 June 2011 are shown

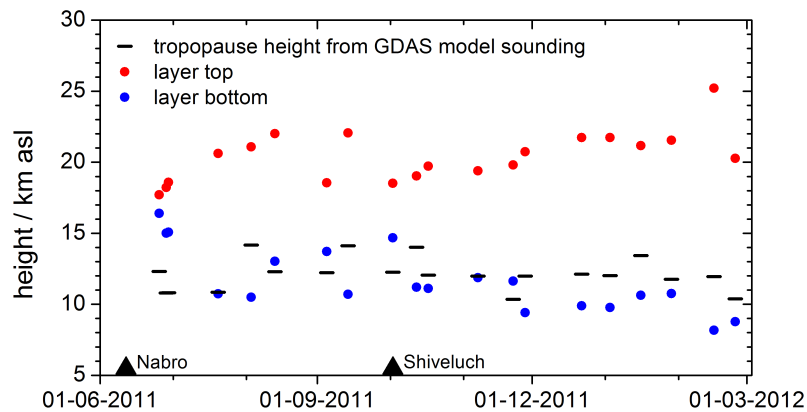


**Figure 4.38.:** Bottom (blue) and top (red) height of the stratospheric aerosol layer obtained from lidar measurements and tropopause height (black lines) from GDAS model sounding from 26 June 2011 to 25 February 2012. The black triangles mark the beginning of the eruptions of Nabro on 12 June 2011 and of Shiveluch on 3 October 2011.

in figure (4.39). Two layers were observed during this period. The layer boundaries and the optical properties found for those layers are shown in table (4.3). The total integrated  $\beta_{par}$  in the stratosphere was  $14 \times 10^{-4} \text{ sr}^{-1}$ ,  $6 \times 10^{-4} \text{ sr}^{-1}$  and  $4 \times 10^{-4} \text{ sr}^{-1}$  at 355, 532 and 1064 nm, respectively. *Deshler* (2008) published an overview over long term observations of stratospheric aerosols with different lidar systems operating between 532 and 694 nm. After the eruption of Mount Pinatubo, the integrated particle backscatter coefficient increased to approximately  $40 \times 10^{-4} \text{ sr}^{-1}$  at two mid-latitude stations. It was almost one order of magnitude higher than observed by PAOLI after the Nabro eruption. The background values presented by *Deshler* (2008) for different observation sites were about  $0.3 \times 10^{-4} \text{ sr}^{-1}$  from the late nineties until 2007. This was more than one order of magnitude smaller than the values observed by PAOLI after the Nabro eruption.

The mean  $\hat{a}_\beta$  (355, 532 nm) was high, indicating a large contribution of small particles. The linear particle depolarisation ratios were small. This hints at plumes of spherical particles. The layer mean  $\hat{a}_\beta$  and  $\delta_{par}$  were equal in both layers.

#### 4.3.5. Free tropospheric aerosol layers observed in Évora and Granada

Combining lidar measurements from different stations gives information on the horizontal distribution of aerosols. In the framework of EARLINET and SPALINET various such studies were conducted before, for example by *Ansmann et al.* (2003); *Balis et al.* (2006); *Wang et al.* (2006) and *Sicard et al.* (2012). Within this study, lidar measurements at the Andalusian Center for Environmental Research (Centro Andaluz de Medio Ambiente) (CEAMA) ( $37.16^\circ \text{ N}$ ,  $3.6^\circ \text{ W}$ , 680 m asl) in Granada (GR), Spain, were combined with correlative measurements from PAOLI in Évora (EV). The distance between both stations is about 410 km. CEAMA is a member of EARLINET and AERONET as well. Therefore, also sun photometer data could be included in those studies. Some results were presented by *Preißler et al.* (2012a,b).

The lidar at CEAMA is a model LR331D400 from Raymetrics S.A., Greece. As PAOLI, it is measuring at 355, 387, 532, 607 and 1064 nm, but furthermore at 408 nm. It detects the depolarisation at 532 nm by measuring the parallel and perpendicular polarised signal.

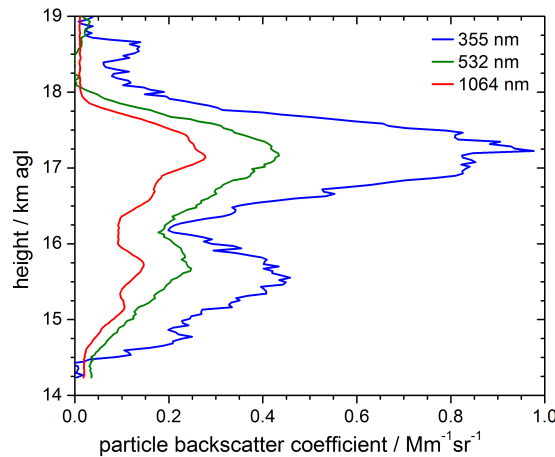


**Figure 4.39.:** Particle backscatter coefficients at 355 nm (blue), 532 nm (green) and 1064 nm (red), measured between 1:45 and 4:00 UTC on 29 June 2011.

#### 4. Aerosol characterisation results

**Table 4.3.:** Optical properties of the stratospheric aerosol layers observed between 1:45 and 4:00 UTC on 29 June 2011.<sup>a</sup>

	unit	$\lambda$	layer 1	layer 2
$z$	km agl		14.69 – 15.82	16.45 – 17.89
int. $\beta_{par}$	sr <sup>-1</sup>	355 nm	0.0004	0.0010
int. $\beta_{par}$	sr <sup>-1</sup>	532 nm	0.0002	0.0005
int. $\beta_{par}$	sr <sup>-1</sup>	1064 nm	0.0001	0.0002
$\dot{a}_{\beta}$		355, 532 nm	1.9±0.4	1.8±0.4
$\dot{a}_{\beta}$		532, 1064 nm	1.3±0.1	1.3±0.1
$\delta_{par}$		532 nm	0.019±0.002	0.019±0.002

<sup>a</sup> Layer bottom and top height, integrated particle backscatter coefficients, as well as layer mean values and standard deviations of the Ångström exponents and linear particle depolarisation ratio are given.

The height resolution of this instrument is with 7.5 m higher than the vertical resolution of PAOLI (30 m). For this study, data were averaged over 30 min. Measurements from the two sites with temporal coincidence were analysed. Therefore, not the same fractions of the aerosol plumes were investigated.

This study is focused on night time measurements taken during the year 2011 in order to take advantage of the full capabilities of both multi-wavelength Raman lidars. In total, PAOLI observed free tropospheric aerosol layers in about 50 night time measurements during this year. However, only 9 of those measurements were in temporal coincidence with measurements in Granada, from which two selected cases are presented in the following. A forest fire smoke plume was observed in June 2011. It originated in North America and provided information on the horizontal distribution of free tropospheric aerosol after a long transportation path. The distance between Évora and Granada was very short compared to the long range between the two continents. Therefore, no great differences were expected between the parts of the plume detected at both stations. Additionally, a Saharan dust event, also in June 2011 was studied. Compared to the smoke case, the transport path and time was much shorter and the distance between the two stations was relatively long. Besides, atmospheric aerosols are most variable close to their source. Therefore, larger inhomogeneities between observations in Évora and Granada were likely in this case.

#### Smoke from North America, 13 June 2011

A free tropospheric aerosol layer was detected by both lidars between 4 and 7 km asl on 13 June 2011. Since the beginning of June 2011 a strong low pressure system over the northern Atlantic ocean favoured the advection of air masses from North America towards the Iberian Peninsula. According to the ten day back trajectories arriving at the layer altitude (see figures (4.40) and (4.41)), possible source regions were the south-west of the USA and the Atlantic Ocean between the Caribbean Sea and the Cape Verde Islands. Over the Atlantic Ocean, the aerosol could be sea salt, anthropogenic pollution from ships

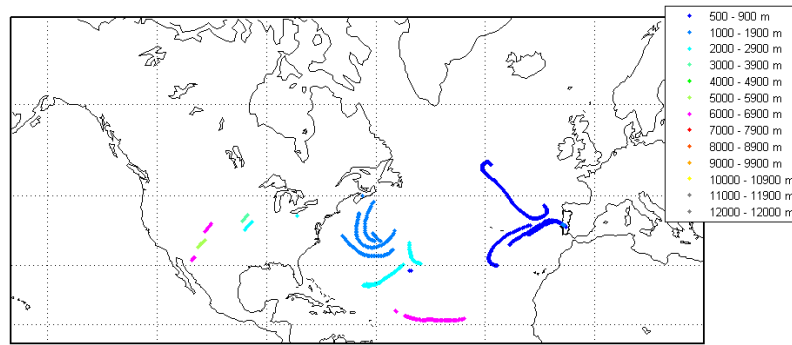


**Figure 4.40.:** Fractions of back trajectories with boundary layer contact arriving over Évora at 21 UTC on 13 June 2011.

or dust from the Sahara, which was transported westward before turning north-eastward. Considering the aerosol model NAAPS for the source region over North America, smoke was the largest contributor. The fire detection by MODIS found fires in Arizona, USA. In figure (4.42) images of the visible composite of MODIS and of Landsat are shown. On the MODIS image from 8 June 2011, a large smoke plume is visible, originating in the east of Arizona and drifting north-eastward. The Landsat image from 7 June 2011 shows the burnt area.

Mean values of the optical properties obtained from lidar measurements between 20:30 and 21:00 UTC on 13 June 2011 are given in table (4.4), at the end of this section. Layer mean  $S_{par}$  and the layer optical depth at 355 nm were similar at both sites. Over Évora, higher  $S_{par}$  at 532 nm than at 355 nm were found in the free tropospheric aerosol layer. A similar behaviour was found for aged Siberian biomass burning smoke by Müller *et al.* (2005). At both sites, low values of  $\delta_{par}$  between 3 and 6% were observed, which indicates mainly spherical particles. The columnar  $\hat{a}_\tau$  from sun photometer measurements was smaller over Évora. This could be due to less small anthropogenic particles within the PBL. In the urban area of Granada, such particles can be expected in higher concentration than in the rural region of Évora. The layer mean  $\hat{a}_\alpha$  was in the range of values published by Müller *et al.* (2005) for aged biomass burning smoke, between 0.0 and 1.3. Over Granada, the layer mean  $\hat{a}_\beta$  (355, 532 nm) was higher than over Évora. This would imply

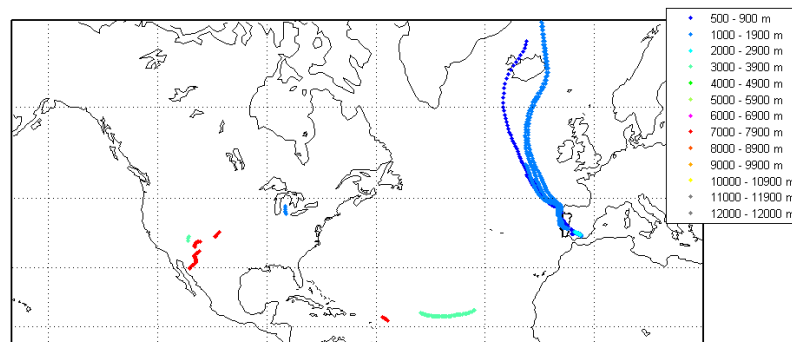


**Figure 4.41.:** Fractions of back trajectories with boundary layer contact arriving over Granada at 21 UTC on 13 June 2011.

#### 4. Aerosol characterisation results

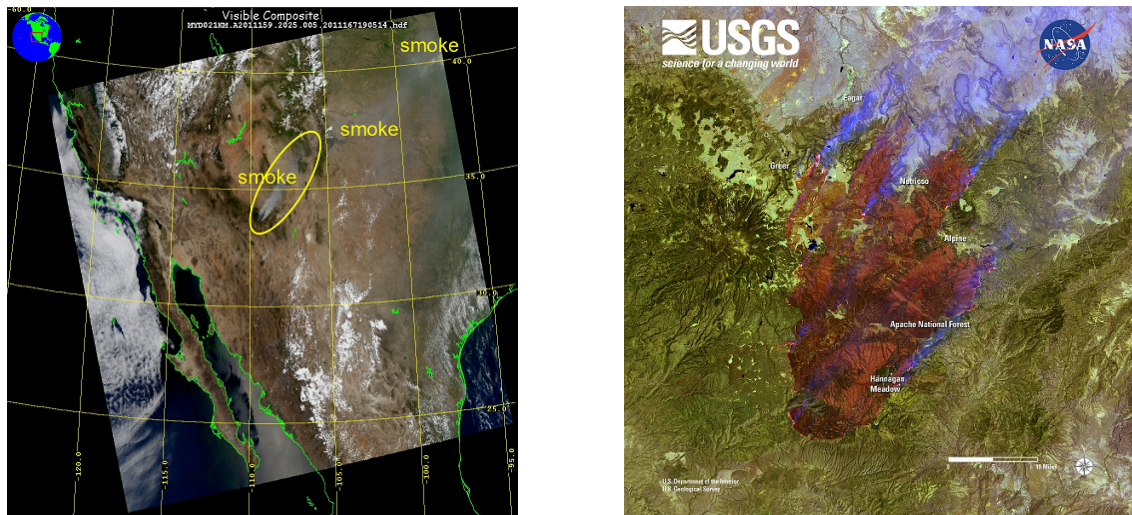


**Figure 4.42.:** Satellite images from MODIS (left) and Landsat (right, centred at 33.84° N, 109.33° E) on 8 and 7 June 2011, respectively.

a larger contribution of small particles over Granada. As  $\hat{a}_\alpha$  and  $\hat{a}_\beta$  (532, 1064 nm) from Granada were not available, the significance of the high  $\hat{a}_\beta$  (355, 532 nm) could not be verified.

#### Saharan dust, 27 June 2011

A Saharan dust event started on 24 June 2011 and lasted several days. It was related to a low pressure system on the north-western coast of Africa. For this study, lidar measurements from 0:00 to 0:30 UTC (GR) and from 0:10 to 0:40 UTC (EV) on 27 June 2011 were analysed. At this time, the dust layer detected over Évora was as high as 5 km asl and slightly lower over Granada. The back trajectories with boundary layer contact arriving over Évora and over Granada are shown in figures (4.43) and (4.44), respectively. According to those trajectories, the aerosol layers mainly originated in the Saharan desert. Some contribution from the Mediterranean Sea and its coastal areas were likely as well. Air masses from North America and the Sahara were transported towards the southern

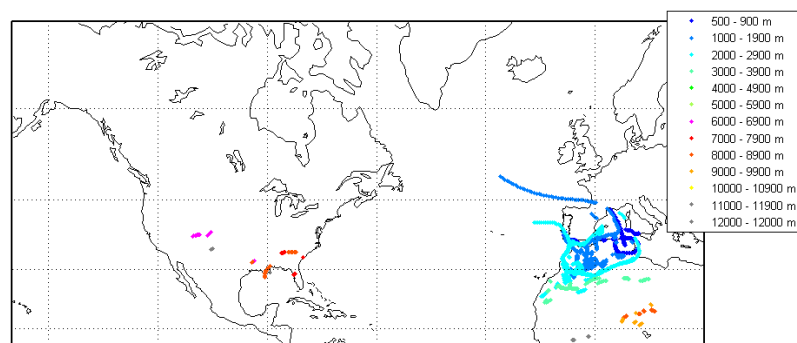


**Figure 4.43.:** Fractions of back trajectories with boundary layer contact arriving over Évora at 0 UTC on 27 June 2011.

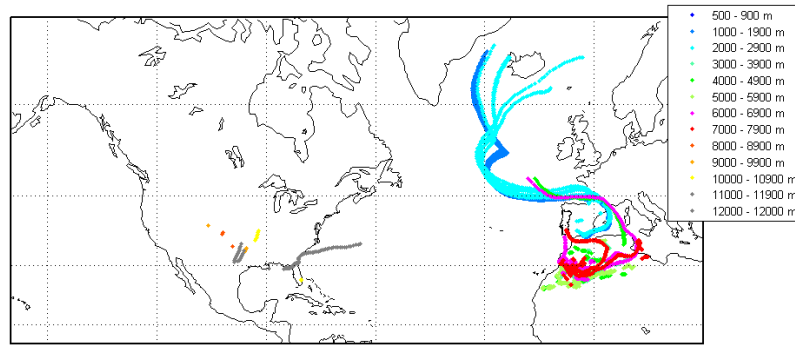


**Figure 4.44.:** Fractions of back trajectories with boundary layer contact arriving over Granada at 0 UTC on 27 June 2011.

Iberian Peninsula in higher altitudes. However, no aerosol was observed in those height ranges. The air masses observed between 1 and 3 km asl over Granada were additionally influenced by the northern Atlantic Ocean.

Profiles of the optical properties obtained from the lidar measurements on 27 June 2011 are shown in figure (4.45). Layer mean values of the optical properties found at both sites are listed in table (4.4). The altitudes of the layer boundaries agreed well. However,  $\tau$  of the upper layer at 355 and 532 nm and  $S_{par}$  of both layers at both wavelengths were slightly smaller over Évora. Smaller  $S_{par}$  indicate less absorbing material. A mixture of dust observed over Granada with stronger absorbing anthropogenic aerosol could be an

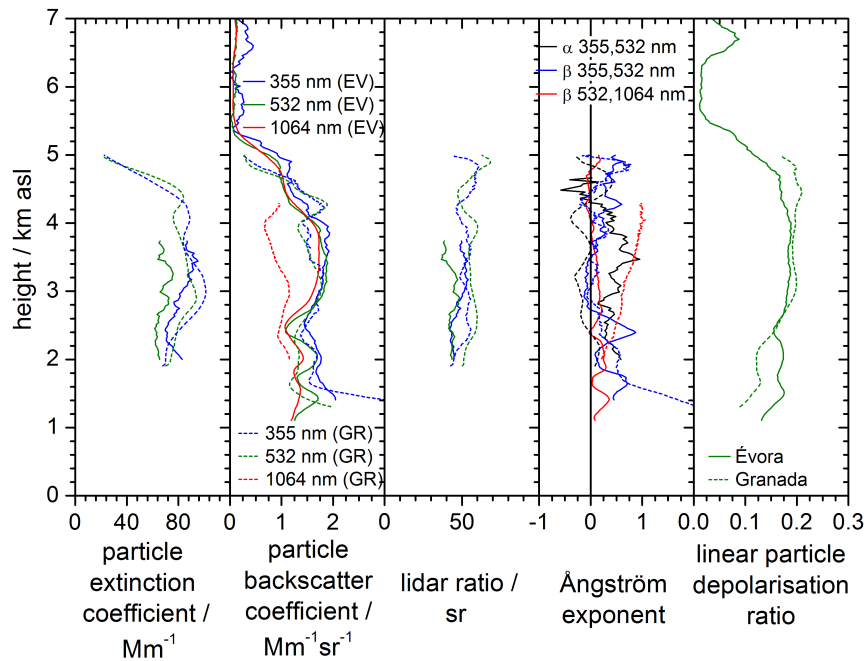


**Figure 4.45.:** Profiles of the particle extinction and backscatter coefficients, lidar ratios, Ångström exponents and linear particle depolarisation ratios observed over Évora (EV, solid lines) and over Granada (GR, dashed lines) on 27 June 2011. Data were averaged from 0:00 to 0:30 UTC (GR) and from 0:10 to 0:40 UTC (EV).

#### 4. Aerosol characterisation results

explanation for those differences. The layer mean  $\delta_{par}$  were between 12 and 19%. Those elevated values over both stations indicate rather non-spherical particles, as expected for desert dust. Over Granada,  $\delta_{par}$  of the lower layer was smaller than over Évora. In the upper layer,  $\delta_{par}$  was higher over Granada than over Évora. Differences in aerosol optical properties were most likely caused by different transportation paths and mixing of other aerosol types into the Saharan dust layer. The values of  $\dot{a}_\alpha$  and  $\dot{a}_\beta$  were comparable at both sites. The small values between -0.1 and 0.8 indicate a high contribution of large particles, which is typical for mineral dust. In a study of a Saharan dust outbreak observed over various EARLINET stations all over Europe, *Ansmann et al.* (2003) found  $\delta_{par}$ ,  $\dot{a}$  and  $S_{par}$  in the ranges from 15 to 25%, -0.5 to 0.5, and 40 to 80 sr, respectively.

**Table 4.4.:** Aerosol layer heights and optical aerosol properties.<sup>a</sup>

site	height / km (asl)	$\tau$		$S_{par}$ / sr		$\hat{a}_\alpha, \hat{a}_\tau^b$		$\hat{a}_\beta$		$\delta_{par}$ 532 nm
		355 nm	532 nm	355 nm	532 nm	355, 532 nm	532, 1064 nm			
<i>13 June 2011: 20:30 to 21:00 UTC</i>										
EV	column <sup>c</sup>	0.15	0.09			1.13±0.02				
EV	4.75 – 5.50	0.01						1.6±0.2	1.8±0.2	0.03±0.01
EV	5.77 – 6.64	0.03	0.02	46±14	66±19	0.9±0.5		1.3±0.5	1.4±0.3	0.06±0.02
GR	column <sup>c</sup>	0.14	0.08			1.50±0.01				
GR	5.42 – 7.01	0.03		40±5				1.9±0.3		0.04±0.01
<i>27 June 2011: 0:00 to 0:30 UTC</i>										
EV	1.74 – 2.18	0.04	0.03	45±1	43±1	0.5±0.1		0.2±0.2	0.2±0.1	0.17±0.01
EV	2.51 – 5.02	0.16	0.14	44±9	39±5	0.4±0.3		0.2±0.2	0.1±0.1	0.17±0.02
GR	1.73 – 2.21	0.02	0.02	46±2	52±1	0.1±0.1		0.5±0.1	0.3±0.1	0.12±0.01
GR	2.40 – 4.73	0.19	0.20	53±3	56±4	-0.1±0.2		0.1±0.1	0.8±0.2	0.19±0.01

<sup>a</sup> Layer mean values and standard deviations of the optical properties are shown.<sup>b</sup> Calculated from  $\tau$  from sun photometer data averaged over 30 min before sunset on 13 June 2011.<sup>c</sup> Columnar data from sun photometer measurements averaged over 30 min before sunset on 13 June 2011.

## 4.4. Climatology

In the framework of EARLINET, three regular weekly measurements are performed, on Mondays in the afternoon and after sunset as well as on Thursdays after sunset. Besides, measurements are conducted correlative to overpasses of the satellite CALIPSO with the lidar CALIOP aboard (*Winker et al.*, 2007) about six times per month. Furthermore, desert dust events, forest fire smoke or volcanic aerosol plumes are monitored by the network whenever possible. For this study, the regular EARLINET observations performed at CGE during more than two years (September 2009 to October 2011) have been investigated. Aerosol layers in the free troposphere and in the lower stratosphere were characterised in terms of their vertical distribution over Évora as well as their optical properties. A climatology of free tropospheric aerosol layers observed in 2010 was presented by *Preißler et al.* (2011b).

The regular measurement schedule of EARLINET assures statistical results unbiased by so-called special events, i.e. periods of high aerosol load caused, for example, by desert dust outbreaks, volcanic eruptions or forest fires. Such special events often lead to more intense observation periods and consequently to more data. On the other hand, lidar observations of aerosols in the free troposphere and lower stratosphere are not possible in case of rain or low clouds. Therefore, statistical results from lidar data are always biased by the weather conditions.

In principle, one third of the regular EARLINET measurements were performed during daytime, on Mondays at noon. Then, the determination of the particle extinction coefficients and the subsequent optical properties was not possible due to a high background signal and consequently a low SNR. Also, the particle backscatter coefficients could not be obtained for all wavelengths at times. For those reasons, layer mean aerosol optical properties shown in sections (4.4.1) and (4.4.2) were mostly calculated from a smaller number of layers than the total one. Besides, the number may also vary from one optical property to the other.

All aerosol layers in the free troposphere and lower stratosphere observed during the regular measurements between September 2009 and October 2011 were analysed regarding their geometrical properties, layer bottom and top height. Besides, layer mean optical properties were calculated. The aerosol origin was determined using the source identification procedure described in section (4.2.5). A classification in seven aerosol types was done, regarding their source region and the origin: European anthropogenic aerosol (EUR), North American anthropogenic aerosol (NAA), Iberian biomass burning smoke (IBF), biomass burning smoke from North America (NAF), mineral dust (DUS) with subdivision into Saharan dust (SD) and Asian dust (AD), aerosol of volcanic origin (VOL) with subdivision into volcanic aerosol from Eyjafjallajökull (EYJ) and volcanic aerosol from Nabro (NAB) and aerosol from the Atlantic (ATL). All layers, which could not be assigned to one of the categories above, were classified as aerosol of unknown origin (UNK).

Anthropogenic aerosol mainly originates from industrial and urban pollution and traffic emissions. In the free troposphere, this aerosol type can be transported towards southern Portugal from industrial and densely populated regions in Europe or North America. Anthropogenic aerosols from the industrial area around Lisbon could be advected to Évora as well. Biomass burning aerosols are caused by wild fires or by controlled agricultural burns. Wild fires can occur frequently on the northern Iberian peninsula during the dry season (May to September). In North America fires can arise from Canada to Mexico

along the year. It then depends on the meteorological situation, if the smoke caused by those fires is transported towards Évora. Possible oceanic aerosol sources included in ATL are, among others, sea spray and ship emissions. However, the ocean is not necessarily the source of the aerosol layers assigned to this type. In such cases, the ten day back trajectories indicated a long transportation path within the boundary layer over the Atlantic. The aerosol might have been older than ten days. However, it was assumed that the aerosol was affected by the ocean, due to the long residence time within the boundary layer. If the ten day back trajectories had no boundary layer contact within a potential aerosol source region, the aerosol layer was assigned to UNK. In such cases the duration of the trajectories was too short. It is also possible, that the trajectory uncertainties prevented a clear assignment of a source region.

All aerosol layers above the PBL observed during regular EARLINET measurements between September 2009 and October 2011 are shown in figure (4.46), including their origin. The not performed regular measurements are indicated as well in figure (4.46). The main reasons for missing measurements were low clouds and rain (46%) and technical problems (38%). In total, 74% of all scheduled regular measurements were performed, which were 247 during the studied time period. In 106 of those measurements, no aerosol layers were detected above the PBL. In total 252 layers in the free troposphere and lower stratosphere were observed during the remaining 141 measurements. Between May and October 87% of the scheduled measurements could be done. During the remaining months, 60% were possible. The studied aerosol layers were generally detected in higher altitudes during the summer months. Also more layers have been observed then. However, more measurements had to be cancelled during winter due to unfavourable weather conditions.

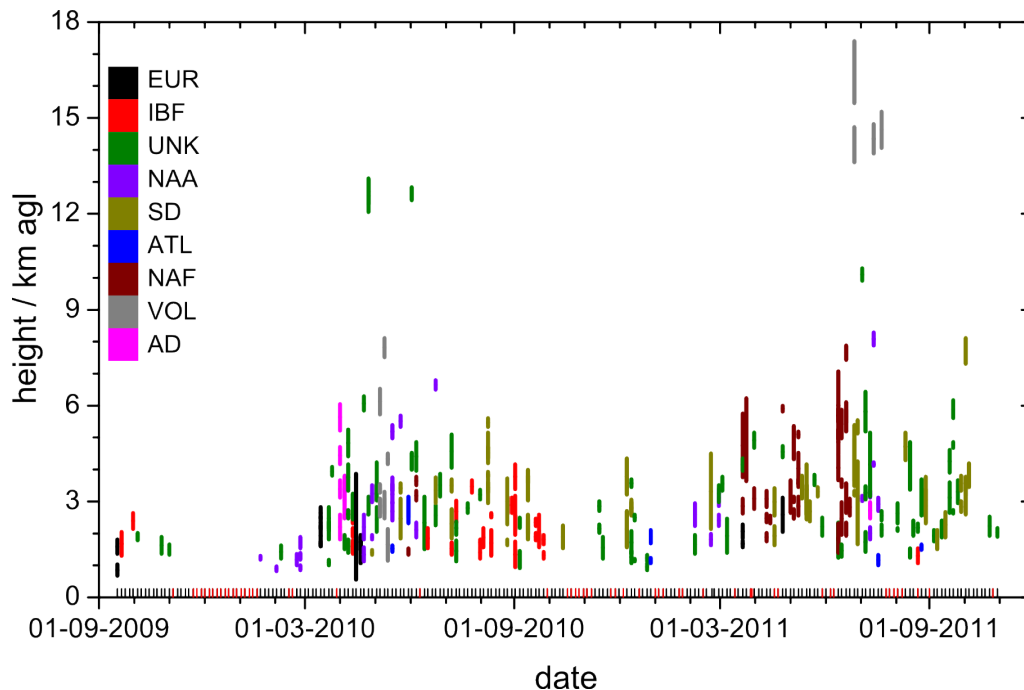


**Figure 4.46.:** Vertical and temporal distribution of aerosol layers in the free troposphere and lower stratosphere, colour coded according to their origin. On the bottom, performed (black) and missing (red) scheduled measurements are marked with vertical bars.

#### 4. Aerosol characterisation results

A more detailed study on the seasonal variation is presented in section (4.4.1). The characterisation of the different aerosol types is given in section (4.4.2). In section (4.4.3), the climatology study is briefly summarised.

##### 4.4.1. Seasonal characterisation

In this section, data from November 2009 to October 2011 were analysed. Two full years were studied. Data from September and October 2009 were not included in order not to bias the seasonal statistics. The number of layers per aerosol type detected during the four seasons is plotted in figure (4.47). Besides, the total number of layers per aerosol type is given. The origin of 79 layers could not be determined. Those 31% of all observed layers were assigned to the class UNK. Most layers, which could be assigned to a source region, were dust layers (DUS). They were observed in all four seasons, but mainly during spring (March, April, May (MAM)) and summer (June, July, August (JJA)). Biomass burning smoke from the Iberian peninsula (IBF) was not observed in winter (December, January, February (DJF)), which is generally the wet and cold season in south-western Europe. Also in spring, only few IBF layers were detected. However, many smoke layers from biomass burning in North America (NAF) were detected in spring and summer. This type of aerosol was not observed in autumn (September, October, November (SON)) or winter. Anthropogenic aerosol from North America (NAA) was also not detected in autumn. Such layers were found in the free troposphere over Évora during spring, summer and winter. Considering the back trajectories, there were air masses transported from North America towards Évora during all seasons. However, no aerosol layers from North American sources were detected during autumn. One reason for this could be less emission, which might be true for biomass burning aerosol, but is unlikely for anthropogenic aerosol. More likely causes are a reduced efficiency in lifting of the aerosols into the free troposphere or a meteorological pattern which favours the wet or dry deposition of the particles before

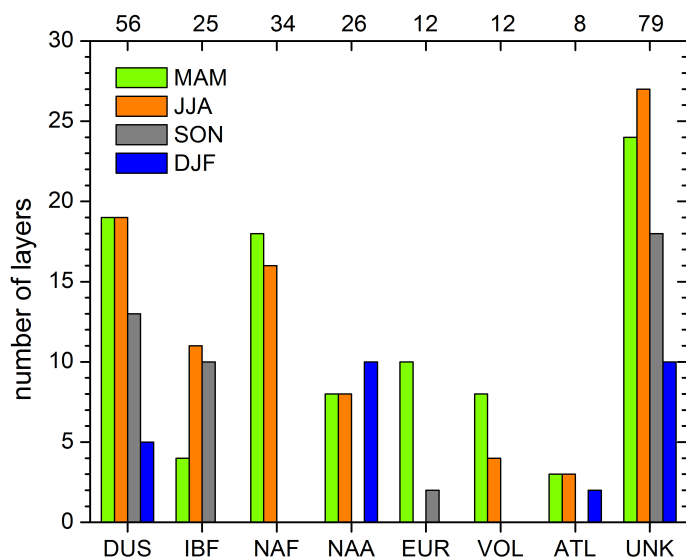


**Figure 4.47.:** Number of layers per season (MAM: spring, JJA: summer, SON: autumn and DJF: winter) for each aerosol type. On the top axis, the number of layers assigned to each aerosol type is shown.

they reach Europe.

The European anthropogenic aerosol (EUR) was only detected in spring and autumn. Air mass advection to Portugal from east would require a high pressure system north of the country over the Atlantic ocean or Great Britain. This is rare and therefore only 5% of all layers came from continental Europe. The detection of aerosol layers of volcanic origin (VOL) naturally depends on volcanic activity. The eruptions of Eyjafjallajökull in April 2010 and of Nabro in June 2011 provided the opportunities to observe this aerosol type over Évora in spring and summer. Fewest layers were classified as aerosol from the Atlantic (ATL). Although Portugal features a general regime of air masses advected from west, aerosols from the Atlantic were seldom lifted into the free troposphere and detected by PAOLI.

The distribution of layer mean heights and the layer depths during the four seasons are shown in figure (4.48). The distributions during the summer months is shown twice, once with and once without the four stratospheric aerosol layers from Nabro. Most layers were detected in spring and fewest in winter. On average, the layers were highest in summer with a median (and mean value) of 3.3 km asl (4.0 km asl), with layers from Nabro and 3.2 km asl (3.5 km asl), without layers from Nabro. They were lowest in winter with 2.0 km asl (2.1 km asl). In all seasons, the mean values were higher than the medians. Concluding, more than half of the layers were lower than the mean height, but few layers were much higher. This is also reflected by the maxima shown in figure (4.48), especially during spring, summer and autumn. Then, the maxima of the layer mean heights were 6.5 km asl, 16.7 km asl (with Nabro layers) and 10.5 km asl (without Nabro layers) as well as 8.0 km asl, respectively. As shown in figure (4.46), highest layers during summer were not only the stratospheric layers observed after the eruption of Nabro during summer 2011, but also layers of unknown origin observed during summer 2010. The stratospheric plume caused by the eruption of Nabro, could be detected until February 2012 (see

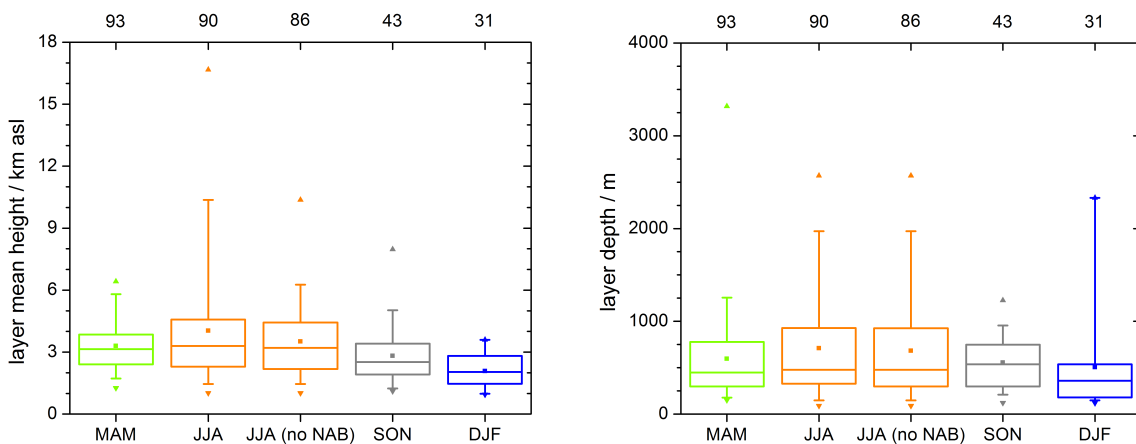


**Figure 4.48.:** Box plot showing mean value (filled squares), minimum (downward pointing triangles), maximum (upward pointing triangles), median (horizontal lines) and 25%, 75%, 5% and 95% percentile (boxes and whiskers, respectively) of the layer mean height above sea level (left) and the layer depth (right) during spring (MAM), summer including stratospheric aerosol layers from Nabro (JJA), summer without stratospheric aerosol layers from Nabro (JJA (no NAB)), autumn (SON) and winter (DJF). On the top axis, the number of layers observed during the seasons is shown.

#### 4. Aerosol characterisation results

section (4.3.4)). However, this information was obtained from measurements averaged over several hours. Here, hourly averages were used. Therefore, in the regular measurements the stratospheric layers could only be detected during the first weeks after the eruption.

The medians of the layer depths, shown on the right hand side of figure (4.48), were similar in spring and summer with 460 and 480 m, respectively. During both seasons, the mean values were higher with 600 and 700 m, respectively. The stratospheric aerosol layers from Nabro had a small effect on the distribution of the layer depth. The median was 480 m as well, and the mean value was with 680 m only slightly smaller, compared to the mean value including the Nabro layers. In autumn, the median was slightly higher with 540 m and in winter lower with 360 m. Maximum layer depths during spring, summer, autumn and winter were 3330, 2580, 1240 and 2330 m, respectively. The minimum layer depth was 90 m in summer and autumn. In spring and winter the minimum layer depths were slightly higher with 150 and 120 m, respectively. The minimum detectable layer depth is determined by the vertical resolution of PAOLI, which is 30 m.

The distribution of the AODs of the individual lofted aerosol layers at 355 and 532 nm are shown in figure (4.49). The AODs could not be determined for all layers, especially from data obtained during daytime or in high altitudes, which was affected by high background signal or low SNR. Calculated were the AODs of 39% (winter, 532 nm) to 68% (summer, 355 nm) of the layers. At both wavelengths, the median (and mean value) of the AOD was highest in autumn with 0.017 (0.040) and 0.014 (0.024) at 355 and 532 nm, respectively. During the other seasons, the medians ranged from 0.010 to 0.013 and from 0.005 to 0.006 at 355 and 532 nm, respectively. As in the layer mean height and depth, the mean values were larger than the medians during all seasons and at both wavelengths. Especially broad were the distributions in autumn. The variability was largest during this season. The higher optical depths observed during autumn correspond to the higher median of the geometrical depth in this season, shown in figure (4.48).

Frequently, several lofted aerosol layers were detected during one measurement. In order to estimate the contribution of layers in the free troposphere and lower stratosphere to the columnar aerosol load, the AODs of all simultaneously observed layers were summed up. On average, the total AODs of the lofted layers were  $0.05 \pm 0.06$  and  $0.03 \pm 0.04$  at 355

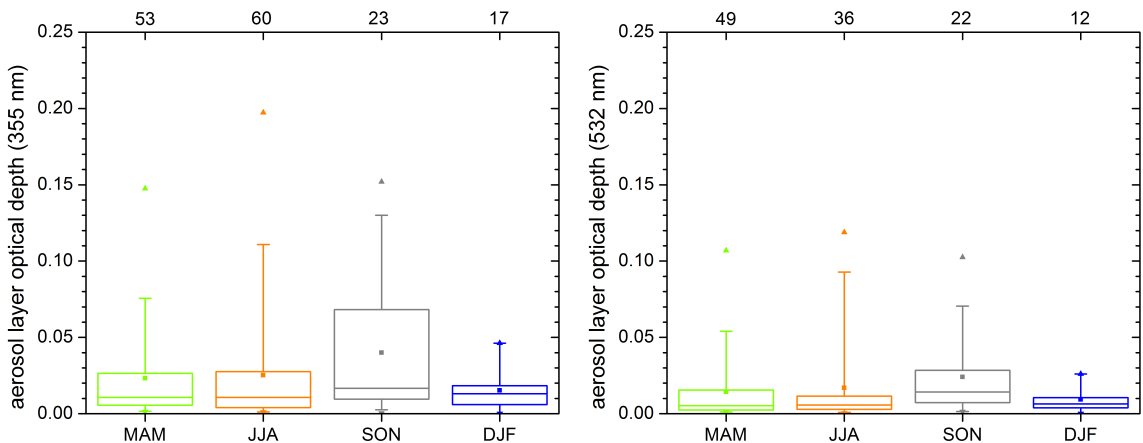


**Figure 4.49.:** Box plots (as figure (4.48)) of the aerosol optical depth at 355 nm (left) and 532 nm (right).

and 532 nm, respectively (not shown). *Obregón et al.* (2012) recently published a five-year climatology of the columnar AOD measured by sun photometers, including data from Évora. For this measurement site, the authors found a mean value and standard deviation at 440 nm of  $0.15 \pm 0.10$ . Considering those values and taking into account that only in 57% of the regular lidar measurements lofted layers were observed, the mean contribution of those layers to the columnar optical depths was about 10 to 20%.

#### 4.4.2. Characterisation of aerosol types

As mentioned above, seven aerosol types were defined. In figure (4.50) an overview over the mean lidar ratio at 355 nm and the mean extinction related Ångström exponent at the pair of wavelengths 355 and 532 nm is given. The mean values and standard deviations of the mean layer properties are shown for each type. The standard deviations were large, which complicates a clear designation of a layer to a certain aerosol type solely by means of the optical properties. However, the mean values of the aerosol types differ clearly. Large differences were found in  $S_{par}$  (355 nm) of anthropogenic aerosols from Europe (EUR) and from North America (NAA), as well as in  $S_{par}$  (355 nm) and  $\hat{a}_\alpha$  (355, 532 nm) of biomass burning smoke from the Iberian peninsula (IBF) and North America (NAF). This affirms the decision, not to assign those classes to joint classes of anthropogenic aerosol and biomass burning smoke, respectively, but to characterise them separately.

The smallest mean  $\hat{a}_\alpha$  (355, 532 nm) was found for layers of DUS, indicating a high contribution of large particles. However, DUS contains mineral dust from Asia as well as from the Sahara. Furthermore, VOL contains volcanic ash in the troposphere as well as volcanic particles in the stratosphere, likely consisting of droplets of sulphuric acid.

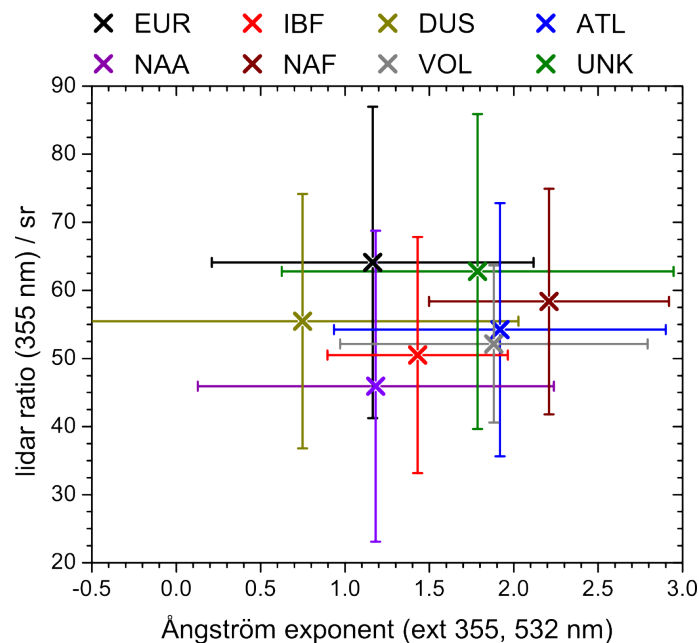


**Figure 4.50.:** Layer mean lidar ratio at 355 nm and extinction related Ångström exponent at the pair of wavelengths 355 and 532 nm for the aerosol types (crosses) and standard deviations (error bars).

#### 4. Aerosol characterisation results

Differences in optical properties between those aerosol subtypes were expected due to the differences in their origins. Those four classes will be investigated separately, later in this section (tables (4.5) and (4.8)).

Aerosol layers of the type ATL showed a large mean  $\hat{a}_\alpha$  (355, 532 nm) and a medium mean value of  $S_{par}$  (355 nm). This indicated a high contribution of small particles and medium absorption. In general, marine aerosol mainly consists of large sea salt particles, which are weakly absorbing. Therefore, low  $\hat{a}$  and  $S_{par}$  could be expected for this aerosol type. However, as mentioned before, the Atlantic is not necessarily the source of the aerosol layers assigned to ATL.

The statistical distributions of the layer mean  $S_{par}$  (355 nm) and  $\hat{a}_\beta$  (532, 1064 nm) of the aerosol types are shown in figure (4.51). For VOL, no  $\hat{a}_\beta$  (532, 1064 nm) could be obtained due to the low SNR for layers from Nabro and the missing information on the depolarisation needed for a depolarisation correction of the particle backscatter coefficient at 532 nm for layers from Eyjafjallajökull. Several aerosol types showed large differences between mean value and median of  $S_{par}$  (355 nm). This indicates uneven distributions of the layer mean values. On the other hand, the mean values and medians of  $\hat{a}_\beta$  (532, 1064 nm) were similar for many of the aerosol types.

The differences in the anthropogenic types EUR and NAA as well as in the biomass burning types IBF and NAF is evident in both images of figure (4.51). Interesting are the high values of  $\hat{a}_\beta$  (532, 1064 nm) of the layers from North America, in both types, biomass burning and anthropogenic aerosol. The medians were 0.9 and 1.8 of EUR and NAA, respectively, as well as 1.0 and 1.7 of IBF and NAF, respectively. Those differences in  $\hat{a}_\beta$  (532, 1064 nm) indicate a higher contribution of small particles in the layers from North America than in the layers originating from the European sources. This could be due to the deposition of large particles during the long range transportation from North America. A detailed comparison of the mean aerosol optical properties of those aerosol types is given below (tables (4.6) and (4.7)).

Mean value and standard deviation of  $S_{par}$  (355 nm) of all dust layers were  $(55 \pm 19)$ sr.

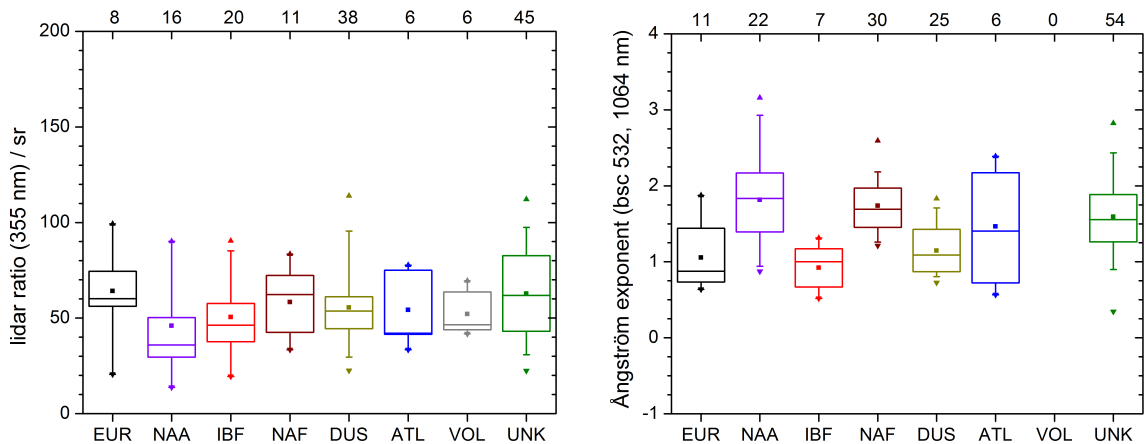


**Figure 4.51.:** Box plot showing mean value (filled squares), minimum (downward pointing triangles), maximum (upward pointing triangles), median (horizontal lines) and 25%, 75%, 5% and 95% percentile (boxes and whiskers, respectively) of the lidar ratio at 355 nm (left) and the backscatter related Ångström exponent at the pair of wavelengths 532 and 1064 nm (right) for the aerosol types. On the top axis, the number of analysed layers is shown.

The median was 54 sr. The mean value and standard deviation of  $\hat{a}_\beta$  (532, 1064 nm) were  $1.1 \pm 0.3$  and the median was 1.1. Besides, the distributions of both optical properties were rather symmetric for DUS, which hints at a normal distribution. Fewest layers were assigned to ATL. The difference between the mean value and the median of  $S_{par}$  (355 nm) was large for this aerosol type. They were  $(54 \pm 19)$ sr and 42 sr, respectively. The mean value and median of  $\hat{a}_\beta$  (532, 1064 nm) was  $1.4 \pm 0.7$  and 1.5. Mean value and median of  $S_{par}$  (355 nm) of VOL differed clearly. They were  $(52 \pm 12)$ sr and 47 sr, respectively. This uneven distribution could be due to the two subtypes, EYJ and NAB, included in VOL. The mean value of  $\hat{a}_\beta$  (532, 1064 nm) was  $1.3 \pm 0.4$  and the median was 1.4 for volcanic aerosol.

### Asian and Saharan dust

The majority of all dust plumes observed by PAOLI was originating in the Sahara. However, in April 2010 Asian dust was transported to Portugal. Nine Asian dust layers detected during this event are included in DUS. A comparison of mean optical properties of Asian and Saharan dust is shown in table (4.5). The mean lidar ratios at both wavelengths were similar for Asian and Saharan dust layers. *Liu et al.* (2002) found lidar ratios at 532 nm between 42 and 55 sr for Asian dust, from lidar observations performed in Japan. Also in Japan, *Murayama et al.* (2004) measured lidar ratios of around 49 and 43 sr at 355 and 532 nm, respectively. The values for AD in table (4.5) were slightly higher. Lidar measurements in Morocco resulted in lidar ratios of Saharan dust of 53 to 55 sr at 355, 532 and 1064 nm, presented by *Tesche et al.* (2009). *Guerrero-Rascado et al.* (2009) observed a Saharan dust event over the southern Iberian peninsula and published lidar ratios between 50 and 65 sr at 532 nm. Lidar ratios of  $(57 \pm 12)$  and  $(52 \pm 12)$  sr at 355 and 532 nm were found during a Saharan dust episode in April 2011 observed by PAOLI (see section (4.3.3), *Preißler et al.* (2011a)). The mean values of SD from more than two years of measurements showed very good agreement with the results of those case studies.

While the mean values of  $\hat{a}_\beta$  (355, 532 nm) were equal for both dust subtypes, mean  $\hat{a}_\alpha$  (355, 532 nm) differed strongly. The mean value of AD was much higher than the one of SD. However, the standard deviations of  $\hat{a}_\alpha$  (355, 532 nm) were high for both dust subtypes. The mean value of  $\hat{a}_\beta$  (532, 1064 nm) of AD was higher as well. Those differences in the Ångström exponents indicate a lower contribution of large particles in the Asian dust layers compared to the Saharan dust layers, where the contribution of large particles was predominant. Dust plumes typically consist of a large fraction of large

**Table 4.5.:** Mean optical properties of dust layers from Asia (AD) and the Sahara (SD).<sup>a</sup>

type	$\hat{a}_\beta$ (355, 532) <sup>b</sup>	$\hat{a}_\beta$ (532, 1064)	$\hat{a}_\alpha$ (355, 532)	$S_{par}$ (355) / sr	$S_{par}$ (532) / sr
AD	$1.1 \pm 0.7$	$1.4 \pm 0.3$	$2.0 \pm 0.9$	$55 \pm 9$	$46 \pm 14$
SD	$1.1 \pm 0.8$	$1.0 \pm 0.2$	$0.5 \pm 1.2$	$56 \pm 20$	$49 \pm 11$

<sup>a</sup> Mean values and standard deviations of the Ångström exponents and lidar ratios calculated by averaging layer mean values.

<sup>b</sup> Wavelengths given in nm.

#### 4. Aerosol characterisation results

particles, when detected close to the source. This would be reflected by small Ångström exponents. *Alfaro et al.* (2003) found an Ångström exponent at the pair of wavelengths 450 and 700 nm of about 0.19 for dust from nephelometer measurements in China. Lidar measurements in Japan resulted in  $\hat{a}_\alpha$  (355, 532 nm) of about 0.8 and  $\hat{a}_\beta$  (355, 532 nm) of about 0.4 (*Murayama et al.*, 2004). The higher mean values of the Ångström exponents of AD shown in table (4.5) were likely a result from the long transportation time and the deposition of large particles during that time. Large variability in the backscatter-related Ångström exponents as well as in lidar ratios were also found by *Papayannis et al.* (2008) in a study on Saharan dust observed in the framework of EARLINET during almost three years.

#### North American and European anthropogenic aerosol

As already shown in figure (4.50), both anthropogenic aerosol types (EUR and NAA) had similar mean  $\hat{a}_\alpha$  (355, 532 nm). However, the mean  $S_{par}$  (355 nm) differed strongly. The mean values of the extinction and backscatter related Ångström exponents as well as the lidar ratios for European and North American anthropogenic aerosol layers are listed in table (4.6). The mean lidar ratios at both wavelengths of EUR were clearly higher than those of NAA. In combination with similar  $\hat{a}_\alpha$  (355, 532 nm), the higher lidar ratios of EUR indicate, that the European aerosol was stronger absorbing than the aerosol from North America. Besides, the mean lidar ratios were higher at 532 nm than at 355 nm for both anthropogenic aerosol types. This spectral behaviour is not typical for anthropogenic aerosol. However, it was observed before in cases of biomass burning aerosols (*Mattis et al.*, 2003; *Murayama et al.*, 2004; *Müller et al.*, 2005). From airborne lidar measurements over central Europe, *Groß et al.* (2012b) found lidar ratios of European anthropogenic aerosols of  $(56 \pm 6)$  sr at 532 nm, which is clearly smaller than the mean value in table (4.6). However, in this work, the lidar ratios were obtained for only 8 and 14 layers of EUR and NAA, respectively, and the standard deviations of the lidar ratios were very high.

The mean values of  $\hat{a}_\alpha$  (355, 532 nm) were equal for both sources. However, the standard deviations were high. The mean  $\hat{a}_\beta$  (355, 532 nm) of EUR and NAA were similar. Differences were found for  $\hat{a}_\beta$  (532, 1064 nm). On average,  $\hat{a}_\beta$  (532, 1064 nm) of NAA was higher than  $\hat{a}_\beta$  (532, 1064 nm) of EUR, indicating a higher contribution of smaller particles within the aerosol layers arriving from North America. As mentioned before, this could be due to the deposition of large particles during the transport from North America.

**Table 4.6.:** Mean optical properties of anthropogenic aerosol layers from North America (NAA) and Europe (EUR).<sup>a</sup>

type	$\hat{a}_\beta$ (355, 532) <sup>b</sup>	$\hat{a}_\beta$ (532, 1064)	$\hat{a}_\alpha$ (355, 532)	$S_{par}$ (355) / sr	$S_{par}$ (532) / sr
EUR	1.5±0.3	1.1±0.4	1.2±1.0	64±23	76±33
NAA	1.6±0.9	1.8±0.6	1.2±1.1	46±23	51±25

<sup>a</sup> Mean values and standard deviations of the Ångström exponents and lidar ratios calculated by averaging layer mean values.

<sup>b</sup> Wavelengths given in nm.

Layers of NAA were detected in a mean altitude of 3.2 km asl (centre of the layer, not shown). Layers of EUR were detected in lower altitudes, at a mean of 2.2 km asl. Layers of NAA were with about 380 m thinner than those of EUR, which were, on average, 720 m deep.

### Biomass burning aerosol from North America and the Iberian peninsula

Relatively fresh forest fire smoke originating in the north of the Iberian peninsula was mainly detected in late summer and autumn of the year 2010 (see figure (4.46)). The mean layer height of IBF layers was 2.4 km asl. Layers of biomass burning smoke from North America were frequently observed in spring and summer of 2011. They were detected in higher altitudes as IBF, at around 4.1 km asl. The mean optical properties of those aerosol types are given in table (4.7). The mean lidar ratios of NAF, were higher than those of IBF. For IBF, the already mentioned spectral behaviour of the lidar ratio was found, lower values at 355 nm compared to those at 532 nm. In case of NAF  $S_{par}$  (532 nm) was slightly smaller than  $S_{par}$  (355 nm). According to findings from Müller *et al.* (2005), the contrary could be expected:  $S_{par}$  (532 nm) similar or smaller than  $S_{par}$  (355 nm) for young smoke (Balis *et al.*, 2003), and  $S_{par}$  (532 nm) higher than  $S_{par}$  (355 nm) for aged smoke (Murayama *et al.*, 2004). However, the standard deviations of the lidar ratios at 532 nm were high.

The Ångström exponents of NAF were all higher than those of IBF. This indicates a smaller contribution of large particles in smoke layers from North America, than in layers from Iberian wild fires. Similar to the Asian dust layers and the anthropogenic aerosol layers from North America, this effect is most likely caused by the deposition of large particles during the long transportation period. Some considerations about the effect of ageing of forest fire smoke on the  $\hat{a}_\alpha$  (355, 532 nm) were given by Müller *et al.* (2005). The authors found  $\hat{a}_\alpha$  (355, 532 nm) between 0 and 1.1 for smoke transported over very long distances with transport times of less than three weeks. For smoke transported for about five days, the  $\hat{a}_\alpha$  (355, 532 nm) was between 1.8 and 2.1. However, according to the authors, some doubts remained about the aerosol origin in this case. The smoke layers from North America detected over Évora were about five to ten days old. Considering this transport time, the  $\hat{a}_\alpha$  (355, 532 nm) presented here is very similar to the findings by Müller *et al.* (2005).

**Table 4.7.:** Mean optical properties of layers from biomass burning in North America (NAF) and on the Iberian peninsula (IBF).<sup>a</sup>

type	$\hat{a}_\beta$ (355, 532) <sup>b</sup>	$\hat{a}_\beta$ (532, 1064)	$\hat{a}_\alpha$ (355, 532)	$S_{par}$ (355) / sr	$S_{par}$ (532) / sr
NAF	1.6±0.7	1.7±0.3	2.2±0.7	58±17	56±25
IBF	1.3±0.5	0.9±0.3	1.4±0.5	51±17	54±28

<sup>a</sup> Mean values and standard deviations of the Ångström exponents and lidar ratios calculated by averaging layer mean values.

<sup>b</sup> Wavelengths given in nm.

### Volcanic aerosol from Eyjafjallajökull and Nabro

The volcanic aerosol layers from the eruptions of Eyjafjallajökull and Nabro were discussed already in sections (4.3.2) and (4.3.4). In this section, the optical properties of the volcanic aerosols are compared, using only regular EARLINET measurements. Eyjafjallajökull emitted large amounts of aerosols into the troposphere. Europe was strongly affected by this eruption and numerous lidar studies could be realised. The tropospheric aerosols caused by the eruption of Nabro were more difficult to monitor. However, this eruption injected a large amount of aerosols into the stratosphere. Therefore, one main difference between EYJ and NAB was the layer heights. The mean altitude of layers of EYJ and NAB were 3.7 km asl and 15.5 km asl, respectively. Besides, the mean layer depths of EYJ and NAB were 620 and 1180 m, respectively

The high altitudes of NAB layers complicated the determination of optical aerosol properties due to a low SNR in such height ranges. From NAB, only  $\hat{a}_\beta$  (532, 1064 nm) could be calculated from two layers. In case of EYJ the values related to the particle backscatter coefficient at 532 nm could not be used, because the volcanic ash observed in the free troposphere was depolarising. However, no depolarisation correction could be done, as mentioned in section (4.3.2). The mean values of  $\hat{a}_\alpha$  (355, 532 nm) and  $S_{par}$  (355 nm) of EYJ were retrieved from seven layers. The obtained optical properties for layers of volcanic origin are given in table (4.8). The high mean  $\hat{a}_\alpha$  (355, 532 nm) of EYJ hints at a small contribution of larger particles. However, the standard deviation of  $\hat{a}_\alpha$  (355, 532 nm) was comparably large.

A direct comparison of the optical properties of the tropospheric and stratospheric volcanic aerosol layers was not possible considering regular measurements only. The data set was limited in both cases for the reasons given above. This type of special events can only be compared by a detailed analysis of intensive measurement periods.

#### 4.4.3. Summary: Aerosol climatology

Mineral dust, anthropogenic aerosol, biomass burning smoke and volcanic aerosol were studied in detail. In some cases, the number of layers per aerosol type or subtype was small. This complicates the statistical analysis of the aerosol climatology. More layers would be necessary for a higher statistical significance and a better estimation of the un-

**Table 4.8.:** Mean optical properties of layers of volcanic aerosol from Eyjafjallajökull (EYJ) and Nabro (NAB).<sup>a</sup>

type	$\hat{a}_\beta$ (355, 532) <sup>b</sup>	$\hat{a}_\beta$ (532, 1064)	$\hat{a}_\alpha$ (355, 532)	$S_{par}$ (355) / sr	$S_{par}$ (532) / sr
EYJ			1.9±0.9	52±12	
NAB		0.9±0.1			

<sup>a</sup> Mean values and standard deviations of the Ångström exponents and lidar ratios calculated by averaging layer mean values.

<sup>b</sup> Wavelengths given in nm.

certainties of the aerosol type characterisation. In this work, this is especially important for Asian dust, volcanic ash in the troposphere, here represented by aerosol from Eyjafjallajökull, and volcanic aerosol in the stratosphere, here represented by aerosol from Nabro. A higher number of layers contributing to the aerosol types could be achieved by including more measurements. If the requirement of regular measurements should be maintained in order to avoid a bias due to varying measurement frequencies, a longer measurement period would be necessary. However, in case of volcanic eruptions this would not necessarily increase the number of layers, depending on the occurrence of volcanic eruptions in the northern hemisphere. Besides, an improvement could be obtained by further increasing the SNR of the Raman signals and generally in high altitudes. This would facilitate the calculation of the layer mean optical properties. From the existing data, improvements in the detection of the aerosol origin, for example by using tracer models instead of trajectories, could increase the number of aerosol layers of known origin. In the present study, 31% of all layers could not be assigned to any of the aerosol types.

Despite the low number of layers of some aerosol types and subtypes, a characterisation was done regarding the lidar ratios at 355 and 532 nm, as well as the extinction and backscatter related Ångström exponents at the pair of wavelengths 355 and 532 nm and the backscatter related Ångström exponent at the pair of wavelengths 532 and 1064 nm. Clear differences were found between the mean optical properties of the investigated aerosol types and subtypes. The mean lidar ratios and Ångström exponents varied for layers of dust from the Sahara and from Asia, of anthropogenic aerosol from Europe and from North America, as well as of biomass burning smoke from the Iberian Peninsula and from North America. This reflects the high variability of aerosol optical properties and hints at difficulties in the characterisation of aerosols. The aerosol type alone is not always sufficient to clearly assign optical properties. The source region and the transport of the aerosols play an important role as well. For example, the mean Ångström exponents of aerosol layers of the same type but from closer source regions were usually smaller than those from aerosol layers transported over a longer distance, as shown in tables (4.5) to (4.7). An increase of the Ångström exponents hints at a decreasing contribution of large particles. This could be caused by the deposition of large particles along the transportation path.

Using regular measurements only, no comparison of optical properties of volcanic aerosol layers from the eruptions of Eyjafjallajökull and Nabro could be done. This was due to lacking information on the depolarisation of the volcanic ash on the one hand and a low SNR in high altitudes on the other hand. However, such special events are usually subject to more intense measurement periods and can be studied individually, as shown in sections (4.3.2) and (4.3.4).

## 5. Summary and conclusions

For the first time, a long term observation of aerosol profiles by means of a ground based multi-wavelength Raman lidar system was conducted in Portugal. The first European Aerosol Research Lidar Network (EARLINET) station in Portugal was established in Évora and enabled the investigation of optical aerosol properties on a high temporal and vertical resolution since September 2009. The performance of the lidar system was tested according to the EARLINET guidelines in order to assure high quality lidar data and comparability of results. The testing procedures were important for identifying and solving problems in the optical alignment. Within this work, a new test for the optimisation of the outgoing beam was developed and employed. The two-dimensional scanning test proved to be a useful tool to adjust the position of the outgoing beam relative to the receiver field of view (FOV). Careful optimisation of the alignment ensured a good performance of such a complex system and is crucial for capturing reliable lidar data. It was shown, that the performance of PAOLI could be improved. The temperature dependent oscillations of the lidar signal could be reduced. Furthermore, the altitude of full overlap between outgoing beam and receiver FOV was reduced, improving the detection behaviour of the system in the near field.

Since 2009, lidar measurements were performed on a regular basis three times a week, but also correlative to overpasses of the satellite Cloud-Aerosol Lidar and Infrared Pathfinder Satellite Observations (CALIPSO), and in cases of high aerosol load in the troposphere or lower stratosphere. From the three weekly regular EARLINET measurements, a characterisation of different aerosol types was done. For this study more than two years of regular measurements were analysed. In total, 74% of the scheduled measurements could be performed due to the favourable weather conditions in southern Portugal. The main reasons for omitting regular measurements were low clouds and rain, which mainly occurred in winter. Most of the free tropospheric and lower stratospheric aerosol layers were detected in spring and summer, which is related to the atmospheric circulation favouring aerosol transport towards Évora. Besides, in summer the largest number of measurements could be performed due to mostly clear sky conditions. On average, layers were highest in summer and lowest in winter. In autumn, layers with the largest mean geometrical and optical depths were observed.

For a characterisation of aerosol types, the knowledge of the aerosol origin is needed. As lidar profiles provide the vertical aerosol distribution, transportation models can be combined with this information. With the joint use of back trajectories with boundary layer information, which was applied within this work, the aerosol source identification was facilitated.

However, for 31% of all layers, the source region could not be identified. Most of the identified layers were mineral dust, mainly from the Saharan desert. Fewest layers were assigned to the source region Atlantic ocean. The mineral dust, anthropogenic aerosols, biomass burning smoke and volcanic aerosols were divided into subtypes depending on

the source region. Those aerosol subtypes show clear differences in their mean aerosol optical properties. Dust layers from Asia showed larger Ångström exponents than Saharan dust. The lidar ratios of anthropogenic aerosol from North America were smaller than the lidar ratios of European anthropogenic aerosols. Besides, the backscatter related Ångström exponents were larger. The Ångström exponents of biomass burning smoke layers from North America were also large compared to smoke plumes from fires on the Iberian Peninsula.

In general, smaller mean Ångström exponents were found for aerosol layers with source regions closer to the detection site. Such Ångström exponents represent prominent fractions of large particles. A possible explanation for the decrease of the Ångström exponents along the travel path is the deposition of large particles.

The characterisation of the stratospheric volcanic aerosol from Nabro was complicated due to the high layer altitude and resulting low signal-to-noise ratio (SNR), which prevented the determination of the particle extinction coefficients. Besides, the retrieval of the optical properties of the tropospheric layers originating from Eyjafjallajökull was limited due to missing information on the depolarisation, which cannot be neglected in the investigation of non-spherical particles, like volcanic ash. Therefore a comparison of those two subtypes of volcanic aerosol was not possible, using the regular measurements only.

However, from the large set of data obtained with PAOLI throughout the last years, several cases were studied in detail. Three different types of volcanic aerosol events could be observed. In September 2009, a high aerosol load was detected in the lower stratosphere. This plume probably resulted from several volcanic eruptions during the years 2008 and 2009. The investigation of this layer showed a significant contribution of the stratospheric aerosol to the columnar aerosol load. The optical depth of the stratospheric aerosol layer was 19% and 18% of the optical depth of the boundary layer at 532 and 1064 nm, respectively, in September 2009. The maximum aerosol optical depth of the stratospheric layer was 0.02 and 0.01 at 532 and 1064 nm, respectively.

The second observation of volcanic aerosol in Évora occurred after the eruption of Eyjafjallajökull in Iceland, which started on 14 April 2010 and lasted until 21 May 2010. The aerosol plumes were transported towards Portugal in the free troposphere. Two different phases were observed over Europe. In April 2010, lidars in central Europe could detect plumes of volcanic ash with lidar ratios between 55 and 65 sr (*Ansmann et al.*, 2010) and linear particle depolarisation ratios of 37% and 25% (*Gasteiger et al.*, 2011; *Mona et al.*, 2012). No volcanic aerosol was detected in Évora at that time. In the beginning of May 2010, the plumes reached Europe from west, arriving first at the Iberian Peninsula. Then, linear particle depolarisation ratios of 16% or less were reported from south and south-west Europe (*Mona et al.*, 2012; *Sicard et al.*, 2012). The depolarisation of the volcanic aerosol could not be obtained from PAOLI measurements because the signal at 532 nm (cross polarised) was not available at that time. The mean lidar ratio at 355 nm of all volcanic layers calculated from PAOLI measurements was  $(40 \pm 17)$ sr and therefore much smaller than lidar ratios observed in central Europe during the first phase of this episode. This indicates a change in the properties of the ejected aerosols during different stages of the volcanic eruption, which is in accordance with results published by *Ilyinskaya et al.* (2011); *Thomas and Prata* (2011) and *Gudmundsson et al.* (2012). Besides, the different transportation paths might have an influence on the particle properties as

## 5. Summary and conclusions

well.

In June 2011 the eruption of Nabro in Eritrea caused a high aerosol load in the lower stratosphere. A deep layer could be observed for several months. Stratospheric aerosol was present over Évora until February 2012. However, contributions from the eruption of Shiveluch in Kamtchatka, Russia in October 2011 were likely. Contrary to the volcanic ash from Eyjafjallajökull detected in the free troposphere, the stratospheric particles from Nabro were mainly spherical and likely sulphuric acid, as can be concluded from small linear particle depolarisation ratios.

A strong outbreak of mineral dust from the Saharan desert was observed in April 2011. It was exceptional in terms of aerosol optical depth and dust load on the ground. The maximum aerosol optical depths of the dust layer reached maxima of 1.8 and 1.9 at 355 and 532 nm, respectively. The mean Ångström exponents, averaged over all dust layers during the whole studied period from 4 to 9 April 2011, were  $0.0 \pm 0.2$  ( $\hat{a}_\alpha$  (355, 532 nm)),  $0.4 \pm 0.6$  ( $\hat{a}_\beta$  (355, 532 nm)),  $0.4 \pm 0.2$  ( $\hat{a}_\beta$  (532, 1064 nm)). The mean lidar ratios were  $(45 \pm 11)$ sr and  $(53 \pm 7)$ sr at 355 and 532 nm, respectively. The mean linear particle depolarisation ratio at 532 nm was  $0.28 \pm 0.04$ . During this event, dust was observed within the PBL by means of ground based in-situ instruments. The maximum particle mass concentration of  $162 \mu\text{g m}^{-3}$  was detected in the afternoon of 6 April 2011. The daily threshold of the mass concentration imposed by the European air quality legislation was exceeded on that day and the two following days.

Furthermore, a joint study was conducted about free tropospheric aerosol layers observed at the EARLINET stations in Granada and Évora. The objective of this study was the investigation of the horizontal homogeneity of aerosol plumes over the southern Iberian peninsula. Two cases were selected, a forest fire smoke plume from North America and a Saharan dust event. In both cases the aerosol layer heights agreed well over both stations. The first case represents aerosol transported over very long distances, compared to which the distance between the two measurement stations is small. The mean lidar ratio at 355 nm of the North American smoke layer was smaller over Granada than over Évora and the backscatter related Ångström exponent at the pair of wavelengths 355 and 532 nm was higher. Different fractions of the smoke plume were detected simultaneously. Therefore, the differences in the optical properties are evidence for an inhomogeneous horizontal distribution over the southern Iberian peninsula. In case of the dust event, the aerosol source was much closer to the observation sites. The Ångström exponents as well as the linear particle depolarisation ratio of the Saharan dust layers observed at both stations were in a similar range. The lidar ratios of the layers detected over Évora were slightly smaller than over Granada. Those small differences were probably caused by different transportation paths and mixing of other aerosol types into the mineral dust layers.

In the framework of this study, a large set of multi-wavelength Raman lidar data was obtained, not only during regular measurements but also during special aerosol events. The potential of this vast amount of data was proofed. Vertically resolved aerosol measurements at Évora can contribute to a better understanding of aerosol transport processes and to an improved knowledge on the vertical aerosol distribution and aerosol properties.

## 6. Future work

This work marks the first stage of establishing a new lidar station in Évora. Initial difficulties were described and could be solved in most of the cases. However, as stated before, a lidar is a complex system which needs continuous careful and attentive treatment to ensure a high data quality. Regular testing of the alignment and a critical assessment of the data and data products is crucial for a persistent reliable operation.

Only parts of the existing data set were presented here. Although many measurements were analysed for the shown studies, further exploitation is ongoing. Besides the regular measurements in the framework of EARLINET and the intensive aerosol studies, measurements were performed correlative to overpasses of CALIPSO. Data from PAOLI and the CALIOP complement each other. Whereas PAOLI monitors the vertical distribution of aerosols in a high temporal resolution, CALIOP detects the vertical and horizontal distribution on a global scale. A systematic analysis of PAOLI data correlative to CALIOP observations could further contribute to the understanding of aerosol transportation processes. Évora is very suitable for this type of studies due to the close overpasses of the satellite with minimum ground track distances of around 8 km.

Two volcanic eruptions over central Europe within two years were a good chance for all EARLINET stations to proof the ability of network coordinated measurements on short notice. Nearly continuous measurements in Portugal during the second phase of the Eyjafjallajökull event provided valuable information for the network on the approach of the aerosol plumes from Iceland. At the moment, a publication about the four-dimensional distribution of the volcanic aerosol plumes over Europe observed by EARLINET during the whole volcanic event (15 April to 26 May 2010) is under preparation (Pappalardo et al., personal communication). This article will also include data from the EARLINET station in Évora.

Besides, some teams of the Spanish and Portuguese Aerosol Lidar Network (SPALINET) presently work on a joint publication about the observation of the stratospheric aerosol layer caused by the eruption of Nabro (Guerrero-Rascado et al., personal communication). The lidar station in Évora contributed to this work with numerous whole-night measurements, which enable long averaging times and therefore not only the retrieval of the layer heights, but also the determination of optical aerosol properties.

Within this work, back trajectories were used for the determination of the source regions of free tropospheric aerosol layers. However, a more particular determination of the origin of aerosol plumes can be achieved by the application of tracer models, as e.g. FLEXPART (Stohl et al., 2005). This Lagrangian particle dispersion model is freely available on-line and could be installed and employed at CGE in the future.

The optical aerosol properties were studied in detail. From the profiles of the optical properties obtained by multi-wavelength Raman lidars, micro-physical properties can be derived by means of inversion algorithms (Twomey, 1977; Veselovskii et al., 2002; Kolgotin and Müller, 2008). The determination of vertical profiles of the volume, surface area and number concentration, the effective radius, as well as the mean refractive index is possible

## 6. Future work

from the data provided by PAOLI: particle extinction coefficients at two wavelengths and particle backscatter coefficients at three wavelengths. However, the inversion problem is ill-posed and can only be solved with mathematical regularization methods (*Müller et al.*, 1999; *Böckmann et al.*, 2005). In the framework of EARLINET different inversion algorithms are applied for lidar data. Furthermore, the software package Lidar-Radiometer Inversion Code (LIRIC) (*Chaikovsky et al.*, 2008; *Wagner*, 2012) was developed for the retrieval of aerosol micro-physical properties from combined multi-wavelength lidar and sun photometer measurements. This package bases on an optimisation procedure and follows a statistical estimation theory with the maximum likelihood method. The inversion algorithms as well as the software package can be used by EARLINET members. Measurements at CGE are suitable for this type of studies, because of the capabilities of the multi-wavelength Raman lidar, and the collocated operation of a sun photometer. Furthermore, the generally low aerosol load close to the ground, as usually found in Évora, facilitates the characterisation of aerosol layers in the free troposphere, also from sun photometer data. Presently, first studies on the application of LIRIC with data from CGE are under preparation (*Guerrero-Rascado et al.*, 2012b).

In the framework of EARLINET, the Single Calculus Chain (SCC) software was developed, improved and tested during the last years. It is expected to be operational on a routine basis in the near future. The advantage is a uniform and objective analysis procedure of the lidar data obtained within the network. A near real time calculation of vertically resolved aerosol optical properties, and eventually also micro-physical properties, is the main achievement of this software. The output of the SCC can be used as input for atmospheric modelling, which presently lacks real time information on the vertical aerosol distribution. As part of this work, PAOLI data was successfully tested within the SCC software.

# A. Appendix

## A.1. Background correction

In the following, range corrected signals with varying background correction height ranges, as well as the respective profiles of the normalised differences are shown. The night time measurements were averaged between 2 to 3 UTC and the daytime measurements between 10 to 11 UTC of 19 February 2012. The plots at 532 nm and 607 nm are presented and explained in section (4.1).

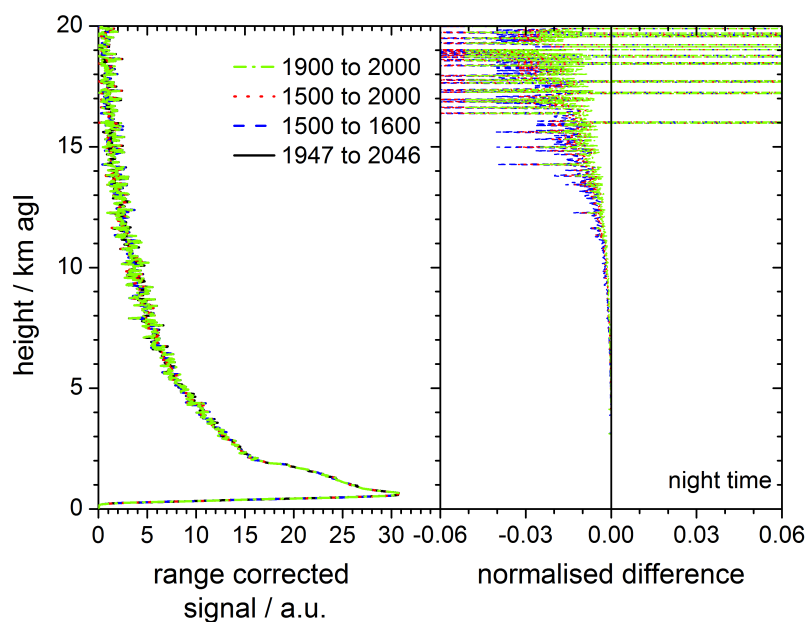


**Figure A.1.:** Left: Background corrected signal at 355 nm for different background correction heights (in bins) for night time data (2 to 3 UTC of 19 February 2012). Right: Normalised difference with reference to the profiles with the background correction between 1947 and 2046 bins. Line styles and colours correspond to those in the left plot.

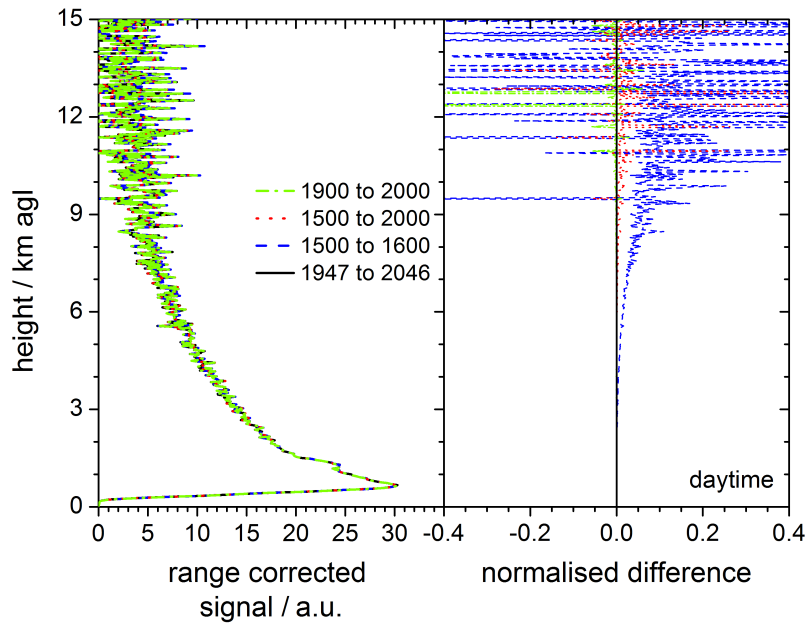


**Figure A.2.:** Same as figure (A.1), but for daytime data (10 to 11 UTC of 19 February 2012).

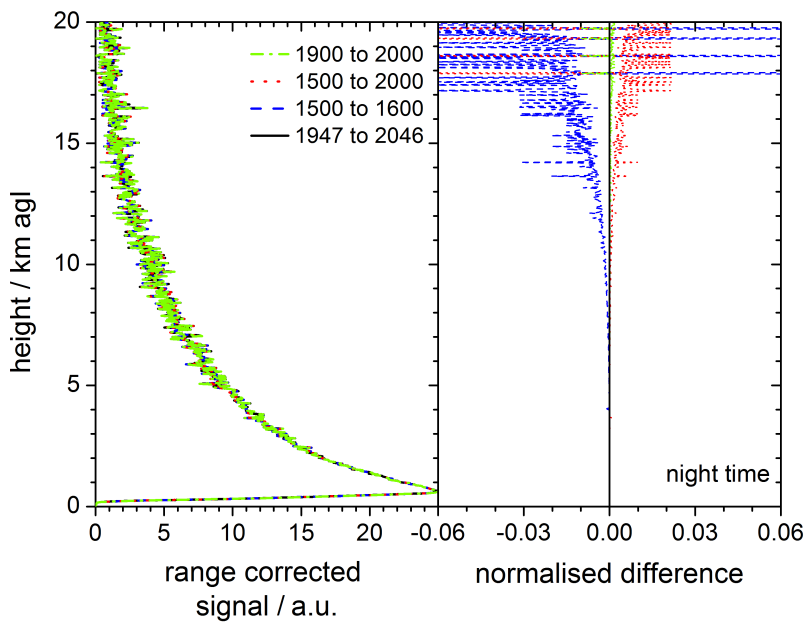


**Figure A.3.:** Left: Background corrected signal at 387 nm for different background correction heights (in bins) for night time data (2 to 3 UTC of 19 February 2012). Right: Normalised difference with reference to the profiles with the background correction between 1947 and 2046 bins. Line styles and colours correspond to those in the left plot.

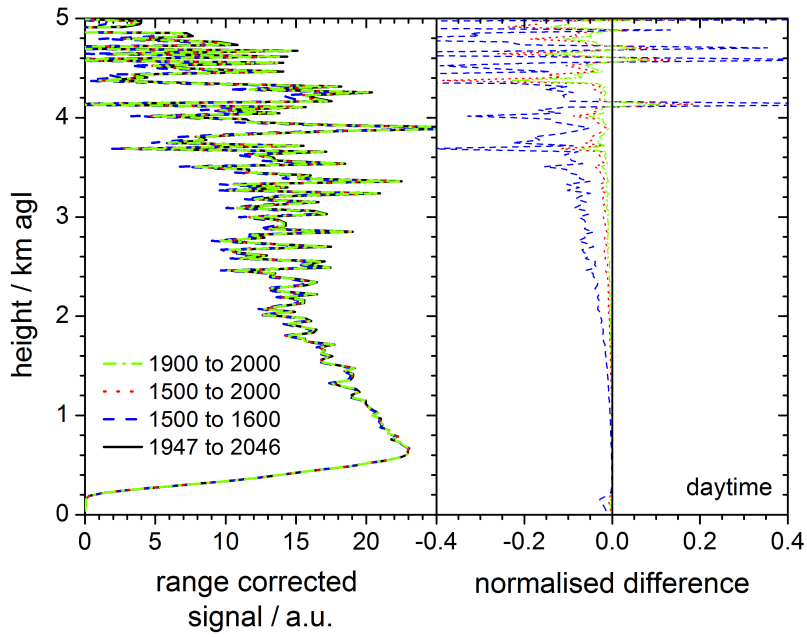


**Figure A.4.:** Same as figure (A.3), but for daytime data (10 to 11 UTC of 19 February 2012).

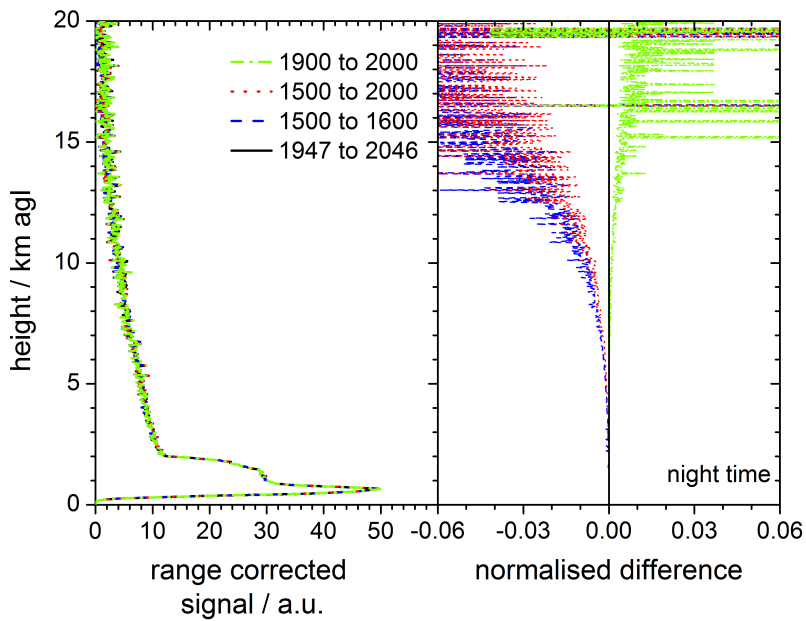


**Figure A.5.:** Left: Background corrected signal at 532 nm (cross) for different background correction heights (in bins) for night time data (2 to 3 UTC of 19 February 2012). Right: Normalised difference with reference to the profiles with the background correction between 1947 and 2046 bins. Line styles and colours correspond to those in the left plot.

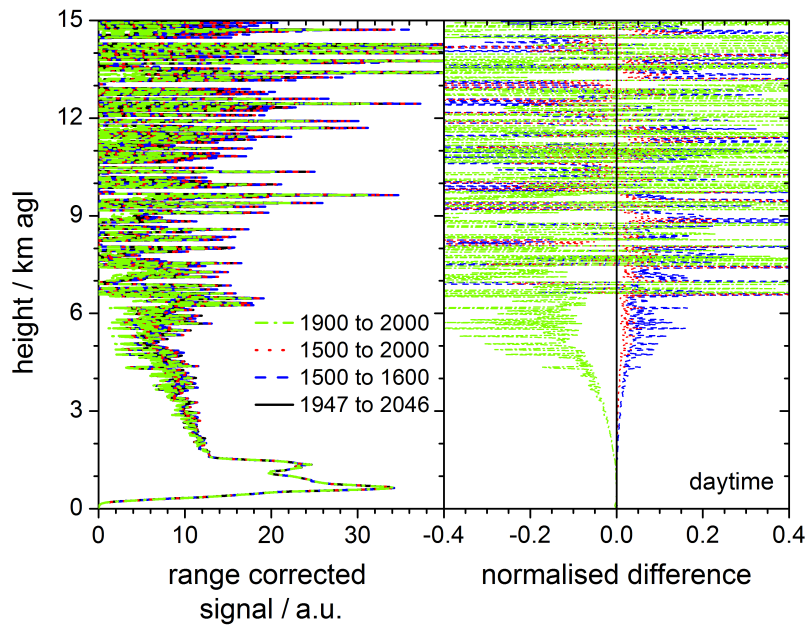


Figure A.6.: Same as figure (A.5), but for daytime data (10 to 11 UTC of 19 February 2012).

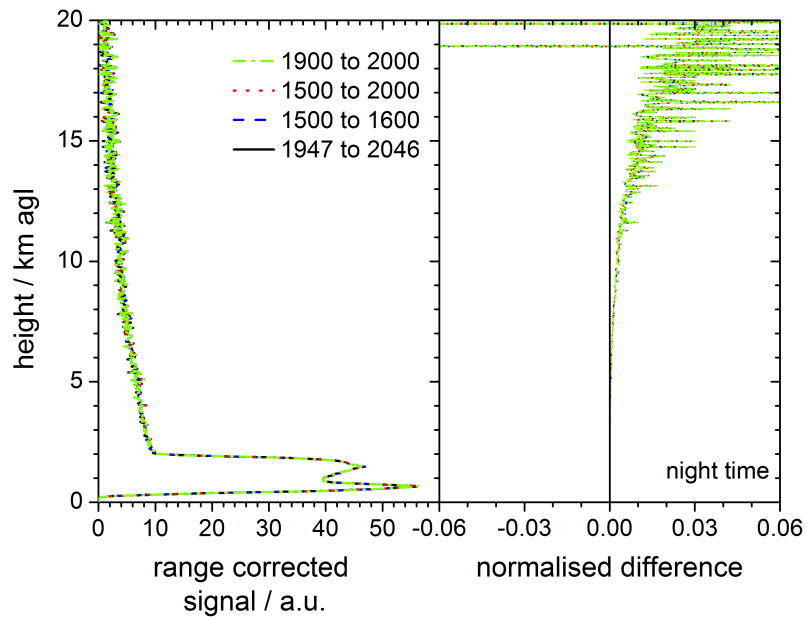
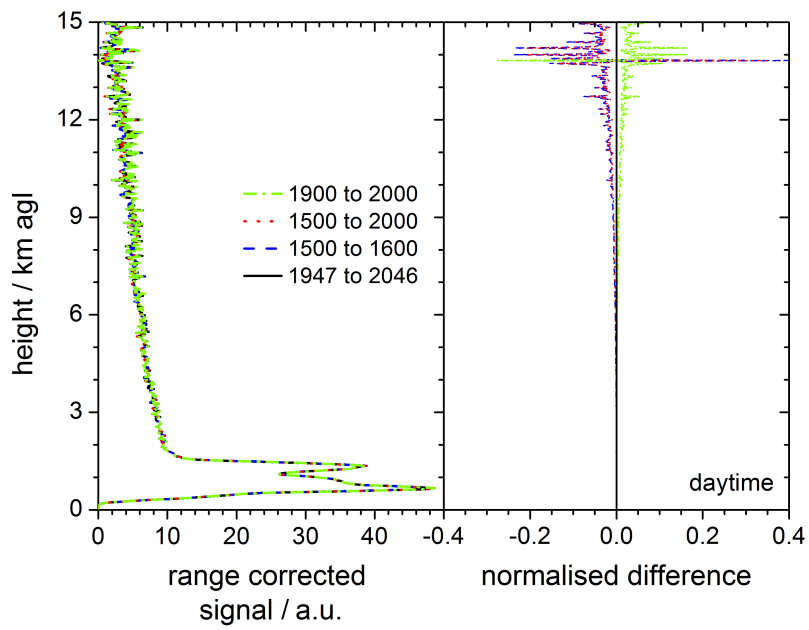


Figure A.7.: Left: Background corrected signal at 1064 nm for different background correction heights (in bins) for night time data (2 to 3 UTC of 19 February 2012). Right: Normalised difference with reference to the profiles with the background correction between 1947 and 2046 bins. Line styles and colours correspond to those in the left plot.



**Figure A.8.:** Same as figure (A.7), but for daytime data (10 to 11 UTC of 19 February 2012).



# Bibliography

- Acker, J. G., and G. Leptoukh (2007), Online analysis enhances use of nasa earth science data, *Eos Transactions American Geophysical Union*, **88**, 14, doi:10.1029/2007EO020003.
- Ackermann, J. (1998), The extinction-to-backscatter ratio of tropospheric aerosol: A numerical study, *Journal of Atmospheric and Oceanic Technology*, **15**, 1043–1050, doi:10.1175/1520-0426(1998)015<1043:TETBRO>2.0.CO;2.
- Alados-Arboledas, L., et al. (2011), Optical and microphysical properties of fresh biomass burning aerosol retrieved by Raman lidar, and star- and sun-photometry, *Geophysical Research Letters*, **38**, doi:10.1029/2010GL045999.
- Alfaro, S. C., et al. (2003), Chemical and optical characterization of aerosols measured in spring 2002 at the ACE-Asia supersite, Zhenbeitai, China, *Journal of Geophysical Research*, **108**, doi:10.1029/2002JD003214.
- Althausen, D., et al. (2009), Portable Raman Lidar PollyXT for Automated Profiling of Aerosol Backscatter, Extinction, and Depolarization, *Journal of Atmospheric and Oceanic Technology*, **26**, 2366–2378, doi:10.1175/2009JTECHA1304.1.
- Alvarez, J. M., M. A. Vaughan, C. A. Hostetler, W. H. Hunt, and D. M. Winker (2006), Calibration Technique for Polarization-Sensitive Lidars, *Journal of Atmospheric and Oceanic Technology*, **23**, 683–699, doi:10.1175/JTECH1872.1.
- Amiridis, V., et al. (2005), Four-year aerosol observations with a Raman lidar at Thessaloniki, Greece, in the framework of European Aerosol Research Lidar Network (EARLINET), *Journal of Geophysical Research*, **110**, doi:10.1029/2005JD006190.
- Amiridis, V., et al. (2009), Optical characteristics of biomass burning aerosols over South-eastern Europe determined from UV-Raman lidar measurements, *Atmospheric Chemistry and Physics*, **9**, 2431–2440, doi:10.5194/acp-9-2431-2009.
- Anderson, T. L., et al. (1996), Performance characteristics of a high-sensitivity, three-wavelength, total scatter/backscatter nephelometer, *Journal of Atmospheric and Oceanic Technology*, **13**, 967–986, doi:10.1175/1520-0426(1996)013<0967:PCOAHS>2.0.CO;2.
- Ångström, A. (1964), The parameters of atmospheric turbidity, *Tellus*, **16**, 64–75.
- Ansmann, A., and D. Müller (2005), Lidar and atmospheric aerosol particles, in *Lidar: Range resolved optical remote sensing of the atmosphere*, edited by C. Weitkamp, pp. 105–138, Springer Science+Business Media Inc., New York, NY, USA.

## Bibliography

- Ansmann, A., M. Riebesell, and C. Weitkamp (1990), Measurement of atmospheric aerosol extinction profiles with a Raman lidar, *Optics Letters*, **15**, 746–748, doi:10.1364/OL.15.000746.
- Ansmann, A., et al. (1992a), Combined Raman Elastic-Backscatter LIDAR for Vertical Profiling of Moisture, Aerosol Extinction, Backscatter, and LIDAR Ratio, *Applied Physics B*, **55**, 18–28, doi:10.1007/BF00348608.
- Ansmann, A., U. Wandinger, M. Riebesell, C. Weitkamp, and W. Michaelis (1992b), Independent measurement of extinction and backscatter profiles in cirrus clouds by using a combined Raman elastic-backscatter lidar, *Applied Optics*, **31**, 7113–7131, doi:10.1364/AO.31.007113.
- Ansmann, A., et al. (2000), Vertical profiling of the Indian aerosol plume with six wavelength lidar during INDOEX: A first case study, *Geophysical Research Letters*, **27**, 963–966, doi:10.1029/1999GL010902.
- Ansmann, A., et al. (2001), European pollution outbreaks during ACE 2: Lofted aerosol plumes observed with Raman lidar at the Portuguese coast, *Journal of Geophysical Research*, **106**, 20,725–20,733, doi:10.1029/2000JD000091.
- Ansmann, A., et al. (2002), European pollution outbreaks during ACE 2: Optical particle properties inferred from multiwavelength lidar and star-sun photometry, *Journal of Geophysical Research*, **107**, doi:10.1029/2001JD001109.
- Ansmann, A., et al. (2003), Long-range transport of Saharan dust to northern Europe: The 11-16 October 2001 outbreak observed with EARLINET, *Journal of Geophysical Research*, **108**, doi:10.1029/2003JD003757.
- Ansmann, A., et al. (2010), The 16 April 2010 major volcanic ash plume over central Europe: EARLINET lidar and AERONET photometer observations at Leipzig and Munich, Germany, *Geophysical Research Letters*, **37**, doi:10.1029/2010GL043809.
- Ansmann, A., et al. (2011), Ash and fine-mode particle mass profiles from EARLINET-AERONET observations over central Europe after the eruptions of the Eyjafjallajökull volcano in 2010, *Journal of Geophysical Research*, **116**, doi:10.1029/2010JD015567.
- Badarinath, K. V. S., S. K. Kharol, and A. R. Sharma (2009), Long-range transport of aerosols from agriculture crop residue burning in Indo-Gangetic Plains – A study using LIDAR, ground measurements and satellite data, *Journal of Atmospheric and Solar-Terrestrial Physics*, **71**, 112–120, doi:10.1016/j.jastp.2008.09.035.
- Balis, D., et al. (2000), Tropospheric LIDAR aerosol measurements and sun photometric observations at Thessaloniki, Greece, *Atmospheric Environment*, **34**, 925–932, doi:10.1016/S1352-2310(99)00317-9.
- Balis, D., V. Amiridis, S. Nickovic, A. Papayannis, and C. Zerefos (2004), Optical properties of Saharan dust layers as detected by a Raman lidar at Thessaloniki, Greece, *Geophysical Research Letters*, **31**, L13,104, doi:10.1029/2004GL019881.
- Balis, D., et al. (2006), Optical characteristics of desert dust over the East Mediterranean during summer: a case study, *Annales Geophysicae*, **24**, 807–821.

- Balis, D. S., et al. (2003), Raman lidar and sunphotometric measurements of aerosol optical properties over Thessaloniki, Greece during a biomass burning episode, *Atmospheric Environment*, **37**, 4529–4538, doi:10.1016/S1352-2310(03)00581-8.
- Bates, T. S., B. J. Huebert, J. L. Gras, F. B. Griffiths, and P. A. Durkee (1998), International Global Atmospheric Chemistry (IGAC) Project's First Aerosol Characterization Experiment (ACE 1): Overview, *Journal of Geophysical Research*, **103**, 16,297–16,318, doi:10.1029/97JD03741.
- Behrendt, A., and T. Nakamura (2002), Calculation of the calibration constant of polarization lidar and its dependency on atmospheric temperature, *Optics Express*, **10**, 805–817.
- Biele, J., G. Beyerle, and G. Baumgarten (2000), Polarization lidar: Corrections of instrumental effects, *Optics Express*, **7**, 427–435, doi:10.1364/OE.7.000427.
- Bissonnette, L. R. (1986), Sensitivity analysis of lidar inversion algorithms, *Applied Optics*, **25**, 2122–2125, doi:10.1364/AO.25.002122.
- Böckmann, C., I. Mironova, D. Müller, L. Schneidenbach, and R. Nessler (2005), Microphysical aerosol parameters from multiwavelength lidar, *Journal of the Optical Society of America A*, **22**, 518–528, doi:10.1364/JOSAA.22.000518.
- Bösenberg, J., et al. (2003), *EARLINET: A European Aerosol Research Lidar Network to Establish an Aerosol Climatology, Report No. 348*, 191 pp., Max Planck Institute for Meteorology, Hamburg, Germany.
- Bösenberg, J., et al. (2008), *Plan for the implementation of the GAW Aerosol Lidar Observation Network GALION, Global Atmosphere Watch Report No. 178*, 52 pp., World Meteorological Organization, Geneva, Switzerland.
- Bourassa, A. E., et al. (2012), Large Volcanic Aerosol Load in the Stratosphere Linked to Asian Monsoon Transport, *Science*, **337**, 78–81, doi:10.1126/science.1219371.
- Brenninkmeijer, C. A. M., et al. (1999), CARIBIC — Civil Aircraft for Global Measurement of Trace Gases and Aerosols in the Tropopause Region, *Journal of Atmospheric and Oceanic Technology*, **16**, 1373–1383, doi:10.1175/1520-0426(1999)016<1373:CCAFGM>2.0.CO;2.
- Carn, S. A., et al. (2007), Extended observations of volcanic SO<sub>2</sub> and sulfate aerosol in the stratosphere, *Atmospheric Chemistry and Physics Discussions*, **7**, 2857–2871.
- Chaikovsky, A., et al. (2006), CIS-LiNet - Lidar Network for Monitoring Aerosol and Ozone in CIS Regions, Proceedings of the 23<sup>rd</sup> International Laser Radar Conference, Nara, Japan (July 24-28, 2006).
- Chaikovsky, A., et al. (2008), *Software package for the retrieval of aerosol microphysical properties in the vertical column using combined lidar/photometer data (test version)*, Institute of Physics, National Academy of Sciences of Belarus, Minsk, Belarus.
- Cooney, J., J. Orr, and C. Tomasetti (1969), Measurements Separating the Gaseous and Aerosol Components of Laser Atmospheric Backscatter, *Nature*, **224**, 1098–1099.

## Bibliography

- Darland, E. J., G. E. Leroi, and C. G. Enke (1979), Pulse (Photon) Counting: Determination of Optimum Measurement System Parameters, *Analytical Chemistry*, **51**, 240–245, doi:10.1021/ac50038a021.
- De Tomasi, F., A. Blanco, and M. R. Perrone (2003), Raman lidar monitoring of extinction and backscattering of African dust layers and dust characterization, *Applied Optics*, **42**, 1699–1709, doi:10.1364/AO.42.001699.
- Deshler, T. (2008), A review of global stratospheric aerosol: Measurements, importance, life cycle, and local stratospheric aerosol, *Atmospheric Research*, **90**, doi:10.1016/j.atmosres.2008.03.016.
- Donovan, D. P., J. A. Whiteman, and A. I. Carswell (1993), Correction for nonlinear photon-counting effects in lidar systems, *Applied Optics*, **32**, 6742–6753, doi:10.1364/AO.32.006742.
- Draxler, R. (2012), HYSPLIT FAQs, July 2012, [http://www.arl.noaa.gov/faq\\_hg11.php](http://www.arl.noaa.gov/faq_hg11.php).
- Draxler, R. R., and G. D. Rolph (2012), HYSPLIT (HYbrid Single-Particle Lagrangian Integrated Trajectory) Model access via NOAA ARL READY Website (<http://ready.arl.noaa.gov/HYSPLIT.php>), *NOAA Air Resources Laboratory, Silver Spring, MD*.
- Elias, T., et al. (2006), Aerosol extinction in a remote continental region of the Iberian Peninsula during summer, *Journal of Geophysical Research*, **111**, doi:10.1029/2005JD006610.
- Elterman, L. (1968), UV, Visible, and IR Attenuation for Altitudes to 50 km, *Environmental Research Papers*, **285**.
- Esteve, A. R., et al. (2012), Sources of discrepancy between aerosol optical depth obtained from AERONET and in-situ aircraft profiles, *Atmospheric Chemistry and Physics*, **12**, 2987–3003, doi:10.5194/acp-12-2987-2012.
- European Parliament, C. (2008), Directive 2008/50/EC of the European Parliament and of the Council of 21 May 2008 on ambient air quality and cleaner air for Europe, European Union Law, pp. 1–44.
- Fernald, F. G. (1984), Analysis of atmospheric lidar observations: some comments, *Applied Optics*, **23**, 652–653, doi:10.1364/AO.23.000652.
- Fernald, F. G., B. M. Herman, and J. A. Reagan (1972), Determination of Aerosol Height Distributions by Lidar, *Journal of Applied Meteorology*, **11**, 482–489, doi:10.1175/1520-0450(1972)011<0482:DOAHDB>2.0.CO;2.
- Flamant, C., J. Pelon, P. H. Flamant, and P. Durand (1997), Lidar determination of the entrainment zone thickness at the top of the unstable marine atmospheric boundary layer, *Boundary Layer Meteorology*, **83**, 247–284, doi:10.1023/A:1000258318944.
- Flamant, C., et al. (2000), Airborne lidar measurements of aerosol spatial distribution and optical properties over the Atlantic Ocean during a European pollution outbreak of ACE-2, *Tellus B*, **52**, 662–677, doi:10.1034/j.1600-0889.2000.00083.x.

- Formenti, P., et al. (2001), Saharan dust in Brazil and Suriname during the Large-Scale Biosphere-Atmosphere Experiment in Amazonia (LBA)- Cooperative LBA Regional Experiment (CLAIRE) in March 1998, *Journal of Geophysical Research*, **106**, 14,919–14,934.
- Franke, K., et al. (2001), One-year observations of particle lidar ratio over the tropical Indian Ocean with Raman lidar, *Geophysical Research Letters*, **56**, 1766–1782, doi:10.1029/2001GL013671.
- Freudenthaler, V. (2008), The telecover test: A quality assurance tool for the optical part of a lidar system, Proceedings of the 24<sup>th</sup> International Laser Radar Conference, Boulder, Colorado, USA (June 23-27, 2008).
- Freudenthaler, V., et al. (2009), Depolarization ratio profiling at several wavelengths in pure Saharan dust during SAMUM 2006, *Tellus B*, **61**, 165–179, doi:10.1111/j.1600-0889.2008.00396.x.
- Froidevaux, M., et al. (2013), A Raman lidar to measure water vapor in the atmospheric boundary layer, *Advances in Water Resources*, **51**, 345–356, doi:10.1016/j.advwatres.2012.04.008.
- Gasteiger, J., S. Groß, V. Freudenthaler, and M. Wiegner (2011), Volcanic ash from Iceland over Munich: mass concentration retrieved from ground-based remote sensing measurements, *Atmospheric Chemistry and Physics*, **11**, 2209–2223, doi:10.5194/acp-11-2209-2011.
- Giannakaki, E., D. S. Balis, V. Amiridis, and C. Zerefos (2010), Optical properties of different aerosol types: seven years of combined Raman-elastic backscatter lidar measurements in Thessaloniki, Greece, *Atmospheric Measurement Techniques*, **3**, 569–578, doi:10.5194/amt-3-569-2010.
- Giglio, L., J. Descloitres, C. O. Justice, and Y. J. Kaufman (2003), An enhanced contextual fire detection algorithm for MODIS, *Remote Sensing of Environment*, **87**, 273–282, doi:10.1016/S0034-4257(03)00184-6.
- Gimmestad, G. G. (2008), Reexamination of depolarization in lidar measurements, *Applied Optics*, **47**, 3795–3802, doi:10.1364/AO.47.003795.
- Grein, M. (2006), Charakterisierung und Erweiterung der Empfängeroptik des IfT-Ramanlidars MARTHA für kombinierte Aerosol- und Wolkenmessungen, Diploma thesis, University of Leipzig, Faculty of Physics and Earth Sciences, Germany.
- Groß, S., et al. (2012a), Dual-wavelength linear depolarization ratio of volcanic aerosols: Lidar measurements of the Eyjafjallajökull plume over Maisach, Germany, *Atmospheric Environment*, **48**, 85–96, doi:10.1016/j.atmosenv.2011.06.017.
- Groß, S., et al. (2012b), Airborne high spectral resolution lidar observation of pollution aerosol during EUCAARI-LONGREX, *Atmospheric Chemistry and Physics Discussion*, **12**, 26,843–26,869, doi:10.5194/acpd-12-26843-2012.
- Gudmundsson, M. T., et al. (2012), Ash generation and distribution from the April-May 2010 eruption of Eyjafjallajökull, Iceland, *Scientific Reports*, **2**, doi:10.1038/srep00572.

## Bibliography

- Guerrero-Rascado, J. L., et al. (2007), Atmospheric vertical profiles obtained by Lidar over Évora during CAPEX project, International Geoscience and Remote Sensing Symposium, Barcelona, Spain (July 23-27, 2007). IEEE International, pp. 1709–1712.
- Guerrero-Rascado, J. L., et al. (2009), Extreme Saharan dust event over the southern Iberian Peninsula in September 2007: active and passive remote sensing from surface and satellite, *Atmospheric Chemistry and Physics*, **9**, 8453–8469, doi:10.5194/acp-9-8453-2009.
- Guerrero-Rascado, J. L., et al. (2010), Infrared lidar overlap function: an experimental determination, *Optics Express*, **18**, 20,350–20,359, doi:10.1364/OE.18.020350.
- Guerrero-Rascado, J. L., et al. (2012a), Detection of the stratospheric volcanic aerosol plume from the Nabro eruption in summer 2011 in the framework of SPALINET, European Aerosol Conference Handbook, Granada, Spain, (September 2-7, 2012).
- Guerrero-Rascado, J. L., et al. (2012b), First profiling of aerosol microphysical properties from combination of multi-wavelength lidar (EARLINET) and sun-photometric (AERONET) data at Évora (Portugal), European Aerosol Conference Handbook, Granada, Spain (September 2-7, 2012).
- Hayes, J. M., and D. A. Schoeller (1977), High precision pulse counting: Limitations and optimal conditions, *Analytical Chemistry*, **49**, 306–311, doi:10.1021/ac50010a031.
- Haywood, J., et al. (2003), Radiative properties and direct radiative effect of Saharan dust measured by the C-130 aircraft during SHADE: 1. Solar spectrum, *Journal of Geophysical Research*, **108**, 8577–8593, doi:10.1029/2002JD002687.
- Heese, B. (2009), *Manual for Polly<sup>XT</sup> Evora, Portugal. Version 1.0*, Leibniz-Institute for Tropospheric Research e. V., Leipzig, Germany.
- Heroux, L. (1968), Photoelectron counting in the extreme ultraviolet, *Applied Optics*, **7**, 2351–2360, doi:10.1364/AO.7.002351.
- Hitschfeld, W., and J. Bordan (1954), Errors inherent in the Radar measurement of rainfall at attenuating wavelengths, *Journal of Meteorology*, **11**, 58–67, doi:10.1175/1520-0469(1954)011(0058:EIITRM)2.0.CO;2.
- Höhn, D. H. (1969), Depolarization of a Laser Beam at 6328 Å due to Atmospheric Transmission, *Applied Optics*, **8**, 367–369, doi:10.1364/AO.8.000367.
- Holben, B. N., et al. (1998), AERONET - A federated instrument network and data archive for aerosol characterization, *Remote Sensing of Environment*, **66**, 1–16, doi:10.1016/S0034-4257(98)00031-5.
- Hoyt, D. V. (1977), A Redetermination of the Rayleigh Optical Depth and its Application to Selected Solar Radiation Problems, *Journal of Applied Meteorology*, **16**, 432–436, doi:10.1175/1520-0450(1977)016(0432:AROTRO)2.0.CO;2.
- Ilyinskaya, E., et al. (2011), Near-source observations of aerosol size distributions in the eruptive plumes from Eyjafjallajökull volcano, March-April 2010, *Atmospheric Environment*, **45**, 3210–3216, doi:10.1016/j.atmosenv.2011.03.017.

- Ishii, S., et al. (2012), Partial CO<sub>2</sub> Column-Averaged Dry-Air Mixing Ratio from Measurements by Coherent 2- $\mu$ m Differential Absorption and Wind Lidar with Laser Frequency Offset Locking, *Journal of Atmospheric and Oceanic Technology*, **29**, 1169–1181, doi:10.1175/JTECH-D-11-00180.1.
- ISO 2533 (1975), Standard atmosphere, International Organization for Standardization, Geneva, Switzerland.
- Keckhut, P., M. L. Chanin, and A. Hauchecorne (1990), Stratosphere temperature measurement using Raman lidar, *Applied Optics*, **29**, 5182–5186, doi:10.1364/AO.29.005182.
- Kent, G. S., and G. M. Hansen (1998), Multiwavelength lidar observations of the decay phase of the stratospheric aerosol layer produced by the eruption of Mount Pinatubo in June 1991, *Applied Optics*, **37**, 3861–3872, doi:10.1364/AO.37.003861.
- Klett, J. D. (1981), Stable analytical inversion solution for processing lidar returns, *Applied Optics*, **20**, 211–220, doi:10.1364/AO.20.000211.
- Klett, J. D. (1985), Lidar inversion with variable backscatter/extinction ratios, *Applied Optics*, **24**, 1638–1643, doi:10.1364/AO.24.001638.
- Kolgotin, A., and D. Müller (2008), Theory of inversion with two-dimensional regularization: profiles of microphysical particle properties derived from multiwavelength lidar measurements, *Applied Optics*, **47**, 4472–4490.
- Kovalev, V. A. (1995), Sensitivity of the lidar solution to errors of the aerosol backscatter-to-extinction ratio: influence of a monotonic change in the aerosol extinction coefficient, *Applied Optics*, **34**, 3457–3462, doi:10.1364/AO.34.003457.
- Kovalev, V. A., and W. E. Eichinger (2004), *Elastic Lidar: Theory, Practice, and Analysis Methods*, John Wiley & Sons, Inc., Hoboken, New Jersey, USA.
- Kovalev, V. A., and H. Moosmüller (1994), Distortion of particulate extinction profiles measured with lidar in a two-component atmosphere, *Applied Optics*, **33**, 6499–6507, doi:10.1364/AO.33.006499.
- Landsat Project Science Office (2012), *Landsat 7 Science Data Users Handbook*, Goddard Space Flight Center (NASA), Greenbelt, Maryland, USA.
- Levy, R. C., et al. (2010), Global evaluation of the Collection 5 MODIS dark-target aerosol products over land, *Atmospheric Chemistry and Physics*, **10**, doi:10.5194/acp-10-10399-2010.
- Li, T., et al. (2011), Middle atmosphere temperature trend and solar cycle revealed by long-term Rayleigh lidar observations, *Journal of Geophysical Research*, **116**, D00P05, doi:10.1029/2010JD015275.
- Liu, Z., N. Sugimoto, and T. Murayama (2002), Extinction-to-backscatter ratio of Asian dust observed with high-spectral-resolution lidar and Raman lidar, *Applied Optics*, **41**, 2760–2767, doi:10.1364/AO.41.002760.

## Bibliography

- Lohmann, U., and J. Feichter (2005), Global indirect aerosol effects: a review, *Atmospheric Chemistry and Physics*, **5**, 715–737, doi:10.5194/acp-5-715-2005.
- Maletto, A., I. G. McKendry, and K. B. Strawbridge (2003), Profiles of particulate matter size distributions using a balloon-borne lightweight aerosol spectrometer in the planetary boundary layer, *Atmospheric Environment*, **37**, 661–670, doi:10.1016/S1352-2310(02)00860-9.
- Mamouri, R. E., et al. (2009), Validation of CALIPSO space-borne-derived attenuated backscatter coefficient profiles using a ground-based lidar in Athens, Greece, *Atmospheric Measurement Techniques*, **2**, 513–522, doi:10.5194/amt-2-513-2009.
- Mattis, I., A. Ansmann, U. Wandinger, and D. Müller (2003), Unexpectedly high aerosol load in the free troposphere over central Europe in spring/summer 2003, *Geophysical Research Letters*, **30**, doi:10.1029/2003GL018442.
- Mattis, I., et al. (2008), Ten years of multiwavelength Raman lidar observations of free-tropospheric aerosol layers over central Europe: Geometrical properties and annual cycle, *Journal of Geophysical Research*, **113**, doi:10.1029/2007JD009636.
- Mattis, I., M. Tesche, M. Grein, V. Freudenthaler, and D. Müller (2009), Systematic error of lidar profiles caused by a polarization-dependent receiver transmission: quantification and error correction scheme, *Applied Optics*, **48**, 2742–2751, doi:10.1364/AO.48.002742.
- Mattis, I., et al. (2010), Volcanic aerosol layers observed with multiwavelength Raman lidar over central Europe in 2008–2009, *Journal of Geophysical Research*, **115**, doi:10.1029/2009JD013472.
- Melfi, S. H. (1972), Remote measurements of the atmosphere using raman scattering, *Applied Optics*, **11**, 1605–1610, doi:10.1364/AO.11.001605.
- Middleton, W. E. K., and A. F. Spilhaus (1953), *Meteorological instruments*, University of Toronto Press, Toronto, Canada.
- Molero, F., et al. (2011a), Aerosol size distribution study by airborne and ground-level in-situ measurements and remote sensing during EARLINET lidar intercomparison campaign: SPALI10, European Aerosol Conference Handbook, Manchester, United Kingdom (September 4–9, 2011), p. 8P144.
- Molero, F., et al. (2011b), Study on aerosol properties over Madrid (Spain) by multiple instrumentation during EARLINET lidar intercomparison campaign: SPALI10, Proceedings of Quinta Reunión Española de Ciencia y Tecnología del Aerosoles (RECTA), Madrid, Spain (June 27–29, 2011), ISBN 978-84-7834-662-2.
- Mona, L., A. Amodeo, M. Pandolfi, and G. Pappalardo (2006), Saharan dust intrusions in the Mediterranean area: Three years of Raman lidar measurements, *Journal of Geophysical Research*, **111**, doi:10.1029/2005JD006569.
- Mona, L., et al. (2009), One year of CNR-IMAA multi-wavelength Raman lidar measurements in coincidence with CALIPSO overpasses: Level 1 products comparison, *Atmospheric Chemistry and Physics*, **9**, 7213–7228, doi:10.5194/acp-9-7213-2009.

- Mona, L., et al. (2012), Multi-wavelength Raman lidar observations of the Eyjafjallajökull volcanic cloud over Potenza, southern Italy, *Atmospheric Chemistry and Physics*, **12**, 2229–2244, doi:10.5194/acp-12-2229-2012.
- Müller, D., U. Wandinger, and A. Ansmann (1999), Microphysical particle parameters from extinction and backscatter lidar data by inversion with regularization: theory, *Applied Optics*, **38**, 2346–2357.
- Müller, D., et al. (2003), Saharan dust over a central European EARLINET-AERONET site: Combined observations with Raman lidar and Sun photometer, *Journal of Geophysical Research*, **108**, doi:10.1029/2002JD002918.
- Müller, D., I. Mattis, U. Wandinger, A. Ansmann, and D. Althausen (2005), Raman lidar observations of aged Siberian and Canadian forest fire smoke in the free troposphere over Germany in 2003: Microphysical particle characterization, *Journal of Geophysical Research*, **110**, doi:10.1029/2004JD005756.
- Müller, D., et al. (2007), Aerosol-type-dependent lidar ratios observed with Raman lidar, *Journal of Geophysical Research*, **112**, doi:10.1029/2006JD008292.
- Murayama, T., et al. (2001), Ground-based network observation of Asian dust events of April 1998 in east Asia, *Journal of Geophysical Research*, **106**, 18,345–18,359, doi:10.1029/2000JD900554.
- Murayama, T., et al. (2004), Characterization of Asian dust and Siberian smoke with multi-wavelength Raman lidar over Tokyo, Japan in spring 2003, *Geophysical Research Letters*, **31**, doi:10.1029/2004GL021105.
- NASA Langley ASDC (2010), CALIPSO Data Quality Statements: Summary Statement for the release of the CALIPSO Lidar Level 2 Cloud and Aerosol Profile Products Version 3.01, May 2010. (available at [http://www-calipso.larc.nasa.gov/resources/calipso\\_users\\_guide](http://www-calipso.larc.nasa.gov/resources/calipso_users_guide)).
- Neal, C. A., et al. (2011), *2008 Volcanic activity in Alaska, Kamchatka, and the Kurile Islands: Summary of events and response of the Alaska Volcano Observatory*, p. 94, U.S. Geological Survey Scientific Investigations Report 2010-5243.
- Nickovic, S., G. Kallos, A. Papadopoulos, and O. Kakaliagou (2001), A model for prediction of desert dust cycle in the atmosphere, *Journal of Geophysical Research*, **106**, 18,113–18,129, doi:10.1029/2000JD900794.
- Obregón, M. A., et al. (2012), Regional differences of column aerosol parameters in western iberian peninsula, *Atmospheric Environment*, **62**, 208–219, doi:10.1016/j.atmosenv.2012.08.016.
- Papayannis, A., G. Ancellet, J. Pelon, and G. Mégie (1990), Multiwavelength lidar for ozone measurements in the troposphere and the lower stratosphere, *Applied Optics*, **29**, 467–476, doi:10.1364/AO.29.000467.

## Bibliography

- Papayannis, A., et al. (2005), Measurements of Saharan dust aerosols over the Eastern Mediterranean using elastic backscatter-Raman lidar, spectrophotometric and satellite observations in the frame of the EARLINET project, *Atmospheric Chemistry and Physics*, **5**, 2065–2079.
- Papayannis, A., et al. (2007), Extraordinary dust event over Beijing, China, during April 2006: Lidar, Sun photometric, satellite observations and model validation, *Geophysical Research Letters*, **34**, doi:10.1029/2006GL029125.
- Papayannis, A., et al. (2008), Systematic lidar observations of Saharan dust over Europe in the frame of EARLINET (2000-2002), *Journal of Geophysical Research*, **113**, doi:10.1029/2007JD009028.
- Pappalardo, G., et al. (2004), Aerosol lidar intercomparison in the framework of the EARLINET project. 3. Raman lidar algorithm for aerosol extinction, backscatter, and lidar ratio, *Applied Optics*, **43**, 5370–5385, doi:10.1364/AO.43.005370.
- Pappalardo, G., et al. (2010), EARLINET correlative measurements for CALIPSO: First intercomparison results, *Journal of Geophysical Research*, **115**, doi:10.1029/2009JD012147.
- Pappalardo, G., et al. (2012), Four-dimensional distribution of the 2010 Eyjafjallajökull volcanic cloud over Europe observed by EARLINET, *Atmospheric Chemistry and Physics Discussion*, **12**, 30,203–30,257, doi:10.5194/acpd-12-30203-2012.
- Patashnick, H., and E. G. Rupprecht (1991), Continuous PM10 measurements using the tapered element oscillating microbalance, *Journal of Air and Waste Management*, **41**, 1079–1083.
- Pereira, S., F. Wagner, and A. M. Silva (2008), Scattering properties and mass concentration of local and long-range transported aerosols over the South Western Iberia Peninsula, *Atmospheric Environment*, **42**, 7623–7631, doi:10.1016/j.atmosenv.2008.06.008.
- Pereira, S., F. Wagner, and A. M. Silva (2009), Continuous measurements of near surface aerosols in the south-western European (Portugal) region in 2006-2008, *Advances in Science and Research*, **3**, 1–4.
- Pereira, S., F. Wagner, and A. M. Silva (2011), Seven years of measurements of aerosol scattering properties, near the surface, in the southwestern Iberia Peninsula, *Atmospheric Chemistry and Physics*, **11**, doi:10.5194/acp-11-17-2011.
- Porter, J. N., K. A. Horton, P. J. Mouginiis-Mark, and B. Lienert (2002), Sun photometer and lidar measurements of the plume from the Hawaii Kilauea Volcano Pu'u O'o vent: Aerosol flux and SO<sub>2</sub> lifetime, *Geophysical Research Letters*, **29**, doi:10.1029/2002GL014,744.
- Prata, A. J., A. Carn, S. A. Stohl, and J. Kerkmann (2007), Long range transport and fate of a stratospheric volcanic cloud from Soufrière Hills volcano, Montserrat, *Atmospheric Chemistry and Physics*, **7**, 5093–5103, doi:10.5194/acp-7-5093-2007.

- Preißler, J. (2008), Geometrische und optische Eigenschaften von Aerosolschichten aus verschiedenen Quellregionen Europas (Geometrical and optical properties of aerosol layers from several European source regions), Diploma thesis, University of Leipzig, Faculty of Physics and Earth Sciences, Leipzig, Germany.
- Preißler, J., F. Wagner, and A. M. Silva (2010a), First regular multi-wavelength Raman lidar measurements in Portugal - a case study, Proceedings of the 25<sup>th</sup> International Laser Radar Conference, Saint Petersburg, Russia (July 5-9, 2010), ISBN 978-5-94458-109-9.
- Preißler, J., F. Wagner, J. L. Guerrero-Rascado, and A. M. Silva (2010b), Ash from the Eyjafjallajökull volcano observed by lidar over Portugal, Proceedings of the 25<sup>th</sup> International Laser Radar Conference, Saint Petersburg, Russia (July 5-9, 2010), ISBN 978-5-94458-109-9.
- Preißler, J., F. Wagner, S. N. Pereira, and J. L. Guerrero-Rascado (2011a), Multi-instrumental observation of an exceptionally strong Saharan dust outbreak over Portugal, *Journal of Geophysical Research*, **116**, D24,204, doi:10.1029/2011JD016527.
- Preißler, J., F. Wagner, J. L. Guerrero-Rascado, and A. M. Silva (2011b), One year of regular aerosol observations with a multi-wavelength Raman lidar in Portugal, Lidar Technologies, Techniques, and Measurements for Atmospheric Remote Sensing VII, Proceedings of SPIE Vol. 8182, p. 81820C, doi:10.1117/12.897453.
- Preißler, J., et al. (2012a), Optical properties of free tropospheric aerosol from multi-wavelength Raman lidars over the southern Iberian Peninsula, Proceedings of the 9<sup>th</sup> International Symposium on Tropospheric Profiling, l'Aquila, Italy (September 3-7, 2012), ISBN 978-90-815839-4-7.
- Preißler, J., et al. (2012b), Combined observations with multi-wavelength Raman lidars and sun photometers on the southern Iberian Peninsula, European Aerosol Conference Handbook, Granada, Spain (September 2-7, 2012).
- Ramanathan, V., et al. (2001), Indian Ocean Experiment: An integrated analysis of the climate forcing and effects of the great Indo-Asian haze, *Journal of Geophysical Research*, **106**, 28,371–28,398, doi:10.1029/2001JD900133.
- Reid, J. S., R. Koppmann, T. F. Eck, and D. P. Eleuterio (2005a), A review of biomass burning emissions part II: intensive physical properties of biomass burning particles, *Atmospheric Chemistry and Physics*, **5**, 799–825, doi:10.5194/acp-5-799-2005.
- Reid, J. S., et al. (2005b), A review of biomass burning emissions part III: intensive optical properties of biomass burning particles, *Atmospheric Chemistry and Physics*, **5**, 827–849, doi:10.5194/acp-5-827-2005.
- Remer, L. A., et al. (2005), The MODIS Aerosol Algorithm, Products, and Validation, *Journal of the Atmospheric Sciences — Special Section*, **62**, 947–973, doi:10.1175/JAS3385.1.
- Rodríguez, E., et al. (2012), Comparison of aerosol optical properties at the sub-arctic stations ALOMAR-Andenes, Abisko and Sodankylä in late spring and summer 2007, *Atmospheric Research*, **107**, 20–30, doi:10.1016/j.atmosres.2011.12.003.

## Bibliography

- Rolph, G. D., and R. R. Draxler (1990), Sensitivity of three-dimensional trajectories to the spatial and temporal densities of the wind field, *Journal of Applied Meteorology*, **29**, 1043–1054, doi:10.1175/1520-0450(1990)029<1043:SOTDTT>2.0.CO;2.
- Russel, P. B., T. J. Swissler, and M. P. McCormick (1979), Methodology for error analysis and simulation of lidar aerosol measurements, *Applied Optics*, **18**, 3783–3797, doi:10.1364/AO.18.003783.
- Russell, P. B., P. V. Hobbs, and L. L. Stowe (1999), Aerosol properties and radiative effects in the United States East Coast haze plume: An overview of the Tropospheric Aerosol Radiative Forcing Observational Experiment (TARFOX), *Journal of Geophysical Research*, **104**, 2213–2222, doi:10.1029/1998JD200028.
- Santos, D., M. J. Costa, and A. M. Silva (2008), Direct SW aerosol radiative forcing over Portugal, *Atmospheric Chemistry and Physics*, **8**, doi:10.5194/acp-8-5771-2008.
- Sasano, Y., E. V. Browell, and S. Ismail (1985), Error caused by using a constant extinction/backscattering ratio in the lidar solution, *Applied Optics*, **24**, 3929–3932, doi:10.1364/AO.24.003929.
- Sassen, K. (2005), Polarization in lidar, in *Lidar: Range resolved optical remote sensing of the atmosphere*, edited by C. Weitkamp, pp. 19–42, Springer Science+Business Media Inc., New York, NY, USA.
- Sawamura, P., et al. (2012), Stratospheric AOD after the 2011 eruption of Nabro volcano measured by lidars over the Northern Hemisphere, *Environmental Research Letters*, **7**, doi:10.1088/1748-9326/7/3/034013.
- Schaefer, J. R. (Ed.) (2012), *Report of Investigations 2011-5 - The 2009 eruption of Redoubt volcano, Alaska*, p. 55, State of Alaska, Department of Natural Resources, Division of Geological and Geophysical Surveys.
- Schotland, R. M., K. Sassen, and R. Stone (1971), Observations by lidar of linear depolarization ratios for hydrometeors, *Journal of Applied Meteorology*, **10**, 1011–1017, doi:10.1175/1520-0450(1971)010<1011:OBLOLD>2.0.CO;2.
- Sicard, M., et al. (2011), SPALINET: The Spanish and Portuguese aerosol lidar network, *Óptica Pura y Aplicada*, **44**, 1–5.
- Sicard, M., et al. (2012), Monitoring of the Eyjafjallajökull volcanic aerosol plume over the Iberian Peninsula by means of four EARLINET lidar stations, *Atmospheric Chemistry and Physics*, **12**, 3115–3130, doi:10.5194/acp-12-3115-2012.
- Silva, A. M., et al. (2002), Aerosol optical properties from columnar data during the second Aerosol Characterization Experiment on the south coast of Portugal, *Journal of Geophysical Research*, **107**, doi:10.1029/2002JD002196.
- Silva, A. M., et al. (2003), Ground based aerosol monitoring at Évora, Portugal, *Global Change Newsletter*, **56**, 5–9.

- Smithsonian Institution (2012), Global Volcanism, 1968 to the Present., Smithsonian Institution, Global Volcanism Program Digital Information Series, GVP-4 (<http://www.volcano.si.edu/reports/>, May 2012).
- Sokolik, I. N., et al. (2001), Introduction to special section: Outstanding problems in quantifying the radiative impacts of mineral dust, *Journal of Geophysical Research*, **106**, 18,015–18,027, doi:10.1029/2000JD900498.
- Solomon, S., et al. (Eds.) (2007), *Climate Change 2007: The Physical Science Basis. Contribution of Working Group I to the Fourth Assessment Report of the Intergovernmental Panel on Climate Change*, Cambridge University Press, Cambridge, United Kingdom and New York, NY, USA.
- Stocks, B. J., et al. (2002), Large forest fires in Canada, 1959-1997, *Journal of Geophysical Research*, **107**, doi:10.1029/2001JD000484.
- Stohl, A. (1998), Computation, accuracy and applications of trajectories - a review and bibliography, *Atmospheric Environment*, **32**, 947–966, doi:10.1016/S1352-2310(97)00457-3.
- Stohl, A., C. Forster, A. Frank, P. Seibert, and G. Wotawa (2005), Technical note: The Lagrangian particle dispersion model FLEXPART version 6.2, *Atmospheric Chemistry and Physics*, **5**, 2461–2474, doi:10.5194/acp-5-2461-2005,.
- Stull, R. B. (1988), *An Introduction to Boundary-Layer Meteorology*, 666 pp., Kluwer Academic Publishers, Dordrecht, The Netherlands.
- Takamura, T., and Y. Sasano (1987), Ratio of aerosol backscatter to extinction coefficients as determined from angular scattering measurements for use in atmospheric lidar applications, *Optical and Quantum Electronics*, **29**, 293–302, doi:10.1007/BF02032687.
- Teillet, P. M. (1990), Rayleigh optical depth comparisons from various sources, *Applied Optics*, **29**, 1897–1900, doi:10.1364/AO.29.001897.
- Tesche, M., et al. (2009), Vertical profiling of Saharan dust with Raman lidars and airborne HSRL in southern Morocco during SAMUM, *Tellus B*, **61**, 144–164, doi:10.1111/j.1600-0889.2008.00390.x.
- Thomas, H. E., and A. J. Prata (2011), Sulphur dioxide as a volcanic ash proxy during the April-May 2010 eruption of Eyjafjallajökull Volcano, Iceland, *Atmospheric Chemistry and Physics*, **11**, 6871–6880, doi:10.5194/acp-11-6871-2011.
- Twomey, S. (Ed.) (1977), *Introduction to the Mathematics of Inversion in Remote Sensing and Indirect Measurements*, Elsevier, Amsterdam, The Netherlands.
- Venzke, E., S. K. Sennert, and R. Wunderman (2009), Reports from the Smithsonian's Global Volcanism Network, June 2009, *Bulletin of Volcanology*, **71**, 1211–1212, doi:10.1007/s00445-009-0323-5.
- Veselovskii, I., et al. (2002), Inversion with regularization for the retrieval of tropospheric aerosol parameters from multiwavelength lidar sounding, *Applied Optics*, **41**, 3685–3699.

## Bibliography

- Villani, M. G., et al. (2006), Transport of volcanic aerosol in the troposphere: The case study of the 2002 Etna plume, *Journal of Geophysical Research*, **111**, doi:10.1029/2006JD007126.
- Wagner, F., and J. Preißler (2012), On the determination of stratospheric aerosol layers, Proceedings of the 26<sup>th</sup> International Laser Radar Conference, Porto Heli, Greece (July 25-29, 2012).
- Wagner, F., et al. (2009), Properties of dust aerosol particles transported to Portugal from the Sahara desert, *Tellus B*, **61**, 297–306, doi:10.1111/j.1600-0889.2008.00393.x.
- Wagner, F., J. Preißler, S. Pereira, and J. L. Guerrero-Rascado (2012), Long-term observations of the Nabro stratospheric aerosol layer over Évora, Portugal, Proceedings of the 26<sup>th</sup> International Laser Radar Conference, Porto Heli, Greece (July 25-29, 2012).
- Wagner, J. (2012), Microphysical aerosol properties retrieved from combined lidar and sun photometer measurements, Diploma thesis, University of Leipzig, Faculty of Physics and Earth Sciences, Germany.
- Wandinger, U. (2005), Introduction to lidar, in *Lidar: Range resolved optical remote sensing of the atmosphere*, edited by C. Weitkamp, pp. 1–18, Springer Science+Business Media Inc., New York, NY, USA.
- Wandinger, U., and A. Ansmann (2002), Experimental determination of the lidar overlap profile with Raman lidar, *Applied Optics*, **41**, 511–514, doi:10.1364/AO.41.000511.
- Wandinger, U., et al. (2010), Size matters: Influence of multiple scattering on CALIPSO light-extinction profiling in desert dust, *Geophysical Research Letters*, **37**, doi:10.1029/2010GL042815.
- Wang, X., et al. (2006), Volcanic dust characterization by EARLINET during Etna’s eruptions in 2001-2002, *Atmospheric Environment*, **42**, 893–905, doi:10.1016/j.atmosenv.2007.10.020.
- Weitkamp, C. (Ed.) (2005), *Lidar: Range resolved optical remote sensing of the atmosphere*, 456 pp., Springer Science+Business Media Inc., New York, NY, USA.
- Welton, E. J., J. R. Campbell, J. D. Spinhirne, and V. S. Scott (2001), Global monitoring of clouds and aerosols using a network of micro-pulse lidar systems, in *Lidar Remote Sensing for Industry and Environmental Monitoring*, Lidar Remote Sensing for Industry and Environment Monitoring, Proceedings of SPIE Vol. 4153, pp. 151–158, ISBN 978-08-1943-806-5.
- Wendler, G. (1984), Effects of the El Chichón Volcanic Cloud on Solar Radiation Received at Fairbanks, Alaska, *Bulletin of the American Meteorological Society*, **65**, 216–218, doi:10.1175/1520-0477(1984)065<0216:EOTECV>2.0.CO;2.
- Whiteman, D. N. (2003a), Examination of the Traditional Raman Lidar Technique. I. Evaluating the Temperature-Dependent Lidar Equations, *Applied Optics*, **42**, 2571–2592, doi:10.1364/AO.42.002571.

- Whiteman, D. N. (2003b), Examination of the Traditional Raman Lidar Technique. II. Evaluating the Ratios for Water Vapor and Aerosols, *Applied Optics*, **42**, 2593–2608, doi:10.1364/AO.42.002593.
- Whiteman, D. N., S. H. Melfi, and R. A. Ferrare (1992), Raman lidar system for the measurement of water vapor and aerosols in the Earth's atmosphere, *Applied Optics*, **31**, 3068–3082, doi:10.1364/AO.31.003068.
- Whiteman, D. N., et al. (2007), Demonstration Measurements of Water Vapor, Cirrus Clouds, and Carbon Dioxide Using a High-Performance Raman Lidar, *Journal of Atmospheric and Oceanic Technology*, **24**, 1377–1388, doi:10.1175/JTECH2058.1.
- Winker, D. M., W. H. Hunt, and M. J. McGill (2007), Initial performance assessment of CALIOP, *Geophysical Research Letters*, **34**, doi:10.1029/2007GL030135.
- Winker, D. M., et al. (2010), The CALIPSO Mission: A Global 3D View of Aerosols and Clouds, *Bulletin of the American Meteorological Society*, **91**, 1211–1229, doi:10.1175/2010BAMS3009.1.
- Wotawa, G., P. C. Novelli, M. Trainer, and C. Granier (2001), Inter-annual variability of summertime CO concentrations in the Northern Hemisphere explained by boreal forest fires in North America and Russia, *Geophysical Research Letters*, **28**, 4575–4578, doi:10.1029/2001GL013686.
- Yu, H., et al. (2006), A review of measurement-based assessments of the aerosol direct radiative effect and forcing, *Atmospheric Chemistry and Physics*, **6**, 613–666, doi:10.5194/acp-6-613-2006.

# List of Acronyms

- ACE2** Second Aerosol Characterization Experiment
- ACTRIS** Aerosols, Clouds, and Trace gases Research Infrastructure Network
- AD** Asian dust (aerosol subtype in section (4.4))
- AD-Net** Asian Dust Network
- AERONET** Aerosol Robotic Network
- agl** above ground level
- AOD** aerosol optical depth
- APS** Aerodynamic Particle Sizer Spectrometer
- asl** above sea level
- ATL** aerosol from the Atlantic (aerosol type in section (4.4))
- a.u.** arbitrary unit
- CALIPSO** Cloud-Aerosol Lidar and Infrared Pathfinder Satellite Observations
- CALIOP** Cloud Aerosol Lidar with Orthogonal Polarization
- CCD** charge-coupled device
- CEAMA** Andalusian Center for Environmental Research (Centro Andaluz de Medio Ambiente)
- CGE** Évora Geophysics Center (Centro de Geofísica de Évora)
- CIS-LINet** Commonwealth of Independent States Lidar Network
- DJF** December, January, February (winter)
- DREAM** Dust Regional Atmospheric Model
- DUS** mineral dust (aerosol type in section (4.4))
- EARLINET** European Aerosol Research Lidar Network
- EUR** European anthropogenic aerosol (aerosol type in section (4.4))
- EYJ** volcanic aerosol from Eyjafjallajökull (aerosol subtype in section (4.4))
- FOV** field of view

- FP7** 7<sup>th</sup> Framework Programme of the European Commission
- FWHM** full width at half maximum
- GALION** Global Atmosphere Watch Aerosol Lidar Observation Network
- GDAS** Global Data Assimilation System
- GIOVANNI** GES-DISC (Goddard Earth Sciences Data and Information Services Center)  
Interactive Online Visualization And Analysis Infrastructure
- HYSPLIT** Hybrid Single-Particle Lagrangian Integrated Trajectory
- IBF** Iberian biomass burning smoke (aerosol type in section (4.4))
- INDOEX** Indian Ocean Experiment
- JJA** June, July, August (summer)
- laser** light amplification by stimulated emission of radiation
- lidar** light detection and ranging
- LISTaR** Leipzig Institute for Science, Technology and Research GmbH
- LIRIC** Lidar-Radiometer Inversion Code
- MAM** March, April, May (spring)
- Mcps** megacounts per second =  $10^6$  counts  $s^{-1}$
- MODIS** Moderate Resolution Imaging Spectroradiometer
- MPLNET** Micro-Pulse Lidar Network
- MRF** Medium Range Forecast
- MUSA** Multiwavelength System for Aerosol
- NAA** North American anthropogenic aerosol (aerosol type in section (4.4))
- NAAPS** Navy Aerosol Analysis and Prediction System
- NAB** volcanic aerosol from Nabro (aerosol subtype in section (4.4))
- NAF** biomass burning smoke from North America (aerosol type in section (4.4))
- NASA** National Aeronautics and Space Administration
- Nd:YAG** neodymium-doped yttrium aluminium garnet
- NDF** neutral density filter
- NOAA ARL** Air Resources Laboratory of the National Oceanic and Atmospheric Administration

## *Bibliography*

- PAOLI** Portable Aerosol and Cloud Lidar
- PBL** planetary boundary layer
- PMT** photomultiplier tube
- Polly<sup>XT</sup>** Portable Raman Lidar System With Extended Capabilities
- SCC** Single Calculus Chain
- SD** Saharan dust (aerosol subtype in section (4.4))
- SHG** second harmonic generator
- SNR** signal-to-noise ratio
- SON** September, October, November (autumn)
- SPALI10** Lidar Intercomparison Campaign in Spain 2010
- SPALINET** Spanish and Portuguese Aerosol Lidar Network
- TEOM** Tapered Element Oscillating Microbalance
- THG** third harmonic generator
- TOA** top of the atmosphere
- TROPOS** Leibniz-Institute for Tropospheric Research e. V. (Leibniz-Institut für Troposphärenforschung e. V.)
- UNK** aerosol of unknown origin (unidentified aerosol layers in section (4.4))
- UTC** coordinated universal time
- VAAC** Volcanic Ash Advisory Centre
- VOL** aerosol of volcanic origin (aerosol type in section (4.4))

# List of Symbols

$\dot{a}$	Ångström exponent (without unit)
$A$	area of the primary receiver optics ( $\text{m}^2$ )
$b$	fitting parameter (without unit)
$c$	speed of light ( $3 \times 10^8 \text{ m s}^{-1}$ )
$C$	factor which contains columnar and molecular number density, refractive index of air and molecular depolarisation factor ( $\text{m}^3$ )
$d$	depolarisation parameter (without unit)
$D$	transmission ratio, ratio of transmission efficiencies (without unit)
$f_{\text{T}}$	transmission function (without unit)
$G$	term of the lidar equation, geometric term which contains the overlap function and the range correction ( $\text{m}^{-2}$ )
$i$	index, detection channel of PAOLI (without unit)
$j$	index, type of scatterer (without unit)
$k$	factor for depolarisation calibration (without unit)
$K$	term of the lidar equation, describes the performance of the lidar system ( $\text{W m}^3 = \text{kg m}^5 \text{ s}^{-3}$ )
$M$	particle mass concentration ( $\mu\text{g m}^{-3}$ )
$n$	count rate ( $\text{s}^{-1}$ )
$N$	concentration of particles ( $\text{m}^{-3}$ )
$dN/d\log D$	particle size distribution ( $\text{m m}^{-3}$ )
$O$	overlap function (without unit)
$p$	pressure ( $\text{hPa} = 100 \text{ kg m}^{-1} \text{ s}^{-2}$ )
$P$	received power ( $\text{W} = \text{kg m}^2 \text{ s}^{-3}$ )
$P_0$	mean power of the emitted pulse ( $\text{W} = \text{kg m}^2 \text{ s}^{-3}$ )
$P_{BG}$	background signal, caused by skylight and light sources on the ground ( $\text{W} = \text{kg m}^2 \text{ s}^{-3}$ )
$P_{corr}$	range and overlap corrected lidar signal ( $\text{W} = \text{kg m}^2 \text{ s}^{-3}$ )
$P_{RC}$	range corrected lidar signal ( $\text{W} = \text{kg m}^2 \text{ s}^{-3}$ )
$p_s$	standard pressure (1013.25 hPa)
$r$	distance from the lidar system, corresponds to the height if the light beam is emitted vertically (m)
$R$	backscatter ratio, ratio of total backscatter coefficient to molecular backscatter coefficient (without unit)
$S$	extinction-to-backscatter ratio (lidar ratio) (sr)
$t$	time (s)
$t_d$	dead time (s)
$t_p$	temporal pulse length (s)

## Bibliography

$T$	term of the lidar equation, transmittance (without unit)
$T$	temperature (K)
$T_s$	standard surface temperature (288.15 K)
$X$	for determination of relative dependence, any parameter (unit depending on parameter)
$Y$	normalised total extinction coefficient ( $\text{m}^{-1}$ )
$z$	height above the lidar system (m)
$z_0$	reference height (m)
$z_{ovl}$	minimum range of full overlap between laser beam and receiver field of view (m)
$\alpha$	extinction coefficient ( $\text{m}^{-1}$ )
$\beta$	backscatter coefficient ( $\text{m}^{-1} \text{sr}^{-1}$ )
$\Delta$	normalised difference (without unit)
$\Delta_{atm}$	atmospheric change during a telecover test (without unit)
$\delta_{par}$	linear particle depolarisation ratio (without unit)
$\delta_v$	linear volume depolarisation ratio (without unit)
$\eta$	system efficiency (without unit)
$\eta_i$	transmission efficiency of the receiver channel i (without unit)
$\Theta$	zenith angle of the laser beam of PAOLI ( $^\circ$ )
$\lambda$	wavelength (nm)
$\lambda_0$	wavelength emitted by the laser (nm)
$\lambda_{Ra}$	Raman wavelength (nm)
$\sigma_j^{sca}$	scattering cross section for scatterer of type j ( $\text{m}^2$ )
$\tau$	aerosol optical depth (without unit)
$\Omega$	solid angle ( $^\circ$ )